Polymer:fullerene bulk-heterojunction solar cells

Polymer:Fullerene Bulk-Heterojunction Solar Cells

Polymer:Fullerene Bulk-Heterojunction Solar Cells

PROEFSCHRIFT

ter verkrijging van de graad van doctor aan de Technische Universiteit Eindhoven, op gezag van de Rector Magnificus, prof.dr. R.A. van Santen, voor een commissie aangewezen door het College voor Promoties in het openbaar te verdedigen op maandag 8 maart 2004 om 16.00 uur

door

Jeroen Karolus Johannes van Duren

geboren te Someren

Dit proefschrift is goedgekeurd door de promotoren:

prof.dr.ir. R.A.J. Janssen
en
prof.dr.ir. P.W.M. Blom

This research has been financially supported by the Dutch government through the E.E.T. program (EETK97115).

Omslagontwerp: Jeroen van Duren

Druk: Universiteitsdrukkerij, Technische Universiteit Eindhoven

CIP-DATA LIBRARY TECHNISCHE UNIVERSITEIT EINDHOVEN

Duren, Jeroen K.J.

Polymer : fullerene bulk-heterojunction solar cells / by Jeroen K.J. van Duren. – Eindhoven : Technische Universiteit Eindhoven, 2004.
Proefschrift. – ISBN 90-386-2905-2
NUR 913
Trefwoorden: zonnecellen / organische halfgeleiders / geleidende polymeren / fullerenen / fotogeïnduceerde elektronenoverdracht / composietpolymeren; morfologie / oppervlakte-onderzoek; diepteprofileren
Subject headings: solar cells / organic semiconductors / conducting polymers / fullerenes / photoinduced electron transfer / polymer morphology; composites /
surface analysis; depth profiling

Contents

Chapter 1

Introduction

Abstract

New photovoltaic (PV) energy technologies can contribute to environmentally friendly, renewable energy production, and the reduction of the carbon dioxide emission associated with fossil fuels and biomass. One new PV technology, plastic solar cell technology, is based on conjugated polymers and molecules. Since the discovery of the huge increase of conductivity in the conjugated polymer polyacetylene when doped with iodine, and electroluminescence in conjugated polymers, the field of plastic electronics has made an enormous progress. Plastic solar cells have attracted considerable attention in the past few years owing to their potential of providing environmentally safe, flexible, lightweight, inexpensive, efficient solar cells. Especially, bulk-heterojunction solar cells consisting of a mixture of a conjugated donor polymer with a methanofullerene acceptor are considered as a promising approach. In this chapter a brief overview is given of the field of plastic solar cells, and a short outline is presented of the thesis.

1.1 Plastic solar cells

It is expected that the global energy demand will double within the next 50 years. Fossil fuels, however, are running out and are held responsible for the increased concentration of carbon dioxide in the earth's atmosphere. Hence, developing environmentally friendly, renewable energy is one of the challenges to society in the 21st century. One of the few renewable energy technologies available, is photovoltaics (PV), the technology that directly converts daylight into electricity. PV is one of the fastest growing of all the renewable energy technologies, in fact, it is one of the fastest growing industries at present.[1] Solar cell manufacturing based on the technology of crystalline, silicon devices is growing by approximately 40% per year and this growth rate is increasing.[1] This has been realized mainly by special market implementation programs and other government grants to encourage a substantial use of the current PV technologies based on silicon. Unfortunately, financial support by governments is under constant pressure.

At present, the active materials used for the fabrication of solar cells are mainly inorganic materials, such as silicon (Si), gallium-arsenide (GaAs), cadmium-telluride (CdTe), and cadmium-indium-selenide (CIS). The power conversion efficiency for these solar cells varies from 8 to 29% (Table 1.1). With regard to the technology used, these solar cells can be divided into two classes. The crystalline solar cells or silicon solar cells are made of either (mono- or poly-) crystalline silicon or GaAs. About 85% of the PV market is shared by these crystalline solar cells.[1] Amorphous silicon, CdTe, and CI(G)S are based on more recent thin-film technologies.

Table 1.1 *Status of the power conversion efficiencies in February 2002, as reached for inorganic solar cells and the technology used to prepare these solar cells. Source: Photovoltaic Network for the Development of a Roadmap for PV (PV-NET).*

Semiconductor material	Power conversion efficiency [%]	Technology
Mono-crystalline silicon	20-24	Crystalline
Poly-crystalline silicon	13-18	Thick and thin-film
Gallium-arsenide	20-29	Crystalline
Amorphous silicon	8-13	Thin-film
Cadmium telluride	10-17	Thin-film
Cadmium indium selenide	10-19	Thin-film

The current status of PV is that it hardly contributes to the energy market, because it is far too expensive. The large production costs for the silicon solar cells is one of the major obstacles. Even when the production costs could be reduced, large-scale production of the current silicon solar cells would be limited by the scarcity of some elements required, e.g. solar-grade silicon. To ensure a sustainable technology path for PV, efforts to reduce the costs of the current silicon technology need

to be balanced with measures to create and sustain variety in PV technology. It is, therefore, clear that 'technodiversity', implying new solar cell technologies, is necessary.[2] In the field of inorganics, thin-film technologies based on cheaper production processes are currently under investigation. Another approach is based on solar cells made of entirely new materials, conjugated polymers and molecules.

Conjugated materials are organics consisting of alternating single and double bonds. The field of electronics based on conjugated materials started in 1977 when Heeger, MacDiarmid, and Shirakawa discovered that the conductivity of the conjugated polymer polyacetylene (PA, Figure 1.1) can be increased by seven orders of magnitude upon oxidation with iodine,[3] for which they were awarded the Nobel Prize in Chemistry in 2000.[4-7] This discovery led, subsequently, to the discovery of electroluminescence in a poly(*p*-phenylene vinylene) (PPV, Figure 1.1) by Burroughes *et al*. in 1990.[8,9] The first light-emitting products based on electroluminescence in conjugated polymers have already been launched at the consumer market by Philips (The Netherlands) in 2002, whereas light-emitting products based on conjugated molecules have been introduced by the joint venture of Kodak and Sanyo (Japan). Going from discovery to product within a little bit more than one decade truly holds a huge promise for the future of plastic electronics. Other emerging applications are coatings for electrostatic dissipation and electromagnetic-interference shielding.[10]

Owing to the enormous progress made in the field of organic light-emitting diodes (LEDs), several other research fields based on organic electronics started to emerge in the past decade. Apart from light-emissive applications, mainly field-effect transistors (FETs),[11-13] and solar cells[14,15] are under investigation. Some other applications of interest are chemical sensors based on conjugated polymers,[16] Bragg reflectors and waveguides,[17] and integrated FET-LED structures.[18]

Conjugated polymers and molecules have the immense advantage of facile, chemical tailoring to alter their properties, such as the bandgap. Conjugated polymers (Figure 1.1) combine the electronic properties known from the traditional semiconductors and conductors with the ease of processing and mechanical flexibility of plastics. Therefore, this new class of materials has attracted considerable attention owing to its potential of providing environmentally safe, flexible, lightweight, inexpensive electronics.

The cost reduction mainly results from the ease of processing from solution. Solution processing requires soluble polymers. Poly[*p*-phenylene vinylene] (PPV, Figure 1.1) is hardly soluble. Attachment of side-groups to the conjugated backbone, as in poly[2-methoxy-5-(3′,7′-dimethyloctyloxy)-1,4-phenylene vinylene] (MDMO-PPV, Figure 1.1), enhances the solubility of the polymer enormously. Furthermore, the nanoscale morphology, affecting the opto-electronic properties of these polymer films, can be controlled by proper choice of the position and nature of these side-groups. The development of regio-regular polythiophenes, such as regio-regular poly[3-hexylthiophene] (P3HT, Figure 1.1) showed the huge effect side-groups can have on charge-carrier mobility.[12]

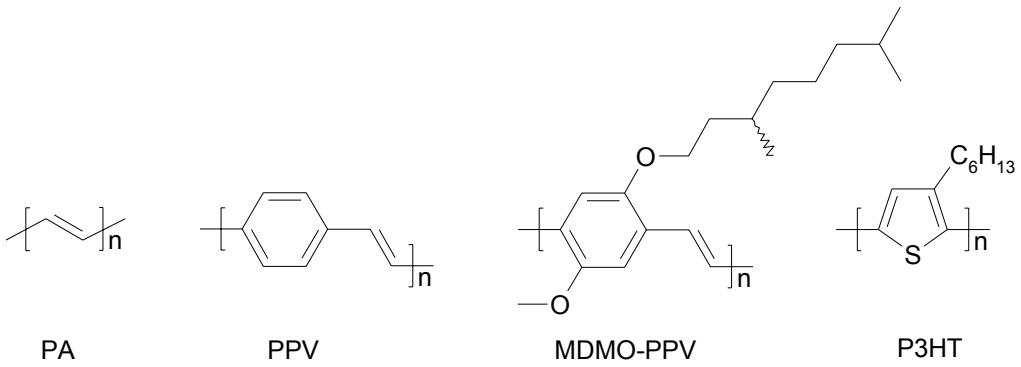

Figure 1.1 *Molecular structures of the conjugated polymers trans-polyacetylene (PA), poly(p-phenylene vinylene) (PPV), a substituted PPV (MDMO-PPV), and a substituted polythiophene (P3HT).*

Recent developments in ink-jet printing, micro-contact printing, and other soft lithography techniques have further improved the potential of conjugated polymers for low-cost fabrication of large-area integrated devices on both rigid and flexible substrates. Architectures to overcome possible electronic scale-up problems related to thin film organics are being developed.[19] In contrast to conjugated polymers, conjugated molecules are mainly thermally evaporated under high vacuum. This deposition technique is much more expensive than solution processing and, therefore, less attractive.

The necessity for new PV technologies together with the opportunities in the field of plastic electronics, such as roll-to-roll production, have drawn considerable attention to plastic solar cells in the past few years. Apart from application in PV, it is expected that plastic solar cells will create a completely new market in the field of cheap electronics.

1.2 Several approaches to plastic solar cells

A plastic solar cell typically consists of a photoactive layer sandwiched between a substrate covered with a transparent electrode, and a top electrode. Charges are generated under the influence of light in the photoactive layer. Subsequently, these charges are collected at both electrodes. This way light is converted into electricity.

The photoactive layer in organic solar cells generally contains two components. One component is an electron-donating material (easily oxidized, the donor, p-type) and the other one an electron-accepting material (easily reduced, the acceptor, n-type). The use of two components with different electronic levels is one of the most important design concepts in organic solar cells. Photoexcitations in an organic semiconductor have exciton character, i.e. a photoexcitation does not result in free charges, but in a bound electron-hole pair. By using a combination of donor and acceptor materials, dissociation of the exciton is achieved at the interface of both materials. The process of

charge separation at the interface between donor and acceptor after absorption of light is referred to as photoinduced charge transfer.

Several types of photoactive layers in organic solar cells are under investigation. In the first type, the photoactive layer consists of two, or multiple layers of different molecules.[20] In these cells, power conversion efficiencies (η_{pc}) of 2-3% under simulated solar light have been reached. Nowadays, bilayer structures with polymers instead of molecules exist as well.[21] One of the first solar cells, comprised of an organic photoactive layer, was a bilayer structure of copper phthalocyanine (CuPc) and a perylene tetracarboxylic derivative (PTC, Figure 1.2) as reported in 1986 by Tang.[22]

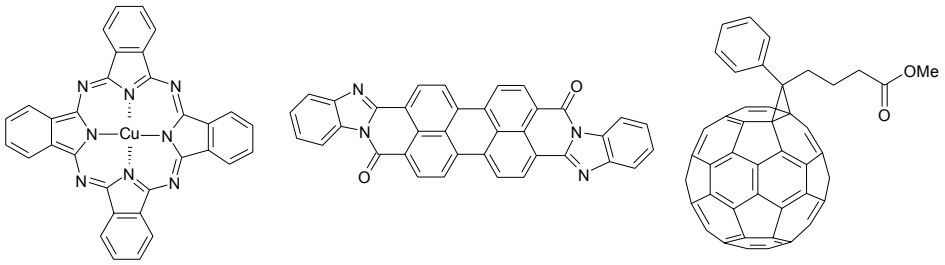

CuPc PTC PCBM

Figure 1.2 *Molecular structures of copper phthalocyanine (CuPc), a perylene tetracarboxylic derivative (PTC), and PCBM.*

Presently, the most widely used photoactive layer is based on a mixture of two (or more) components. This type of solar cell is called the bulk-heterojunction solar cell, because the interface (heterojunction) between both components is all over the bulk (Figure 1.3), in contrast to the classical (bilayer-) heterojunction. As a result of the intimate mixing, the interface where charge transfer can occur, has increased enormously. The exciton, created after the absorption of light, has to diffuse towards this charge-transfer interface for charge generation to occur. The diffusion length of the exciton in organic materials, however, is typically 10 nm or less. This means that for efficient charge generation after absorption of light, each exciton has to find a donor-acceptor interface within a few nm, otherwise it will be lost without charge generation. An intimate bicontinuous network of donor and acceptor materials in the nanometer range should suppress exciton loss prior to charge generation. Control of morphology is not only required for a large charge-generating interface and suppression of exciton loss, but also to ensure percolation pathways for both electron and hole transport to the collecting electrodes.

The first bulk-heterojunction solar cell, as developed in 1990 by Grätzel, was a dye-sensitized solar cell consisting of a porous TiO_2 solid (acceptor) covered with a monolayer of the dye (donor) where the pores are filled with a liquid electrolyte (Figure 1.3).[23] Nowadays, these cells reach power

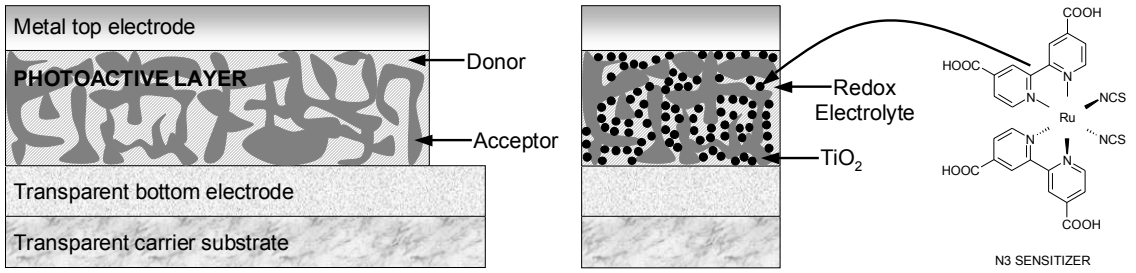

Figure 1.3 *Left: In a bulk-heterojunction solar cell the interface between the donor (p-type) and the acceptor (n-type) material is all over the bulk. Right: The dye-sensitized solar cell. After absorption of light by the N3 sensitizer, an electron is transferred to the porous TiO_2 solid and via TiO_2 transported to the transparent bottom electrode. The electron transfer is followed by reduction of the N3 sensitizer by the liquid redox electrolyte. Subsequently, the electrolyte is reduced by the metal top electrode. The reduction of the dye followed by reduction of the electrolyte is equivalent to transport of a positive charge to the metal top electrode.*

conversion efficiencies (η_{pc}) of 10-11%. Unfortunately, the liquid is corrosive and is less attractive from a manufacturing technology point of view. In 1998 Grätzel successfully replaced the corrosive, liquid electrolyte of the dye-sensitized solar cell by a solid component.[24] Power conversion efficiencies (η_{pc}) of 2-3% have been reached. Apart from this type of solid, hybrid solar cells, other hybrid approaches are under investigation. One approach uses mixtures of conjugated donor polymers with nanorods[25] or nanoparticles[26] as acceptors. Another approach is based on self-assembled, mesoporous metal oxide films filled with a conjugated donor polymer.[27] A last approach creates the porous inorganic solid in situ after mixing of the donor polymer with a soluble precursor of the metal oxide.[28] The main advantage of hybrid solar cells is the larger electron mobility of the inorganic material compared to the low electron mobility of most conjugated organics. The main disadvantage is that the metal oxides hardly absorb visible light and the open-circuit voltage V_{oc} is often limited. Furthermore, for mixtures of organic and inorganic components, solubility of the inorganic component and compatibility with the organic component is often limited as well. For porous or self-assembled solids, mostly other processing techniques than facile solution processing techniques are required.

The first fully organic, photoactive layers in bulk-heterojunction solar cells were reported in 1995. In these solar cells, the photoactive layer consists of either a mixture of a conjugated donor polymer (PPV) with a molecular acceptor,[29] or a mixture of two polymers.[30] Mixtures of two molecules are being studied as well.[31,32] Furthermore, a very attractive approach to control the nanoscale morphology is based on one material with covalently-linked donor and acceptor moieties.[33-35] Additionally, in an attempt to combine the advantages of both the bilayer and bulk-

heterojunction concepts, stratified[32,36] structures of two components have been investigated. The first truly promising results for bulk-heterojunction solar cells with a fully organic, photoactive layer were obtained in 2001 by Shaheen *et al*. when mixing poly[2-methoxy-5-(3′,7′-dimethyloctyloxy)-1,4-phenylene vinylene] (MDMO-PPV, Figure 1.1) with 1-(3-methoxycarbonyl)propyl-1-phenyl-[6,6]-methanofullerene (PCBM, Figure 1.2).[37] Recently, power conversion efficiencies (η_{pc}) of > 3% have been reached for polymer:fullerene bulk-heterojunction solar cells.[38-40]

In order to improve performance, stability, and lifetime of bulk-heterojunction solar cells, researchers are faced with the following challenges. First of all, the operation principle of bulk-heterojunction solar cells needs to be unraveled to guide the way for future material and device design. So far, mainly materials from the fields of LEDs and FETs have been used in organic solar cells. It is obvious that more materials dedicated to PV have to be developed. Appropriate design and synthesis will prove to be of paramount importance for maturity of the plastic solar cell. Furthermore, control of the nanoscale morphology needs to be improved. For the latter, synergy of material design and film deposition is required. Finally, the rich physics and chemistry at the interfaces of the multiple-layered device structures needs to be understood and controlled.

1.3 Aim and outline of the thesis

In 2000 polymer:fullerene bulk-heterojunction solar cells reached power conversion efficiencies of < 1%. Improving the performance, stability, and lifetime of bulk-heterojunction solar cells requires more insight in the preparation, and operation of these devices. This thesis discusses the preparation and the morphological and electrical characterization of devices made from MDMO-PPV, PCBM, and their mixtures. The understanding of the influence of morphology on the device performance should aid in obtaining insight in the fundamental issues of the bulk-heterojunction concept. Furthermore, new materials are introduced in an attempt to improve performance.

In chapter 2, it is shown that bulk-heterojunction solar cells made from MDMO-PPV and PCBM reach power conversion efficiencies of 2.5% under simulated solar light. It is shown for the first time that replacing the orange MDMO-PPV with a low-bandgap conjugated material results in a more red-shifted spectral response of these solar cells. Additionally, in an attempt to control the nanoscale morphology of the photoactive layer, the first example of a covalently linked donor polymer with pendant fullerenes incorporated in working solar cells is reported. The results indicated that more fundamental questions concerning the operation of the device and the influence of morphology must be addressed, before a rational improvement in device performance can be expected.

Chapter 3 discusses the influence of morphology on transport in disordered organic semiconductors. Morphological investigations on films of PCBM and several PPVs are combined with the analysis of charge-carrier-mobility data. The morphological disorder observed in the PCBM

films is in agreement with its charge-transport properties. Imaging individual conjugated polymer chains and aggregates on cast films with scanning force microscopy (SFM) is shown for the first time. For thin cast films of symmetrically substituted PPVs, the larger tendency to aggregate into ordered domains and, consequently, the larger zero-field hole mobility observed for symmetrically substituted PPVs seem to result from more linear conformations, as compared to asymmetrically substituted PPVs.

A combination of techniques is used in chapter 4 to resolve the morphology of spin cast films of MDMO-PPV:PCBM blends in three dimensions on a nanometer scale. Combining the results of the several techniques, shows that a rather homogeneous polymer matrix containing tiny PCBM crystals is present up to 50 weight-percentages (wt.-%) PCBM. Phase separation resulting in large, separate domains of rather pure PCBM in a homogenous matrix of 50:50 wt.-% MDMO-PPV:PCBM sets in for concentrations of more than 67 wt.-% PCBM. Also the large, almost pure PCBM domains consist of tiny PCBM crystals, similar to the nanocrystals of pure PCBM films.

In chapter 5, the morphological insights of chapter 4 are related to the performance of the corresponding solar cells. Electrical characterization, under illumination and in the dark, of the photovoltaic devices revealed a strong increase of the power conversion efficiency when the phase-separated network develops, with a sharp increase of the photocurrent and fill factor between 50 and 67 wt.-% PCBM. As the phase separation sets in, enhanced electron transport and a reduction of bimolecular charge recombination provide the conditions for improved performance. The results are interpreted in terms of a model that proposes a hierarchical build up of two cooperative interpenetrating networks at different length scales.

The final chapter describes the applicability and results of the full-depth analysis of bulk-heterojunction solar cells. These analysis techniques are used to study interface integrity, layer-to-layer diffusion, and contamination levels. Enrichment of oxygen at the interface between Al and the photoactive layer is observed. Furthermore, depth-profiling showed that during preparation diffusion of indium into the PEDOT:PSS occurs under the influence of water, while the diffusion of aluminum into the polymer layers is negligible. Transmission electron microscopy of cross-sections, as prepared with a focused ion beam, of fully processed photovoltaic cells, provide a clear view of the individual layers and their interfaces. No dissociation of LiF upon evaporation of Al onto LiF-covered photoactive layers could be observed with static secondary ion mass spectrometry (SIMS), excluding the doping model as the dominant mechanism for the explanation of the enhanced electron injection by LiF.

1.4 References and notes

1 A. Jäger-Waldau, *PV Status Report 2003* **2003**, *European Commission*, EUR 20850 EN.

2 B.A. Sandén, *Materials Availability for Thin-Film PV and the Need for 'Technodiversity', at the EUROPV 2003 Conference* **2003**, Bologna (Spain).

3 (a) H. Shirakawa, E.J. Louis, A.G. MacDiarmid, C.K. Chiang, A.J. Heeger, *J. Chem. Soc. Chem. Commun.* **1997**, *16*, 578; (b) C.K. Chiang, C.R. Fincher, Y.W. Park, A.J. Heeger, H. Shirakawa, E.J. Louis, S.C. Gau, A.G. MacDiarmid, *Phys. Rev. Lett.* **1977**, *39*, 1098.

4 H. Shirakawa, A.G. MacDiarmid, A.J. Heeger, *Chem. Commun.* **2003**, 1.

5 H. Shirakawa, *Angew. Chem. Int. Ed.* **2001**, *40*, 2574.

6 A.G. MacDiarmid, *Angew. Chem. Int. Ed.* **2001**, *40*, 2581.

7 A.J. Heeger, *Angew. Chem. Int. Ed.* **2001**, *40*, 2591.

8 R.H. Friend, R.W. Gymer, A.B. Holmes, J.H. Burroughes, R.N. Marks, C. Taliani, D.D.C. Bradley, D.A. Dos Santos, J.L. Brédas, M. Löglund, W.R. Salaneck, *Nature* **1999**, *397*, 121.

9 J.H. Burroughes, D.D.C. Bradley, A.R. Brown, R.N. Marks, K. Mackay, R.H. Friend, P.L. Burns, A.B. Holmes, *Nature* **1990**, *347*, 539.

10 A.J. Epstein, Y. Yang (Eds.), *Polymeric and Organic Electronic Materials: from Scientific Curiosity to Applications, MRS Bull.* **1997**, *22*, 13.

11 C.D. Dimitrakopolous, P.R.L. Malenfant, *Adv. Mater.* **2002**, *14*, 99.

12 H. Sirringhaus, P.J. Brown, R.H. Friend, M.M. Nielsen, K. Bechgaard, B.M.W. Langeveld-Voss, A.J.H. Spiering, R.A.J. Janssen, E.W. Meijer, P. Herwig, D.M. de Leeuw, *Nature* **1999**, *401*, 685.

13 A.R. Brown, A. Pomp, C.M. Hart, D.M. de Leeuw, *Science* **1995**, *270*, 972.

14 C.J. Brabec, V. Dyakonov, J. Parisi, N.S. Sariciftci (Eds.), *Organic Photovoltaics*: *Concepts and Realization, Springer Series in Materials Science Vol. 60* Springer-Verlag, London, **2003**.

15 J.-M. Nunzi, *C. R. Physique* **2002**, *3*, 523.

16 J. Janata, M. Josowicz, *Nature Mater.* **2003**, *2*, 19.

17 P.K.H. Ho, D.S. Thomas, R.H. Friend, N. Tessler, *Science* **1999**, *285*, 233.

18 H. Sirringhaus, N. Tessler, R.H. Friend, *Science* **1998**, *280*, 1741.

19 A.R. Duggal, D.F. Foust, W.F. Nealon, C.M. Heller, *Appl. Phys. Lett.* **2003**, *82*, 2580.

20 P. Peumans, A. Yakimov, S.R. Forrest, *J. Appl. Phys.* **2003**, *93*, 3693.

21 M. Granström, K. Petritsch, A.C. Arias, A. Lux, M.R. Andersson, R.H. Friend, *Nature* **1998**, *395*, 257.

22 C.W. Tang, *Appl. Phys. Lett.* **1986**, *48*, 183.

23 (a) M. Grätzel, *Nature* **2001**, *414*, 338; (b) B. O'Regan, M. Grätzel, *Nature* **1991**, *353*, 737.

24 U. Bach, D. Lupo, P. Comte, J.E. Moser, F. Weissörtel, J. Salbeck, H. Spreitzer, M. Grätzel, *Nature* **1998**, *395*, 583.

25 (a) W.U. Huynh, J.J. Dittmer, W.C. Libby, G.L. Whiting, A.P. Alivisatos, *Adv. Funct. Mater.* **2003**, *13*, 73; (b) W.U. Huynh, J.J. Dittmer, A.P. Alivisatos, *Science* **2001**, *295*, 2425.

26 W.J.E. Beek, M.M. Wienk, R.A.J. Janssen, *submitted*.

27 K.M. Coakley, Y. Liu, M.D. McGehee, K.L. Frindell, G.D. Stucky, *Adv. Funct. Mater.* **2003**, *13*, 301.

28 P.A. van Hal, M.M. Wienk, J.M. Kroon, W.J.H. Verhees, L.H. Slooff, W.J.H. van Gennip, P. Jonkheijm, R.A.J. Janssen, *Adv. Mater.* **2003**, *15*, 118.

29 G. Yu, J. Gao, J.C. Hummelen, F. Wudl, A.J. Heeger, *Science* **1995**, *270*, 1789.

30 J.J.M. Halls, C.A. Walsh, N.C. Greenham, E.A. Marseglia, R.H. Friend, S.C. Moratti, A.B. Holmes, *Nature* **1995**, *376*, 498.

31 P. Peumans, S. Uchida, S.R. Forrest, *Nature* **2003**, *425*, 158.

32 (a) L. Schmidt-Mende, A. Fechtenkötter, K. Müllen, E. Moons, R.H. Friend, J.D. MacKenzie, *Science* **2001**, *293*, 1119; (b) L. Schmidt-Mende, M. Watson, K. Müllen, R.H. Friend, *Mol. Cryst. Liq. Cryst.* **2003**, *396*, 73.

33 E.E. Neuteboom, S.C.J. Meskers, P.A. van Hal, J.K.J. van Duren, E.W. Meijer, R.A.J. Janssen, H. Dupin, G. Pourtois, J. Cornil, R. Lazzaroni, J.L. Brédas, D. Beljonne, *J. Am. Chem. Soc.* **2003**, *125*, 8625.

34 A. Marcos Ramos, M.T. Rispens, J.K.J. van Duren, J.C. Hummelen, R.A.J. Janssen, *J. Am. Chem. Soc.* **2001**, *123*, 6714.

35 (a) B. de Boer, U. Stalmach, P.F. van Hutten, C. Melzer, V.V. Krasnikov, G. Hadziioannou, *Polymer* **2001**, *42*, 9097; (b) U. Stalmach, B. de Boer, C. Videlot, P.F. van Hutten, G. Hadziioannou, *J. Am. Chem. Soc.* **2000**, *122*, 5464.

36 M. Drees, K. Premaratne, W. Graupner, J.R. Heflin, R.M. Davis, D. Marciu, M. Miller, *Appl. Phys. Lett*. **2002**, *81*, 4607.

37 S.E. Shaheen, C.J. Brabec, N.S. Sariciftci, F. Padinger, T. Fromherz, J.C. Hummelen, *Appl. Phys. Lett*. **2001**, *78*, 841.

38 M.M. Wienk, J.M. Kroon, W.J.H. Verhees, J. Knol, J.C. Hummelen, P.A. van Hal, R.A.J. Janssen, *Angew. Chem. Int. Ed*. **2003**, *42*, 3371.

39 F. Padinger, R.S. Rittberger, N.S. Sariciftci, *Adv. Funct. Mater*. **2003**, *13*, 85.

40 P. Schilinsky, C. Waldauf, C.J. Brabec, *Appl. Phys. Lett.* **2002**, *81*, 3885.

Chapter 2

Exploring conjugated polymer:methano-fullerene bulk-heterojunction solar cells*

Abstract

Bulk-heterojunction solar cells based on a phase-separated mixture of donor and acceptor materials are intensively studied owing to their potential of providing lightweight, flexible, inexpensive, efficient solar cells. In order to improve device performance, new donor materials are mixed with one of the most successful acceptor materials in these solar cells, viz. 1-(3-methoxycarbonyl)propyl-1-phenyl-[6,6]-methanofullerene (PCBM). Bulk-heterojunction solar cells made from poly[2-methoxy-5-(3′,7′-dimethyloctyloxy)-1,4-phenylene vinylene] (MDMO-PPV) and PCBM reach power conversion efficiencies of 2.5% under simulated solar light. It is shown for the first time that replacing the orange MDMO-PPV with a low-bandgap conjugated material results in a more red-shifted spectral response of these solar cells, necessary for a larger overlap with the solar emission spectrum. Additionally, in an attempt to control the nanoscale morphology of the photoactive layer the first example of a covalently linked donor polymer with pendant fullerenes incorporated in working solar cells is reported. Unfortunately, both experiments resulted in a decrease of the power conversion efficiency compared to the mixture of MDMO-PPV and PCBM. These results indicated that more fundamental questions concerning the operation of the device and the influence of morphology must be addressed, before a rational improvement can be expected. This sets the stage for the remainder of this thesis.

*Part of this work has been published: (a) A. Dhanabalan, J.K.J. van Duren, P.A. van Hal, J.L.J. van Dongen, R.A.J. Janssen, *Adv. Funct. Mater.* **2001**, *11*, 255; (b) A. Marcos Ramos, M.T. Rispens, J.K.J. van Duren, J.C. Hummelen, R.A.J. Janssen, *J. Am. Chem. Soc.* **2001**, *123*, 6714; (c) J.K.J. van Duren, A. Dhanabalan, P.A. van Hal, R.A.J. Janssen, *Synth. Met.* **2001**, *121*, 1587; (d) A. Dhanabalan, P.A. van Hal, J.K.J. van Duren, J.L.J. van Dongen, R.A.J. Janssen, *Synth. Met.* **2001**, *119*, 169.

2.1 Introduction

Since the discovery of photoinduced charge transfer between a poly(*p*-phenylene vinylene) and Buckminsterfullerene in 1992,[1] conjugated polymers and molecules have been studied intensively because of their potential of providing lightweight, flexible, inexpensive, efficient solar cells.[2-5] A very attractive approach is the bulk-heterojunction solar cell consisting of a mixture of an electron-donating organic material (easily oxidized, p-type, called the donor) and an electron-accepting organic material (easily reduced, n-type, called the acceptor) sandwiched between two electrodes (Figure 2.1).[6,7] The donor and acceptor have different electronic levels. The use of two materials with different electronic levels is one of the most important design concepts in organic solar cells. Photoexcitations in an organic semiconductor have an exciton character, i.e. a photoexcitation does not result in free charges, but in a bound electron-hole pair. By using a combination of donor and acceptor materials, dissociation of the exciton is achieved at the interface of both materials (charge transfer).

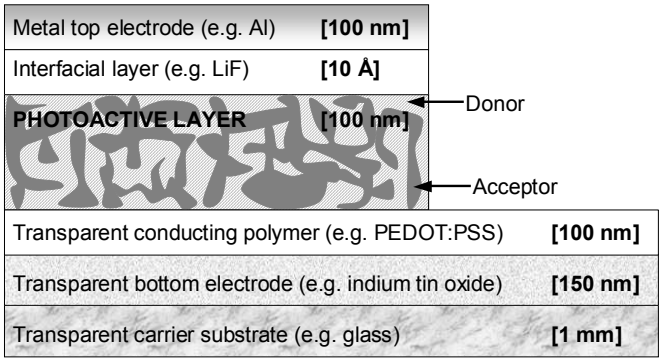

Figure 2.1 *The device structure typically used for bulk-heterojunction solar cells.*

The photoactive layer of bulk-heterojunction solar cells may consist of a large variety of materials. In this context, mixtures of a conjugated donor polymer with a fullerene derivative[8-24] or a nanotube[25,26] as acceptor, mixtures of a supramolecular polymer with PCBM (Figure 2.2),[27,28] mixtures of a donor polymer with the acceptor perylene (Figure 2.2),[29] blends of a donor and an acceptor polymer,[30-33] mixtures of molecules,[34-38] or covalently linked donor-acceptor systems[39-45] have been used. Especially, processing these materials from solution to obtain thin semiconductive films has attracted considerable attention, owing to its potential for roll-to-roll production of large-area solar cell foils.

These bulk-heterojunction solar cells typically consist of a photoactive layer on top of a transparent bottom electrode supported by a transparent carrier substrate, such as indium tin oxide (ITO) on glass, covered with a transparent, conducting polymer layer, such as polyethylenedioxy-thiophene:polystyrenesulfonate (PEDOT:PSS, Figure 2.4). On top of the photoactive layer, an aluminum electrode is deposited to complete the solar cell. Occasionally, an additional thin intermediate layer is used, such as LiF (Figure 2.1), to improve device performance.[46]

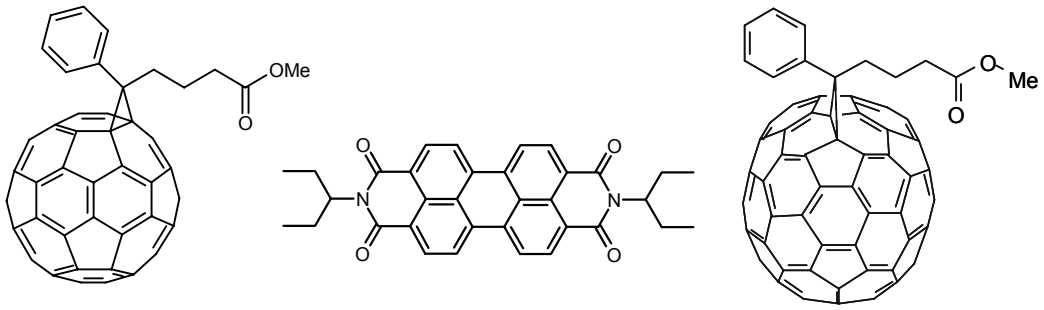

[60]PCBM (or PCBM) EP-PTC [70]PCBM

Figure 2.2 *Structures of the molecular acceptors [60]PCBM (or PCBM), a perylene tetracarboxylic derivative (EP-PTC, see Dittmer et al.), and [70]PCBM (see Wienk et al.).*

Promising power conversion efficiencies of >3% under simulated solar light have recently been reported for solar cells based on this approach utilizing conjugated polymers as a donor and fullerene derivatives as an acceptor.[8,12,14] In these cells a sub-picosecond photoinduced charge transfer[47] between donor and acceptor ensures efficient charge generation, while the collection of charges is facilitated by a slow recombination that extends into the millisecond domain.[48,49] In order to improve performance, new materials with better properties have to be developed.

This chapter describes the state-of-the-art in this field and explores the use of new materials in solar cells. It will be organized as follows. First, some general material requirements will be described together with the procedures for solar cell fabrication that will be used in this thesis. Second, the various efficiency definitions used in solar cell research will be explained. Third, state-of-the-art solar cells will be presented consisting of MDMO-PPV (Figure 2.6) and PCBM (Figure 2.2). Finally, two new materials will be introduced in bulk-heterojunction solar cells. It will be shown that replacing the orange MDMO-PPV with a lower bandgap material in the mixture with PCBM results in a more red-shifted spectral response of these solar cells. Additionally, a donor backbone with pendant fullerenes will be introduced. Their performance will be characterized and compared to the MDMO-PPV:PCBM solar cells.

2.2 General requirements for the components in the photoactive layer

The most straightforward requirements for the two components in the photoactive layer are the following.

First of all, at least one, but preferably both components should have a large absorption coefficient and a broad absorption spectrum in order to create a good overlap with the solar emission spectrum (Figure 2.3). Most conjugated materials are very strong absorbers in the visible region with the exception of some, such as PCBM.[3] The absorption spectrum of most undoped polymers, however, consists of several narrow bands from which only a part is located in the solar emission spectrum, typically in the blue-orange region (400-600 nm).

Second, the donor material should have a high hole mobility, whereas the acceptor should have a high electron mobility. Most donor materials are reasonably good hole transporters with hole mobilities μ_h in the range of 10^{-6}-10^{-3} cm^2/Vs.[50-52] Only a few examples exist of good electron transporters with electron mobilities μ_e in the range of 10^{-6}-10^{-3} cm^2/Vs.[51-53] Recent insight suggests that the hole and electron mobility in the mixture, however, not necessarily reflect the mobility of the pure components, even for compositions where both components are expected to percolate.[54,55] It is expected that the magnitude of both mobilities should be rather similar to minimize space-charge built-up. Furthermore, the film should have a high dielectric constant, thereby facilitating a high charge density and more efficient exciton dissociation within the film. Typical values for the relative dielectric constant ε_r of conjugated organics are 3-4.[53,56] More details on the relation between material properties and charge-carrier mobility will be described in chapter 3.

Third, one of both components should be easily oxidized (the donor), whereas the other one should be easily reduced (the acceptor).[2-4] In a first approximation, this means that for efficient photoinduced electron transfer from donor to acceptor, the lowest unoccupied molecular orbital (LUMO) of the donor should be located at a higher potential energy than the LUMO of the acceptor (Figure 2.3). Likewise, for efficient photoinduced hole transfer from acceptor to donor, the highest occupied molecular orbital (HOMO) of the acceptor should be located below the HOMO of the donor (Figure 2.3). In this way, photoinduced charge transfer can become the main decay mechanism of the excited state that was created by absorption of light. This charge transfer, however, should not be so facile that it occurs in the ground state, resulting in a stable charge-transfer complex. Furthermore, other decay mechanisms than charge transfer should be negligible, such that the excited state (exciton) can diffuse over a long distance to the interface between donor and acceptor without decay. Exciton diffusion lengths, however, are typically 10 nm or less,[57] as a result of intrinsic decay processes which occur at the nanosecond timescale.

Fourth, material design of both donor and acceptor should allow for a large open-circuit voltage (V_{oc}). The open-circuit voltage is related to the distance between the HOMO level of the donor and the LUMO level of the acceptor.[58] Additionally, the position of the LUMO level of the acceptor with respect to the workfunction or Fermi-level (E_F) of the electron-collecting electrode should provide easy electron collection at the contact. The same holds for the HOMO of the donor with the hole-collecting electrode. Proper choice of electrode materials should ensure efficient charge collection at the contacts. The importance of proper choice of electrode materials to improve performance of plastic electronics has been extensively demonstrated in the field of polymer and organic LEDs.[46,59,60] The difference in (effective) workfunction between both electrodes should provide the built-in electric field necessary to extract the photogenerated charges.

Apart from these opto-electronic properties, the materials should allow facile processing from solution. Additionally, they should allow easy purification after synthesis. Preferably, the glass-

transition temperature T_g should be far above room temperature to form a stable morphology. For conjugated poymers, T_g typically lies above 65 °C. The material should be chemically stable. Photo-oxidation is known to occur, but can be prevented to a large extent by proper device processing and encapsulation (see below). Finally, the film morphology should ensure good percolation pathways for efficient charge collection and minimal charge recombination. The influence of morphology on performance of solar cells is the subject of chapters 4 and 5.

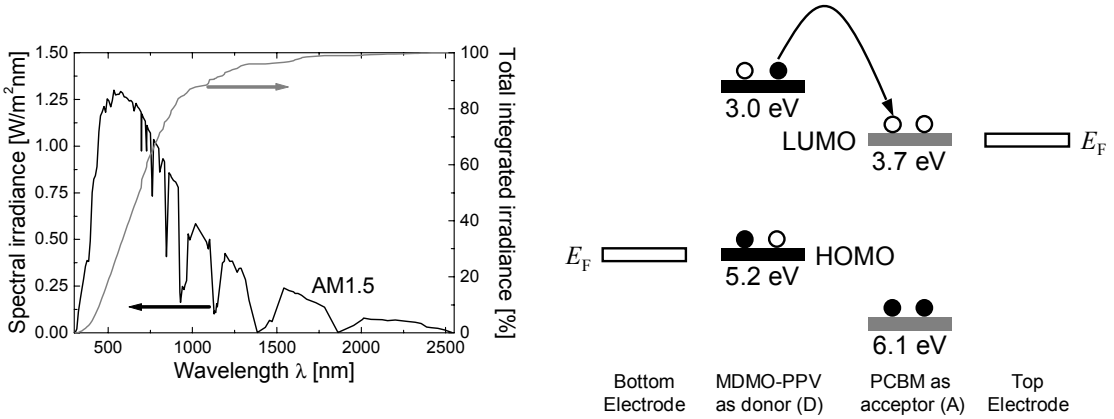

Figure 2.3 *Left: Solar emission spectrum. Right: HOMO and LUMO levels as depicted for MDMO-PPV and PCBM, exemplifying the relative position in LUMO (or HOMO) levels required for charge transfer. The black dots represent electrons whereas the black circles represent electron vacancies. MDMO-PPV is depicted in the neutral excited state. Additionally, the Fermi-level (E_F) of both electrodes is given that would lead to an Ohmic contact for the holes between the bottom electrode and MDMO-PPV and for the electrons between the top electrode and PCBM.*

Although it is clear to a large extent what properties are required for both donor and acceptor, the design and synthesis of a new material possessing all of the necessary properties as outlined above remains a challenge. Apart from the design challenge, new synthetic routes are often required to prepare these materials. Fortunately, the existing knowledge on material design,[50-52,61-66] and synthesis[66-71] in the field of conjugated materials is increasing rapidly.

2.3 Preparation and structure of bulk-heterojunction solar cells

Bulk-heterojunction solar cells typically consist of a multi-layer (sandwich) configuration: carrier substrate/transparent bottom electrode/photoactive layer/top electrode (see Figure 2.1). Although this thesis mainly focuses on the photoactive layer, a general overview of the most relevant properties and processing issues of the complete device structure will be given in this section. Details on the material properties, as required for the photoactive layer, are given above.

Carrier substrate. Glass has been used as the carrier substrate throughout this thesis because of its ease of handling for laboratory research activities. As a result of its good gas-barrier, optical, adherence, and highly insulating properties, glass is an excellent substrate, albeit for non-flexible applications only. Both the development and testing of flexible substrates for plastic electronic applications are receiving large attention in recent years[72-76] and will eventually become important to achieve roll-to-roll processing for solar cells.

Transparent bottom electrode. For a solar cell (and other opto-electronic applications, as light-emitting diodes) at least one transparent electrode is required. Typically, a transparent conductive oxide (TCO) is used, deposited on the carrier substrate. A TCO should combine a high conductivity (or low sheet resistance) with a high transparency, good substrate adherence, and a low surface roughness.[77] The latter is necessary to prevent shunting in solar cells,[78] and the growth of dark spots in organic light-emitting diodes (LEDs).[79] Additionally, the workfunction of the TCO should allow for a large open-circuit voltage (V_{oc}) without introducing a collection barrier. Finally, the TCO should be stable, and not degrade the organic semiconductor.

The most widely used TCO in bulk-heterojunction solar cells (and other plastic electronics) is indium tin oxide (ITO), a composite oxide where indium oxide (typically > 90%) is doped with tin oxide (< 10%). Glass substrates coated with a thin ITO layer can be obtained from commercial sources.[80] Prior to deposition of the organic layers onto ITO, a variety of cleaning procedures, and both chemical and physical surface treatments are generally used to improve the properties of ITO. These steps are introduced to remove (carbon) contaminants, smoothen the surface, and improve both the wetting behavior of ITO and its workfunction.[81-89] In this thesis, the ITO-covered glass substrates are cleaned by ultrasonic treatment in acetone, followed by rubbing with soap, rinsing with de-mineralized water, subsequent refluxing with iso-propanol, and finally a UV ozone treatment for 20 minutes. This procedure gives reproducible results. Details on the ITO surface topography are described in chapter 6.

After the appropriate treatments, ITO meets most of the necessary TCO requirements reasonably well. Interfacial chemistry, however, as a result of diffusion of oxygen out of ITO, and free acid present in the polymer layer, can occur at the interface with the polymer.[90-94] In order to increase both the mechanical flexibility of the devices and to avoid use of the expensive element indium, the first examples where ITO is replaced completely by organic conductors have already been published.[95,96]

Despite the improvements made over the past few years in preparing and treating ITO, a thin conductive organic layer is typically applied from solution to cover ITO before the actual active organic semiconductor is deposited.[97-99] These organic conductive cover layers are used for several reasons. First of all, the reproducibility of the devices increases when using these conductive organics.

This seems to result from the better film formation, and consequently film homogeneity, of these conductive organics on ITO in comparison with the poor film quality of the photoactive materials when directly cast on ITO. Second, the higher workfunction of these conductive organic layers compared to ITO improves device performance by enhancing the built-in voltage in solar cells and decreasing the injection barrier in LEDs.[59,60,100] Finally, introducing these smooth organic films between the active layer and ITO enhances device stability by suppressing shunting-spot growth as a result of spikes, and by reducing chemical interaction of ITO with the photoactive layer.

The most widely used conductive cover layer on ITO is the conductive, transparent composite PEDOT:PSS, consisting of polyethylenedioxythiophene (PEDOT) doped with the polyanion polystyrenesulfonate (PSS, Figure 2.4).[90,98] PEDOT:PSS is a commercial product and received as a dispersion in water. It is spin coated as such, resulting in a film thickness of typically 100 nm. The use of PEDOT:PSS improves both the device stability and performance enormously. A further improvement on device lifetime and performance, however, is limited by the acidity of PEDOT:PSS, causing degradation of both ITO underneath and the active conjugated materials on top.[90-94,101] Therefore, other solution-processable electrodes are being developed.[102-104]

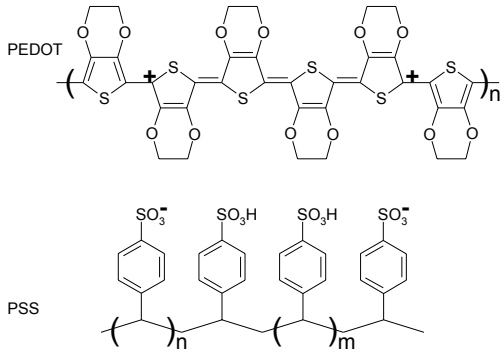

Figure 2.4 *Molecular structure of PEDOT doped with the polyanion PSS.*

The morphology and, consequently, the properties of the two-component system PEDOT:PSS are strongly influenced by preparation, processing, and post-production treatment.[90,105-109] An additional drying step after applying the film is necessary to remove remaining water that would otherwise liberate the proton of PSS and, consequently, result in device degradation.[90-94] Removal of water is also necessary to prevent degradation of the top metal electrode (see sub-section 'top electrode' below). Furthermore, post-production treatment is used to control both the conductivity[90,105-108] and the (surface) workfunction[90] of PEDOT:PSS, via its morphology. The effective workfunction of the composite PEDOT:PSS, and therefore the contact barrier, has been found to strongly depend on its surface composition.[90] Additionally, apart from the surface composition, a mixed interface region opposite to an abrupt interface with the active layer can influence the contact barrier as well.[110] The PEDOT:PSS blend is thought to consist typically of

small metallic PEDOT domains in a low-conducting PSS-rich matrix.[90,111] Protons possibly contribute to the conduction within this matrix.[112] Investigations on both post-production treatment as used in this thesis, and the influence of ambient conditions are described in chapter 6.

Active layer. Creating a sharp, well-defined interface between two organic layers, both applied from solution, is only possible when the bottom organic (conductive) layer is not dissolved by the solution used to deposit the top (active) layer. Owing to its ionic character, PEDOT:PSS hardly dissolves in the aromatic solvents typically used for conjugated polymers. For stacked layers of polymers with comparable solubility characteristics, crosslinking the polymer in the bottom layer before applying the top layer can prevent redissolving.[103,113,114] The same procedures can also be used for stabilization of the morphology in general.[115]

In this thesis, both PEDOT:PSS and the active layer are applied via spin casting (spin coating). In spin casting, application of the solution consisting of a volatile solvent with the material to be deposited, followed by coating and drying of the film on a rotating disk can be accomplished in less than a minute.[116] For moderately volatile solvents in which the material readily dissolves, extremely smooth films can be obtained (nonuniformity less than 1%), and the film thickness can easily be controlled within a few nanometers.[116-118] Even leveling or planarization over topographic substrate unevenness can be controlled to a large extent.[116] Spin cast films of PEDOT:PSS are indeed found to be very smooth. The same holds for the photoactive layer, although, some unevenness appears when phase separation sets in. Details can be found in chapters 4 and 6.

Top electrode. The top electrode is usually a metal that is thermally evaporated under high vacuum. Depending on (the application and) the LUMO level of the underlying photoactive organic, metals with low (~3 eV, such as Ca, Ba, and Yb) or moderate (~4 eV, such as Al, and Ag) workfunctions are required. For polymer:fullerene bulk-heterojunction solar cells aluminum is typically used as the top electrode.

Thermal evaporation[119] of the top electrode on conjugated organic films typically results in polycrystalline (granular) electrodes. Depending on the conditions and materials used to deposit metals onto conjugated organic films, formation of covalent bonds between the metal and the underlying organic, diffusion of the metal into the organic film resulting in mixed interfaces, and doping of the organic by the metal can occur.[60,120,121] In practice, interfacial chemistry always occurs to a certain extent, especially with residual gas in the vacuum chamber during evaporation,[122] but how it affects device performance is still not completely understood.[60,120] The rich physics and chemistry of interface formation between conjugated organics and metal electrodes make it very difficult to predict interface properties and performance solely on the basis of separately determined material parameters such as the workfunction and electron affinity.

To improve the electron collection for plastic solar cells or the electron injection for LEDs, interfacial layers, such as LiF, CsF, and NaF, are often used at the contact with aluminum. LiF has proven to improve the performance for polymer:fullerene bulk-heterojunction solar cells.[46] The origin of the beneficial effect of LiF on the performance of plastic electronics is a subject under debate and will be discussed in more detail in chapter 6.

Surface measurements on top electrodes, and interface studies of bulk-heterojunction solar cells will be discussed in chapter 6. The device areas used in this thesis are 0.1-1.0 cm^2, and result from thermal evaporation of the metal through a mask on the patterned ITO substrates.

Encapsulation. After all conductive and semiconductive layers are applied, the devices are typically encapsulated. Encapsulation or packaging of organic semiconductor devices is crucial to extent the device lifetime. Especially water and oxygen have to be excluded to prevent photo-oxidation of the conjugated polymer and conversion of the metal electrode into an oxide (or hydroxide).[122-131] Mixing fullerenes into a conjugated polymer matrix has been found to suppress photo-oxidation dramatically.[132,133] Apart from a gas barrier and resistance to moisture, the packaging material must fulfill several requirements, such as, for heat dissipation and electrical insulation.[123] Except for the cleaning and short spin cast procedure, all photo-electrical characterizations as described in this thesis are performed in an inert atmosphere making encapsulation redundant for device characterization. The influence of dust during the device preparation did not have a strong effect on the reproducibility. Spin casting was performed in a laminar flowbox under further normal laboratory conditions.

2.4 Solar cell efficiencies

Several efficiencies exist that describe the electrical characteristics of solar cells under illumination. The most relevant one is the power conversion efficiency η_{pc} being the ratio of the maximum obtainable electrical power P_{max} and the incident light power (ILP, see Figure 2.5). The point of maximum obtainable electrical power P_{max} is located in the fourth quadrant on the current density-voltage (*J-V*) curve where the product of current density *J* and voltage *V* reaches its maximum value. In order to relate this maximum power point to the short-circuit current density J_{sc}, the open-circuit voltage V_{oc}, and the diode behavior of the solar cell, the fill factor (FF) is introduced. The FF describes the ratio of (or the rectangle of) P_{max} with the product of (or the rectangle defined by) J_{sc} and V_{oc}. For a simple single-semiconductor photovoltaic model FF lies in between 0.25 and 1.0.[134] The power conversion efficiency η_{pc} should be measured under standard test conditions. These conditions are specified as a radiant density of 100 mW/cm^2 with a spectral distribution defined as 'Air Mass 1.5 Global' (AM1.5G, IEC 904-3) at a cell temperature of 25 °C.[135] AM1.5 approximates the intensity of

sunlight that would be received on a tilted plane surface on a clear day, and for a model atmosphere containing specified concentrations of e.g. water vapor, and aerosol.[136]

Apart from η_{pc}, the incident photon to current conversion efficiency (IPCE), also known as the external quantum efficiency (EQE), is often used. The IPCE compares the number of charge carriers collected at zero bias (J_{sc}) to the number of incident monochromatic photons. Measuring the IPCE at different wavelengths results in a spectral response of the solar cell. Because the short-circuit current density (J_{sc}) not necessarily increases linearly with incident light power (ILP), the absolute IPCE-values generally depend on the ILP of the monochromatic light.[137] The same, of course, holds for η_{pc}. Again, this explains the necessity for both η_{pc} and IPCE measurements under appropriate standard test conditions. This means that apart from the monochromatic light, continuous irradiation under standard test conditions is required for meaningful comparison of IPCE spectra.[135]

Another characteristic value is the internal quantum efficiency (IQE). The IQE is the ratio of the number of charge carriers collected at zero bias (J_{sc}) and the number of actually absorbed monochromatic photons. The IQE gives insight on the efficiency of the charge generation, transport, and collection processes.[14] At a given wavelength λ, the product of the absorption A and IQE equals IPCE (Figure 2.5).

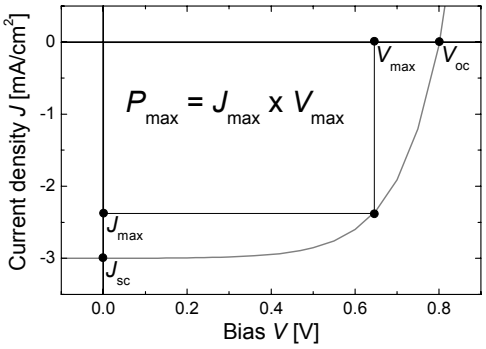

$$\eta_{pc} = \frac{P_{max}}{ILP} \times 100 = \frac{J_{max} \times V_{max}}{ILP} \times 100$$

$$FF = \frac{J_{max} \times V_{max}}{J_{sc} \times V_{oc}}$$

$$\eta_{pc} = \frac{J_{sc} \times V_{oc} \times FF}{ILP} \times 100$$

$$IPCE(\lambda) = EQE(\lambda) = A(\lambda) \times IQE(\lambda) = \frac{1.24 \times 10^5 \times J_{sc}(\lambda)}{ILP(\lambda) \times \lambda}$$

Figure 2.5 *Left: Current density-voltage (J-V) curve under illumination with the maximum obtainable electrical power (P_{max}) depicted as the rectangle. Right: The power conversion efficiency (η_{pc} in %) is defined as the ratio of P_{max} and the incident light power (ILP). Below: The incident photon to current conversion efficiency (IPCE in %) or external quantum efficiency (EQE) is the product of the absorption of the photoactive layer (A) and the internal quantum efficiency (IQE) with J_{sc}, ILP, and the wavelength λ in mA/cm², mW/cm², and nm, respectively.*

Apart from the different types, many ill-defined "efficiencies" are reported, often hampering a meaningful comparison of solar cell data reported.[135,138] One of the reasons for this is the difficulty in measuring absolute light intensities at different wavelengths.

Over the past few years, the equipment for measuring solar cells in our laboratory has improved, although, no equipment with appropriate standard test conditions is available.[135] This means that solar cells have been characterized with light sources varying in spectral shape and intensity. For accurate power conversion efficiency η_{pc} measurements, the shape and intensity of these light sources has to be determined. Determining the exact shape and intensity of a light source can be a tedious task, and must be repeated at regular intervals to monitor small changes in light intensity and spectral distribution. Nevertheless, for internal comparison a white light source, whose shape and intensity are roughly known, is more than sufficient to characterize different solar cells. Combined with η_{pc} measured at varying incident light power (ILP), and IPCE spectra, these data even provide the necessary information on the performance for comparison with data of others.

2.5 A mixture of a substituted poly(*p*-phenylene vinylene) and a methanofullerene

Ever since PCBM was mixed with poly[2-methoxy-5-(2'-ethylhexyloxy)-1,4-phenylene vinylene] (MEH-PPV) and applied in a solar cell in 1995,[6] considerable efforts have been made to improve solar cells based on this methanofullerene. Spin cast films of the mixture of a high-MW[139] MDMO-PPV with PCBM showed a huge decrease in photoluminescence of MDMO-PPV, indicative for either energy or charge transfer and in agreement with the positions of the energy levels of both MDMO-PPV[140] and PCBM[3] (Figure 2.2). Photoinduced absorption measurements showed charge transfer to be the main decay mechanism.[3,47]

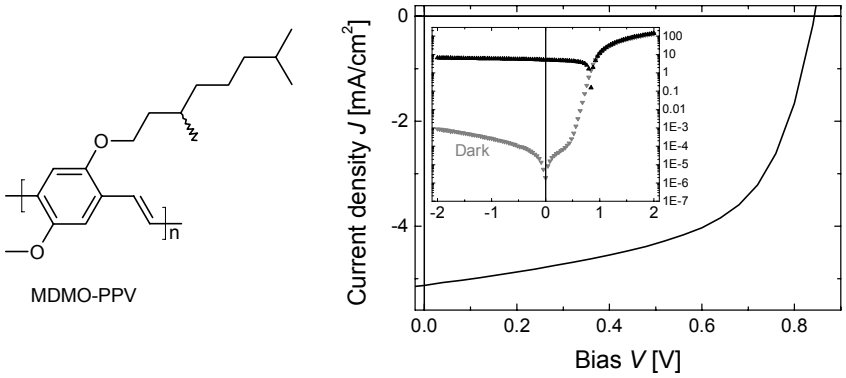

Figure 2.6 *Left: Molecular structure of MDMO-PPV. Right: J-V characteristics of a glass/ITO/PEDOT:PSS/MDMO-PPV:PCBM(1:4 by weight, 160 nm)/LiF(1.0 nm)/Al device under illumination of a solar simulator. The inset shows the J-V characteristics on a single-logarithmic scale, both in the dark and under illumination.*

Power conversion efficiency. Mixing MDMO-PPV with PCBM resulted in solar cells with J_{sc} = 5.13 mA/cm^2, V_{oc} = 0.84 V, FF = 0.57, and η_{pc} = 2.5% under a Steuernagel SolarConstant 1200 solar simulator (Figure 2.6).[141] To reach this efficiency, a mixture of MDMO-PPV and PCBM containing 80 weight-percentages (wt.-%) PCBM was spin coated from chlorobenzene resulting in a film thickness of 160 nm. Additionally, a thin intermediate layer of 1.0 nm LiF underneath the aluminum top electrode was required.[46] Furthermore ITO was covered with PEDOT:PSS. Similar results were first reported by Shaheen *et al.* who demonstrated the importance of the solvent used for spin casting.[18] The *J-V* characteristics show an excellent diode behavior with a rectification ratio (RR) of 1×10^5 at ±2 V in the dark, which shows that the device has little or no shunts, in agreement with AFM height images.

Performance with varying incident light power. The short-circuit current density J_{sc} was found to increase with incident light power (ILP) according to a power-law behavior $J_{sc} \propto \mathrm{ILP}^{\alpha}$ with $\alpha = 0.95$. A simple physical model describing the double extraction of uniformly generated electron-hole pairs from insulators with blocking contacts,[142] as discussed in detail in chapter 5, relates the exponent α to the amount of space charge present, and is either ¾ (space-charge-limited) or 1 (space-charge-free). Comparison of the experimental results with this model suggests that the photocurrent might be slightly influenced by space charge. This space charge finds its origin in unbalanced mean carrier drift lengths for electrons and holes with a part of the layer suffering from charge recombination.[142] Recent work by others[14,55] also suggests that the slightly sub-linear dependence (α = 0.95) is related to some bimolecular recombination of positive and negative photogenerated charges. Morphological investigations showed the importance of phase separation as present in the 80 wt.-%

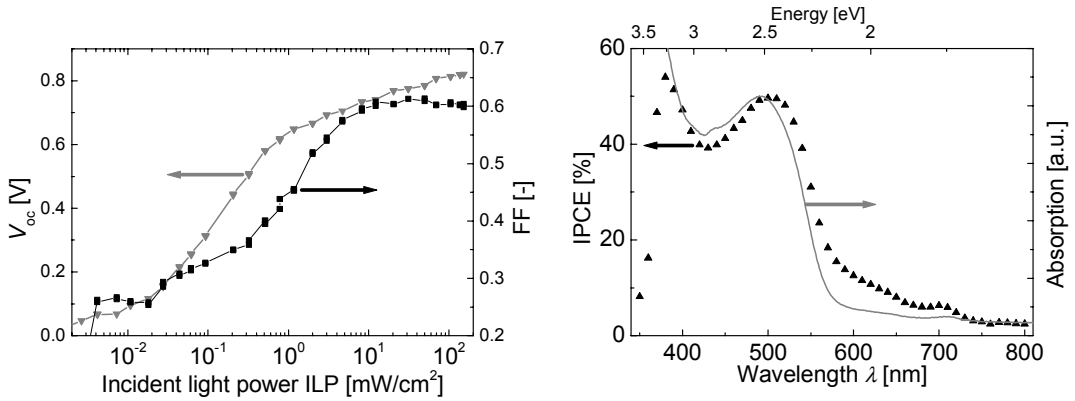

Figure 2.7 *Left: Open-circuit voltage (V_{oc}) and fill factor (FF) with varying incident light power (ILP) for a glass/ITO/PEDOT:PSS/MDMO-PPV:PCBM(1:4 by weight, 130 nm)/LiF(1.0 nm)/Al device. Right: Corresponding IPCE spectrum and absorption spectrum of the photoactive layer on glass (normalized to the IPCE spectrum at ~500 nm).*

PCBM composite in order to minimize charge-recombination losses (for details, see chapters 4 and 5). The solar cell shows an onset of V_{oc} at ILP ≈ 10^{-2} mW/cm^2, where the sharp increase in V_{oc} with ILP is followed by a less steep increase above ~1 mW/cm^2 (Figure 2.7). Just as V_{oc}, the fill factor FF starts to rise at ILP ≈ 10^{-2} mW/cm^2 but then goes through a maximum value, followed by a small decrease. The η_{pc} exhibits the same behavior with ILP as V_{oc}. A detailed electrical characterization and discussion for this type of solar cells are described in chapter 5.

Spectral response. The shape of the IPCE spectrum resembles the shape of the absorption spectrum (Figure 2.7). The overlap with the solar emission spectrum is rather small. At the maximum absorption wavelength λ_{max} = 500 nm of MDMO-PPV 50% of all incident photons result in a collected electron in the external circuit.

2.6 A mixture of a low-bandgap material and a methanofullerene

At present one of the limiting parameters for polymer photovoltaic energy conversion is the mismatch of the absorption spectrum of the photoactive layer with the solar emission. The donor polymers that are typically used in the construction of bulk-heterojunction solar cells, find their origin in the fields of LEDs and field-effect transistors (FETs). The optical bandgap of these polymers, such as poly(*p*-phenylene vinylene) and polythiophenes, lies in the range of E_g ~ 2.0-2.2 eV, and is not optimized with respect to the solar spectrum.[2,3,18] The use of low-bandgap (E_g < 1.8 eV) polymers would allow for an improved overlap of the polymer absorption spectrum with the solar emission. The latter reaches the first 50% of the total irradiance at 700 nm (1.77 eV, see Figure 2.3), more than a twofold increase compared to the spectral range reached with the current donor polymers. This improved overlap could lead to an enhancement in the efficiency of the solar cells. Another approach uses additional dyes as sensitizers,[143,144] typically resulting in three-component systems.

In designing new low-bandgap polymers for bulk-heterojunction solar cells various aspects need to be considered. For a conventional single-semiconductor homojunction solar cell, a reduction of E_g results in an increased absorption of light but at the same time lowers the open-circuit voltage (V_{oc}). As a consequence the optimum bandgap of such devices lies at 1.4 eV.[134] Recent studies by Michailetchi *et al.* show that for Ohmic contacts in bulk-heterojunction solar cells the negative and positive electrodes match the LUMO of the acceptor PCBM and the HOMO of the donor polymer, respectively, which govern the V_{oc}.[58] A reduction of the bandgap of the polymer by decreasing the oxidation potential (i.e. increasing the polymer HOMO level) may therefore reduce V_{oc}. On the other hand, a lowering of the bandgap by reducing the reduction potential (i.e. bringing down the polymer LUMO level) will reduce the driving force for the polymer to transfer an electron into the LUMO of PCBM. A final, non-trivial, issue is that low-bandgap conjugated polymers often exhibit efficient

non-radiative decay, which limits the natural lifetime of the excited state and hence the exciton diffusion length.

The synthetic principles for lowering the bandgap of linear π-conjugated polymers have been reviewed by Roncali.[145] A reduction of the bandgap of conjugated polymers can be accomplished, among others, by minimizing the bond length alternation and by reducing the energy difference between aromatic and quinoid canonical resonance structures. One successful, and potentially versatile, strategy to achieve low-bandgap conjugated polymers follows the pioneering work of Havinga[69] and involves the alternation of electron-rich (rich, R) and electron-deficient (poor, P) units in a conjugated polymer chain. Within the class of low-bandgap alternating R-P polymers, solution-processable materials are scarce and only a precursor polymer based on pyrrole and 2,1,3-benzothiadiazole has been reported.[146]

Condensation polymerization of 2,5-bis(5-trimethylstannyl-2-thienyl)-N-dodecylpyrrole (TPT) and 4,7-dibromo-2,1,3-benzothiadiazole (B) in the presence of $Pd(PPh_3)_2Cl_2$ as a catalyst (Stille coupling) afforded a novel conjugated oligomeric material polyTPTB (PTPTB), which exhibits a low optical bandgap as a result of the alternation of the electron-rich group thiophene-pyrrole-thiophene with the electron-deficient moiety benzothiadiazole along the chain (Figure 2.8).[147,148] A molecular weight fraction containing 5–17 aromatic units (n = 1-4) was isolated. Thin films of PTPTB exhibit an optical bandgap of 1.60 eV. Photoinduced absorption (PIA) and photoluminescence spectroscopy of blends of PTPTB and PCBM gave direct spectral evidence of the photoinduced electron transfer reaction from PTPTB as a donor to the fullerene derivative as an acceptor.[147]

Power conversion efficiency. Solar cells consisting of a 70 nm thick PTPTB:PCBM (1:1 by wt.) composite film spin cast from toluene sandwiched between ITO/PEDOT:PSS and Al electrodes showed J_{sc} = 0.80 mA/cm^2, V_{oc} = 0.67 V, FF = 0.35, and η_{pc} = 0.34% under white-light illumination of

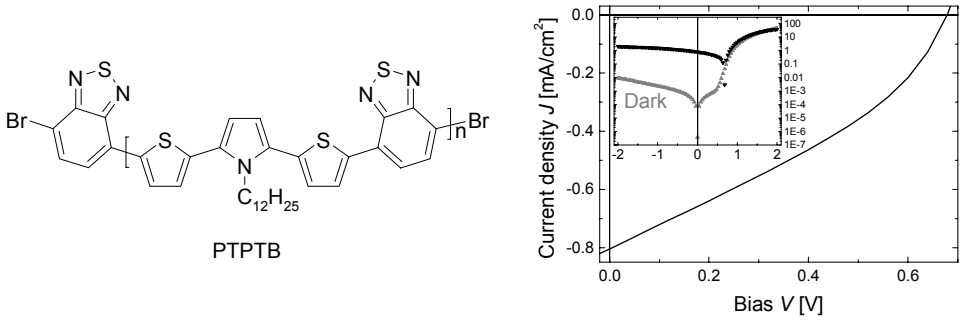

Figure 2.8 *Left: Molecular structure of PTPTB. Right: J-V characteristics of a glass/ITO/PEDOT:PSS/PTPTB:PCBM(1:1 by weight, 70 nm)/Al device under illumination of a white-light source filtered with a Schott KG1 filter (55 mW/cm^2). The inset shows the J-V characteristics on a single-logarithmic scale, both in the dark and under illumination.*

a filtered tungsten halogen lamp at ~55 mW/cm^2 (Figure 2.8). The low values of both J_{sc} and FF are mainly attributed to a combination of bulk and contact resistance. It is interesting to note that while the bandgap of PTPTB is ~0.5 eV less than that of MDMO-PPV, V_{oc} is lowered by only ~0.17 V compared to cells based on these PPV derivatives. The dark *J-V* characteristics show a good diode behavior with a rectification ratio (RR) of 5×10^3 at ±2 V in the dark, which shows that the device has little or no shunts in agreement with the smooth films as observed with AFM.

Performance with varying incident light power. The short-circuit current density J_{sc} shows a sub-linear dependence on ILP ($\alpha = 0.87$ in $J_{sc} \propto \mathrm{ILP}^{\alpha}$). For the ILP range investigated, the solar cell shows a gradual increase in V_{oc} with ILP, and a continuous decrease for FF (Figure 2.9). The development of η_{pc} with ILP is similar to that of FF. This behavior is attributed to huge recombination losses as a result of inefficient charge transport of at least one charge carrier. The latter might be due to either discontinuous charge-transport pathways or poor charge-carrier mobilities. No phase separation could be detected with AFM.

Spectral response. The spectral dependence of the device shows an onset of the photocurrent at 1.65 eV (750 nm, see Figure 2.9). The IPCE spectrum closely follows the absorption spectrum of the mixed film and confirms the contribution of PTPTB to the photocurrent for wavelengths up to 750 nm. At the maximum of the π-π* absorption band (570 nm) the IPCE is about 7%.

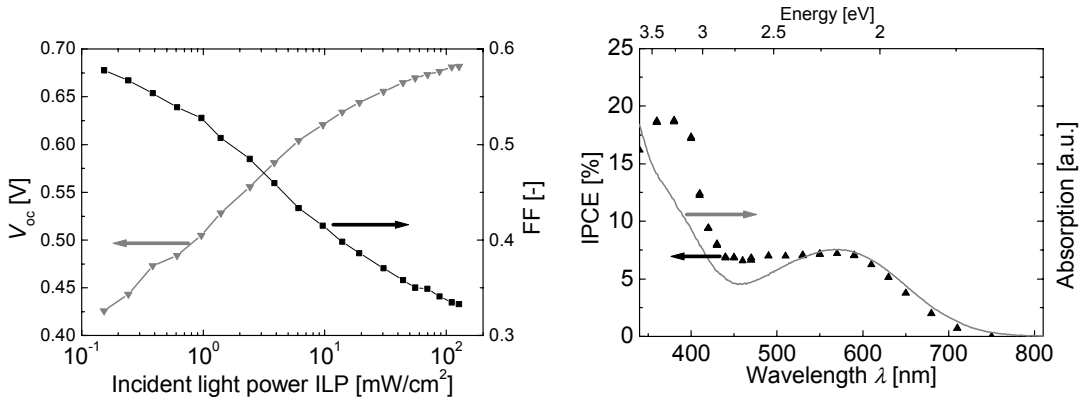

Figure 2.9 *Left: Open-circuit voltage (V_{oc}) and fill factor (FF) with varying incident light power (ILP) for a glass/ITO/PEDOT:PSS/PTPTB:PCBM(1:1 by weight, 70 nm)/Al device. Right: Corresponding IPCE spectrum and absorption spectrum of the photoactive layer on glass (normalized to the IPCE spectrum at ~540 nm).*

Recently, the performance of bulk-heterojunction solar cells based on PTPTB has been improved.[24] Since the design and incorporation of PTPTB in bulk-heterojunction solar cells, several

other examples of solution-processable low-bandgap polymers have been shown,[149,150] some of them incorporated in solar cells as well.[21-23] However, up to date PTPTB remains the best-performing material with an absorption beyond 700 nm.

2.7 A donor polymer backbone with pendant fullerenes

To ensure a large charge-generation interface between donor and acceptor phase, and efficient transport of the positive charge carriers through the donor phase and of electrons via the acceptor phase to the electrodes, a phase-segregated bicontinuous network is required. A convenient route to obtain a predefined nanoscopic phase-segregated network is linking donor and acceptor via a covalent bond. Two appealing approaches are the synthesis of block copolymers or polymers with pendant groups.[39-43,151]

The preparation of well-defined, solution-processable polymers incorporating fullerenes has remained a challenge over the years. Poly[OPV_3-E(C_{60})PE] (Figure 2.10) is the first processable π-conjugated donor polymer with pendant methanofullerenes that could be incorporated into working solar cells. Poly[OPV_3-E(C_{60})PE] was synthesized using a palladium-catalyzed cross-coupling reaction.[152,153] photoluminescence (PL) quenching as observed in thin films results from photoinduced charge transfer, as inferred from photoinduced absorption (PIA) spectroscopy.[152]

Power conversion efficiency. Photovoltaic cells were prepared by spin coating a 30 nm thick film of poly[OPV_3-E(C_{60})PE] from chloroform onto ITO/PEDOT:PSS followed by deposition of Al. The photocurrent of the device under white-light illumination (88 mW/cm^2, 400-900 nm[154]) reveals the following characteristics (Figure 2.10): J_{sc} = 0.42 mA/cm^2, V_{oc} = 0.83 V, FF = 0.29, and η_{pc} = 0.11%. The low value of J_{sc} is mainly attributed to the yellow color of the film and the low optical

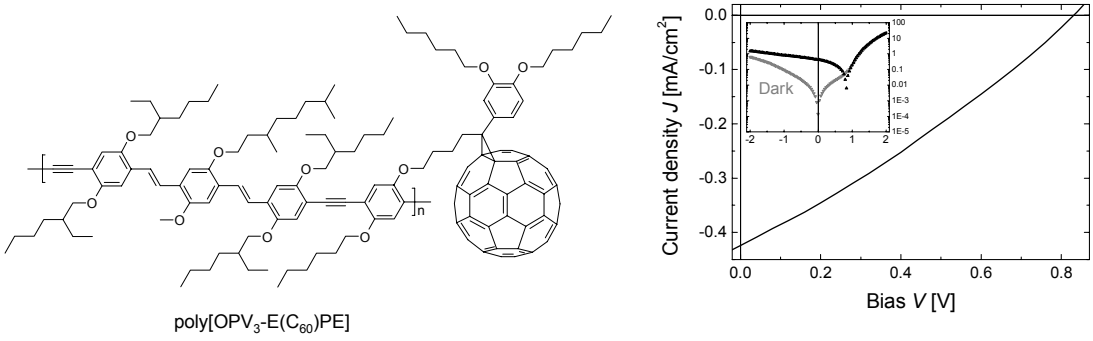

Figure 2.10 *Left: Molecular structure of poly[OPV_3-E(C_{60})PE]. Right: J-V characteristics of a glass/ITO/PEDOT:PSS/poly[OPV_3-E(C_{60})PE](30 nm)/Al device under illumination of a white-light source filtered with a Schott KG1 and GG385 filter (88 mW/cm^2, 400-900 nm). The inset shows the J-V characteristics on a single-logarithmic scale, both in the dark and under illumination.*

density as a result of the very low film thickness. The low value of FF is mainly attributed to the small parallel resistance, again as a result of the thickness. The same holds for the rather low rectification ratio (RR) of 36 at ±2 V in the dark. Because of the low film thickness, recombination losses are expected to be small. AFM showed the films to be smooth. Attempts to make thicker films with tape casting were unsuccessful, and hampered by the limited amount poly[OPV_3-E(C_{60})PE] available.

Performance with varying incident light power. The short-circuit current density J_{sc} shows a sub-linear dependence on ILP ($\alpha = 0.92$ in $J_{sc} \propto ILP^{\alpha}$). For the ILP range investigated, the solar cell shows a gradual increase in V_{oc} with ILP, whereas FF goes through a maximum (Figure 2.11). The development of η_{pc} with ILP is similar to that of FF.

Spectral response. The spectral dependence of the device shows an onset of the photocurrent at 550 nm (Figure 2.11). The IPCE spectrum resembles the absorption spectrum of the material, and exhibits a maximum of 6% at 480 nm.

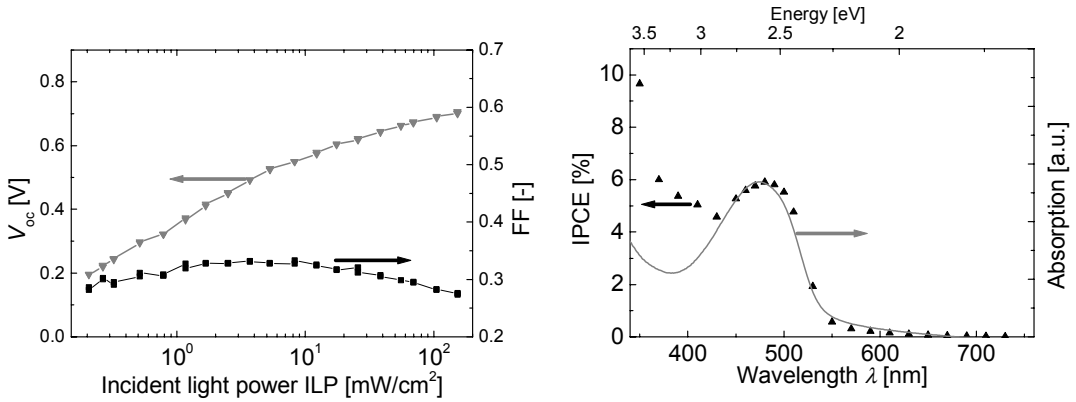

Figure 2.11 *Left: Open-circuit voltage (V_{oc}) and fill factor (FF) with varying incident light power (ILP) for a glass/ITO/PEDOT:PSS/poly[OPV_3-E(C_{60})PE](30 nm)/Al device. Right: Corresponding IPCE spectrum and absorption spectrum of the photoactive layer on glass (normalized to the IPCE spectrum at ~450 nm).*

Although the morphological structure of poly[OPV_3-E(C_{60})PE] has not been investigated, thicker films might result in discontinuities in the charge-transport pathways, consequently limiting both FF and RR. As outlined in chapter 5, efficient escape of the photogenerated charges from the donor-acceptor interface seems to be related to domain size. This suggests the existence of a lower limit for the domain size to guarantee efficient escape. Even when the nanoscale morphology ensures efficient percolation for both phases in thicker films of poly[OPV_3-E(C_{60})PE], the small domain size might, therefore, prevent efficient escape of the photogenerated charges from the interface.

2.8 Conclusions

State-of-the-art MDMO-PPV:PCBM bulk-heterojunction solar cells have been made and reach power conversion efficiencies of 2.5% under simulated solar light. To improve the power conversion efficiency, the use of new materials in bulk-heterojunction solar cells has been explored. Only two of the many new materials as applied in these solar cells over the past few years are described in this chapter. Replacing the orange MDMO-PPV with the low-bandgap material PTPTB resulted in a more red-shifted spectral response of these solar cells. Furthermore, the first example of a covalently linked donor polymer with pendant fullerenes in these solar cells is shown. Unfortunately, both new materials showed a decrease of the power conversion efficiency compared to the mixture of MDMO-PPV and PCBM. The same holds for all the other new materials explored.

In the field of polymer:fullerene bulk-heterojunction solar cells efficiencies have now been reached of >3% with IPCE values reaching 76%.[12,14] The increase in power conversion efficiency has been reached in part by an increase in overlap between the absorption spectrum of the photoactive layer with the solar emission spectrum, as compared to MDMO-PPV:PCBM solar cells. Additionally, the IPCE values also increased, as compared to those of MDMO-PPV:PCBM. It is not immediately apparent, however, why mixtures of some donor polymers with PCBM result in higher IPCE values than others. Differences in morphology, meaning differences in both the charge-generation interface and the number of percolation pathways, are believed to be the main cause. Furthermore, differences in the charge-carrier mobility are expected to contribute as well. Nevertheless, a clear and consistent view of the interplay of these parameters is lacking. The following chapters, therefore, deal with more fundamental issues concerning charge-carrier mobility and morphology. In these chapters MDMO-PPV, PCBM and their mixtures are used as an example.

2.9 Experimental section

Materials. The materials used were poly[2-methoxy-5-(3′,7′-dimethyloctyloxy)-1,4-phenylene vinylene] (MDMO-PPV) synthesized via the Gilch-route[155], PTPTB,[147] 1-(3-methoxy-carbonyl)propyl-1-phenyl-[6,6]-methanofullerene (PCBM)[156], poly[OPV_3-E(C_{60})PE],[152] polyethylenedioxythiophene:polystyrenesulfonate[98] (PEDOT:PSS) from Bayer AG (Baytron P VPAI 4083), LiF from Aldrich, and Al from Engelhard-Clal. Glass plates covered with 160 nm patterned ITO resulting in 4 different device areas (0.1, 0.15, 0.33, 1.0 cm^2) were used for device preparation.[80] Schott D263 glass plates were used for spectroscopic investigations.

Device preparation. The ITO covered glass substrates were first cleaned by ultrasonic treatment in acetone, rubbing with soap, rinsing with de-mineralized water, refluxing with iso-propanol, and finally 20 minutes UV ozone treatment. Subsequently, a ~100 nm thick layer of PEDOT:PSS was spin coated from an aqueous dispersion under ambient conditions on the cleaned substrates and the layer was dried by annealing the substrate for 1 minute, either at 100 °C without cooling, or at 180 °C and subsequently cooled for 1 minute at 25 °C. Then the photoactive layer was spin coated from an organic solution on top of the PEDOT:PSS layer and the sample was transferred to an N_2 atmosphere glove box. The organic solutions are stirred vigorously overnight while keeping them in the dark. All

polymer layers were spin cast via a two-step procedure employing a home-made chuck, which requires no vacuum, on a Chemat Technology spin coater model KW-4A placed in a laminar flowbox. First 7 seconds at 500 rpm followed by 35 seconds at 1500 rpm. Finally, (~10 Å LiF and subsequently) 100-110 nm aluminum layers were deposited by thermal evaporation in a vacuum chamber (5×10^{-6} mbar, 1 ppm O_2 and < 1 ppm H_2O). The samples were rotated at ~1 Hz during deposition to guarantee homogeneous films. All samples are stored in the dark in an N_2 atmosphere glove box.

Device measurements All measurements were performed in a N_2 atmosphere at room temperature. In forward bias the ITO electrode was positively biased. The devices were illuminated at the transparent ITO electrode. *J-V* characteristics were measured with a computer-controlled Keithley 2400 Source Meter, sweeping in steps of 0.04 V with a delay of 0.10 sec, in the dark or under white-light illumination. Light power is measured with an Ophir Laser Power Meter set at 610 nm, unless stated otherwise. Incident light power dependence measurements were performed using a similar setup where the light power (ILP) is varied over 5 orders of magnitude with a series of metal-coated neutral-density filters (Melles Griot) with a constant optical density for the involved spectral range. Spectrally resolved photocurrents were measured using either monochromatic light (~0.03 mW/cm^2), calibrated against a mc-Si solar cell with known spectral response or with monochromatic light (~1.0 mW/cm^2) calibrated with an Ophir Laser Power Meter. The stability of the devices was found to be more than sufficient to perform all the above measurements.

2.10 References and notes

1 N.S. Sariciftci, L. Smilowitz, A.J. Heeger, F. Wudl, *Science* **1992**, *258*, 1474.

2 E.A. Katz, in Encyclopedia of Nanoscience and Nanotechnology (Ed: H.S. Nalwa), **2003**, 10, 1.

3 C.J. Brabec, V. Dyakonov, J. Parisi, N.S. Sariciftci (Eds.), *Organic Photovoltaics*: *Concepts and Realization, Springer Series in Materials Science Vol. 60* Springer-Verlag, London, **2003**.

4 P. Peumans, A. Yakimov, S.R. Forrest, *J. Appl. Phys.* **2003**, *93*, 3693.

5 J.-M. Nunzi, *C. R. Physique* **2002**, *3*, 523.

6 G. Yu, J. Gao, J.C. Hummelen, F. Wudl, A.J. Heeger, *Science* **1995**, *270*, 1789.

7 J.J.M. Halls, C.A. Walsh, N.C. Greenham, E.A. Marseglia, R.H. Friend, S.C. Moratti, A.B. Holmes, *Nature* **1995**, *376*, 498.

8 M.M. Wienk, J.M. Kroon, W.J.H. Verhees, J. Knol, J.C. Hummelen, P.A. van Hal, R.A.J. Janssen, *Angew. Chem. Int. Ed*. **2003**, *42*, 3371.

9 Q. Zhou, L. Zheng, D. Sun, X. Deng, G. Yu, and Y. Cao, *Synth. Met.* **2003**, *135-136*, 825.

10 F.L. Zhang, M. Johansson, M.R. Andersson, J.C. Hummelen, O. Inganäs, *Synth. Met.* **2003**, *137*, 1401.

11 (a) J.V. Manca, T. Munters, T. Martens, Z. Beelen, L. Goris, J. D'Haen, M. D'Olieslaeger, L. Lutsen, D.Vanderzande, L. De Schepper, K. Haenen, M. Nesladek, W. Geens, J. Poortmans, R. Andriessen, *SPIE Proc.* **2003**, *4801*, 15; (b) T. Munters, T. Martens, L. Goris, V. Vrindts, J. Manca, L. Lutsen, W. De Ceuninck, D. Vanderzande, L. De Schepper, J. Gelan, N.S.Sariciftci, C.J. Brabec, *Thin Solid Films* **2002**, *403-404*, 247.

12 F. Padinger, R.S. Rittberger, N.S. Sariciftci, *Adv. Funct. Mater.* **2003**, *13*, 85.

13 R. Pacios, D.D.C. Bradley, J. Nelson, C.J. Brabec, *Synth. Met.* **2003**, *137*, 1469.

14 P. Schilinsky, C. Waldauf, C.J. Brabec, *Appl. Phys. Lett.* **2002**, *81*, 3885.

15 (a) J. Li, N. Sun, Z.X. Guo, C. Li, Y. Li, L. Dai, D. Zhu, D. Sun, Y. Cao, L. Fan, *Synth. Met.* **2003**, *137*, 1527; (b) J. Li, N. Sun, Z.X. Guo, C. Li, Y. Li, L. Dai, D. Zhu, D. Sun, Y. Cao, L. Fan, *J. Phys. Chem. B* **2002**, *106*, 11509.

16 A.P.H.J. Schenning, M. Fransen, J.K.J. van Duren, P.A. van Hal, R.A.J. Janssen, E.W. Meijer, *Macromol. Rapid Commun.* **2002**, *23*, 271.

17 J. Liu, Y. Shi, Y. Yang, *Adv. Funct. Mater.* **2001**, *11*, 420.

18 S.E. Shaheen, C.J. Brabec, N.S. Sariciftci, F. Padinger, T. Fromherz, J.C. Hummelen, *Appl. Phys. Lett*. **2001**, *78*, 841.

19 A. Dhanabalan, J.L.J. van Dongen, J.K.J. van Duren, H.M. Janssen, P.A. van Hal, R.A.J. Janssen, *Macromolecules* **2001**, *34*, 2495.

20 L. Chen, L.S. Roman, D.M. Johansson, M. Svensson, M.R. Andersson, R.A.J. Janssen, J.C. Hummelen, *Adv. Mater.* **2000**, *12*, 1110.

21 (a) M. Svensson, F. Zhang, S.C. Veenstra, W.J.H. Verhees, J.C. Hummelen, J.M. Kroon, O. Inganäs, M.R. Andersson, *Adv. Mater.* **2003**, *15*, 988; (b) M. Svensson, F. Zhang, O. Inganäs, M.R. Andersson, *Synth. Met.* **2003**, *135-136*, 137.

22 L. Goris, M.A. Loi, A. Cravino, H. Neugebauer, N.S. Sariciftci, I. Polec, L. Lutsen, E. Andries, J. Manca, L. De Schepper, D. Vanderzande, *Synth. Met.* **2003**, *138*, 249.

23 S.E. Shaheen, D. Vangeneugden, R. Kiebooms, D. Vanderzande, T. Fromherz, F. Padinger, C.J. Brabec, N.S. Sariciftci, *Synth. Met.* **2001**, *121*, 1583.

24 (a) C. Winder, D. Muehlbacher, H. Neugebauer, N.S. Sariciftci, C.J. Brabec, R.A.J. Janssen, J.C. Hummelen, *Mol. Cryst. Liq. Cryst.* **2002**, *385*, 93; (b) D. Muehlbacher, H. Neugebauer, A. Cravino, N.S. Sariciftci, J.K.J. van Duren, A. Dhanabalan, P.A. van Hal, R.A.J. Janssen, J.C. Hummelen, *Mol. Cryst. Liq. Cryst.* **2002**, *385*, 85; (c) C.J. Brabec, C. Winder, N.S. Sariciftci, J.C. Hummelen, R.A.J. Janssen, P.A. van Hal, A. Dhanabalan, *Adv. Funct. Mater.* **2002**, *12*, 709; (d) C.J. Brabec, S.E. Shaheen, T. Fromherz, F. Padinger, J.C. Hummelen, A. Dhanabalan, R.A.J. Janssen, N.S. Sariciftci, *Synth. Met.* **2001**, *121*, 1517.

25 (a) E. Kymakis, I. Alexandrou, G.A.J. Aramatunga, *J. Appl. Phys.* **2003**, *93*, 1764; (b) E. Kymakis, G.A.J. Aramatunga, *Appl. Phys. Lett.* **2002**, *80*, 112.

26 (a) S. Lee, T. Sonoda, H. Kajii, H. Araki, K. Yoshino, *J. Soc. Elect. Mat. Eng.* **2000**, *9*, 69; (b) K. Yoshino, H. Kajii, H. Araki, T. Sonoda, H. Take, S. Lee, *Full. Sci. Techn.* **1999**, *7*, 695.

27 P. Jonkheijm, J.K.J. van Duren, M. Kemerink, R.A.J. Janssen, E.W. Meijer, A.P.H.J. Schenning, *manuscript in preparation*.

28 A. El-Ghayoury, A.P.H.J. Schenning, P.A. van Hal, J.K.J. van Duren, R.A.J. Janssen, E.W. Meijer, *Angew. Chem. Int. Ed.* **2001**, *40*, 3660.

29 (a) J.J. Dittmer, E.A. Marseglia, R.H. Friend, *Adv. Mater.* **2000**, *12*, 1270; (b) J.J. Dittmer, R. Lazzaroni, Ph. Leclère, P. Moretti, M. Granström, K. Petritsch, E.A. Marseglia, R.H. Friend, J.L. Brédas, H. Rost, A.B. Holmes, *Sol. Energy Mater. Sol. Cells* **2000**, *61*, 53.

30 T. Kietzke, D. Neher, K. Landfester, R. Montenegro, R. Güntner, U. Scherf, *Nature Mater.* **2003**, *2*, 408.

31 D.M. Russell, A.C. Arias, R.H. Friend, C. Silva, C. Ego, A.C. Grimsdale, K. Müllen, *Appl. Phys. Lett.* **2002**, *80*, 2204.

32 M. Gutiérrez Nava, S. Setayesh, A. Rameau, P. Masson, J.F. Nierengarten, *New J. Chem.* **2002**, *26*, 1584.

33 A.C. Arias, J.D. MacKenzie, R. Stevenson, J.J.M. Halls, M. Inbasekaran, E.P. Woo, D. Richards, R.H. Friend, *Macromolecules* **2001**, *34*, 6005.

34 P. Peumans, S. Uchida, S.R. Forrest, *Nature* **2003**, *425*, 158.

35 (a) C. Melzer, V.V. Krasnikov, G. Hadziioannou, *Appl. Phys. Lett.* **2003**, *82*, 3101; (b) W. Geens, T. Aernouts, J. Poortmans, G. Hadziioannou, *Thin Solid Films*, **2002**, *403-404*, 438; (c) L. Ouali, V.V. Krasnikov, U. Stalmach, G. Hadziioannou, *Adv. Mater.* **1999**, *11*, 1515.

36 G. Matsunobu, Y. Oishi, M. Yokoyama, M. Hiramoto, *Appl. Phys. Lett.* **2002**, *81*, 1321.

37 D. Gebeyehu, B. Maennig, J. Drechsel, K. Leo, M. Pfeiffer, *Sol. Energy Mater. Sol. Cells* **2003**, *79*, 81.

38 (a) L. Schmidt-Mende, A. Fechtenkötter, K. Müllen, E. Moons, R.H. Friend, J.D. MacKenzie, *Science* **2001**, *293*, 1119; (b) L. Schmidt-Mende, M. Watson, K. Müllen, R.H. Friend, *Mol. Cryst. Liq. Cryst.* **2003**, *396*, 73.

39 E.E. Neuteboom, S.C.J. Meskers, P.A. van Hal, J.K.J. van Duren, E.W. Meijer, R.A.J. Janssen, H. Dupin, G. Pourtois, J. Cornil, R. Lazzaroni, J.L. Brédas, D. Beljonne, *J. Am. Chem. Soc.* **2003**, *125*, 8625.

40 A. Cravino, N.S. Sariciftci, *J. Mater. Chem.* **2002**, *12*, 1931.

41 F. Zhang, M. Svensson, M.R. Andersson, M. Maggini, S. Bucella, E. Menna, O. Inganäs, *Adv. Mater.* **2001**, *13*, 1871.

42 (a) B. de Boer, U. Stalmach, P.F. van Hutten, C. Melzer, V.V. Krasnikov, G. Hadziioannou, *Polymer* **2001**, *42*, 9097; (b) U. Stalmach, B. de Boer, C. Videlot, P.F. van Hutten, G. Hadziioannou, *J. Am. Chem. Soc.* **2000**, *122*, 5464.

43 Y. Eichen, G. Nakhmanovich, O. Epshtein, E. Ehrenfreund, *J. Phys. Chem. B* **2000**, *104*, 770.

44 E. Peeters, P.A. van Hal, J. Knol, C.J. Brabec, N.S. Sariciftci, J.C. Hummelen, R.A.J. Janssen, *J. Phys. Chem. B* **2000**, *104*, 10174.

45 J.F. Eckert, J.F. Nicoud, J.F. Nierengarten, S.G. Liu, L. Echegoyen, F. Barigelletti, N. Armaroli, L. Ouali, V. Krasnikov, G. Hadziioannou, *J. Am. Chem. Soc.* **2000**, *122*, 7467.

46 C.J. Brabec, S.E. Shaheen, C. Winder, N.S. Sariciftci, P. Denk, *Appl. Phys. Lett.* **2002**, *80*, 1288.

47 C.J. Brabec, G. Zerza, G. Cerullo, S. De Silvestri, S. Luzzati, J.C. Hummelen, N.S. Sariciftci, *Chem. Phys. Lett.* **2001**, *340*, 232.

48 T. Offermans, S.C.J. Meskers, R.A.J. Janssen, *J. Chem. Phys*. **2003**, *119*, 10467.

49 I. Montanari, A.F. Nogueira, J. Nelson, J.R. Durrant, C. Winder, M.A. Loi, N.S. Sariciftci, C.J. Brabec, *Appl. Phys. Lett.* **2002**, *81*, 3001.

50 D. Braun, *Materials Today* **2002**, *5*, 32.

51 C.D. Dimitrakopolous, P.R.L. Malenfant, *Adv. Mater.* **2002**, *14*, 99.

52 A.M. Stoneham, M.M.D. Ramos, A.M. Almeida, H.M.G. Correia, R.M. Ribeiro, H. Ness, A.J. Fisher, *J. Phys.*: *Condens. Matter* **2002**, *14*, 9877.

53 V.D. Mihailetchi, J.K.J. van Duren, P.W.M. Blom, J.C. Hummelen, R.A.J. Janssen, J.M. Kroon, M.T. Rispens, W.J.H. Verhees, M.M. Wienk, *Adv. Funct. Mater.* **2003**, *13*, 43.

54 R. Pacios, J. Nelson, D.D.C. Bradley, C.J. Brabec, *Appl. Phys. Lett.* **2003**, *83*, 4764.

55 S.A. Choulis, J. Nelson, Y. Kim, D. Poplavskyy, T. Kreouzis, J.R. Durrant, D.D.C. Bradley, *Appl. Phys. Lett.* **2003**, *83*, 3812.

56 P.W.M. Blom, M.C.J.M. Vissenberg, *Mater. Sci. Eng. R* **2000**, *27*, 53.

57 (a) K. Yoshino, Y.X. Hong, K. Muro, S. Kiyomatsu, S. Morita, A.A. Zakhidov, T. Noguchi, T. Ohnishi, *Jpn. J. Appl. Phys., Part 2* **1993**, *32*, L357; (b) J.J.M. Halls, K. Pichler, R.H. Friend, S.C. Moratti, A.B. Holmes, *Appl. Phys. Lett.* **1996**, *68*, 3120; (c) A. Haugeneder, M Neges, C. Kallinger, W. Spirkl, U. Lemmer, J. Feldmann, *Phys. Rev. B* **1999**, *59*, 15346.

58 V.D. Michailetchi, P.W.M. Blom, J.C. Hummelen, M.T. Rispens, *J. Appl. Phys.* **2003**, *94*, 6849.

59 (a) T.M. Brown, F. Cacialli, *J. Pol. Sci. B* **2003**, *41*, 2649; (b) T.M. Brown, J.S. Kim, R.H. Friend, F. Cacialli, R. Daik, W.J. Feast, *Appl. Phys. Lett.* **1999**, *75*, 1679.

60 (a) M. Fahlman, W.R. Salaneck, *Surf. Sci.* **2002**, *500*, 904; (b) W.R. Salaneck, M. Lögdlund, M. Fahlman, G. Greczynski, Th. Kugler, *Mater. Sci. Eng. R* **2001**, *34*, 121.

61 M. O'Neill, S.M. Kelly, *Adv. Mater.* **2003**, *15*, 1135.

62 J. Kim, *Pure Appl. Chem.* **2002**, *74*, 2031.

63 J. Cornil, D. Beljonne, J.P. Calbert, J.L. Brédas, *Adv. Mater.* **2001**, *13*, 1053.

64 D. Neher, *Macromol. Rapid Commun.* **2001**, *22*, 1365.

65 M. Leclerc, *J. Pol. Sci. A* **2001**, *39*, 2867.

66 Y. Shirota, *J. Mater. Chem.* **2000**, *10*, 1.

67 A. Ajayaghosh, *Chem. Soc. Rev.* **2003**, *32*, 181.

68 F. Wudl, *J. Mater. Chem.* **2002**, *12*, 1959.

69 H.A.M. van Mullekom, J.A.J.M. Vekemans, E.E. Havinga, E.W. Meijer, *Mat. Sci. Eng. R* **2001**, *32*, 1.

70 A. Kraft, A.C. Grimsdale, A.B. Holmes, *Angew. Chem. Int. Ed.* **1998**, *37*, 402.

71 Q.T. Zhang, J.M. Tour, *J. Am. Chem. Soc.* **1998**, *120*, 5355.

72 A.B. Chwang, M.A. Rothman, S.Y. Mao, R.H. Hewitt, M.S. Weaver, J.A. Silvernail, K. Rajan, M. Hack, J.J. Brown, X. Chu, L. Moro, T. Krajewski, N. Rutherford, *Appl. Phys. Lett.* **2003**, *83*, 413.

73 (a) R. Paetzold, K. Heuser, D. Henseler, S. Roeger, G. Wittmann, A. Winnacker, *Appl. Phys. Lett.* **2003**, *82*, 3342; (b) R. Peatzold, A. Winnacker, D. Henseler, V. Cesari, K. Heuser, *Rev. Sci. Instrum.* **2003**, *74*, 5147.

74 M. Hanika, H.C. Langowski, U. Moosheimer, W. Peukert, *Chem. Eng. Technol.* **2003**, *26*, 605.

75 M.S. Weaver, L.A. Michalski, K. Rajan, M.A. Rothman, J.A. Silvernail, J.J. Brown, P.E. Burrows, G.L. Graff, M.E. Gross, P.M. Martin, M. Hall, E. Mast, C. Bonham, W. Bennett, M. Zumhoff, *Appl. Phys. Lett.* **2002**, *81*, 2929.

76 R.S. Kumar, M. Auch, E. Ou, G. Ewald, S.J. Chua, *Thin Solid Films* **2002**, *417*, 120.

77 Y.S. Jung, J.Y. Seo, D.W. Lee, D.Y. Jeon, *Thin Solid Films* **2003**, *445*, 63.

78 K.B. Kim, Y.H. Tak, Y.S. Han, K.H. Baik, M.H. Yoon, M.H. Lee, *Jpn. J. Appl. Phys.* **2003**, *42*, L438.

79 H.T. Lu, M. Yokoyama, *J. Cryst. Growth* **2004**, *260*, 186.

80 ITO covered glass substrates were generously provided by Philips Research Laboratories Eindhoven.

81 N.R. Armstrong, C. Carter, C. Donley, A. Simmonds, P. Lee, M. Brumbach, B. Kippelen, B. Domercq, S. Yoo, *Thin Solid Films* **2003**, *445*, 342.

82 (a) A.B. Djurisic, C.Y. Kwong, P.C. Chui, W.K. Chan, *J. Appl. Phys.* **2003**, *93*, 5472; (b) C.Y. Kwong, A.B. Djurisic, P.C. Chui, L.S.M. Lam, W.K. Chan, *Appl. Phys. A* **2003**, *77*, 555.

83 (a) Z. Zhong, Y. Zhong, C. Liu, S. Yin, W. Zhang, D. Shi, *Phys. Stat. Sol. A* **2003**, *198*, 197; (b) Z. Zhong, S. Yin, C. Liu, Y. Zhong, W. Zhang, D. Shi, C. Wang, *Appl. Surf. Sci.* **2003**, *207*, 183.

84 P. He, S.D. Wang, W.K. Wong, L.F. Cheng, C.S. Lee, S.T. Lee, S.Y. Liu, *Chem. Phys. Lett.* **2003**, *370*, 795.

85 D. Lu, Y. Wu, J. Guo, G. Lu, Y. Wang, J. Shen, *Mat. Sci. Eng. B* **2003**, *97*, 141.

86 Q. Sun, C. Yang, G. He, Y. Li, H. Wang, *Synth. Met.* **2003**, *138*, 561.

87 T.P. Nguyen, P. Le Rendu, N.N. Dinh, M. Fourmigué, C. Mézière, *Synth. Met.* **2003**, *138*, 229.

88 I.M. Chan, F.C.N. Hong, *Thin Solid Films* **2003**, *444*, 254.

89 S. Jung, N.G. Park, M.Y. Kwak, B.O. Kim, K.H. Choi, Y.J. Cho, Y.K. Kim, Y.S. Kim, *Opt. Mater.* **2002**, *21*, 235.

90 X. Crispin, S. Marciniak, W. Osikowicz, G. Zotti, A.W. Denier van der Gon, F. Louwet, M. Fahlman, L. Groenendaal, F. De Schryver, W.R. Salaneck, *J. Pol. Sci. B* **2003**, *41*, 2561.

91 X. Crispin, A. Crispin, M.P. de Jong, S. Marciniak, W. Osikowicz, S. Jönsson, M. Fahlman, Th. Kugler, L.J. van IJzendoorn, M.J.A. de Voigt, W.R. Salaneck, *MRS Symp. Proc.* **2003**, *747*, 315.

92 F.J.J. Janssen, J.M. Sturm, A.W. Denier van der Gon, L.J. van IJzendoorn, M. Kemerink, H.F.M. Schoo, M.J.A. de Voigt, H.H. Brongersma, *Org. Electr.* **2003**, *4*, 209.

93 Th. Kugler, W.R. Salaneck, *C.R. Acad. Sci. IV* **2000**, *1*, 409.

94 M.P. de Jong, L.J. van IJzendoorn, M.J.A. de Voigt, *Appl. Phys. Lett.* **2000**, *77*, 2255.

95 A.A. Argun, A. Cirpan, J.R. Reynolds, *Adv. Mater.* **2003**, *15*, 1338.

96 F. Zhang, M. Johansson, M.R. Andersson, J.C. Hummelen, O. Inganäs, *Adv. Mater.* **2002**, *14*, 662.

97 A. Pud, N. Ogurtsov, A. Korzhenko, G. Shapoval, *Prog. Polym. Sci.* **2003**, *28*, 1701.

98 (a) L. Groenendaal, G. Zotti, P.H. Aubert, S.M. Waybright, J.R. Reynolds, *Adv. Mater.* **2003**, *15*, 855; (b) L. Groenendaal, F. Jonas, D. Freitag, H. Pielartzik, J. R. Reynolds, *Adv. Mat*. **2000**, *12*, 481.

99 A. Marletta, E. Piovesan, N.O. Dantas, N.C. de Souza, C.A. Olivati, D.T. Balogh, R.M. Faria, O.N. Oliveira, Jr., *J. Appl. Phys.* **2003**, *94*, 5592.

100 H. Frohne, S.E. Shaheen, C.J. Brabec, D.C. Müller, N.S. Sariciftci, K. Meerholz, *ChemPhysChem* **2002**, *3*, 795.

101 A. van Dijken, A. Perro, E.A. Meulenkamp, K. Brunner, *Org. Electr.* **2003**, *4*, 131.

102 X. Gong, D. Moses, A.J. Heeger, S. Liu, A.K.Y. Jen, *Appl. Phys. Lett.* **2003**, *83*, 183.

103 B. Domercq, R.D. Hreha, Y.D. Zhang, A. Haldi, S. Barlow, S.R. Marder, B. Kippelen, *J. Pol. Sci. B* **2003**, *41*, 2726.

104 (a) G.L. Frey, K.J. Reynolds, R.H. Friend, H. Cohen, Y. Feldman, *J. Am. Chem. Soc.* **2003**, *125*, 5998; (b) K.J. Reynolds, J.A. Barker, N.C. Greenham, R.H. Friend, G.L. Frey, *J. Appl. Phys.* **2002**, *92*, 7556; (c) G.L. Frey, K.J. Reynolds, R.H. Friend, *Adv. Mater.* **2002**, *14*, 265.

105 W. Osikowicz, A.W. Denier van der Gon, X. Crispin, M.P. de Jong, R. Friedlein, L. Groenendaal, M. Fahlman, D. Beljonne, R. Lazzaroni, W.R. Salaneck, *J. Chem. Phys.* **2003**, *119*, 10415.

106 J. Huang, P.F. Miller, J.C. de Mello, A.C. de Mello, D.D.C. Bradley, *Synth. Met.* **2003**, *139*, 569.

107 W.H. Kim, G.P. Kushto, H. Kim, Z.H. Kafafi, *J. Pol. Sci. B* **2003**, *41*, 2522.

108 L.A.A. Pettersson, S. Ghosh, O. Inganäs, *Org. Elect.* **2002**, *3*, 143.

109 P. Adriaensens, R. Carleer, L. Storme, D. Vanderzande, J. Gelan, *Polymer* **2002**, *43*, 7003.

110 H. Peisert, M. Knupfer, F. Zhang, A. Petr, L. Dunsch, J. Fink, *Appl. Phys. Lett.* **2003**, *83*, 3930.

111 J. Lu, N.J. Pinto, A.G. MacDiarmid, *J. Appl. Phys.* **2002**, *92*, 6033.

112 A.J. Epstein, F.C. Hsu, N.R. Chiou, V.N. Prigodin, *Synth. Met.* **2003**, *137*, 859.

113 R.A.M. Hikmet, R. Thomassen, *Adv. Mater.* **2003**, *15*, 115.

114 D. Marsitzky, J. Murray, J.C. Scott, K.R. Carter, *Chem. Mater.* **2001**, *13*, 4285.

115 L.D. Bozano, K.R. Carter, V.Y. Lee, R.D. Miller, R. Dipietro, J.C. Scott, *J. Appl. Phys.* **2003**, *94*, 3061.

116 R.G. Larson, T.J. Rehg, in *Liquid Film Coating* (Ed: S.F. Kistler, P.M. Schweizer), Chapman & Hall, London, **1997**.

117 K.E. Strawhecker, S.K. Kumar, *Macromolecules* **2001**, *34*, 4669.

118 L.L. Spangler, J.M. Torkelson, J.S. Royal, *Pol. Eng. Sci.* **1990**, *30*, 644.

119 L.I. Maissel, R. Glang, *Handbook of Thin Film Technology*, McGraw-Hill, New York, **1970**.

120 (a) D. Cahen, A. Kahn, *Adv. Mater.* **2003**, *15*, 271; (b) A. Kahn, N. Koch, W. Gao, *J. Pol. Sci. B* **2003**, *41*, 2529.

121 H.H.P. Gommans, A.W. Denier van der Gon, G.G. Andersson, L.J. van IJzendoorn, R.M.T. Pijper, H.H. Brongersma, *J. Appl. Phys.* **2003**, *94*, 5756.

122 (a) G.G. Andersson, W.J.H. van Gennip, J.W. Niemantsverdriet, H.H. Brongersma, *Chem. Phys.* **2002**, *278*, 159 (for corrections made to this manuscript, see W.J.H. van Gennip, *The Analysis of Polymer Interfaces, a Combined*

Approach, Ph. D. Thesis, Eindhoven University of Technology, **2003**); (b) G.G. Andersson, M.P. de Jong, F.J.J. Janssen, J.M. Sturm, L.J. van IJzendoorn, A.W. Denier van der Gon, M.J.A. de Voigt, H.H. Brongersma, *J. Appl. Phys.* **2001**, *90*, 1376.

123 G. Xu, *Chin. J. Pol. Sci.* **2003**, *21*, 527.

124 (a) L. Ke, K. Zhang, N. Yakovlev, S.J. Chua, P. Chen, *Mater. Sci. Eng. B* **2003**, *97*, 1; (b) L. Ke, S.J. Chua, K. Zhang, N. Yakovlev, *Appl. Phys. Lett.* **2002**, *80*, 2195; (c) S.J. Chua, L. Ke, R.S. Kumar, K. Zhang, *Appl. Phys. Lett.* **2002**, *81*, 1119; (d) K.K. Lin, S.J. Chua, W. Wang, *Thin Solid Films* **2002**, *417*, 36; (e) K.K. Lin, S.J. Chua, S.F. Lim, *J. Appl. Phys.* **2001**, *90*, 976; (f) S.F. Lim, L. Ke, W. Wang, S.J. Chua, *Appl. Phys. Lett.* **2001**, *78*, 2116.

125 M. Koeberg, D.S. Elson, P.M.W. French, D.D.C. Bradley, *Synth. Met.* **2003**, *139*, 925.

126 J.S. Kim, P.K.H. Ho, C.E. Murphy, N. Baynes, R.H. Friend, *Adv. Mater.* **2002**, *14*, 206.

127 F.J.J. Janssen, L.J. van IJzendoorn, H.F.M. Schoo, J.M. Sturm, G.G. Andersson, A.W. Denier van der Gon, H.H. Brongersma, M.J.A. de Voigt, *Synth. Met.* **2002**, *131*, 167.

128 M. Schaer, F. Nüesch, D. Berner, W. Leo, L. Zuppiroli, *Adv. Funct. Mater.* **2001**, *11*, 116.

129 R.E. Gill, P. van de Weijer, C.T.H. Liedenbaum, H.F.M. Schoo, A. Berntsen, J.J.M. Vleggaar, R.J. Visser, *Opt. Mater.* **1999**, *12*, 183.

130 N. Chawdhury, A. Köhler, M.G. Harrison, D.H. Hwang, A.B. Holmes, R.H. Friend, *Synth. Met.* **1999**, *102*, 871.

131 (a) B.H. Cumpston, K.F. Jensen, *Synth. Met.* **1995**, *73*, 195; (b) D.G.J. Sutherland, J.A. Carlisle, P. Elliker, G. Fox, T.W. Hagler, I. Jimenez, H.W. Lee, K. Pakbaz, L.J. Terminello, S.C. Williams, F.J. Himpsel, D.K. Shuh, W.M. Tong, J.J. Jia, T.A. Callcott, D.L. Ederer, *Appl. Phys. Lett.* **1996**, *68*, 2046; (c) K.Z. Xing, N. Johansson, G. Beamson, D.T. Clark, J.L. Brédas, W.R. Salaneck, *Adv. Mater.* **1997**, *9*, 1027; (d) L. Ma, X. Wang, B. Wang, J. Chen, J. Wang, K. Huang, B. Zhang, Y. Cao, Z. Han, S. Qian, S. Yao, *Chem. Phys.* **2002**, *285*, 85; (e) H.Y. Low, *Thin Solid Films* **2002**, *413,* 160; (f) B.J. Schwartz, *Annu. Rev. Phys. Chem.* **2003**, *54*, 141.

132 N. Camaioni, G. Ridolfi, G. Casalbore-Miceli, G. Possamai, L. Garlaschelli, M. Maggini, *Sol. Enery Mater. Sol. Cells* **2003**, *76*, 107.

133 (a) H. Neugebauer, C. Brabec, A. Cravino, T. Yohannes, P. Denk, S. Luzzati, M. Catellani, N.S. Sariciftci, *SPIE Proc.* **2002**, *4465*, 129; (b) H. Neugebauer, C. Brabec, J.C. Hummelen, N.S. Sariciftci, *Sol. Energy Mater. Sol. Cells* **2000**, *61*, 35.

134 A.L. Fahrenbruch, R.H. Bube, *Fundamentals of Solar Cells*, Academic Press, New York, **1983**.

135 J.M. Kroon, M.M. Wienk, W.J.H. Verhees, J.C. Hummelen, *Thin Solid Films* **2002**, *403-404*, 223.

136 (a) C. Riordan, R.L. Hulstrom, *Conference Record of the IEEE PVSC* **1990**, *21*, 1085; (b) Internal standard: *Photovoltaic devices, Part 3; Measurement principles for terrestrial photovoltaic (PV) solar devices with reference spectral irradiance data, CEI/IEC 904-3*, **1989**; (c) R.E. Bird, R.L. Hulstrom, *ASME J. Solar Energy Eng.* **1981**, *103*, 182.

137 T. Trupke, T. Würfel, I. Uhlendorf, *J. Phys. Chem. B* **2000**, *104*, 11484.

138 J. Rostalski, D. Meissner, *Sol. Energy Mater. Sol. Cells* **2000**, *61*, 87.

139 MDMO-PPV had a Mw of ~1 × 10^6 g/mol and a polydispersity of about 7 as measured by gel permeation chromatography, using a GPC column calibrated with polystyrene.

140 I. H. Campbell, T.W. Hagler, D.L. Smith, J.P. Ferraris, *Phys. Rev. Lett.* **1996**, *76*, 1900.

141 The Steuernagel SolarConstant 1200 was calibrated with an MDMO-PPV:PCBM reference cell from ECN.

142 A.M. Goodman, A. Rose, *J. Appl. Phys.* **1971**, *42*, 2823.

143 C. Winder, G. Matt, J.C. Hummelen, R.A.J. Janssen, N.S. Sariciftci, C.J. Brabec, *Thin Solid Films* **2002**, *403-404*, 373.

144 L.C. Chen, O. Inganäs, L.S. Roman, M. Johansson, M. Andersson, *Thin Solid Films* **2000**, *363*, 286.

145 J. Roncali, *Chem. Rev.* **1997**, *97*, 173.

146 H.A.M. van Mullekom, J.A.J.M. Vekemans, E.W. Meijer, *Chem. Commun.* **1996**, 2163.

147 A. Dhanabalan, J.K.J. van Duren, P.A. van Hal, J.L.J. van Dongen, R.A.J. Janssen, *Adv. Funct. Mater.* **2001**, *11*, 255.

148 PTPTB was synthesized by Dr. A. Dhanabalan.

149 H. Neugebauer, A. Cravino, S. Luzzati, M. Catellani, A. Petr, L. Dunsch, N.S. Sariciftci, *Synth. Met.* **2003**, *139*, 747.

150 H. Meng, D. Tucker, S. Chaffins, Y. Chen, R. Helgeson, B. Dunn, F. Wudl, *Adv. Mater.* **2003**, *15*, 146.

151 (a) S. Sun, Z. Fan, Y. Wang, J. Haliburton, C. Taft, S. Maaref, K. Seo, C.E. Bonner, *Synth. Met.* **2003**, *137*, 883; (b) S. Sun, *Pol. Mat.*: *Sci. Eng.* **2003**, *88*, 158.

152 A. Marcos Ramos, M.T. Rispens, J.K.J. van Duren, J.C. Hummelen, R.A.J. Janssen, *J. Am. Chem. Soc.* **2001**, *123*, 6714.

153 Poly[OPV_3-E(C_{60})PE] was synthesized by Dr. A. Marcos Ramos.

154 A tungsten-halogen lamp was used and filtered by a Schott KG1 and GG385 filter resulting in a spectral range of 400-900 nm with its maximum at ~650 nm as determined with a calibrated Avantes AVS-PC2000 fiberoptic spectrometer.

155 MDMO-PPV was generously provided by Philips Research Laboratories Eindhoven. Synthesis as described in H. Becker, H. Spreitzer, W. Kreuder, E. Kluge, H. Schenk, I. Parker, Y. Cao, *Adv. Mater*. **2000**, *12*, 42 and references therein.

156 J.C. Hummelen, B.W. Knight, F. LePeq, F. Wudl, J. Yao, C.L. Wilkins, *J. Org. Chem.* **1995**, *60*, 532.

Chapter 3

Disorder and charge transport in a methanofullerene and poly(*p*-phenylene vinylene)*

Abstract

Transport of charge carriers in organic semiconductor films is known to be strongly dependent on the morphology. Here morphological investigations on films of 1-(3-methoxycarbonyl)propyl-1-phenyl-[6,6]-methanofullerene (PCBM) and several poly(p-phenylene vinylene)s (PPVs) are combined with the analysis of charge-carrier-mobility data. It has been found that electron transport through spin cast PCBM films can consistently be described by the correlated Gaussian disorder model (CDM). Transmission electron microscopy (TEM) shows these spin cast films to be homogeneous in appearance, whereas selected-area electron diffraction (SAED) indicates that the films consist of a large number of randomly oriented nanocrystals. The latter, therefore, confirms the disorder as inferred from the CDM-behavior. Imaging individual conjugated polymer chains and aggregates on cast films with scanning force microscopy (SFM) is shown for the first time. A preference for straight and worm-like conformations is observed for cast films of symmetrically substituted PPVs, compared to more spiraling conformations for asymmetrically substituted PPVs. For thin cast films of symmetrically substituted PPVs, the larger tendency to aggregate into ordered domains and, consequently, the larger zero-field hole mobility observed for symmetrically substituted PPVs seem to result from more linear conformations, as compared to asymmetrically substituted PPVs.

*Part of this work has been published: (a) M. Kemerink, J.K.J. van Duren, J. Wildeman, A.J.J.M. van Breemen, H.F.M. Schoo, R.A.J. Janssen, *manuscript in preparation*; (b) X. Yang, J.K.J. van Duren, M.T. Rispens, J.C. Hummelen, R.A.J. Janssen, M.A.J. Michels, J. Loos, *Adv. Mater.* **2004**, *in press*; (c) M. Kemerink, J.K.J. van Duren, P. Jonkheijm, W.F. Pasveer, P.M. Koenraad, R.A.J. Janssen, H.W.M. Salemink, J.H. Wolter, *Nano Lett.* **2003**, *3*, 1191; (d) M. Kemerink, J.K.J. van Duren, P. Jonkheijm, P.M. Koenraad, R.A.J. Janssen, H.W.M. Salemink, J.H. Wolter, *MRS Symp. Proc.* **2003**, *771*, 23; (e) V.D. Mihailetchi, J.K.J. van Duren, P.W.M. Blom, J.C. Hummelen, R.A.J. Janssen, J.M. Kroon, M.T. Rispens, W.J.H. Verhees, M.M. Wienk, *Adv. Funct. Mater.* **2003**, *13*, 43.

3.1 Introduction

In the field of organic electronics conjugated polymers or molecules are used as the active material for e.g. field-effect transistors (FETs),[1] light-emitting diodes (LEDs),[2,3] and photovoltaic diodes (PVDs).[4,5] It has been shown that surface alignment layers,[6-10] choice of substrate,[11] conditions for deposition of the conjugated organics,[12-17] post-production treatment,[18-20] appropriate choice of side-chains,[21-26] variation of polymer molecular weight,[27-30] and regio-regularity of polymers,[31,32] all have a large influence on the charge-carrier mobility in these devices, because they affect the morphology of the active layer dramatically. With the choice of molecular core or polymer backbone, and the influence of precursor routes, purity, defects and end groups not even included in the previous list, it might be clear that morphology of conjugated organic films is far from being well controlled or understood. In addition, most conjugated organic films are highly inhomogeneous, and even in relatively well-ordered films the ordering generally occurs in domains of sub-micron dimensions.[1,12,15,31,33-38] Improving charge-carrier mobility in organic electronics therefore starts already at the molecular level where polymer chain conformations and molecular aggregation strongly influence the charge transport in the solid state.[1,39-43] However, this is not limited to the size of, and the order within domains, because also the orientation of these domains, as a result of the anisotropy of charge-carrier mobility in organic semiconductors, plays an additional role in determining the macroscopic mobility.[6-10,19,29,31]

$$\mu(E,T) = \mu(E=0,T) \times \exp\left(\gamma(T) \times \sqrt{E}\right)$$

Equation 3.1 *For many disordered organic materials the electric field E and temperature T dependence of the charge carrier mobility μ is described by a stretched exponential dependence. Both the zero-field mobility $\mu(E=0)$ and the field-activation pre-factor γ change with temperature.*

Transport in these disordered organic semiconductors, both polar and nonpolar, occurs via a thermally assisted or phonon-assisted intermolecular hopping process.[44,45] The charge-carrier mobility[46] μ of these materials, e.g. poly[2-methoxy-5-(3′,7′-dimethyloctyloxy)-1,4-phenylene vinylene] (MDMO-PPV),[47] is dependent on the electric field E following the stretched exponential form as shown in Equation 3.1. This expression for the field and temperature dependent charge-carrier mobility $\mu(E,T)$ consists of a field-independent thermally activated mobility ($\mu[E=0,T]$) and a field-dependent term ($\exp[\gamma \times \sqrt{E}]$). The stretched exponential form of the electric field dependence for the charge-carrier mobility (μ) makes charge transport in these materials strongly dependent on the applied bias.

Several one-, two-, and three-dimensional transport models for disordered semiconductors exist. However, all introduce energetic disorder, structural disorder (Figure 3.1), either static or dynamic, and local interactions in a different way.[48-62] Most of these models are only able to describe the transport in a limited field, temperature, and charge-density range. Because a detailed comparison of the various models with new or existing experimental data is beyond the scope of this thesis, the temperature- and field-dependent mobility data will be analyzed with the correlated Gaussian disorder model (see section 3.2.2), which is one of the most widely used models, and compared to morphology investigations on the same films.

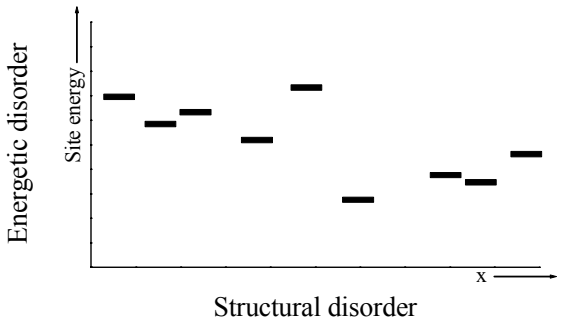

Figure 3.1 *Inhomogeneity (disorder) in site energy and structure (position) for transport sites in a disordered semiconductor exemplified for a one-dimensional case.*

Since the discovery of electroluminescence in poly(*p*-phenylene vinylene) (PPV),[63] and photoinduced charge transfer between PPV and Buckminsterfullerene,[64,65] a large amount of PPV and fullerene derivatives have been studied in a variety of electronic applications. In this chapter spin cast films of several derivatives of poly(*p*-phenylene vinylene) are investigated on a molecular level using scanning force microscopy (SFM) to relate the substitution pattern of the PPV-backbone to single-chain conformation and aggregation, and possibly to the differences observed in hole mobility as reported in literature. Additionally, analysis of temperature-dependent current density-voltage characteristics of devices based on PCBM films is performed to determine the electron mobility in PCBM and these investigations are combined with transmission electron microscopy (TEM) and selected-area electron diffraction (SAED) measurements to get insight in the influence of disorder. Finally, the charge-carrier mobility for MDMO-PPV is compared to that of PCBM and discussed in relation to the morphology of both spin cast films.

3.2 Charge-carrier mobility

In this paragraph the experimental technique, as used in this thesis to determine the charge-carrier mobility, will be discussed briefly. Subsequently, the theoretical model, most frequently used to describe charge transport in disordered organic materials, will be explained shortly.

3.2.1 Mobility measurements with the space-charge-limited (SCL) technique

With the higher quality materials, higher quality sample preparation, and more than a decade of scientific and technical progress, the understanding of organic semiconductor devices has improved enormously.[58,66-69] Literature has shown that the charge transport in a large amount of organic diodes provided with the appropriate contacts, is bulk-limited, because of the combination of low contact barriers and low charge-carrier mobilities. The contact barriers are often so small, that the contacts can be considered Ohmic. In the following only single-carrier bulk-limited devices will be considered, which allows one to extract the charge-carrier mobility. This technique is also known as the space-charge-limited technique for mobility measurements.

For single-carrier bulk-limited conduction (treating the active layer essentially as an insulator), the total current that flows is determined by the electric field and by the presence of carrier concentration gradients. These contributions are referred to as drift and diffusion currents, respectively. Due to the combination of a low contact barrier for injection with a low charge-carrier mobility, space charge will accumulate at the injecting contact until a steady state is reached. The present space charge at the injecting contact results in band bending (Figure 3.2). The space-charge distribution $dE(x)/dx$ (and $E[x]$) in SCL devices is governed by Poisson's equation with a constant (steady-state) device current across a homogeneous layer for a field-independent mobility (trap-free square law, see Figure 3.2).[70,71]

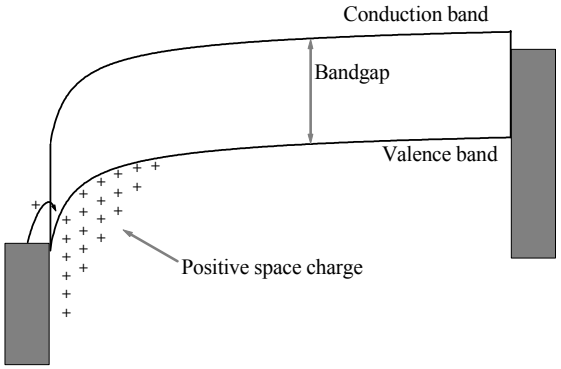

$$SCLC \quad J = \frac{9}{8}\varepsilon\mu\frac{V^2}{L^3}$$

$$J \propto CV \times \frac{\mu V}{L}$$

Figure 3.2 *Band diagram of a hole-only device for conventional space-charge limited (SCL) current (bulk-limited) showing the injection of holes from a high-workfunction electrode in a low-mobility material. Accumulation of space charge (holes) at the injecting contact results in band bending. For SCL conduction (SCLC) the current density J is quadratically dependent on the applied voltage V (with the charge carrier mobility μ constant). Treating the device as a capacitor with capacitance C, it's immediately apparent that the current density J, the product of the charge CV and the velocity μV/L, depends quadratically on V.*

As stated above, the mobility is actually field-dependent for these systems and, therefore, the space-charge-limited conduction (SCLC) model has to be combined with the typical stretched

exponential field dependence $\mu = \mu(E=0) \times \exp(\gamma \times \sqrt{E})$ observed for these materials. This combination can be solved numerically for a given single-carrier current,[72,73] and will result in the field-independent activated mobility $\mu(E=0)$ and the pre-factor γ for the field-dependent part of the mobility at each temperature.

3.2.2 Transport through disordered organic semiconductors

The stretched exponential dependence $\mu \propto \exp(\gamma \times \sqrt{E})$ is often found for the charge-carrier mobility in very different classes of organic materials, thereby ruling out a universal explanation based on charged traps.[48,74] The first successful transport model that explained many features of the charge transport in disordered organic materials is the Gaussian disorder model (GDM).[75,76] This model assumes a Gaussian shape of the distribution of the hopping site energies (the energetic spread or density of localized states, DOS) where the hopping rate is of the Miller-Abrahams type,[77,78] and the charges hop in a regular cubic lattice with spacing *a* from site to site (Figure 3.3). Although the target site should be on the cubic lattice, its direction and distance are not fixed. This way, both energetic and positional disorder are introduced.[79]

The hopping model assumes that the coupling of the charge to intramolecular modes is weak. This results in a transport mechanism in which the activation energy is ruled by the (intermolecular) static energetic disorder only and fully ignores intramolecular deformation energies.

A further improvement on GDM was made, after it was recognized that a correlated nature of the distribution of the site energies, as might be expected for conjugated organic films where order typically is larger on a smaller length scale, significantly affects charge transport in a disordered medium.[80] In striking contrast to GDM, spatially close sites should therefore be assigned closer energies. This resulted in the correlated Gaussian disorder model (CDM) where spatial correlations because of charge-dipole interactions, originating from the dipolar glass (DG) model,[81] are taken into account.[82,83]

Although, the quadrupolar glass (QG) model[84,85] (and the Los Alamos (LA) model for PPV)[54,86] might be a suitable candidate as well to describe transport through MDMO-PPV and PCBM, the good agreement with experimental data for the CDM and the absence of 3D charge-transport simulations for the QG (and LA) model has led to the choice of CDM in this thesis.[87] Recent insights[52,88] suggest that transport *J* is *not* linear with charge density ρ_f ($\mu[\rho_f]$),[89] as assumed within the most widely used device modeling incorporating CDM. How this influences device modeling and the exact form of the charge-carrier mobility will become clear within the coming years.

$$\mu(E,T) = \mu(E=0)\exp\left(\gamma\sqrt{E}\right) = \mu_{T\to\infty}\exp\left[-\left(\frac{3\sigma}{5k_BT}\right)^2 + 0.78\left(\left(\frac{\sigma}{k_BT}\right)^{3/2} - 2\right)\sqrt{\frac{eaE}{\sigma}}\right]$$

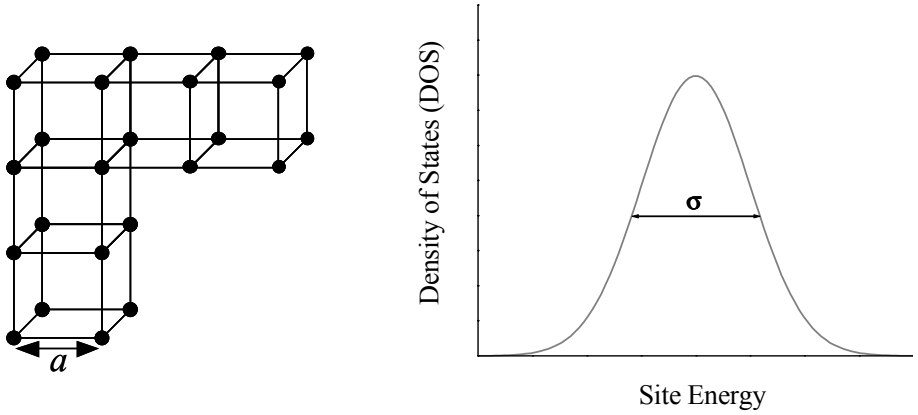

Figure 3.3 *Above: Empirical relation for the electric field E and temperature T dependence of the charge-carrier mobility μ based on simulations of transport in a correlated Gaussian disorder model (CDM) where transport occurs via hops between sites in a cubic lattice with spacing a (left picture) and with a Gaussian distribution of the site energy (DOS) with band width σ (right graph). The hopping rate is of the Miller-Abrahams type. CDM takes into account spatial correlations resulting from charge-dipole interactions.*

3.3 Disorder and transport in a methanofullerene film

In order to investigate whether disorder, governing charge transport in many conjugated materials, also influences the electron transport through spin cast films of PCBM, the space-charge limited (SCL) technique was used to determine the electron mobility and combined with morphological investigations using transmission electron microscopy (TEM) and selected-area electron diffraction (SAED).

As previously recognized, casting fullerenes using solvent evaporation typically results in polymorphous fullerene films,[90] where the film morphology will strongly depend on processing kinetics and substrate choice,[91] as pointed out in the introduction. As a result of the solubilizing substituent attached to the C_{60} in PCBM (Figure 3.4), the tendency to crystallize reduces, and therefore the order within the films is expected to decrease even further than for C_{60}. In many of its properties, PCBM is expected to resemble charge-transporting molecular glasses.[92]

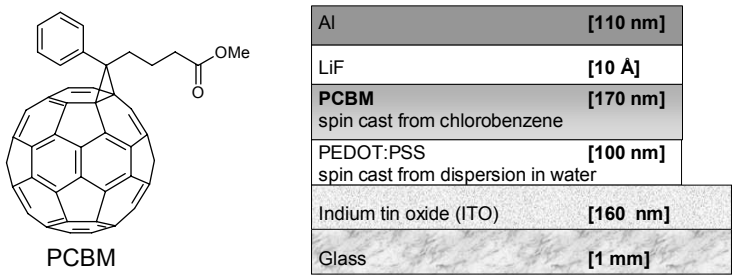

Figure 3.4 *Molecular structure of PCBM and the device structure as used for mobility measurements.*

3.3.1 Electron transport in a methanofullerene film

In order to measure the electron mobility in PCBM, devices have been made with LiF/Al as the injecting contact and ITO/PEDOT:PSS as the collecting contact for the electron. Note that the *J-V* characteristics are measured in the dark. LiF as intermediate layer between the conjugated organic and Al is known to enhance electron injection.[93] Although, the exact mechanism that leads to the enhanced electron injection when incorporating LiF is still under debate,[93,94] recent results show that doping of either MDMO-PPV or PCBM by Li is unlikely for the improvement of electron injection which leaves the aligned dipole mechanism as the most probable mechanism.[95] The latter will be discussed in detail in chapter 6.

The inset of Figure 3.5a shows an energy band diagram of the device. It is expected that LiF/Al will form an Ohmic contact for electron injection on PCBM. The work function of

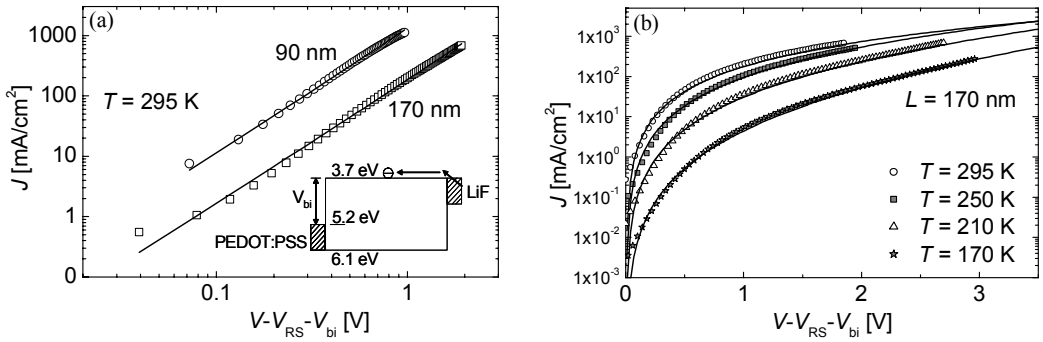

Figure 3.5 (a) *Experimental (symbols) and calculated (solid lines) J-V characteristics for ITO/PEDOT:PSS/PCBM/LiF/Al devices with thickness L = 90 nm and 170 nm, using V_{bi} = 1.4 V and $V_{RS} = I \times R_S$ with R_S = 30 Ω (see text). The device band diagram is indicated in the inset. The transport is described by electron-only space-charge-limited conduction (SCLC) with $\mu_e = 2 \times 10^{-3}$ cm²/Vs.* **(b)** *Experimental (symbols) and calculated (solid lines) J-V characteristics at various temperatures. Calculations are performed for electron-only SCLC using the stretched exponential field-dependent mobility* $\mu = \mu(E{=}0) \times \exp(\gamma \times \sqrt{E})$.

PEDOT:PSS (5.2 eV)[96] does not match the highest occupied molecular orbital (HOMO) level of PCBM (6.1 eV),[5] thus hole injection from PEDOT:PSS into PCBM can be neglected.[97] Consequently, only electrons are expected to flow in the PCBM under forward bias conditions. Furthermore, a built-in voltage V_{bi} of around 1.5 V is expected at room temperature from the energy band diagram. With decreasing temperature V_{bi} is expected to typically increase by 0.3 V from 300 K to 150 K, because of a concurrent decrease in diffusion of thermally injected charges.[98]

Figure 3.5a shows the experimental *J-V* characteristics at room temperature (T = 295 K) for PCBM devices with layer thicknesses L of 90 nm and 170 nm. Using V_{bi} = 1.4 V, and correcting for the voltage drop (V_{RS}) over the contacts,[99] it is observed from the slope of the double logarithmic *J-V* plot that the current density depends on the voltage squared.[100] With ε_r = 3.9,[101] the *J-V* characteristics of the devices with L = 90 and 170 nm are well described by SCLC using $\mu_e = 2 \times 10^{-3}$ cm^2/Vs. Recently, similar values have been reported by others with different mobility techniques.[102,103] Thus, the observation of SCLC provides direct information on the electron mobility in PCBM.

The observed electron mobility of 2×10^{-3} cm^2/Vs in spin cast films of PCBM is a factor of 40 less than mobilities reported on thin films of evaporated C_{60} in FETs, which are typically 0.08 cm^2/Vs,[104,105] whereas C_{60} powder, measured by pulse-radiolysis time-resolved microwave conductivity (PR-TRMC), gave a minimum value of 0.1 cm^2/Vs for the sum of both charge carriers.[106] Recently, improved processing under a high vacuum[107] resulted in a field-effect mobility of 0.5 cm^2/Vs similar to those observed for C_{60} single-crystals by time-of-flight (TOF) experiments.[108,109] A typical value of 1 cm^2/Vs has been reported for sublimed C_{60} films characterized by the moving photocarrier grating technique.[110] Although electronic differences as a result of adding the solubilizing group will,[111] and oxygen[110] might contribute to the observed difference in charge-carrier mobility between C_{60} and PCBM, a change in morphology, as a result of a decrease in the tendency to crystallize for PCBM compared to C_{60},[13,112] is seen as the most important parameter in reducing the electron mobility observed for PCBM.

Figure 3.5b shows the *J-V* characteristics of a PCBM device with L = 170 nm as a function of temperature.[113] In order to describe the electron current in PCBM the SCL conduction model is combined with the stretched exponential field-dependence (see previous sections). In the studied temperature range, the built-in voltage V_{bi} gradually increases from 1.4 V (295 K) to 1.7 V (150 K).[98] It appears that the E and T dependence of the *J-V* characteristics are consistently described by the combination of SCLC and the empirical mobility of Equation 3.1. This demonstrates that the stretched exponential field-dependence is also applicable to the electron transport in PCBM. From these *J-V* characteristics the temperature dependence of $\mu(E=0)$ and γ (Equation 3.1) are determined. According to the empirical relation for CDM (Figure 3.3) the slope of a plot of the zero-field mobility $\mu(E=0) \propto T^{-2}$ then directly provides a value for σ. In Figure 3.6a the experimental $\mu(E=0)$ is plotted against T^{-2}.

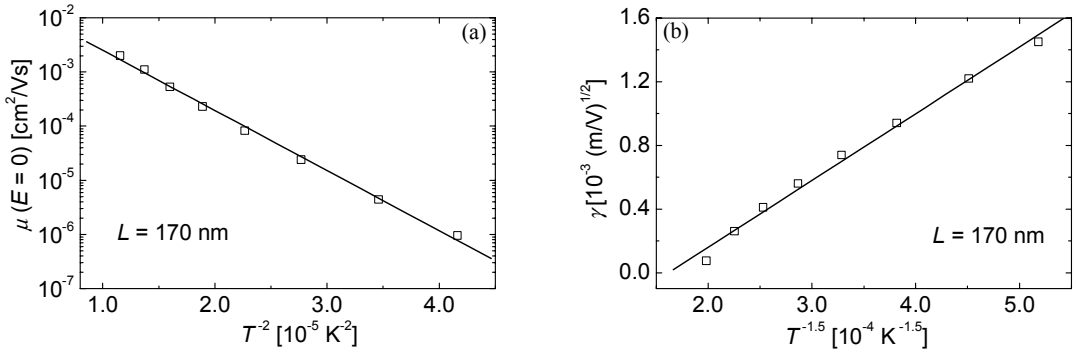

Figure 3.6 (a) *Experimental zero-field mobility μ(E=0) (squares), as obtained from the SCL electron-only devices using a stretched exponential field-dependence* $\mu = \mu(E=0) \times \exp(\gamma\times\sqrt{E})$, *versus* T^{-2} *with the solid line the T-dependence* $\ln[\mu(E=0)] \propto T^{-2}$ *according to the correlated Gaussian disorder model (CDM) with an energetic bandwidth* σ *= 73 meV.* **(b)** *Experimental pre-factor* γ *(squares) with the solid line the CDM T-dependence* $\gamma \propto T^{-1.5}$ *with an average hopping distance* ***a*** *= 3.4 nm.*

For σ = 73 meV, the predictions of CDM are in excellent agreement with the experimental electron mobilities. Subsequently, with σ known the intersite spacing *a* can be determined from the slope of $\gamma \propto T^{-3/2}$. As shown in Figure 3.6b the experimental γ is consistently described by using an intersite spacing *a* = 3.4 nm.

In conclusion, the temperature-dependent SCLC technique has provided the electron mobility of PCBM of $\mu_e = 2 \times 10^{-3}$ cm^2/Vs. Furthermore, the temperature dependence can be described with the CDM providing a bandwidth σ = 73 meV and an intersite spacing of 3.4 nm.

3.3.2 Morphology of a methanofullerene film

Spin cast PCBM films from chlorobenzene typically are both homogeneous and transparent. Figure 3.7 shows the bright-field transmission electron microscopy (TEM) images and the corresponding electron diffraction patterns of thin PCBM films prepared by various casting methods. The first method is spin coating from chlorobenzene onto glass/ITO/PEDOT:PSS, the second method is slow evaporation of a droplet of chlorobenzene solution under a saturated atmosphere onto an amorphous carbon-coated TEM-grid, and the third method is annealing a film spin cast from toluene directly onto an amorphous carbon-coated TEM-grid at 130 ºC for ca. 50 hours.[114] The spin cast films can be completely separated from the glass/ITO/PEDOT:PSS substrates, and thus self-supported films were obtained for TEM investigation.

The spin cast films demonstrate a quite homogeneous morphology, although there are some thickness fluctuations, as can be seen from the existence of darker and brighter regions in the films (Figure 3.7a). If the solvent is evaporated slowly under a saturated atmosphere, large PCBM clusters

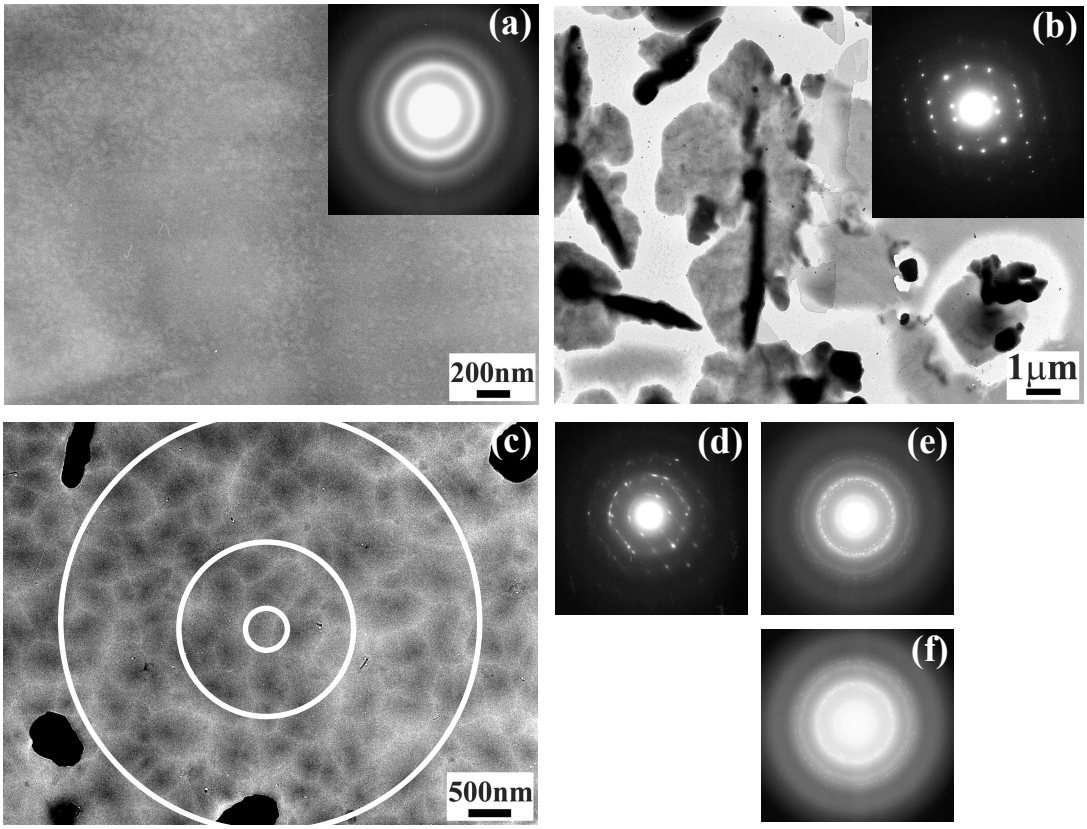

Figure 3.7 *Bright-field TEM images (a-c) and corresponding SAED patterns (insets in a and b, and d-f) for (a) a spin cast PCBM film from chlorobenzene, (b) slow evaporation under a saturated chlorobenzene atmosphere, and (c) annealing a spin cast film from toluene at 130 ºC for ca. 50 hours. The SAED patterns d-f are taken on the annealed film in c, applying a field-limiting aperture size of (d) 20 μm (e) 100 μm and (f) 300 μm in diameter with the respective increase in selected area corresponding to the area within the white rings in c. The SAED patterns a, e, and f show the nanocrystalline structure of the PCBM film, whereas b and d show the single crystals of PCBM.*

with regular shape are frequently observed (Figure 3.7b). Performing selected area electron diffraction (SAED) analysis on these clusters results in a clear electron diffraction pattern composed of many well-aligned spots, which gives strong evidence that these clusters are PCBM single crystals. Surprisingly, the SAED patterns of the spin cast films also consist of several diffraction rings, despite the homogeneous appearance of these films in the bright-field TEM images (even at high magnification). Even though the rings are broad and blurred, this evidences the presence of crystallites in the 'homogeneous' film. Similar results were obtained when replacing chlorobenzene, the solvent for spin casting, with toluene.

Larger single crystals compared to those present in spin cast films (Figure 3.7a) were prepared by annealing a spin cast film. By changing the aperture size to vary the selected area, a detailed comparison of the diffraction patterns as obtained for these larger single crystals (Figure 3.7c-

f) could be made with the patterns as obtained for the regular spin cast films. This confirmed that these spin cast PCBM films consist of a large number of homogeneously distributed, randomly oriented nanocrystals.[115]

3.3.3 Conclusions

Electron-only space-charge-limited conduction (SCLC) combined with the stretched exponential electric field-dependence $\mu \propto \exp(\gamma \times \sqrt{E})$ adequately describes the dark current density-voltage characteristics above V_{bi} at varying temperatures for devices with the configuration glass/ITO/PEDOT:PSS/PCBM/LiF/Al. The zero-field electron mobility in PCBM at room temperature equals 2×10^{-3} cm^2/Vs. The electron transport through spin cast PCBM films can consistently be described by the correlated Gaussian disorder model (CDM) with an energetic bandwidth σ = 73 meV, and an intersite spacing a = 3.4 nm.[116] Spin cast PCBM films appear homogeneous in TEM images, but SAED indicates unambiguously that the films consist of a large number of randomly oriented nanocrystals. Unfortunately, the size of the nanocrystals could not be determined. The boundaries between these ordered crystalline domains will likely have a large effect on the macroscopic mobility, because crystalline boundaries often act as transport barriers. Therefore, it is not surprising that the average hopping distance a = 3.4 nm, as obtained with CDM, exceeds the diameter of a single fullerene molecule (10 Å).[117]

3.4 Disorder and transport in poly(*p*-phenylene vinylene) films

Both photospectroscopic[15,38,118-121] and mobility measurements[122] have shown the large influence of conformational disorder on the electro-optical properties of PPV derivatives. The origin of this disorder seems to be twofold. First of all, rotational energy barriers around single bonds in conjugated systems have been found to be of the same order as kT.[120,123,124] Although intra-chain rotational motion will contribute to the disorder observed, particularly tetrahedral chemical defects introduced during synthesis,[125,126] and to some extent chemical changes resulting from photodamage,[15,127] seem to govern the conformational freedom of the PPV backbone,[128,129] and the charge-carrier mobility.[124,130] In agreement with these observations and calculations, most PPV films have been found to be highly inhomogeneous, and even in relatively well-ordered films the ordering generally occurs in domains of sub-micron dimensions.[15,36-38] Polarization modulation near-field optical microscopy (PM-NSOM) measurements indicate that even within these domains the PPV chains are only partially aligned.[37]

Despite the insight gained over the past few years, knowledge on the influence of the substitution pattern of the conjugated backbone on the film morphology, and, consequently, the charge-carrier mobility is still limited. So far, no one has been able to visualize the backbone conformations of individual conjugated polymers on their cast films. Visualizing identical backbones

with a different substitution pattern might give some insight in the relation between the substitution with the conformational preference of the backbone, and aggregation behavior. Combining these insights with the charge-carrier mobility found for these polymer films should enlarge the understanding of the influence of substitution patterns on charge-carrier mobility.

3.4.1 Comparison of hole mobility in poly(*p*-phenylene vinylene) films

Only a few examples exist where the influence of substitution of the backbone on the charge-carrier mobility has been investigated.[23-26,131] The most widely studied substituted PPVs in literature are the asymmetrically substituted MDMO-PPV and poly[2-methoxy-5-(2′-ethylhexyloxy)-1,4-phenylene vinylene] (MEH-PPV, Figure 3.8). The hole mobility in thin cast films of these and other PPVs have been measured with a variety of techniques.[58,67,131] Charge transport in these cast films can be consistently described with CDM, as investigated for some of these PPVs.[23] In table 3.1 mobility data are collected for several (a)symmetrically substituted PPVs. The symmetrically substituted PPVs typically give a larger zero-field hole mobility μ(E=0) than asymmetrically substituted PPVs. Furthermore, for poly[2,5-bis(2´-ethylhexyloxy)-1,4-phenylene vinylene] (BisEH-PPV) a significantly smaller dependence on the electric field has been found, as can be concluded from the smaller pre-factor γ. The CDM relates the smaller field-dependence for the symmetrically substituted PPV compared to the asymmetrically substituted PPV to a higher degree of order, expressed via a narrower bandwidth σ for the distribution of the energy sites.

The differences in hole mobility between the symmetrically substituted PPVs and asymmetrically substituted PPVs are much larger than the variance typically observed for the hole

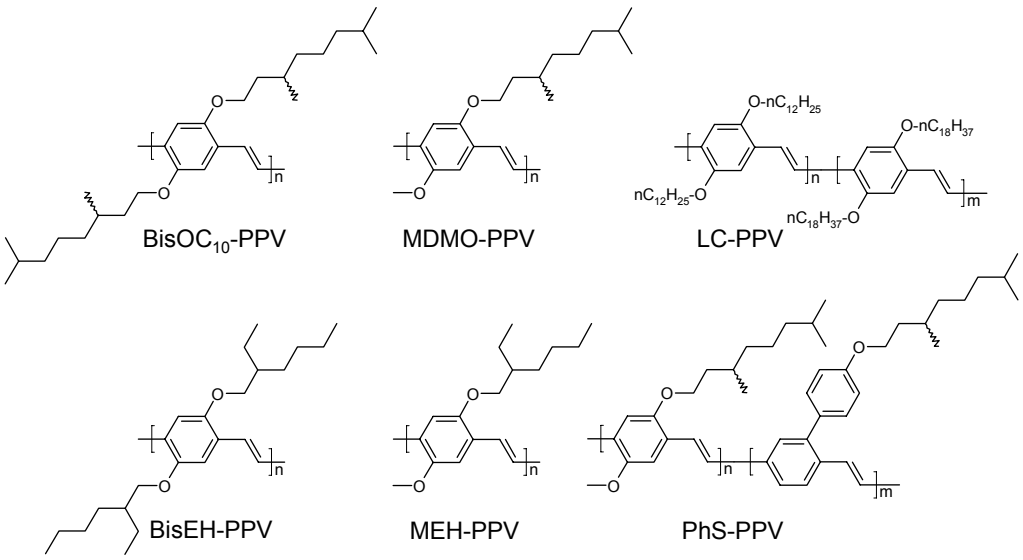

Figure 3.8 *Molecular structures of the symmetrically substituted BisOC$_{10}$-PPV, BisEH-PPV, and the random copolymer LC-PPV, and the asymmetrically substituted MDMO-PPV, MEH-PPV, and PhS-PPV. For both random copolymers n = m.*

mobility between different laboratories for the same molecular structure. The latter can be mainly attributed to differences in processing, and material properties (molecular weight, polydispersity, defects, and purity). So far, no huge differences for the same structure were found as long as the spin cast solvent was aromatic resulting in good quality films. Therefore, a comparison as made in the table below is allowed.

Table 3.1. *Zero-field hole mobility $\mu(E=0)$, and pre-factor γ in $\mu = \mu(E=0) \times \exp(\gamma\sqrt{E})$ for several substituted PPVs, as found with mainly the space-charge-limited technique. The energetic bandwidth σ and average hopping distance **a** from the correlated Gaussian disorder model are given for MDMO-PPV and BisOC$_{10}$-PPV. For molecular structures, see Figure 3.8.*

Structure	$\mu(E=0)_{rt}$ [cm^2/Vs]	γ [(m/V)$^{1/2}$]	σ [meV]	a [nm]	Ref.
MDMO-PPV	5×10^{-7}	5.4×10^{-4}	112	1.2	23,58,132
MEH-PPV	2×10^{-7}	3.4×10^{-4}	-	-	67
PhS-PPV	2×10^{-8}	-	-	-	133,134
BisOC$_{10}$-PPV	6×10^{-6}	4.0×10^{-4}	93	1.1	23,58
BisEH-PPV	5×10^{-5}	7.5×10^{-5}	-	-	135
LC-PPV	2×10^{-6}	-	-	-	136

3.4.2 Relating substitution to single-chain conformation and aggregation in poly(*p*-phenylene vinylene) films

So far, high-resolution surface analysis of conjugated polymer films, consisting of at least several monolayers thick, has been limited by probing mostly height or optical properties via scanning force microscopy (SFM) and near-field scanning optical microscopy (NSOM),[137] respectively, where only separate domains could be visualized.[15,36,37] By using sharp, metal-coated tips on good quality (Q factor ≈ 200) cantilevers with a small spring constant (1 N/m) for use in resonant-mode[138] SFM, the contrast in phase images can be enhanced significantly.[139] Phase-imaging with these metal-coated tips makes it possible to probe individual polymer chain conformations and aggregation on PPV films.

Figures 3.9a and b show typical examples of a height image and of a simultaneously taken phase image, measured with a metal-coated tip on a spin-cast film of the asymmetrically substituted MDMO-PPV. The typical lack of molecular resolution in the topography image is apparent. In contrast, the phase image clearly shows spiraling chains, i.e. the chains lay on the surface in a circular fashion, with a rather constant diameter of about 10±2 nm.[140] Because of the constancy of the observed edge width over the sample surface these structures are interpreted as individual polymer

chains, rather than as an arbitrary number of tightly packed chains. The measured width of about 4.8±1 nm inevitably exceeds the 0.55 nm that is obtained from a molecular mechanics calculation for the width of the conjugated backbone of MDMO-PPV,[141] because of the finite tip apex radius and the nature of the interaction.

It is surprising that the individual polymers in Figure 3.9b seem to form connected ring-shaped structures. The constant diameter of these rings can only be explained by an average bending angle in the polymer chain of around 8° at each monomer unit (360°/number of monomer units that fit in one circumference). The most likely candidate for the bending force is an interaction, either attractive or repulsive, between the aliphatic side chains of successive monomer units. This requires that the monomer units are predominantly in the *syn* conformation, i.e. most OC_{10} side chains point to one side of the polymer and, consequently, the OC_1 chains to the other side. Such orientation and interaction could explain the observed rings, but not their connectedness. A tentative explanation for the latter can be given by assuming the presence of conformational or chemical defects, at which the prevailing orientation of the side chains is flipped from one side of the polymer chain to the other. Since the bending direction of the polymer is reversed at such a defect, a new (part of a) ring,

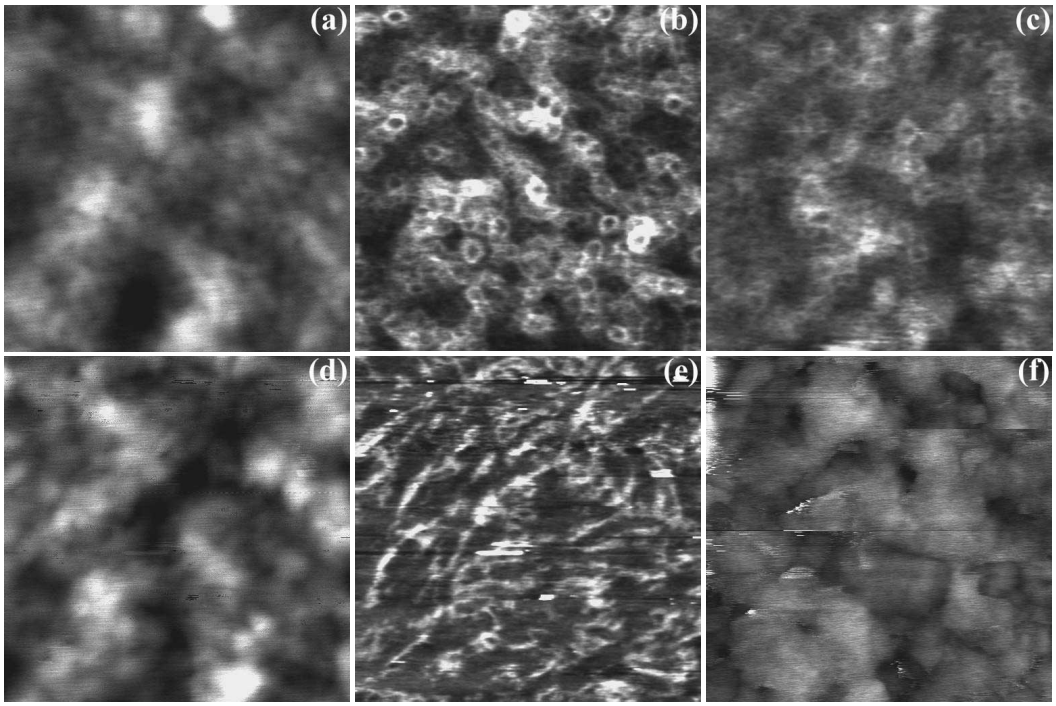

Figure 3.9 *Surface topography and phase images of MDMO-PPV (a-c) and BisOC$_{10}$-PPV (d-f).* **(a,d)** *Surface topography (full height scale 5 nm) measured by resonant-mode SFM.* **(b,e)** *Phase images, simultaneously measured with a, respectively, d. The tip apex radius was 10 nm.* **(c,f)** *Phase images, measured with a blunt tip on another spot of the same samples as a (and b), respectively, d (and e). The tip apex radius was 40 nm. Images a-e are 200 × 200 nm^2, whereas f is 500 × 500 nm^2.*

connected to the previous one, starts at each defect (as shown in Figure 3.10a). A simple 2D Monte Carlo (MC) model, based on these considerations, is able to reproduce the characteristic features of Figure 3.9b.[139] Although the resulting morphologies are in principle 3D as chain crossings do occur, a 2D model is adequate, as the used conjugated polymers have a thickness of only a few Å.[141] Therefore, multiple rings with an approximate diameter of 100 Å can be stacked while maintaining an almost 2D situation. The presence of chemical defects, and the influence of conformational and configurational defects in poly(*p*-phenylene vinylene)s on the conformational freedom and the electro-optical properties was already pointed out above.

The same measurements were performed on a similar film of the symmetrically substituted polymer poly[2,5-bis(3′,7′-dimethyloctyloxy)-1,4-phenylene vinylene] (BisOC_{10}-PPV, for molecular structure, see Figure 3.8) in order to verify whether the driving force for the bending of the PPV backbone is indeed governed by the side chains. Compared to MDMO-PPV, the OC_1 side chain is replaced by another OC_{10} chain, so any effect of the interaction between side chains on the conformation will be cancelled by the symmetry of the polymer. From the absence of a net driving force for bending in a particular direction, a more or less straight molecular conformation is expected for BisOC_{10}-PPV, which is indeed observed (Figure 3.9e). The strong spiraling observed on MDMO-PPV is now clearly absent, consistent with the proposed role of structural symmetry. The fact that the topography taken together with the phase image on BisOC_{10}-PPV (panel d) is very similar to that observed on MDMO-PPV demonstrates that the topography is not at all a good measure of the morphology. Molecular dynamics simulations performed on isolated chains of either MDMO-PPV or BisOC_{10}-PPV are consistent with the interpretation given above.[139]

A striking feature of Figure 3.9e is the preferential orientation of the polymer chains along the lower-left to upper-right diagonal. On larger scale images this alignment can be seen to occur within 50-200 nm domains (Figure 3.10b). It is tempting to identify such domains as aggregates, i.e. regions in which a significant overlap between the wave functions of single chains enables the formation of one or more states that are delocalized over several chains.[40] Although alignment of conjugated backbones over multiple monomer units is probably a prerequisite for aggregate formation, it may not be sufficient. To probe the coupling within these domains, the same measurements were performed on different areas of the same samples with a deliberately blunted tip, prepared by thermally evaporating 80 nm of Al on tip and cantilever, resulting in an apex radius of approximately 40 nm. For BisOC_{10}-PPV, more or less homogeneous domains with typical lateral dimensions of 100 nm are found, see Figure 3.9f. In contrast, for MDMO-PPV no domains are visible, and only a faint version of Figure 3.9b is obtained, see panel c. The loss of detail is what one would expect for a measurement with intrinsically less resolution because of a blunt tip. The different morphology observed for the two polymers excludes the possibility that Figure 3.9f is a mere tip artifact. In that case, one would also expect all domains to have the same shape, reflecting shape and dimension of the tip apex. This is not

the case. Having excluded the possibility of a tip artifact, interpretation of these domains as aggregates is a viable option.

Similar sharp metal-coated tip SFM measurements were performed on other (a)symmetrically substituted PPVs (for molecular structures, see Figure 3.8). As for MDMO-PPV, predominantly spiraling chains are present at the surface of MEH-PPV films. In contrast to probing with sharp tips on $BisOC_{10}$-PPV films where only more or less straight (worm-like) chain conformations were found, on the symmetrically substituted BisEH-PPV and LC-PPV either aggregates or more or less straight (worm-like) chain conformations were found, depending on processing conditions. Varying the concentration from 1 to 5 mg polymer/ml chlorobenzene does not significantly affect the images observed for MDMO-PPV and MEH-PPV. In contrast, the domain size and the tendency to aggregate

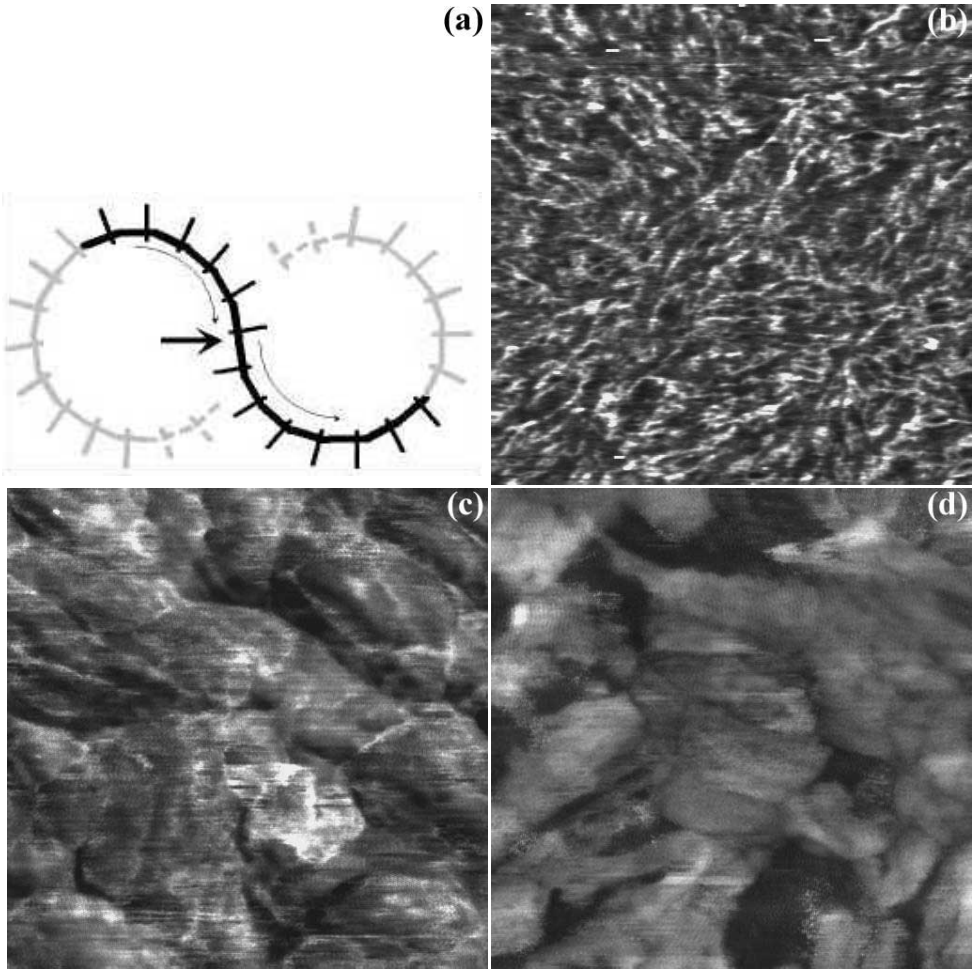

Figure 3.10 (a) *Illustration of the proposed side-chain orientation for MDMO-PPV, an asymmetrically substituted PPV. At a defect (thick arrow), the sense of spiraling (thin arrows) reverses, leading to a morphology that consists of connected rings.* **(b-d)** *Sharp-tip phase images for (b) $BisOC_{10}$-PPV, and BisEH-PPV cast from (c) 3, and (d) 5 mg BisEH-PPV/ml chlorobenzene. Images are (b) 500 × 500 nm^2, and (c,d) 200 × 200 nm^2. Whereas for 3 mg/ml individual chains still can be recognized, for 5 mg/ml only aggregates are probed.*

clearly increases with increasing concentration from 1 to 5 mg/ml for BisEH-PPV (Figure 3.10c and d) and LC-PPV. It should be noted that with increasing concentration the film thickness increases as well, for all polymers, with the thickness in the range of 10-100 nm. So far, the asymmetrically substituted PhS-PPV did not show a preference for spiraling chains, nor for straight conformations, but a more randomly coiling network was observed.

3.4.3 Conclusions

For the thin cast films investigated, the larger tendency to aggregate into ordered domains, and, consequently, the larger zero-field hole mobility observed for symmetrically substituted PPV seem to result from more linear conformations for the PPV backbone, as compared to asymmetrically substituted PPV. This conclusion is based on the preferential occurrence of straight and worm-like conformations observed at cast films of symmetrically substituted PPV, compared to the predominance of spiraling conformations for asymmetrically substituted PPV. The latter is likely enhanced by some self-aggregation. This difference in conformational behavior is ascribed to both the increasing incompatibility with the aromatic solvents and bulkiness of the larger solubilizing substituents for the symmetrically substituted PPVs.[142]

Although a clear relation can be observed between the macroscopic charge-carrier mobility (a bulk property) and the microscopic surface measurements, it must be noted that the degree of order present at the surface may not be identical to that in the bulk. Nevertheless, the results indicate a correlation between the order at the surface and the bulk-charge-carrier mobility.

3.5 Comparing a methanofullerene with a poly(*p*-phenylene vinylene)

The zero-field hole mobility in pure MDMO-PPV (5×10^{-7} cm^2/Vs) is found to be 4000 times smaller than the zero-field electron mobility in pure PCBM (2×10^{-3} cm^2/Vs). It is therefore surprising to find that the most efficient composite solar cells made with these two components need 80 wt.-% of PCBM (see chapter 5), a material that hardly absorbs light and more efficiently transports charges. Intuitively one would reason that increasing the concentration of MDMO-PPV would be beneficial, for absorption and the number of hole-transporting percolation pathways, but apparently it is not. As described in detail in the following two chapters, it has been recognized that morphology and molecular organization on the nanometer scale for these composites is a key issue in this respect.

The smaller energetic bandwidth σ inferred from analysis of mobility data with the CDM for spin cast PCBM films (σ = 73 meV) as compared to spin cast MDMO-PPV films (σ = 112 meV) demonstrates that the energetic disorder is significantly smaller in spin cast PCBM films, which gives rise to a higher zero-field mobility.

The high degree of disorder in films of asymmetrically substituted PPV-derivatives, as observed with SPM and NSOM, is indicative for a rather broad distribution of the effective

conjugation length of the hole-transporting chain segments. Additionally, anisotropy and domain boundaries will affect the macroscopic mobility. Rephrasing, for these PPV-derivatives order (or more specific the absence of order) and the related electronic overlap, both within and between domains influences the macroscopic mobility.

The observation of randomly clustered nanocrystals in spin cast PCBM films could imply that only the crystal boundaries govern the macroscopic mobility, because of the large degree of order and electronic overlap that is present within the nanocrystals. Based on the high symmetry of the C_{60} molecule, it can be expected that the distribution in hopping activation energy at crystal boundaries will be rather small compared to domain boundaries for conjugated polymers as PPV. This difference in the distribution of the electronic overlap between 'planar' polymers and 3D-molecules, expressed in the morphological disorder, therefore explains to a large extent the difference in energetic bandwidths σ between asymmetrically substituted PPV-derivatives and PCBM.

Whereas the zero-field mobility is only governed by the energetic disorder σ, the field-activation pre-factor γ is influenced by both the energetic and spatial disorder (Figure 3.3). For increasingly ordered systems, the zero-field mobility is typically higher and less strongly field dependent.[67] The smaller pre-factor γ at rt obtained for pure PCBM ($\gamma = 1\times10^{-4}$ $m^{½}/V^{½}$) compared to pure MDMO-PPV ($\gamma = 5.4\times10^{-4}$ $m^{½}/V^{½}$) is indicative for less disorder in the PCBM film, in agreement with both the morphological investigations, and the decrease observed in the dispersiveness of ToF photocurrent measurements for the electron transport states in PCBM, as found in MDMO-PPV:PCBM blends.[143]

3.6 Experimental section

Materials. The materials used were poly[2-methoxy-5-(3′,7′-dimethyloctyloxy)-1,4-phenylene vinylene] (MDMO-PPV),[144] poly[2,5-bis(3′,7′-dimethyloctyloxy)-1,4-phenylene vinylene] (BisOC$_{10}$-PPV),[145] a 50:50 random copolymer of 2,5-bischloromethyl-4-methoxy-1-(3′,7′-dimethyloctyloxy)-benzene and 2,5-bischloromethyl-4′-(3′′,7′′-dimethyloctyloxy)-1,1′-diphenyl (PhS-PPV),[145] and a 50:50 random copolymer of 2,5-bischloromethyl-1,4-bis(*n*-dodecyloxy)-benzene and 2,5-bischloromethyl-1,4-bis(*n*-octadecyloxy)-benzene (LC-PPV),[145] all synthesized via the Gilch-route[125], poly[2,5-bis(2′-ethylhexyloxy)-1,4-phenylene vinylene] (BisEH-PPV),[146,147] poly[2-methoxy-5-(2′-ethylhexyloxy)-1,4-phenylene vinylene] (MEH-PPV) from Aldrich, 1-(3-methoxycarbonyl)propyl-1-phenyl-[6,6]-methanofullerene (PCBM)[148], polyethylenedioxythiophene: polystyrenesulfonate[149] (PEDOT:PSS) from Bayer AG (Baytron P VPAI 4083), LiF from Aldrich, Au and Al from Engelhard-Clal. A glass plate fully covered with a 40 nm thick layer of indium tin oxide (ITO) was used as the substrate for preparing TEM and SAED samples. Glass plates covered with 160 nm patterned ITO resulting in 4 different device areas (0.1, 0.15, 0.33, 1.0 cm^2) were used for device preparation.[150] For SFM measurements the substrates consisted of a 100 nm thick Au electrode on top of 5 nm Cr, both thermally evaporated onto cleaned Schott D263 glass plates.

Device and sample preparation. The ITO covered glass substrates were first cleaned by ultrasonic treatment in acetone, rubbing with soap, rinsing with de-mineralized water, refluxing with iso-propanol, and finally 20 minutes UV ozone treatment. Subsequently, a ~100 nm thick layer of PEDOT:PSS was spin coated from an aqueous dispersion under ambient conditions on the cleaned

substrates and the layer was dried by annealing the substrate for 1 minute at 100 °C. Then PCBM was spin coated from a chlorobenzene solution on top of the PEDOT:PSS layer and the sample was transferred to an N_2 atmosphere glove box. The organic solutions are stirred vigorously overnight while keeping them in the dark. Film thickness measurements were performed with a Tencor P10 surface profiler. All organic layers were spin cast via a two-step procedure employing a home-made chuck, which requires no vacuum, on a Chemat Technology spin coater model KW-4A placed in a laminar flowbox. First 7 seconds at 500 rpm followed by 35 seconds at 1500 rpm. Finally, ~10 Å LiF and subsequently ~100 nm aluminum layers were deposited by thermal evaporation in a vacuum chamber (5×10^{-6} mbar, 1 ppm O_2 and < 1 ppm H_2O). The samples were rotated at ~1 Hz during deposition to guarantee homogeneous films. All samples are stored in the dark in an N_2 atmosphere glove box. Au and Cr were thermally evaporated onto the cleaned glass substrates in the same vacuum chamber. The same spin casting procedure was used to prepare the samples for TEM, SAED and SFM measurements. Drying the PEDOT:PSS layer for the TEM and SAED samples was performed by annealing the substrate for 1 minute at 180 °C, followed by cooling for 1 minute at 25 °C before spin casting the PCBM solution.

Device measurements. *J-V* curves were measured with a computer-controlled Keithley 2400 Source Meter in an Oxford Optistat continuous flow, exchange gas cryostat, sweeping in steps of 0.04 V with a delay of 0.10 sec, in the dark. Contacts were improved by applying a thin indium foil between the copper contacts of the external circuit and the device electrodes. The stability of the devices was found to be more than sufficient to perform all the above measurements.

Transmission electron microscopy and selected-area electron diffraction. A free-standing or so-called self-supported film is definitely a prerequisite for TEM investigation. Two methods were used to prepare the TEM specimen. One is mechanically removing from its substrate with adhesive tape. The other one is the floatation technique by using de-ionized water. The films were floated onto the surface of de-ionized water and finally picked up by a 400 mesh copper grid. The bright-field morphology observations and SAED measurements were conducted on a JEOL JEM-2000FX transmission electron microscope operated at 80 kV.

Scanning force microscopy. Either a Digital Instruments Dimension 3100 scanning probe microscope in resonant-mode[138] in combination with a home-built phase detection system or a Digital Instruments MultiMode in resonant-mode with a NanoScope IV controller was used to simultaneously measure topography (via the amplitude) and tip-sample interaction (via the phase angle). All SFM measurements were performed under ambient conditions using either Pt or W_2C covered Si cantilevers (NT-MDT CSC12) or Ti-Pt covered Si cantilevers (NT-MDT NSC12). Tip apex radii were determined by measuring a test grid (NT-MDT TGT01).

3.7 References and notes

Deriving the trap-free square law for space-charge-limited conduction (SCLC).

$$V = \frac{\Delta W}{e} - V_{in} = V_{bi} - V_{in}$$

$$J = \mu[E(x)] \times \rho_f(x) \times E(x) - D\frac{d\rho_f}{dx} \qquad \rho_f = e\,c_f$$

$$\varepsilon\frac{dE(x)}{dx} = \rho(x) = \rho_f(x) + \rho_t(x) \qquad \textit{Poisson's equation}$$

$$\rho_t(x) = 0 \wedge D\frac{d\rho_f}{dx} = 0 \;\; \textit{gives} \;\; J = \varepsilon\frac{dE(x)}{dx} \times \mu[E(x)] \times E(x)$$

$$E(0) = 0 \wedge \mu \neq f(E) \;\; \textit{gives} \quad Jx = \tfrac{1}{2}\varepsilon\mu \times (E(x))^2 \quad \textit{or} \quad E(x) = \sqrt{\frac{2Jx}{\varepsilon\mu}}$$

$$\textit{With} \quad V_{in} \equiv V_L - V_0 = -\int_0^L E(x)dx \quad \textit{and ignoring } V_{bi} \textit{ gives}$$

$$V = -V_{in} = \int_0^L E(x)dx = \int_0^L \sqrt{\frac{2Jx}{\varepsilon\mu}}dx = \tfrac{2}{3}\sqrt{\frac{2J}{\varepsilon\mu}}x^{3/2}\Big|_0^L \quad \textit{or} \quad J = \tfrac{9}{8}\varepsilon\mu\frac{V^2}{L^3}$$

V = external potential difference [V (= J/C = Nm/C)]

ΔW = difference in the electronic workfunction of the electrodes [J (=Nm)]

e = charge of electron [C]

V_{bi} = built-in voltage [V]

V_{in} = internal potential difference [V]

J = current density [A/m^2]

μ = charge-carrier mobility [m^2/Vs]

E = electric field [V/m]

x = position [m]

ρ = total charge density [C/m^3]

ρ_f = free (mobile) charge density [C/m^3]

c_f = particle density [1/m^3]

ρ_t = trapped-charge density [C/m^3]

D = charge-carrier diffusion coefficient [m^2/s]

ε = dielectric constant [C^2/Nm^2]

1 C.D. Dimitrakopolous, P.R.L. Malenfant, *Adv. Mater.* **2002**, *14*, 99.

2 D. Braun, *Materials Today* **2002**, *5*, 32.

3 R.H. Friend, R.W. Gymer, A.B. Holmes, J.H. Burroughes, R.N. Marks, C. Taliani, D.D.C. Bradley, D.A. Dos Santos, J.L. Brédas, M. Löglund, W.R. Salaneck, *Nature* **1999**, *397*, 121.

4 J.-M. Nunzi, *C. R. Physique* **2002**, *3*, 523.

5 C.J. Brabec, V. Dyakonov, J. Parisi, N.S. Sariciftci (Eds.), *Organic Photovoltaics*: *Concepts and Realization, Springer Series in Materials Science Vol. 60* Springer-Verlag, London, **2003**.

6 (a) H. Sirringhaus, R.J. Wilson, R.H. Friend, M. Inbasekaran, W. Wu, E.P. Woo, M. Grell, D.D.C. Bradley, *Appl. Phys. Lett.* **2000**, *77*, 406; (b) M. Redecker, D.D.C. Bradley, M. Inbasekaran, E.P. Woo, *Appl. Phys. Lett.* **1999**, *74*, 1400.

7 M.L. Swiggers, G. Xia, J.D. Slinker, A.A. Gorodetsky, G.G. Malliaras, R.L. Headrick, B.T. Weslowski, R.N. Shashidhar, C.S. Dulcey, *Appl. Phys. Lett.* **2001**, *79*, 1300.

8 X.L. Chen, A.J. Lovinger, Z. Bao, J. Sapjeta, *Chem. Mater.* **2001**, *13*, 1341.

9 K.R. Amundson, B.J. Sapjeta, A.J. Lovinger, Z. Bao, *Thin Solid Films* **2002**, *414*, 143.

10 A.M. van de Craats, N. Stutzmann, O. Bunk, M.M. Nielsen, M. Watson, K. Mullen, H.D. Chanzy, H. Sirringhaus, R.H. Friend, *Adv. Mater.* **2003**, *15*, 495.

11 H. Peisert, T. Swieger, J.M. Auerhammer, M. Knupfer, M.S. Golden, J. Fink, P.R. Bressler, M. Mast, *J. Appl. Phys.* **2001**, *90*, 466.

12 H.E. Katz, Z. Bao, *J. Phys. Chem. B* **2000**, *104*, 671.

13 N. Karl, *Synth. Met.* **2003**, *133-134*, 649.

14 G. Wang, J. Swensen, D. Moses, A.J. Heeger, *J. Appl. Phys.* **2003**, *93*, 6137.

15 (a) B.J. Schwartz, *Annu. Rev. Phys. Chem.* **2003**, *54*, 141; (b) R.D. Schaller, L.F. Lee, T.Q. Nguyen, P.T. Snee, R.J. Saykally, *Jpn. J. Appl. Phys. Part 1* **2003**, *42*, 4799.

16 W. Geens, S.E. Shaheen, B. Wessling, C.J. Brabec, J. Poortmans, N.S. Sariciftci, *Org. Electr.* **2002**, *3*, 105.

17 (a) Y. Shi, J. Liu, Y. Yang, *J. Appl. Phys.* **2000**, *87*, 4254; (b) J. Liu, Y. Shi, L. Ma, Y. Yang, *J. Appl. Phys.* **2000**, *88*, 605.

18 (a) J. Liu, T.F. Guo, Y. Yang, *J. Appl. Phys.* **2002**, *91*, 1595; (b) G. He, Y. Li, T.F. Guo, Y. Yang, *Synth. Met.* **2003**, *137*, 1091.

19 H. Heil, T. Finnberg, N. von Malm, R. Schmechel, H. von Seggern, *J. Appl. Phys.* **2003**, *93*, 1636.

20 W. Geens, D. Tsamouras, J. Poortmans, G. Hadziioannou, *Synth. Met.* **2001**, *122*, 191.

21 J.E. Anthony, J.S. Brooks, D.L. Eaton, S.R. Parkin, *J. Am. Chem. Soc.* **2001**, *123*, 9482.

22 (a) A.C. Grimsdale, P. Leclère, R. Lazzaroni, J.D. Mackenzie, C. Murphy, S. Setayesh, C. Silva, R.H. Friend, K. Müllen, *Adv. Funct. Mater.* **2002**, *12*, 729; (b) C. Silva, D.M. Russell, A.S. Dhoot, L.M. Herz, C. Daniel, N.C. Greenham, A.C. Arias, S. Setayesh, K. Müllen, R.H. Friend, *J. Phys.*: *Condens. Matter* **2002**, *14*, 9803.

23 H.C.F. Martens, P.W.M. Blom, H.F.M. Schoo, *Phys. Rev. B* **2000**, *61*, 7489.

24 M.J. Winokur, W. Chunwachirasiri, *J. Pol. Sci. B* **2003**, *41*, 2630.

25 L.S. Yu, H.E. Tseng, H.H. Lu, S.A. Chen, *Appl. Phys. Lett.* **2002**, *81*, 2014.

26 F.C. Krebs, M. Jørgensen, *Macromolecules* **2003**, *36*, 4374.

27 R.J. Kline, M.D. McGehee, E.N. Kadnikova, J. Liu, J.M.J. Fréchet, *Adv. Mater.* **2003**, *15*, 1519.

28 S. Shaked, S. Tal, Y. Roichman, A. Razin, S. Xiao, Y. Eichen, N. Tessler, *Adv. Mater.* **2003**, *15*, 913.

29 M.J. Banach, R.H. Friend, H. Sirringhaus, *Macromolecules* **2003**, *36*, 2838.

30 P. Herguth, X. Jiang, M.S. Liu, A.K.Y. Jen, *Proc. SPIE* **2003**, *4800*, 138.

31 H. Sirringhaus, P.J. Brown, R.H. Friend, M.M. Nielsen, K. Bechgaard, B.M.W. Langeveld-Voss, A.J.H. Spiering, R.A.J. Janssen, E.W. Meijer, P. Herwig, D.M. de Leeuw, *Nature* **1999**, *401*, 685.

32 G. Dicker, T.J. Savenije, B.H. Huisman, D.M. de Leeuw, M.P. de Haas, J.M. Warman, *Synth. Met.* **2003**, *137*, 863.

33 J. Teetsov, D.A. Vanden Bout, *Langmuir* **2002**, *18*, 897.

34 J.W. Blatchford, T.L. Gustafson, A.J. Epstein, D.A. Vanden Bout, J. Kerimo, D.A. Higgins, P.F. Barbara, D.K. Fu, T.M. Swager, A.G. MacDiarmid, *Phys. Rev. B* **1996**, *54*, R3683.

35 T. Hassenkam, D. R. Greve, T. Bjørnholm, *Adv. Mater.* **2001**, *13*, 631.

36 C.H. Tan, A.R. Inigo, J.H. Hsu, W. Fann, P.K. Wei, *J. Phys. Chem. Solids* **2001**, *62*, 1643.

37 P.K. Wei, Y.F. Lin, W. Fann, Y.Z. Lee, S.A. Chen, *Phys. Rev. B* **2001**, *63*, 045417.

38 S.H. Chen, A.C. Su, H.L. Chou, K.Y. Peng, S.A. Chen, *Macromolecules*, **2004**, *37*, 167.

39 K. Senthilkumar, F.C. Grozema, F.M. Bickelhaupt, L.D.A. Siebbeles, *J. Chem. Phys.* **2003**, *119*, 9809.

40 J. Cornil, D. Beljonne, J.P. Calbert, J.L. Brédas, *Adv. Mater.* **2001**, *13*, 1053.

41 J. Ye, H. Chen, M. Shi, M. Wang, *Progress in Natural Science* **2003**, *13*, 81.

42 J. Kim, *Pure Appl. Chem.* **2002**, *74*, 2031.

43 A.M. Stoneham, M.M.D. Ramos, A.M. Almeida, H.M.G. Correia, R.M. Ribeiro, H. Ness, A.J. Fisher, *J. Phys.*: *Condens. Matter* **2002**, *14*, 9877.

44 W.D. Gill, *J. Appl. Phys.* **1972**, *43*, 5033.

45 The stepwise hopping process in conjugated organics finds its origin in the strong localization of charge carriers on individual molecules, due to the rather weak intermolecular interactions. Furthermore, it should be noted that the orientational molecular disorder (and temperature range involved) for the materials discussed in this chapter make hopping transport the dominant mechanism and fully suppresses band transport.

46 Mobility μ is defined as $\mu = \langle v \rangle / E$ with $\langle v \rangle$ the average carrier velocity, and E the electric field.

47 P.W.M. Blom, M.J.M. de Jong, M.G. van Munster, *Phys Rev B.* **1997**, *55*, R656.

48 S.V. Novikov, *J. Pol. Sci. B* **2003**, *41*, 2584.

49 V.R. Nikitenko, H. Heil, H. von Seggern, *J. Appl. Phys.* **2003**, *94*, 2480.

50 G. Horowitz, *Adv. Funct. Mater.* **2003**, *13*, 53.

51 D. Braun, *J. Pol. Sci. B* **2003**, *41*, 2622.

52 (a) Y. Roichman, N. Tessler, *Appl. Phys. Lett.* **2002**, *80*, 1948; (b) Y. Preezant, Y. Roichman, N. Tessler, *J. Phys.*: *Condens. Matter.* **2002**, *14*, 9913; (c) Y. Roichman, N. Tessler, *Synth. Met.* **2003**, *135-136*, 443.

53 (a) H. Cordes, S.D. Baranovskii, K. Kohary, P. Thomas, S. Yamasaki, F. Hensel, J.H. Wendorff, *Phys. Rev. B* **2001**, *63*, 094201; (b) K. Kohary, H. Cordes, S.D. Baranovskii, P. Thomas, S. Yamasaki, F. Hensel, J.H. Wendorff, *Phys. Rev. B* **2001**, *63*, 094202.

54 S.V. Rakhmanova, E.M. Conwell, *Synth. Met.* **2001**, *116*, 389.

55 (a) Z.G. Yu, D.L. Smith, A. Saxena, R.L. Martin, A.R. Bishop, *Phys. Rev. Lett.* **2000**, *84*, 721; (b) Z.G. Yu, D.L. Smith, A. Saxena, R.L. Martin, A.R. Bishop, *Phys. Rev. B* **2001**, *63*, 085202.

56 J. Stephan, S. Schrader, L. Brehmer, *Synth. Met.* **2000**, *111-112*, 353.

57 J.A. Freire, M.G.E. da Luz, D. Ma, I.A. Hümmelgen, *Appl. Phys. Lett.* **2000**, *77*, 693.

58 P.W.M. Blom, M.C.J.M. Vissenberg, *Mater. Sci. Eng. R* **2000**, *27*, 53.

59 M. Pope, C.E. Swenberg, *Electronic Processes in Organic Crystals and Polymers*, Chapter 14, p. 963, Oxford Univ. Press, Oxford, **1999**.

60 S. Rackovsky, H. Scher, *J. Chem. Phys.* **1999**, *111*, 3668.

61 A.M. van de Craats, L.D.A. Siebbeles, I. Bleyl, D. Haarer, Y.A. Berlin, A.A. Zharikov, J.M. Warman, *J. Phys. Chem. B* **1998**, *102*, 9625.

62 (a) N.F. Mott, E.A. Davis, *Electronic Processes in Non-Crystalline Materials*, Clarendon Press, Oxford, **1979**; (b) N. Mott, *Conduction in Non-Crystalline Materials*, Clarendon Press, Oxford, **1993**.

63 J.H. Burroughes, D.D.C. Bradley, A.R. Brown, R.N. Marks, K. Mackay, R.H. Friend, P.L. Burns, A.B. Holmes, *Nature* **1990**, *347*, 539.

64 N.S. Sariciftci, L. Smilowitz, A.J. Heeger, F. Wudl, *Science* **1992**, *258*, 1474.

65 G. Yu, J. Gao, J.C. Hummelen, F. Wudl, A.J. Heeger, *Science* **1995**, *270*, 1789.

66 A.B. Walker, A. Kambili, S.J. Martin, *J. Phys.*: *Condens. Matter* **2002**, *14*, 9825.

67 I. H. Campbell, D.L. Smith, in *Solid State Physics* Vol. 55, p. 1, Academic Press, San Diego, **2001**.

68 W. Brütting, S. Berleb, A.G. Mückl, *Org. Elect.* **2001**, *2*, 1.

69 M. Pope, C.E. Swenberg, *Electronic Processes in Organic Crystals and Polymers*, Chapter 15, p. 1005, Oxford Univ. Press, Oxford, **1999**.

70 The trap-free square law is based on the following assumptions; (1) no additional band bending occurs and no image forces are present at the contacts, (2) the built-in voltage V_{bi} can be ignored, (3) bulk diffusion (superimposed over drift) current is negligible, (4) only free (mobile) injected carriers are present, (5) the injecting contact is Ohmic $E(0) = 0$, and (6) the charge-carrier mobility is constant. At the beginning of this paragraph the trap-free square law is derived in order to clarify its origin.

71 M.A. Lampert, P. Mark, *Current injection in solids*, Academic Press, London, **1970**.

72 Because the current is position independent, the SCL conduction with field-dependent mobility results in a higher charge density at low electric field (close to the injecting contact) due to the lower mobility and a low charge density at high electric field (close to the collecting contact).

73 Recently, it has been shown that the exact form of the field-dependent mobility can also be derived directly from the single-carrier space-charge-limited *J-V* characteristics, thereby avoiding a too large number of fitting parameters, see D. Natali, M. Sampietro, *J. Appl. Phys.* **2002**, *92*, 5310.

74 Solely impurities in organic materials serving as traps cannot explain the stretched exponential behaviour $\mu = \mu(E{=}0) \times \exp(\gamma \times \sqrt{E})$ for such a large amount of experimental data on such a variety of materials.

75 H. Bässler, *Phys. Stat. Sol. B* **1993**, *175*, 15.

76 GDM explains the temperature dependence experimentally observed accurately, but the electric field dependence only in a very limited field range.

77 A. Miller, E. Abrahams, *Phys. Rev.* **1960**, *120*, 745.

78 The Miller-Abrahams hopping rate $\nu_{ij}(E_j,E_i,r_{ij})$ from site i with energy E_i to site j with energy E_j separated by a distance r_{ij} is the product of three factors, (1) a pre-factor ν_0 the attempt-to-hop frequency, (2) an electronic wave function overlap factor $\exp(-\Gamma \times r_{ij}/a)$ with the overlap parameter $\Gamma = 2\gamma a$, γ the inverse localization radius, and a the average hopping distance, and (3) a Boltzmann factor for hops upward in energy ($E_j > E_i$), $\exp(-[E_j - E_i]/[k_bT])$ where the latter equals 1 for downward hops ($E_j < E_i$). Note that (i) there is no other contribution to the activation energy than the difference in electronic site energies (no coupling to intramolecular modes), and (ii) that the overlap parameter Γ, affected by disorder, would be best described by a distribution function. Finally, (iii) in this form downward hops are not accelerated by an (external) electric field.

79 Notice that apart from the Gaussian distribution for the site energy, and the freedom in target-site, additional energetic and positional disorder, respectively, can be introduced in the overlap parameter Γ in the Miller-Abrahams hopping rate $\nu_{ij}(E_j,E_i,r_{ij})$.

80 Y.N. Gartstein, E.M. Conwell, *Chem. Phys. Lett.* **1995**, *245*, 351.

81 S.V. Novikov, A.V. Vannikov, *J. Phys. Chem.* **1995**, *99*, 14573.

82 S.V. Novikov, D.H. Dunlap, V.M. Kenkre, P.E. Parris, A.V. Vannikov, *Phys. Rev. Lett.* **1998**, *81*, 4472.

83 The physical reason for the stretched exponential field dependence $\mu \propto \exp(\gamma \times \sqrt{E})$ in a correlated medium is that the deepest valleys in the energy landscape are also the widest, resulting in a drastic decrease in escape time with electric field. Note that the incorporation of dipolar contributions to the total energetic disorder in organic materials can only be an explanation for polar materials (with no orientationally ordered dipoles), not for nonpolar materials like MDMO-PPV.

84 S.V. Novikov, D.H. Dunlap, V.M. Kenkre, *Proc. SPIE*, **1998**, *3471*, 181.

85 1D gives $\mu \propto \exp(E^{3/4})$ for the quadrupolar glass (QG) model.

86 1D gives $\mu \propto \exp(\sqrt{E})$ for the Los Alamos (LA) model.

87 For the (high) temperatures, and (low) charge densities (doping levels) involved, nearest-neighbour and variable-range hopping as introduced by Sir N.F. Mott are expected to be inappropriate to describe conduction in these disordered organic semiconductors.

88 C. Tanase, E.J. Meijer, P.W.M. Blom, D.M. de Leeuw, *Phys. Rev. Lett.* **2003**, *91*, 216601.

89 See derivation of the trap-free square law at the beginning of this section. Recent insights seem to suggest that the diffusion current cannot be neglected.

90 S. Barazzouk, S. Hotchandani, P.V. Kamat, *Adv. Mater.* **2001**, *13*, 1614.

91 J. Fraxedas, *Adv. Mater.* **2002**, *14*, 1603.

92 P. Strohriegl, J.V. Grazulevicius, *Adv. Mater.* **2002**, *14*, 1439.

93 (a) T.M. Brown, F. Cacialli, *J. Pol. Sci. B* **2003**, *41*, 2649; (b) T.M. Brown, R.H. Friend, I.S. Millard, D.J. Lacey, T. Butler, J.H. Burroughes, F. Cacialli, *J. Appl. Phys.* **2003**, *93*, 6159; (c) M. Fahlman, W.R. Salaneck, *Surf. Sci.* **2002**, *500*, 904; (d) C.J. Brabec, S.E. Shaheen, C. Winder, N.S. Sariciftci, P. Denk, *Appl. Phys. Lett.* **2002**, *80*, 1288.

94 It should be noted that for LiF/Al top contacts the chemistry occurring at the interface with the underlying organic layer clearly depends on the nature of this organic and a general explanation for the electron injection enhancement, therefore, seems to be unlikely.

95 W.J.H. van Gennip, J.K.J. van Duren, P.C. Thüne, R.A.J. Janssen, J.W. Niemantsverdriet, *J. Chem. Phys*. **2002**, *117*, 5031.

96 T.M. Brown, J.S. Kim, R.H. Friend, F. Cacialli, R. Daik, W.J. Feast, *Appl. Phys. Lett.* **1999**, *75*, 1679.

97 The injection barrier for holes from PEDOT:PSS (5.2 eV) into the HOMO of PCBM (6.1 eV) equals 0.9 eV, assuming vacuum level alignment and the absence of both dipole layer formation (as a result of e.g. interfacial chemistry) and strong band bending. Notice that for disordered organic semiconductors the HOMO or LUMO level is considered instead of its workfunction or polaronic levels.

98 G.G. Malliaras, J.R. Salem, P.J. Brock, J.C. Scott, *J. Appl. Phys.* **1998**, *84*, 1583.

99 For current densities larger than 100 mA/cm^2, the applied voltage should be corrected for the voltage drop (V_{RS}) across the indium tin oxide (ITO) series resistance (R_S), which typically amounts to R_S = 30 Ω in our substrates.

100 For current densities larger than 100 mA/cm^2, the applied voltage should be corrected for the voltage drop across the indium tin oxide (ITO) series resistance V_{RS}, which typically amounts to 25-30 Ω in the substrates used.

101 From capacitance-voltage measurements performed in the group of Prof. P.W.M. Blom at Groningen University a relative dielectric constant ε_r of 3.9 for PCBM was obtained.

102 C. Waldauf, P. Schilinsky, M. Perisutti, J. Hausch, C.J. Brabec, *Adv. Mater.* **2003**, *15*, 2084.

103 R. Pacios, J. Nelson, D.D.C. Bradley, C.J. Brabec, *Appl. Phys. Lett.* **2003**, *83*, 4764.

104 R.C. Haddon, A.S. Perel, R.C. Morris, T.T.M. Palstra, A.F. Hebard, R.M. Fleming, *Appl. Phys. Lett.* **1995**, *67*, 121.

105 T. Kanbara, K. Shibata, S. Fujiki, Y. Kubozono, S. Kashino, T. Urisu, M. Sakai, A. Fujiwara, R. Kumashiro, K. Tanigaki, *Chem. Phys. Lett*. **2003**, *379*, 223.

106 R.J.O.M. Hoofman, G.P. van der Laan, M.P. de Haas, K. Tanigaki, *Synth. Met.* **1997**, *86*, 2355.

107 S. Kobayashi, T. Takenobu, S. Mori, A. Fujiwara, Y. Iwasa, *Appl. Phys. Lett.* **2003**, *82*, 4581.

108 (a) E. Frankevich, Y. Maruyama, H. Ogata, Y. Achiba, K. Kikuchi, *Solid State Commun*. **1993**, *88*, 177; (b) E. Frankevich, Y. Maruyama, H. Ogata, *Chem. Phys. Lett*. **1993**, *214*, 39.

109 M. Pope, C.E. Swenberg, *Electronic Processes in Organic Crystals and Polymers*, Chapter 12, p. 902, Oxford Univ. Press, Oxford, **1999**.

110 R. Könenkamp, G. Priebe, B. Pietzak, *Phys. Rev. B* **1999**, *60*, 11804.

111 The first reduction wave, indicative for the electron acceptor strength, shows that C_{60} (E_{red} = 0.60 eV) is a stronger acceptor than PCBM (E_{red} = 0.69 eV), see C.J. Brabec, A. Cravino, D. Meissner, N.S. Sariciftci, T. Fromherz, M.T. Rispens, L. Sanchez, J.C. Hummelen, *Adv. Funct. Mater.* **2001**, *11*, 374.

112 (a) E.A. Katz, D. Faiman, K. Lakoubovskii, A. Isakina, K.A. Yagotintsev, M.A. Strzhemechny, I.Balberg, *J. Appl. Phys*. **2003**, *93*, 3401; (b) E.A. Katz, D. Faiman, B. Mishori, Y. Shapira, A. Isakina, M.A. Strzhemechny, *J. Appl. Phys.* **2003**, *94*, 7173.

113 The influence of a possible phase transition on the transport properties, as observed for C_{60} (T_c = 250 K, see E.A. Katz *et al.*) is expected to be negligible for the less symmetrical PCBM.

114 TEM and SAED investigations were performed by Dr. X. Yang at the Dutch Polymer Institute.

115 X. Yang, J.K.J. van Duren, M.T. Rispens, J.C. Hummelen, R.A.J. Janssen, M.A.J. Michels, J. Loos, *Adv. Mater.* **2004**, *in press*.

116 It should be noted that due to the limited field range investigated, distinguishing between the correlated Gaussian disorder model (CDM) and the quadrupolar glass model (QG) might not be possible.

117 Apart from the discrepancies between the model used and the system investigated, introducing the stretched exponential field-dependence already during the fitting procedure of the SCL *J-V* curves might influence the accuracy of the hopping distance as well.

118 S. Wachsmann-Hogiu, L.A. Peteanu, L.A. Liu, D.J. Yaron, J. Wildeman, *J. Phys. Chem. B* **2003**, *107*, 5133.

119 S.C.J. Meskers, R.A.J. Janssen, J.E.M. Haverkort, J.H. Wolter, *Chem. Phys.* **2000**, *260*, 415.

120 G.D. Scholes, D.S. Larsen, G.R. Fleming, G. Rumbles, P.L. Burn, *Phys. Rev. B* **2000**, *61*, 13670 (and references therein).

121 M. Pope, C.E. Swenberg, *Electronic Processes in Organic Crystals and Polymers*, Chapter 9, p. 825, Oxford Univ. Press, Oxford, **1999**.

122 R.J.O.M. Hoofman, M.P. de Haas, L.D.A. Siebbeles, J.M. Warman, *Nature* **1998**, *392*, 54.

123 X. Gong, H. Xiao, *Int. J. Quant. Chem.* **1998**, *69*, 659.

124 F.C. Grozema, P.Th. van Duijnen, Y.A. Berlin, M.A. Ratner, L.D.A. Siebbeles, *J. Phys. Chem. B* **2002**, *106*, 7791.

125 H. Becker, H. Spreitzer, W. Kreuder, E. Kluge, H. Schenk, I. Parker, Y. Cao, *Adv. Mater*. **2000**, *12*, 42 (and references therein).

126 H. Roex, P. Adriaensens, D. Vanderzande, J. Gelan, *Macromolecules* **2003**, *36*, 5613.

127 (a) B.H. Cumpston, K.F. Jensen, *Synth. Met.* **1995**, *73*, 195; (b) D.G.J. Sutherland, J.A. Carlisle, P. Elliker, G. Fox, T.W. Hagler, I. Jimenez, H.W. Lee, K. Pakbaz, L.J. Terminello, S.C. Williams, F.J. Himpsel, D.K. Shuh, W.M. Tong, J.J. Jia, T.A. Callcott, D.L. Ederer, *Appl. Phys. Lett.* **1996**, *68*, 2046; (c) K.Z. Xing, N. Johansson, G. Beamson, D.T. Clark, J.L. Brédas, W.R. Salaneck, *Adv. Mater.* **1997**, *9*, 1027; (d) L. Ma, X. Wang, B. Wang, J. Chen, J. Wang, K. Huang, B. Zhang, Y. Cao, Z. Han, S. Qian, S. Yao, *Chem. Phys.* **2002**, *285*, 85; (e) H.Y. Low, *Thin Solid Films* **2002**, *413,* 160.

128 (a) P. Kumar, A. Mehta, M.D. Dadmun, J. Zheng, L. Peyser, A.P. Bartko, R.M. Dickson, T. Thundat, B.G. Sumpter, D.W. Noid, M.D. Barnes, *J. Phys. Chem. B* **2003**, *107*, 6252; (b) A. Mehta, P. Kumar, M.D. Dadmun, J. Zheng, R.M. Dickson, T. Thundat, B.G. Sumpter, M.D. Barnes, *Nano Lett.* **2003**, *3*, 603.

129 D. Hu, J. Yu, K. Wong, B. Bagchi, P.J. Rossky, P.F. Barbara, *Nature* **2000**, *405*, 1030.

130 L.P. Candeias, F.C. Grozema, G. Padmanaban, S. Ramakrishnan, L.D.A. Siebbeles, J.M. Warman, *J. Phys. Chem. B* **2003**, *107*, 1554.

131 J.M. Warman, G.H. Gelinck, M.P. de Haas, *J. Phys.*: *Condens. Matter* **2002**, *14*, 9935.

132 It should be noted that mobility measurements on SCL hole-only devices of MDMO-PPV, spin cast from chlorobenzene, gave similar hole mobilities as reported in literature where mostly toluene was used as casting solvent.

133 P.W.M. Blom, H.F.M. Schoo, M. Matters, *Appl. Phys. Lett.* **1998**, *73*, 3914.

134 The mobility for the batch PhS-PPV used in the SFM studies was measured in the group of Prof. P.W.M. Blom at Groningen University, and gave somewhat lower values as reported earlier for another batch.

135 The mobility for BisEH-PPV was measured via the SCL technique at $T = 295$ K by V.D. Michailetchi and C. Tanase in the group of Prof. P.W.M. Blom at Groningen University. Hole-only SCL devices were prepared with the configuration glass/ITO/PEDOT:PSS/BisEH-PPV/Au, spin casting BisEH-PPV from either *o*-dichlorobenzene ($\mu_h = 5 \times 10^{-5}$ cm^2/Vs) or toluene ($\mu_h = 1 \times 10^{-5}$ cm^2/Vs).

136 The mobility for LC-PPV was measured via the SCL technique at room temperature by C. Tanase in the group of Prof. P.W.M. Blom at Groningen University. Hole-only SCL devices were prepared with the configuration glass/ITO/PEDOT:PSS/LC-PPV/Au. Additionally, the field-effect mobility for LC-PPV was measured at room temperature in the group of Dr. H.F.M. Schoo at TNO (Eindhoven, The Netherlands), and found to be 7×10^{-3} cm^2/Vs. FETs were prepared with both gold source and drain bottom-electrodes. LC-PPV was spin coated from chlorobenzene. As a comparison, for MDMO-PPV typically 4×10^{-4} cm^2/Vs is found for the field-effect mobility on the same substrates. Notice that because of the increase of the carrier mobility with charge density, field-effect mobilities (higher carrier density) are typically much larger than those measured in LED-configurations.

137 (a) P. Samori, J.P. Rabe, *J. Phys.*: *Condens. Matter* **2002**, *14*, 9955; (b) T. Saiki, Y. Narita, *Jap. Soc. Appl. Phys. Int.* **2002**, *5*, 22; (c) J.W.P. Hsu, *Mater. Sci. Eng. R* **2001**, *33*, 1; (d) P. Zhang, R. Kopelman, W. Tan, *Crit. Rev. Solid State Mater. Sci.* **2000**, *25*, 87; (e) S.S. Sheiko, *Adv. Pol. Sci.* **2000**, *151*, 61.

138 Synonymous to resonant mode is dynamic, vibrational, and tapping mode.

139 M. Kemerink, J.K.J. van Duren, P. Jonkheijm, W.F. Pasveer, P.M. Koenraad, R.A.J. Janssen, H.W.M. Salemink, J.H. Wolter, *Nano Lett.* **2003**, *3*, 1191.

140 As these rings show some similarity to a well-known artifact in phase images that results from improper feedback operation, usually due to too fast scanning, it should explicitly be pointed out that these rings are independent of scan parameters. In addition, the artifact rings center around topographic maxima, which the rings in Figure 3.9b do not.

141 HyperChem V7.04, Molecular Modeling System, Hypercube, Inc., using MM+ force fields.

142 It should be noted that the molecular weights of the polymers investigated are similar (~ 1×10^6 g/mol). Whether a systematic change in defect content (and sys/trans ratio) with increasing substituent-size might play an additional role on the conformational behavior observed has not been investigated. Furthermore, it is assumed that the stereoisomers of the monomer (as a result of the chirality in the side-chains) polymerize randomly and therefore do not result in preferred polymer conformations.

143 S.A. Choulis, J. Nelson, Y. Kim, D. Poplavskyy, T. Kreouzis, J.R. Durrant, D.D.C. Bradley, *Appl. Phys. Lett.* **2003**, *83*, 3812.

144 MDMO-PPV was generously provided by Philips Research Laboratories Eindhoven.

145 BisOC_{10}-PPV, LC-PPV, and PhS-PPV were generously provided by Dr. H.F.M. Schoo, Dr. A.J.J.M. van Breemen, and Dr. B.M.W. Langeveld-Voss, respectively (TNO).

146 C.J. Neef, J.P. Ferraris, *Macromolecules* **2000**, *33*, 2311.

147 BisEH-PPV was generously provided by J. Wildeman (Groningen University).

148 J.C. Hummelen, B.W. Knight, F. LePeq, F. Wudl, J. Yao, C.L. Wilkins, *J. Org. Chem.* **1995**, *60*, 532.

149 (a) X. Crispin, S. Marciniak, W. Osikowicz, G. Zotti, A.W. Denier van der Gon, F. Louwet, M. Fahlman, L. Groenendaal, F. De Schryver, W.R. Salaneck, *J. Pol. Sci. B* **2003**, *41*, 2561; (b) L. Groenendaal, G. Zotti, P.H. Aubert, S.M. Waybright, J.R. Reynolds, *Adv. Mater.* **2003**, *15*, 855; (c) L. Groenendaal, F. Jonas, D. Freitag, H. Pielartzik, J. R. Reynolds, *Adv. Mat*. **2000**, *12*, 481.

150 ITO covered glass substrates were generously provided by Philips Research Laboratories Eindhoven.

Chapter 4

Morphology of poly(*p*-phenylene vinylene): methanofullerene composites*

Abstract

The performance of bulk-heterojunction solar cells based on a phase-separated mixture of donor and acceptor materials is known to be critically dependent on the morphology of the active layer. Here a combination of techniques is used to resolve the morphology of spin cast films of poly(p-phenylene vinylene):methanofullerene blends in three dimensions on a nanometer scale. Atomic force microscopy (AFM), transmission electron microscopy (TEM), selected-area electron diffraction (SAED), depth-profiling by dynamic time-of-flight secondary ion mass spectrometry (TOF-SIMS), and photospectroscopy clearly show that for the two materials used in this study, viz. 1-(3-methoxy-carbonyl)propyl-1-phenyl-[6,6]-methanofullerene (PCBM) and poly[2-methoxy-5-(3′,7′-dimethyloctyloxy)-1,4-phenylene vinylene] (MDMO-PPV), a rather homogeneous polymer matrix containing tiny PCBM crystals is present up to 50 weight-percentages (wt.-%) PCBM. Phase separation resulting in large, separate domains of rather pure PCBM in a homogenous matrix of 50:50 wt.-% MDMO-PPV:PCBM sets in for concentrations of more than 67 wt.-% PCBM. The large, almost pure PCBM domains also consist of tiny PCBM crystals, similar to the nanocrystals of pure PCBM films.

*This work has been published: (a) C.W.T. Bulle-Lieuwma, J.K.J. van Duren, X. Yang, J. Loos, A.B. Sieval, J.C. Hummelen, R.A.J. Janssen, *Appl. Surf. Sci.* **2004**, *in press*; (b) X. Yang, J.K.J. van Duren, R.A.J. Janssen, M.A.J. Michels, J. Loos, *Macromolecules* **2004**, *in press*; (c) J.K.J. van Duren, X. Yang, J. Loos, C.W.T. Bulle-Lieuwma, A.B. Sieval, J.C. Hummelen, R.A.J. Janssen, *Adv. Funct. Mater.* **2004**, *in press*; (d) J.K.J. van Duren, X. Yang, J. Loos, C.W.T. Bulle-Lieuwma, A.B. Sieval, J.C. Hummelen, R.A.J. Janssen, *Proceedings of SPIE Vol. 5215 Organic Photovoltaics IV*, (Ed: Z.H. Kafafi), SPIE, Bellingham WA, **2004**, *in press*; (e) J.K.J. van Duren, J. Loos, F. Morrisey, C.M. Leewis, K.P.H. Kivits, L.J. van IJzendoorn, M.T. Rispens, J.C. Hummelen, R.A.J. Janssen, *Adv. Funct. Mater.* **2002**, *12*, 665.

4.1 Introduction

In bulk-heterojunction organic solar cells two different organic materials with donor and acceptor properties, respectively, are mixed to create a composite material that is capable of generating charges under illumination, followed by transporting and collecting these photogenerated charges into an external circuit.[1,2] Promising power conversion efficiencies of >3% have recently been reported for solar cells based on this approach utilizing conjugated polymers as a donor and fullerene derivatives as an acceptor.[3,4] In these cells a sub-picosecond photoinduced charge transfer[5-7] ensures efficient charge generation, while the collection of charges is facilitated by a slow recombination that extends into the millisecond domain.[8,9] It has been shown that both the conditions for processing of these (and other) mixtures from solution[4,10-12] and post-production treatment[12-17] can have a large influence on the performance of these devices, because they affect the morphology and phase separation of the active layer dramatically. The generation, transport, and collection of the charges are strongly influenced by the characteristic dimensions[18] of the phase separation of the photoactive film and the presence of percolation pathways.

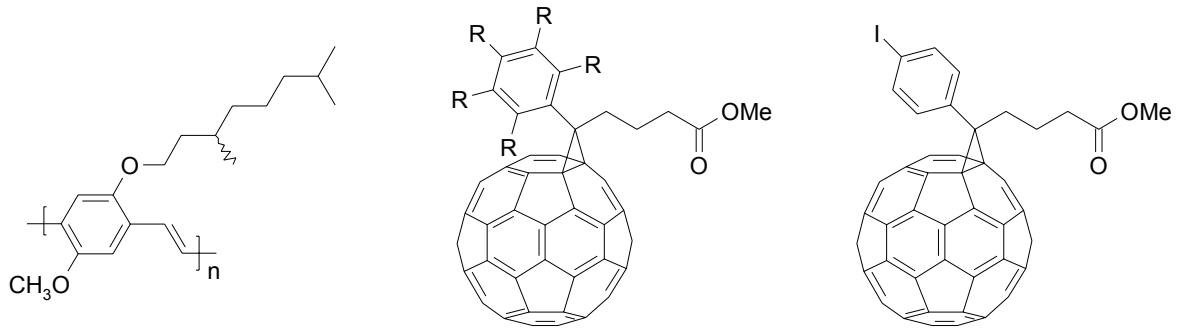

MDMO-PPV

R = H, PCBM
R = D, *d*5-PCBM

I-PCBM

Figure 4.1 *Molecular structures of materials used.*

Although some useful insights on the interplay between morphology and solar cell performance have been obtained,[4,10,13,16,19-23] a comprehensive understanding is lacking and so far no systematic study has been performed in which morphology and performance have been studied in detail for polymer:fullerene blends. On the other hand, detailed studies on the relation between morphology and performance have been described for photoactive layers based on donor and acceptor polymer blends.[24,25] In the following two chapters the phase separation and the performance of solar cells based on MDMO-PPV as a donor and PCBM as an acceptor (Figure 4.1) will be considered. Since the breakthrough discovery by the Linz group that solar cells with a power conversion efficiency of 2.5% under AM1.5 conditions can be obtained by using chlorobenzene as a solvent for spin coating,[10] this combination of materials has become subject of detailed studies.

To obtain a deeper insight in the relation between morphology and performance of polymer:fullerene bulk-heterojunction solar cells, both have to be characterized. The same, as for these composite photovoltaic diodes,[26] holds for composite light-emitting diodes,[27-31] and even for diodes based on only one component.[32-34] However, few techniques are available where the morphology of organic blends can be determined in all three dimensions on a nanometer scale. One way to achieve this goal is by combining different methods. Here a comprehensive study is presented on solar cells made with varying weight percentages of PCBM in MDMO-PPV in the active layer. The composite films have been investigated with atomic force microscopy (AFM), transmission electron microscopy (TEM), selected-area electron diffraction (SAED), dynamic time of flight-secondary ion mass spectrometry (TOF-SIMS), and time-correlated single photon counting fluorescence spectroscopy to reveal the morphology of these composites. Whereas this chapter deals with the morphology, the following chapter focuses on the device characteristics and the relation between the two.

4.2 Surface characterization

4.2.1 Atomic force microscopy

Figure 4.2 shows the height and corresponding phase images obtained by AFM for composite MDMO-PPV:PCBM films (~100 nm) for four different compositions. The height images are similar to those previously reported.[19] To match the conditions used for device preparation and to exclude any possible influence of the substrate, all films in this study were spin cast from chlorobenzene on ITO covered glass substrates carrying an additional layer of a transparent conducting polymer

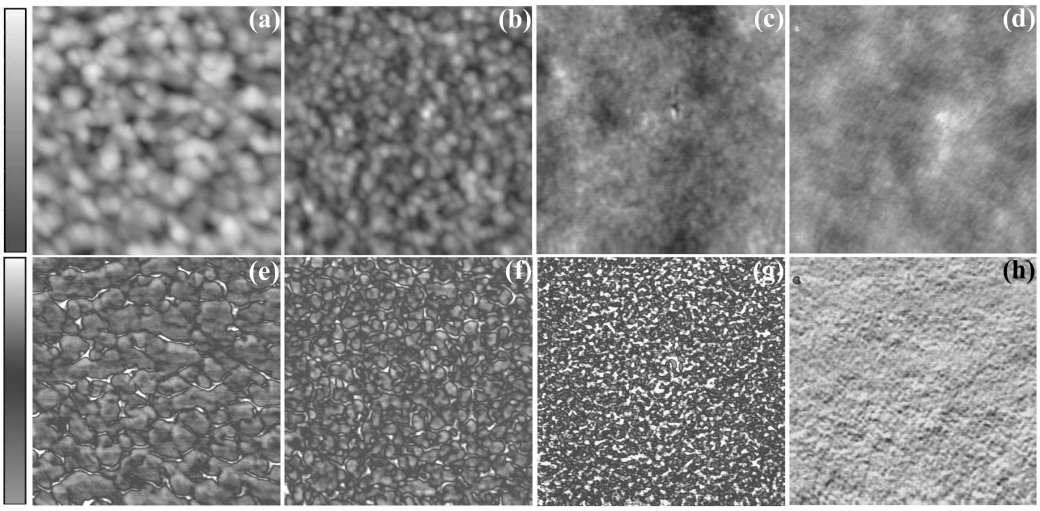

Figure 4.2 *The 2.0 × 2.0 μm^2 AFM height (a-d) and simultaneously taken phase (e-h) images of the MDMO-PPV:PCBM composite films of 90 (a and e), 80 (b and f), 67 (c and g), and 50 wt.-% PCBM (d and h). Height bar (maximum peak-to-valley) represents 20 nm (a), 10 nm (b), 3 nm (c), and 3 nm (d).*

(PEDOT:PSS). Apart from the images shown in Figure 4.2, compositions of 0, 33, 50, 67, 75, 80, 90, and 100 wt.-% PCBM in MDMO-PPV have been studied with AFM. The height images reveal extremely smooth surfaces for the pure films and for the blends with a PCBM concentration of 2-50 wt.-% (peak-to-valley roughness of 3 nm and root-mean-square (RMS) values of 0.4 nm for 2.0×2.0 μm^2). The surface becomes increasingly uneven for 67-90 wt.-% PCBM (peak-to-valley roughness of 3-22 nm and RMS values of 0.4-3.3 nm for 2.0×2.0 μm^2) and a reproducible phase contrast appears. Separate domains of one phase in a matrix of another phase can easily be recognized at these higher concentrations of PCBM. The domain size increases from 40-65 nm for 67 wt.-% to 110-200 nm for 90 wt.-% PCBM. For 80 wt.-% PCBM composite films, a gradual but small increase in domain size from 60-80 nm to 100-130 nm was observed when the film thickness was increased in steps from 65 to 270 nm.

Preliminary investigations using a metal-coated tip combined with a small spring constant and a relatively high Q-factor (≈200) to obtain molecular resolution[35] (as described in chapter 3) on these blends have resulted so far in no new insights.

4.2.2 X-ray photoelectron spectroscopy

Whereas AFM provides details on roughness and phase separation with high spatial resolution (typically 10-20 nm), X-ray photoelectron spectroscopy (XPS) can give details on the composition of the components at the surface (actually, the top 9 nm of the film). It has been suggested in literature[36] that these systems could give spontaneous stratification, meaning that during spin casting the small molecule preferentially appears at the top of the film and the polymer at the bottom. Therefore, XPS investigations have been performed[37] and, as shown in Figure 4.3 for the O 1*s* binding energy, the peak for the 80 wt.-% PCBM composite clearly is a superposition of the peak

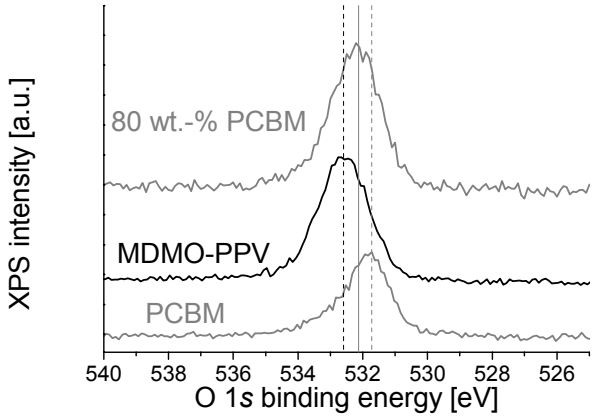

Figure 4.3 *Comparison of the O 1s regions of pure PCBM, pure MDMO-PPV and 80 wt.-% PCBM composite with MDMO-PPV shows the presence of both compounds at the surface.*

originating from pure PCBM and pure MDMO-PPV. The same conclusions could be drawn based on the C 1*s* binding energy and, for samples with an additional top layer of 5 Å Al, on the shift in the Al 2*p* and O 1*s* binding energy. This latter shift is suggested to result from reaction of PCBM with Al upon adsorption, where MDMO-PPV is found to be insensitive for this reaction.[38] No attempt has been made to quantify the amount of MDMO-PPV and PCBM at the surface.

4.3 Depth-profiling

Attempts have been made to improve solar cell performance by controlling the vertical phase separation aiming for a stratified photoactive layer in order to take advantage of the positive characteristics of both the bilayer and bulk-heterojunction concepts.[22,36,39-42] One example describes the stratification of MDMO-PPV and PCBM by making use of the temperature dependent solubility of MDMO-PPV in *o*-xylene by first spin coating MDMO-PPV from a hot solution and subsequently PCBM at room temperature.[36] These stratified layers have a diffuse interface and resulted in higher fill factors and power conversion efficiencies than the homogeneous composite films.[36] However, the possibility that spontaneous stratification of MDMO-PPV and PCBM occurs when spin casting these composites or that a concentration profile is formed in the photoactive layer, has not been tested. Therefore, two different depth-profiling techniques were used in order to investigate the extent of stratification for spin casting composites.

4.3.1 Cryogenic Rutherford backscattering spectrometry

Cryogenic Rutherford backscattering[43] (RBS) has been used to determine the concentration-depth profile of PCBM in the active layer of the solar cell.[44] For this purpose I-PCBM,[45] an

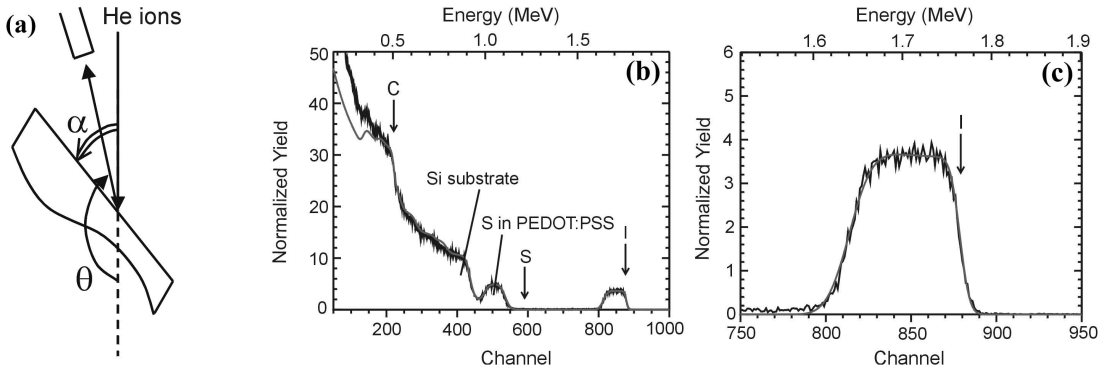

Figure 4.4 *RBS spectra (black) and their RUMP simulations (gray). The arrows indicate the energies that correspond to elements located at the surface.* **(a)** *RBS scattering geometry.* **(b)** *A glass/PEDOT:PSS/MDMO-PPV:I-PCBM (1:3 by wt.) stack, analyzed at a geometry of* $\alpha = 15°$ *and* $\theta = 170°$*. The composite was spin coated at 60-65 °C from o-xylene.* **(c)** *Enlargement of the I profile of graph* **(b)**.

iodinated fullerene derivative (Figure 4.1), was used to distinguish between PCBM and the polymer in the RBS spectra.[46] Iodine serves as a label of the PCBM and thereby resolves the problem of overlapping C, H, and O-peaks of PCBM and MDMO-PPV in the RBS spectrum.

The iodine distribution in the active layer has been investigated for several glass/PEDOT:PSS/MDMO-PPV:I-PCBM samples, spin cast from *o*-xylene (ratio MDMO-PPV:I-PCBM of 4:1, 1:3 and 1:4 by wt.) at 60-65 ºC. The RBS spectrum and RUMP[47] simulation of a sample with MDMO-PPV and I-PCBM (1:3 wt.-%) is shown in Figure 4.4B and 4.4C. The arrows shown indicate the energy of iodine at the surface, 1.77 MeV, as well as those for S (PEDOT:PSS), and C (photoactive layer). The enlargement of the iodine (I) part of the RBS spectrum in Figure 4.4C shows a homogeneous iodine concentration in the active layer corresponding to a concentration of 5.0 ± 0.2 10^{-3} at.-%. To explain the slope of the I signal on the low-energy side, a roughness of 15 nm had to be introduced for the interface between PEDOT:PSS and the active layer. The absence of a strong tendency for MDMO-PPV and I-PCBM to give stratification did not change when different weight ratios (MDMO-PPV:I-PCBM 4:1, 1:3, or 1:4 wt.-%) were analyzed.

Despite the structural similarity of I-PCBM and PCBM, they may behave differently when mixed with MDMO-PPV. In this respect the present study cannot give an unambiguous conclusion with respect to possible stratification in MDMO-PPV:PCBM layers. Layers of MDMO-PPV with I-PCBM layers turned out to have a larger surface roughness than layers with PCBM. This suggests that the (lateral) phase separation in layers of MDMO-PPV with PCBM is less than with I-PCBM. Based on this result it is believed that absence of stratification observed by RBS for MDMO-PPV:I-PCBM, also pertains to MDMO-PPV:PCBM thin films.

4.3.2 Time-of-flight secondary ion mass spectroscopy

Determining a distribution in depth of an organic component in a composite film where both components do not have a distinctive element can be accomplished by labeling one of the two components, as shown in the previous paragraph. Deuterium labeling in combination with dynamic SIMS has proven its usefulness for this purpose.[48-51] To enable recording depth profiles of PCBM in the photoactive films with MDMO-PPV, a deuterated derivative (*d*5-PCBM, Figure 4.1) has been synthesized[52] that carries five deuterium atoms on the phenyl ring. Using dynamic TOF-SIMS in dual-beam mode,[53] deuterium-related mass fragments can be used to measure a concentration-depth profile of *d*5-PCBM in the photoactive films. AFM, TEM, and solar cell characteristics demonstrated that the morphology and performance of MDMO-PPV:*d*5-PCBM blends was identical to that of MDMO-PPV:PCBM composites. Various MDMO-PPV:*d*5-PCBM (0, 20, 40, 60, 75, 80, 90 and 100 wt.-% *d*5-PCBM) films (~100 nm) spin cast from chlorobenzene on glass/ITO/PEDOT:PSS have been investigated with dynamic TOF-SIMS.[54] Although a single secondary ion, specific for the deuterium label, would be enough for depth-profiling, several secondary ions specific to the label

were observed and used as such. Hence, apart from D, also CD, CHD, OD and C_2D were monitored. CHD and OD obviously result from deuterium transfer during sputtering, just as proton transfer, commonly observed in dynamic TOF-SIMS for organic samples.[55] As shown in Figure 4.5 for 80 wt.-%, *d*5-PCBM is present from top to bottom. The same result has been observed for all other compositions with a clear increase in counts for the deuterium-related mass-fragments going from 0 to 100 wt.-% *d*5-PCBM in the film. The first region with the initial increase in secondary ion intensities is attributed, at least in part, to the pre-equilibrium regime. For 80 wt.-% *d*5-PCBM, it was found that *d*5-PCBM was present all over depth, regardless of the film thickness when it was varied from 65 to 270 nm.

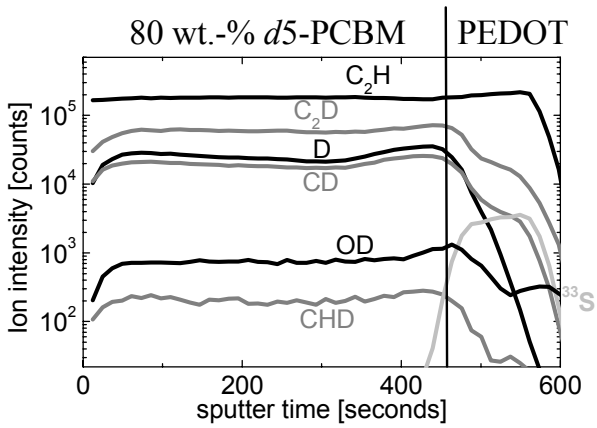

Figure 4.5 *Depth profile of an 80 wt.-% d5-PCBM blend with MDMO-PPV as measured with dynamic TOF-SIMS. Several deuterium-related negative ions are depicted versus sputter time (depth).*

Where others expect spontaneous stratification,[36] the TOF-SIMS results show that no spontaneous stratification occurs, consistent with our previous conclusion for composites of MDMO-PPV with an iodinated PCBM derivative studied by cryogenic Rutherford backscattering, as described in the previous paragraph.[45] In addition, TEM images of a cross-section made with cryo-ultramicrotomy of a spin cast film of an MDMO-PPV:PCBM composite on top of a PET substrate[19] and SEM images of a cross-section of the same composite film spin cast on glass/ITO[56] showed PCBM-rich domains all over depth.

For a more detailed description of TOF-SIMS depth-profiling on device structures of multiple thin layers of organic and inorganic materials, see chapter 6.

4.4 Bulk characterization

4.4.1 Transmission electron microscopy

Where AFM provides surface characteristics, TEM can be used for lateral resolution in the bulk of the film.[19] For TEM, the films were either floated with water from the glass/ITO/PEDOT:PSS substrates or mechanically removed, and subsequently transferred as a free-standing film to a Cu grid.[57] Composites varying from 0, 20, 40, 60, 75, 80, 90, and 100 wt.-% PCBM were investigated. The TEM images (Figure 4.6) show that the bulk characteristics are similar to those at the surface. Films with PCBM concentrations below 75 wt.-% demonstrate a very homogeneous morphology, and hardly any phase separation can be resolved. A detailed analysis, however, shows an average domain size of 15-20 nm for the dark regions.[58] Similar as for AFM, clearly visible phase separation is setting in somewhere between 60 and 75 wt.-% PCBM. The dark regions are PCBM-rich as can be concluded from the higher density for pure spin cast films of PCBM (1500 kg/m^3) compared to that of MDMO-PPV (910 kg/m^3).[59] From TEM, it can be concluded that MDMO-PPV can contain at least 50 wt.-% PCBM before clearly visible phase separation sets in.

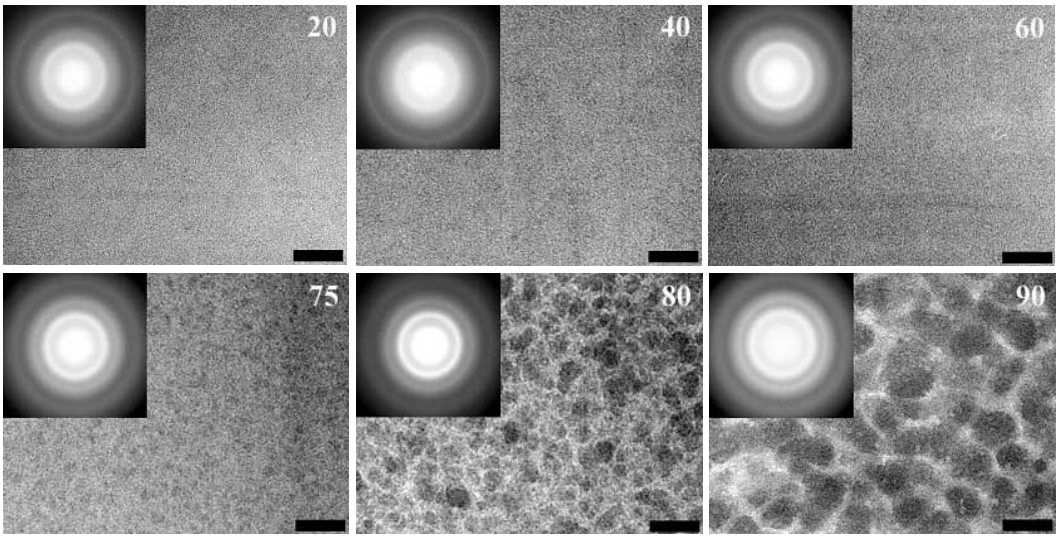

Figure 4.6 *TEM images and the corresponding SAED patterns (insets) of MDMO-PPV:PCBM composite films with the wt.-% PCBM in the upper right corner. Scale bar = 200 nm.*

Changing the solvent used for spin coating has shown to increase the power conversion efficiency ($\eta_{AM1.5}$) of these composite solar cells drastically going from toluene ($\eta_{AM1.5}$ = 0.9%) to chlorobenzene ($\eta_{AM1.5}$ = 2.5%) and has been attributed to a change in bulk morphology[10]. TEM-images for films cast from toluene on glass/ITO/PEDOT:PSS show large dark regions in a lighter matrix (Figure 4.7). Again, these darker regions are PCBM-rich domains. Both the domain-size and the observed contrast are much larger than for the same 80 wt.-% PCBM composite film spin cast from chlorobenzene. The difference in domain-size when changing spin cast solvent is attributed to a lower solubility of PCBM in toluene. The larger observed contrast is attributed to a larger difference

in mass density between matrix and domains for the toluene cast film and a clear contribution of height differences between matrix and domains. The dark regions coincide with ~75 nm large bumps in AFM height images (Figure 4.7). The increase in performance of the solar cell for the film cast from chlorobenzene compared to toluene is clearly related to the more intimate mixing for the chlorobenzene-cast film. Similar results were obtained on PET substrates[19] and glass/ITO.[56]

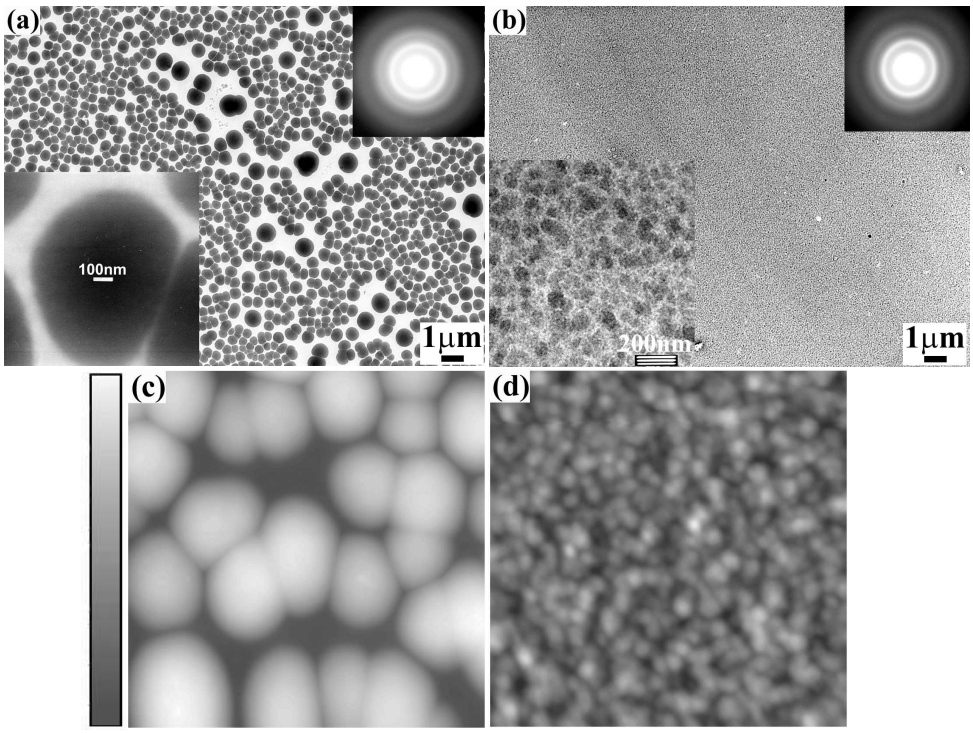

Figure 4.7 *TEM images together with the corresponding SAED patterns as insets in the upper right corner (a and b) and the 3.0 × 3.0 μm² (c) and 2.0 × 2.0 μm² AFM height (d) images of the MDMO-PPV:PCBM (1:4 by wt.) composite films cast from toluene (a and c) and chlorobenzene (b and d). Height bar (maximum peak-to-valley) represents 85 nm (c), and 10 nm (d).*

4.4.2 Selected-area electron diffraction

The same films as prepared for TEM were also investigated with selected-area electron diffraction (SAED).[57] The 20-90 wt.-% PCBM samples possess a similar SAED pattern (Figure 4.6). This pattern is indicative for the presence of PCBM nanocrystals randomly distributed in the film. A detailed discussion of the interpretation of the SAED patterns can be found in literature.[60] Briefly, the broad Debye-Scherrer rings result from the superposition of many single crystal diffraction patterns originating from PCBM nanocrystals, with different crystallographic orientations, that are simultaneously selected into the region of the field-limited aperture. The SAED pattern for these composites are identical to the SAED pattern found for spin cast films of pure PCBM.[60] It should be

emphasized that even below 50 wt.-% PCBM the SAED pattern is observed. Pure MDMO-PPV has also been measured as a reference and gave a different SAED pattern indicative for the amorphous state of the polymer. In agreement with the conclusions drawn based on our SAED observations, others found tiny nanospheres, that could not be detected with AFM and TEM, in SEM images made of cross-sections of the same composite film spin cast on glass/ITO.[56]

Although changing the solvent used for spin coating does change the scale of phase separation (Figure 4.7), it does not affect the SAED pattern indicating that for both films a random distribution of nanocrystals is present.

4.4.3 Atomic force microscopy on crater bottoms

To study the morphology at different depths, six craters were sputtered with a Cs^+ ion beam at depths ranging from 10 to 90 nm in the ~100 nm 80 wt.-% MDMO-PPV:*d*5-PCBM film. When studied with AFM, the bottoms of these craters (Figure 4.8) showed that the lateral phase distribution present at the top surface is present all over depth, although with slightly increasing domain size.

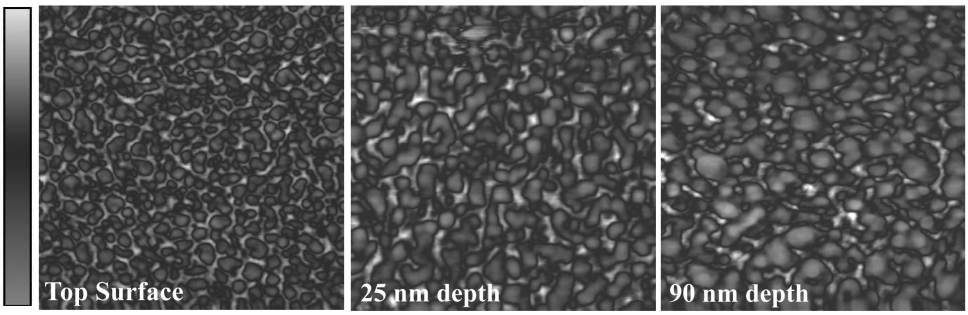

Figure 4.8 *The 2.0 × 2.0 μm^2 AFM phase images at the top surface and on two crater bottoms for the 80 wt.-% d5-PCBM blend with MDMO-PPV.*

4.4.4 Photospectroscopy

The optical absorption spectra of films spin cast on glass from chlorobenzene with concentrations varying from 0 to 100 wt.-% PCBM (0, 2, 5, 10, 14, 20, 30, 40, 50, 60, 67, 75, 80, 85, 90, 95, and 100 wt.-%) show the expected variation in composition (Figure 4.9). Savenije *et al*. recently showed that the spectra of such composite films correspond to a linear superposition of the spectra of the individual compounds with the same concentration PCBM in the film as in the solution used for spin casting these films.[61] Apart from absorption, photoluminescence (PL), and PL lifetime measurements are performed for all these compositions.

When the composite films are illuminated with light of 655 nm, *i.e.* outside the absorption spectrum of MDMO-PPV, such that only PCBM is photoexcited, the photoluminescence (PL) spectra clearly show the presence of a weak fullerene fluorescence with a maximum at ~722 nm for films

with 75-100 wt.-% PCBM, decreasing further in intensity with decreasing amount of PCBM. For blends with 67 wt.-% PCBM or less, fullerene emission can no longer be observed under these conditions.

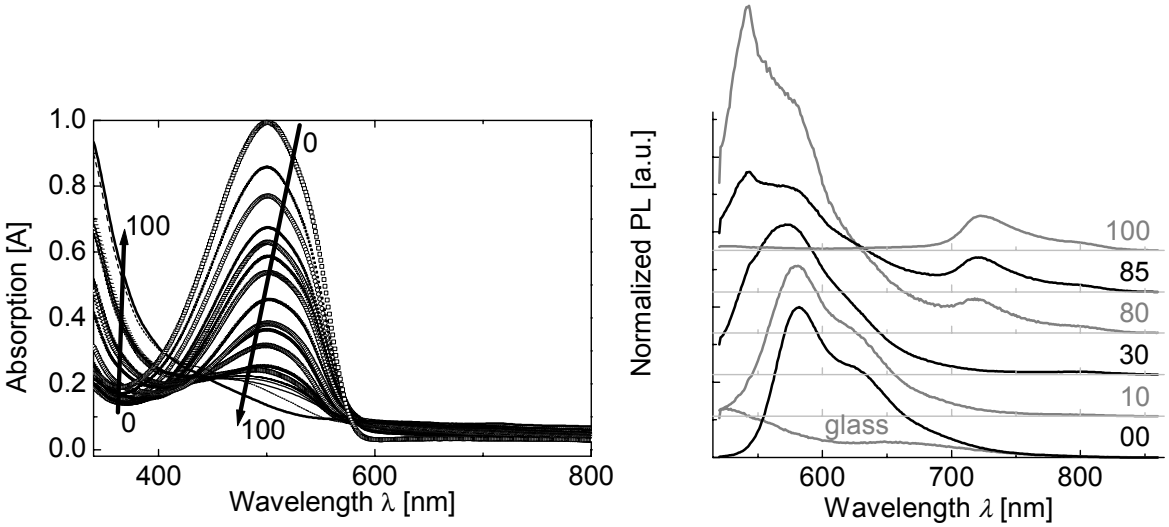

Figure 4.9 *Left: Absorption spectra for ~100 nm MDMO-PPV:PCBM composite films on glass, ranging from pure MDMO-PPV (0 wt.-% PCBM) to pure PCBM (100 wt.-%) on glass (uncorrected for variations in film thickness). Right: Normalized photoluminescence (PL) spectra of MDMO-PPV:PCBM blends for several compositions (in wt.-% PCBM) with excitation at 500 nm. 00-30 wt.-% PCBM are normalized at ~580 nm, whereas 80-100 wt.-% PCBM are normalized at ~722 nm. The feature near 543 nm is an artifact of the measurement (see text).*

When the excitation wavelength is shifted to 500 or 400 nm, where both MDMO-PPV and PCBM absorb light, the PCBM emission can again be detected down to 75 wt.-% (Figure 4.9). In addition to the fullerene emission around 722 nm, a signal centered at ~580 nm can be seen up to at least 85 wt.-% PCBM. It must be noted that already at 2 wt.-% of PCBM virtually all MDMO-PPV fluorescence is quenched. Hence, the ~580 nm signal must be regarded as a small residual effect. The extremely low signals prevented us from quantifying the amount of PL quenching reproducibly. However, the spectral information can still be used. Up to 30 wt.-% PCBM, a gradual blue shift of ~10 nm is observed for the emission maximum of MDMO-PPV while at the same time the shoulder at higher wavelengths (~625 nm) disappears. This observation is consistent with the idea that the residual emission originates from increasingly short-lived MDMO-PPV excitations that have not equilibrated. Above 30 wt.-% PCBM, the signal is increasingly contaminated with stray light and Raman effects, as was evidenced by a linear shift of some features with changing excitation wavelength (see e.g. the narrow peak at ~543 nm in Figure 4.9).

PL lifetime measurements can give important additional information on the nature of the blends. Time-correlated single-photon counting PL lifetime measurements have been performed, probing at characteristic fluorescence wavelengths for MDMO-PPV (584 nm) and PCBM (722 nm) while exciting at 400 nm.

At 584 nm an almost mono-exponential fluorescence decay is observed for pure MDMO-PPV (Figure 4.10a), corresponding to the lifetime of the singlet-excited state. Adding only 2 wt.-% PCBM immediately reduces the observed fluorescence lifetime of MDMO-PPV to the time resolution of the setup (~ 40 ps) and for higher wt.-% the curves remain almost identical (for clarity only a few are shown in Figure 4.10a, together with the signal due to stray light from uncoated glass as a reference). Because photoinduced electron transfer from the polymer to the fullerene is known to occur within ~45 fs,[7] this result indicates that already at 2 wt.-% PCBM virtually all photoexcitations in MDMO-PPV decay via photoinduced charge transfer. This huge effect at such a low concentration of PCBM is only possible when the fullerenes are rather homogeneously distributed over the film, either molecularly or as a large number of small domains. In either case, fullerenes must be present within the exciton diffusion length (~10 nm)[62] of the polymer to explain the strong quenching.

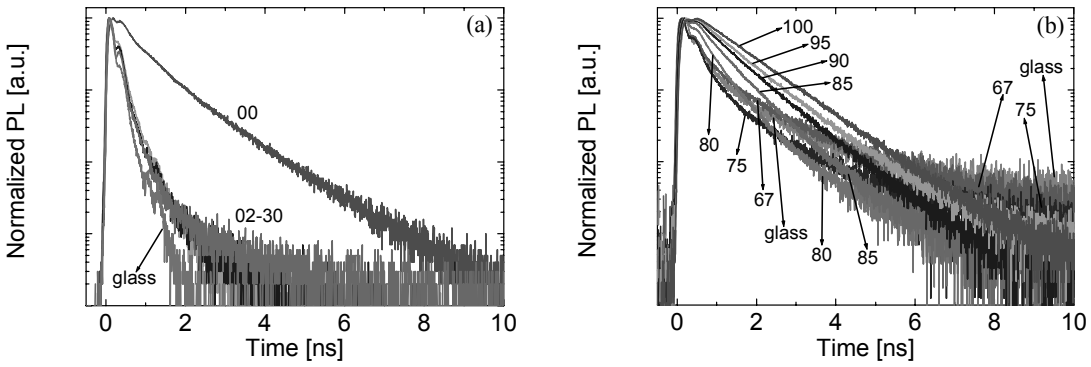

Figure 4.10 *Normalized fluorescence lifetime traces for several MDMO-PPV:PCBM blends with excitation at 400 nm and detection at (a) 584 nm, and (b) 722 nm. The numbers in the legends refer to the wt.-% PCBM.*

For pure PCBM, the fluorescence at 722 nm of PCBM appears to be nicely mono-exponential (Figure 4.10b). Upon adding MDMO-PPV to PCBM down to 67 wt.-% PCBM the fluorescence lifetime decreases only gradually, in strong contrast to the abrupt changes observed for the MDMO-PPV fluorescence. The gradual reduction in fullerene lifetime with increasing polymer concentration accompanies the decreasing domain size of the PCBM phase observed in AFM and TEM. It should be noted that with decreasing wt.-% PCBM the measurement time and therefore the baseline (dark counts) increases. As a result sensitivity problems of the setup prevent fluorescence lifetime measurements below 75 wt.-% PCBM.

These results are interpreted by considering that the PCBM domains in the phase-separated composites are rather pure. In such case, the intrinsic decay of the PCBM singlet-excited state (intersystem crossing and fluorescence) competes with hole transfer to the polymer. The fluorescence intensity and lifetime will then critically depend on the balance between the characteristic size of the domains and the exciton diffusion length of the singlet-excited state of PCBM. The observed gradual decrease in lifetime can be explained by considering that for increasingly smaller PCBM domains, photoinduced hole transfer from PCBM to MDMO-PPV becomes more likely because excitations created in the PCBM domains will be able to reach the interface with the polymer where they are quenched.

For 0-67 wt.-% PCBM no fullerene emission can be detected, neither with PL nor PL lifetime. Furthermore, the gradual reduction in PCBM fluorescence lifetime from 100 wt.-% down to 75 wt.-% PCBM accompanies the decrease in domain size of the PCBM phase, as observed with AFM and TEM. These results indicate that the tiny PCBM domains (15-20 nm), as observed by SAED, hardly give fluorescence and therefore have dimensions comparable to the fullerene exciton diffusion length.

4.4.5 Imaging time-of-flight secondary ion mass spectroscopy

In evaluating polymer blends, imaging TOF-SIMS[63] has shown to be useful to map surface morphology[64,65]. With imaging TOF-SIMS mass fragments can be detected pixel-wise. At each depth images can be recorded for a large number of mass fragments.

Initially, attempts were made to image the morphology of the 80 wt.-% *d*5-PCBM blend. With both size and spatial separation of the *d*5-PCBM domains[66] comparable to the ~100 nm analysis beam diameter, interpretation is rather ambiguous. Therefore, MDMO-PPV:PCBM composites were annealed for several minutes at T = 130 °C, well above its glass transition temperature $T_g \approx 80$ °C.[33,67-69] Some secondary ion distribution maps of the composite films are shown for two annealing times in Figure 4.11 with the emphasis on t = 38 min recorded after a short period of sputtering.[54] A clear correlation can be observed for the D, C, and C_2D images with a reversed contrast for the correlating images of C_2H, O, and S. Based on the elemental composition, D and C_2D can only be attributed to *d*5-PCBM, and S to PEDOT:PSS. The strong correlation of O and C_2H with S indicates that these are mainly from PEDOT:PSS. With increasing annealing time the number and size of the separated structures increases. Ring-shaped structures can be recognized at t = 20 min as shown for two different pixel-sizes.

In order to understand these images, AFM and TEM measurements have been performed (Figure 4.12). The AFM height images show clear topography of fine-structured hills surrounded by a ditch distributed in an extremely smooth matrix as shown for 20 min. Similar to the TOF-SIMS images these separate structures increase in both number and size, but also height, with increasing

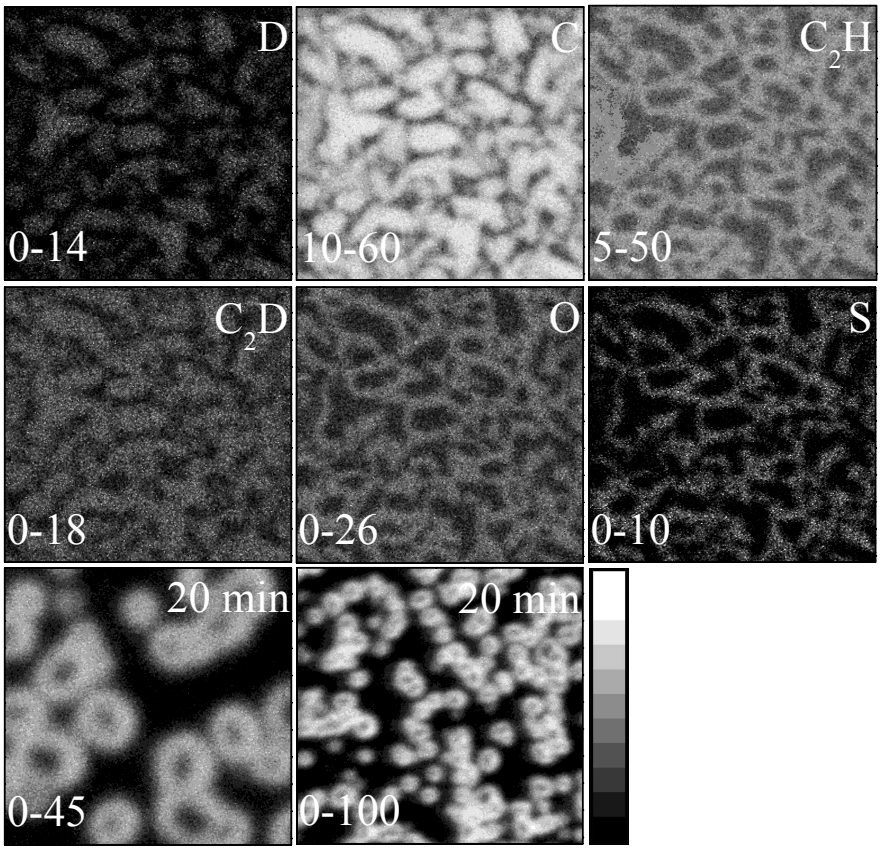

Figure 4.11 *Above 6 images: 29.3 × 29.3 μm² distribution maps (57 scans) of the MDMO-PPV:d5-PCBM composite film (80 wt.-% d5-PCBM) after 38 min annealing. Below: 9.8 × 9.8 μm² Sulfur (S) distribution map (32 scans, left) and 35.1 × 35.1μm² (102 scans, right) for 20 min annealing. The bar extends from the lowest to the highest number of counts as given in the lower left corner for each image.*

annealing time. Furthermore, they show crystalline features. The TEM images show separate dark structures tightly surrounded by a narrow light region within a grayish matrix for all annealing times. Contrast in TEM can be because of both a difference in composition and height. Taking into account the AFM height images, contrast in these TEM images is strongly influenced by height (thickness) differences. The similarity with the TOF-SIMS and AFM images is obvious. The separate structures are attributed to PCBM crystals and selected-area electron diffraction (SAED) indeed showed the crystal structure of PCBM.[58] The ditch around the crystals suggests that the crystal growth is limited by the diffusion of *d*5-PCBM from the surrounding matrix. The presence of this ditch also explains why at those positions PEDOT:PSS is reached sooner while sputtering (S image for 20 min, see Figure 4.11). It should be noted that the sputter rate of pure MDMO-PPV is at least twice that of pure PCBM[59]. Furthermore, with increasing annealing time the polymer matrix will become less dense[59] and thinner.

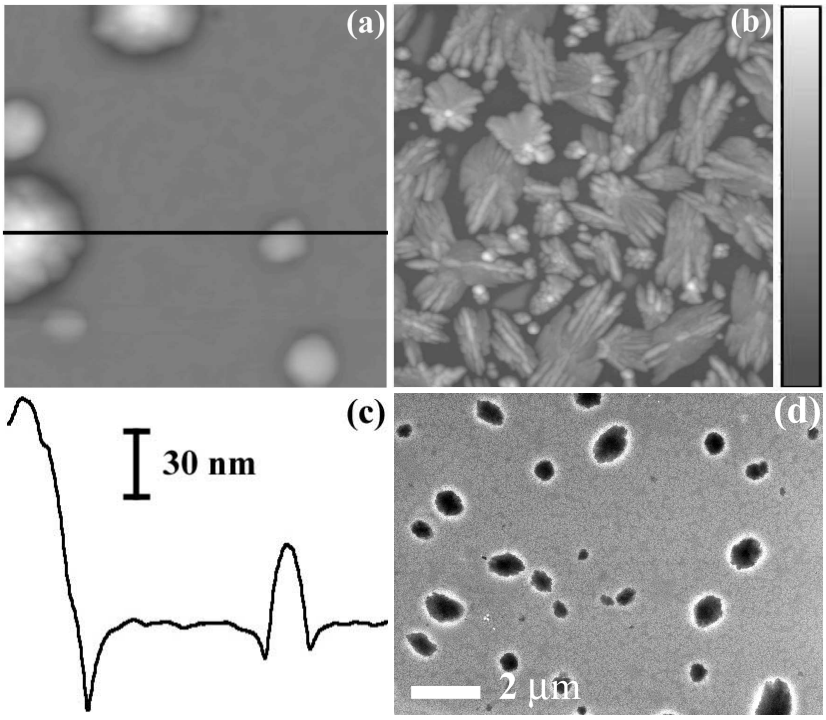

Figure 4.12 *The 5.0 × 5.0 µm² (a) and 20.0 × 20.0 µm² (b) AFM height image of the MDMO-PPV:d5-PCBM composite film (80 wt.-% d5-PCBM) after 20 min (a) and 38 min (b) annealing. Height bar (maximum peak-to-valley) represents 160 nm (a), and 300 nm (b). The black line in (a) indicates the position of the horizontal 5.0 µm line scan as shown in (c). Height scale of line scan is 130 nm. Additionally, a TEM image for 20 min annealing is shown (d).*

While annealing at T = 130 °C, the diffusion of the small *d*5-PCBM molecule through the MDMO-PPV matrix results in large single PCBM crystals and thus, forces phase segregation. The same has been observed at lower temperatures.[58] The limited thermal stability of the morphology of the active MDMO-PPV:PCBM layer will limit the performance and long-term stability of this type of solar cells, even though the kinetics of these processes will likely be reduced when a metal top electrode further confines the volume available to the phase separation.[16]

4.5 Conclusions

It has been shown by AFM, TEM, and SAED that for ~100 nm composite MDMO-PPV:PCBM films, spin cast from chlorobenzene, clearly visible phase separation sets in at approximately 67 wt.-% PCBM. The phase separation gives rise to almost pure PCBM domains containing clustered nanocrystals in a surrounding matrix of MDMO-PPV that contains up to 50 wt.-% PCBM. AFM measurements on the bottoms of sputtered craters and TEM have shown that this lateral phase separation is present all over depth and dynamic TOF-SIMS has confirmed the absence of a spontaneous stratification in the vertical direction. Additionally, time-correlated single-photon

counting fluorescence measurements revealed that up to 50 wt.-% PCBM the fullerenes are homogeneously distributed over the film either molecularly or in the form of tiny domains. Finally, the presence of these tiny domains for compositions below 50 wt.-% PCBM has been confirmed by SAED.

4.6 Experimental section

Materials. The materials used were poly[2-methoxy-5-(3′,7′-dimethyloctyloxy)-1,4-phenylene vinylene] (MDMO-PPV) synthesized via the Gilch-route[70], 1-(3-methoxycarbonyl)propyl-1-phenyl-[6,6]-methanofullerene (PCBM)[71], 1-[3-(methoxycarbonyl)propyl]-1-(*d*5-phenyl)[6,6]C_{61} (*d*5-PCBM)[52], 1-(3-methoxycarbonyl)propyl-1-(*p*-iodine-phenyl)-[6,6]-methanofullerene (I-PCBM),[45] polyethylenedioxythiophene:polystyrenesulfonate[72] (PEDOT:PSS) from Bayer AG (Baytron P VPAI 4083), and Al from Engelhard-Clal. For molecular structures, see Figure 4.1. A glass plate fully covered with a 40 nm thick layer of indium tin oxide (ITO) was used as the substrate for AFM, XPS, TOF-SIMS, TEM, and SAED. For RBS the ITO layer was 155 nm thick.[73] Schott D263 glass plates were used for spectroscopic investigations.

Sample preparation. Samples for AFM, TOF-SIMS, TEM, and SAED were prepared as follows. The ITO covered glass substrates were first cleaned by ultrasonic treatment in acetone, rubbing with soap, rinsing with de-mineralized water, refluxing with iso-propanol, and finally 20 minutes UV ozone treatment. Subsequently, a ~75 nm thick layer of PEDOT:PSS was spin coated from an aqueous dispersion under ambient conditions on the cleaned substrates and the layer was dried by annealing the substrate for 1 minute at 180 °C and subsequently cooled for 1 minute at 25 °C. Then the 70-115 nm thick composite layer of MDMO-PPV and PCBM (thickness variation between compositions) was spin coated from a chlorobenzene solution on top of the PEDOT:PSS layer and the sample was transferred to an N_2 atmosphere glove box. The organic solutions are stirred vigorously overnight while keeping them in the dark. Film thickness for the different composite samples was controlled by reducing the concentration of the composite solution from 5.4 to 0.5 mg MDMO-PPV/ml chlorobenzene with increasing wt.-% PCBM. It should be noted that the variation in film thickness between substrates per composition is below 4 nm, whereas the film thickness varies randomly going from 0 wt.-% to 100 wt.-% PCBM. Film thickness measurements were performed with a Tencor P10 surface profiler. All polymer layers were spin cast via a two-step procedure employing a home-made chuck, which requires no vacuum, on a Chemat Technology spin coater model KW-4A placed in a laminar flowbox. First 7 seconds at 500 rpm followed by 35 seconds at 1500 rpm. The same processing procedure applies for photoactive films directly cast on glass.

For XPS and RBS measurements PEDOT:PSS was dried by annealing the substrate on a hot plate at 100 °C for 1 min, immediately followed by spin coating the active layer. For RBS the MDMO-PPV:I-PCBM composite was cast from *o*-xylene solution at ~60 °C, resulting in ~160 nm active layer on top of 70 nm PEDOT:PSS. Annealing for imaging TOF-SIMS was performed at T = 130 °C in an inert atmosphere. After annealing the substrates were cooled down immediately to room temperature. All samples are stored in the dark in an N_2 atmosphere glove box. Finally, for some XPS-samples aluminum was deposited by thermal evaporation under vacuum (5×10^{-6} mbar, 1 ppm O_2 and < 1 ppm H_2O) using a rotation sample holder to guarantee homogeneous layers.

Atomic force microscopy. A solver P47H scanning probe microscope (NT-MDT Co., Moscow, Russia) in resonant mode[74] was used to measure under ambient conditions the simultaneously taken height and phase images with both NT-MDT NSG01 (force constant is typically 5.5 N/m) and NSG10 (force constant is typically 11.5 N/m) cantilevers. Scanning speed, tapping force, scan-size and AFM-tips have been varied to ensure that the phase contrast was a sample characteristic and not an artifact of the chosen AFM-conditions.

X-ray photoelectron spectroscopy. All samples were transported in a dry nitrogen atmosphere to a VG Ionex system equipped with a VG Clam II analyzer, and Mg/Al Kα dual anode X-ray source. The XPS measurements were carried out using the Al anode. All C 1*s* peaks corresponding to hydrocarbon were calibrated at a binding energy of 285.0 eV to correct for the energy shift caused by charging.

Rutherford backscattering spectrometry*:* Samples for RBS of approximately 1.1×2.5 cm^2 were mounted on the sample holder in the glove box. A cryo paste was used to improve heat conduction between the sample and sample holder during the cryogenic measurements. The samples were transported to the cryogenic RBS setup in a sealed holder in N_2 atmosphere and transferred to the analysis chamber by a load lock, without exposure to air. The RBS measurements were performed using a 2 MeV He^+ beam from the 2-30 MeV AVF cyclotron at Eindhoven University of Technology using a current of typically 10 nA. Using a solid-state detector with a solid angle of 2.5 mrad, the count rate was limited to approximately 1000 counts/s minimizing pile up. The size of the beam spot is 1 × 1 mm^2. The angle of incidence of the beam relative to the sample surface could be adjusted between 0° and 90°, while the RBS detector could be moved to select any scattering angle between 0° and 180°. The simulations of the RBS measurements were performed with the RUMP code.[47] For accurate RUMP simulations it was necessary to determine the composition of the glass and ITO in separate experiments. The composition of the glass was determined with the beam directed along the surface normal ($\alpha = 90°$ and $\theta = 165°$) and gave 62.0 at.-% O, 25.6 at.-% Si, 9.6 at.-% Na and 2.8 at.-% Ca. The composition of ITO, determined at the same geometry equals 61 at.-% O and 39 at.-% In. The Sn fraction was disregarded because In and Sn were indistinguishable in the RBS measurements and the Sn fraction in ITO is small (1-10%).[75] In the simulations the composition of the PEDOT:PSS was assumed to be 43 at.-% C, 34 at.-% H, 17 at.-% O and 5 at.-% S.[76]

Dynamic TOF-SIMS. The samples have been exposed to an ambient atmosphere while mounting the samples on the sample holder (~30 min.). The dynamic SIMS profiling measurements were performed on an ION-TOF TOF-SIMS IV apparatus (which saturates at 3 × 10^5 counts) in dual-beam[53] mode: 73 nA 1 keV Cs^+ at 45° rastered over 300×300 μm^2 for sputtering and a 15 keV Ga^+ beam (1.9, 2.5, and 3.0 pA ac) at 45° rastered over 50×50 μm^2 for analysis. The depth profiles were measured in the non-interlaced mode (longer sputter and data acquisition cycles) to avoid charging. Effective charge compensation was obtained by using an electron flood gun (20 eV). Imaging TOF-SIMS was performed in collimated mode with 60 pA dc 25 keV Ga^+ for analysis with a beam diameter of ~100 nm while rastering over 256×256 pixels with one shot per pixel. Each image has its own number of scans and size. All depth profiles and images were taken in the negative mode and mass calibrated on C_xH_y fragments.

Transmission electron microscopy and selected-area electron diffraction. A free-standing or so-called self-supported film is definitely prerequisite for TEM investigation. Two methods were used to prepare the TEM specimen. One is mechanically removing from its substrate with adhesive tape. The other one is the floatation technique by using de-ionized water. The films were floated onto the surface of de-ionized water and finally picked up by a 400 mesh copper grid. The bright-field morphology observations and SAED measurements were conducted on a JEOL JEM-2000FX transmission electron microscope operated at 80 kV.

Photospectroscopy. Absorption spectra were recorded on a Perkin-Elmer Lambda 900 UV-vis-near-IR spectrometer against glass (instead of air), whereas fluorescence and excitation spectra were recorded on an Edinburgh Instruments FS920 double-monochromator spectrometer with a Peltier-cooled red-sensitive photomultiplier. Depending on the spectral range investigated for the fluorescence and excitation spectra, Schott GG385, GG435, or Oriel Corp. 59511 (590 nm) cutoff filters were put in the excitation beam. Time-correlated single-photon counting fluorescence studies were performed using an Edinburgh Instruments LifeSpec-PS spectrometer, consisting of a 400 nm picosecond laser (PicoQuant PDL 800B) operated at 2.5 MHz and a Peltier-cooled Hamamatsu micro-

channel plate photomultiplier (R3809U-50) where either a Schott GG435 or an Oriel Corp. 59512 (610 nm) cutoff filter was put in the detection beam.

4.7 References and notes

1 G. Yu, J. Gao, J.C. Hummelen, F. Wudl, A.J. Heeger, *Science* **1995**, *270*, 1789.

2 J.J.M. Halls, C.A. Walsh, N.C. Greenham, E.A. Marseglia, R.H. Friend, S.C. Moratti, A.B. Holmes, *Nature* **1995**, *376*, 498.

3 P. Schilinsky, C. Waldauf, C.J. Brabec, *Appl. Phys. Lett.* **2002**, *81*, 3885.

4 M.M. Wienk, J.M. Kroon, W.J.H. Verhees, J. Knol, J.C. Hummelen, P.A. van Hal, R.A.J. Janssen, *Angew. Chem. Int. Ed*. **2003**, *42*, 3371.

5 N.S. Sariciftci, L. Smilowitz, A.J. Heeger, F. Wudl, *Science* **1992**, *258*, 1474.

6 N.S. Sariciftci, A.J. Heeger, *Handbook of Organic Conductive Molecules & Polymers* Vol. 1 (Ed: H.S. Nalwa), Chapter 8, p. 413, Wiley, New York, **1997**.

7 C.J. Brabec, G. Zerza, G. Cerullo, S. De Silvestri, S. Luzzati, J.C. Hummelen, N.S. Sariciftci, *Chem. Phys. Lett.* **2001**, *340*, 232.

8 I. Montanari, A.F. Nogueira, J. Nelson, J.R. Durrant, C. Winder, M.A. Loi, N.S. Sariciftci, C.J. Brabec, *Appl. Phys. Lett.* **2002**, *81*, 3001.

9 T. Offermans, S.C.J. Meskers, R.A.J. Janssen, *J. Chem. Phys*. **2003**, *119*, 10467.

10 S.E. Shaheen, C.J. Brabec, N.S. Sariciftci, F. Padinger, T. Fromherz, J.C. Hummelen, *Appl. Phys. Lett*. **2001**, *78*, 841.

11 J. Liu, Y. Shi, Y. Yang, *Adv. Funct. Mater.* **2001**, *11*, 420.

12 C.J. Brabec, C. Winder, M.C. Scharber, N.S. Sariciftci, J.C. Hummelen, M. Svensson, M.R. Andersson, *J. Chem. Phys.* **2001**, *115*, 7235.

13 (a) J.J. Dittmer, E.A. Marseglia, R.H. Friend, *Adv. Mater.* **2000**, *12*, 1270; (b) J.J. Dittmer, R. Lazzaroni, Ph. Leclère, P. Moretti, M. Granström, K. Petritsch, E.A. Marseglia, R.H. Friend, J.L. Brédas, H. Rost, A.B. Holmes, *Sol. Energy Mater. Sol. Cells* **2000**, *61*, 53.

14 N. Camaioni, G. Ridolfi, G. Casalbore-Miceli, G. Possamai, M. Maggini, *Adv. Mater*. **2002**, *14*, 1735.

15 F. Padinger, R.S. Rittberger, N.S. Sariciftci, *Adv. Funct. Mater.* **2003**, *13*, 85.

16 P. Peumans, S. Uchida, S.R. Forrest, *Nature* **2003**, *425*, 158.

17 J. Cabanillas-Gonzalez, S. Yeates, D.D.C. Bradley, *Synth. Met.* **2003**, *139*, 637.

18 B. Kannan, K. Castelino, A. Majumdar, *Nano Lett.* **2003**, *3*, 1729.

19 T. Martens, J. D'Haen, T. Munters, Z. Beelen, L. Goris, J. Manca, M. D'Olieslaeger, D. Vanderzande, L. De Schepper, R. Andriessen, *Synth. Met.* **2003**, *138*, 243.

20 (a) W.U. Huynh, J.J. Dittmer, W.C. Libby, G.L. Whiting, A.P. Alivisatos, *Adv. Funct. Mater.* **2003**, *13*, 73; (b) W.U. Huynh, J.J. Dittmer, A.P. Alivisatos, *Science* **2001**, *295*, 2425.

21 W. Feng, Y.L. Xu, W.H. Yi, F. Zhou, X.G. Wang, K. Yoshino, *Chinese Physics* **2003**, *12*, 426.

22 (a) L. Schmidt-Mende, A. Fechtenkötter, K. Müllen, E. Moons, R.H. Friend, J.D. MacKenzie, *Science* **2001**, *293*, 1119; (b) L. Schmidt-Mende, M. Watson, K. Müllen, R.H. Friend, *Mol. Cryst. Liq. Cryst.* **2003**, *396*, 73.

23 L.S. Roman, M.R. Andersson, T. Yohannes, O. Inganäs, *Adv. Mater.* **1997**, *9*, 1165.

24 A.C. Arias, J.D. MacKenzie, R. Stevenson, J.J.M. Halls, M. Inbasekaran, E.P. Woo, D. Richards, R.H. Friend, *Macromolecules* **2001**, *34*, 6005.

25 H.J. Snaith, A.C. Arias, A.C. Morteani, C. Silva, R.H. Friend, *Nano Lett*. **2002**, *2*, 1353.

26 J. Chappell, D.G. Lidzey, P.C. Jukes, A.M. Higgins, R.L. Thompson, S. O'Connor, I. Grizzi, R. Fletcher, J. O'Brien, M. Geoghegan, R.A.L. Jones, *Nature Mater.* **2003**, *2*, 616.

27 E. Moons, *J. Phys.*: *Condens. Matter* **2002**, *14*, 12235.

28 (a) M.M. Alam, C.J. Tonzola, S.A. Jenekhe, *Macromolecules* **2003**, *36*, 6577; (b) A.P. Kulkarni, S.A. Jenekhe, *Macromolecules* **2003**, *36*, 5258; (c) X. Zhang, D.M. Kale, S.A. Jenekhe, *Macromolecules* **2002**, *35*, 382; (d) X. Zhang, S.A. Jenekhe, *Macromolecules* **2000**, *33*, 2069.

29 N. Corcoran, A.C. Arias, J.S. Kim, J.D. MacKenzie, R.H. Friend, *Appl. Phys. Lett.* **2003**, *82*, 299.

30 H. Hänsel, D.C. Müller, M. Gross, K. Meerholz, G. Krausch, *Macromolecules* **2003**, *36*, 4932.

31 M. Berggren, O. Inganäs, G. Gustafsson, J. Rasmusson, M.R. Andersson, T. Hjertberg, O. Wennerström, *Nature* **1994**, *372*, 444.

32 (a) B.J. Schwartz, *Annu. Rev. Phys. Chem.* **2003**, *54*, 141; (b) R.D. Schaller, L.F. Lee, T.Q. Nguyen, P.T. Snee, R.J. Saykally, *Jpn. J. Appl. Phys. Part 1* **2003**, *42*, 4799.

33 (a) J. Liu, T.F. Guo, Y. Yang, *J. Appl. Phys.* **2002**, *91*, 1595; (b) G. He, Y. Li, T.F. Guo, Y. Yang, *Synth. Met.* **2003**, *137*, 1091.

34 For more references, see chapter 3.

35 M. Kemerink, J.K.J. van Duren, P. Jonkheijm, W.F. Pasveer, P.M. Koenraad, R.A.J. Janssen, H.W.M. Salemink, J.H. Wolter, *Nano Lett.* **2003**, *3*, 1191.

36 L.C. Chen, D. Godovsky, O. Inganäs, J.C. Hummelen, R.A.J. Janssen, M.R. Andersson, *Adv. Mater.* **2000**, *12*, 1367.

37 XPS measurements have been performed by Dr. W.J.H. van Gennip in the group of Prof. J.W. Niemantsverdriet at the Eindhoven University of Technology.

38 W.J.H. van Gennip, J.K.J. van Duren, P.C. Thüne, R.A.J. Janssen, J.W. Niemantsverdriet, *J. Chem. Phys*. **2002**, *117*, 5031.

39 T. Umeda, T. Shirakawa, A. Fujii, K. Yoshino, *Jpn. J. Appl. Phys.* **2003**, *42*, L1475.

40 A.C. Arias, N. Corcoran, M. Banach, R.H. Friend, J.D. MacKenzie, W.T.S. Huck, *Appl. Phys. Lett.* **2002**, *80*, 1695.

41 M. Drees, K. Premaratne, W. Graupner, J.R. Heflin, R.M. Davis, D. Marciu, M. Miller, *Appl. Phys. Lett*. **2002**, *81*, 4607.

42 L. Ouali, V.V. Krasnikov, U. Stalmach, G. Hadziioannou, *Adv. Mater.* **1999**, *11*, 1515.

43 Cryogenic (~30 K) RBS enables depth-profiling of the elemental composition in the sample without the use of sputtering. For samples containing polymers, the cryogenic temperature during analysis is required in order to trap the radicals and small molecules formed by bond cleavage resulting from the large amount of energy introduced by the monoenergetic beam of He ions (2 MeV, few nA). The RBS spectra show the energy distribution of the He ions after scattering. This energy depends on the masses of the projectile and scattering atom, the scattering geometry (depicted in Figure 4.4a) and moreover on the depth at which the scattering atom is located. By carefully choosing the scattering angle θ and the angle between the incoming beam and the sample surface α, overlap of signals of different atoms can be circumvented. Both concentration-depth profiles (resolution typically 10 nm) in separate layers as well as layer-to-layer diffusion can be determined. The RBS measurements are simulated using the RUMP code which provides the atomic composition and the thickness of the layer. For further details, see M.P. de Jong, *Interface Stability in Polymer Light-Emitting Diodes*, Ph. D. thesis **2000**, Eindhoven University of Technology.

44 RBS measurements have been performed by K.P.H. Kivits and Dr. C.M. Leewis in the group of Dr. L.J. van IJzendoorn and Prof. M.J.A. de Voigt at the Eindhoven University of Technology.

45 J.K.J. van Duren, J. Loos, F. Morrisey, C.M. Leewis, K.P.H. Kivits, L.J. van IJzendoorn, M.T. Rispens, J.C. Hummelen, R.A.J. Janssen, *Adv. Funct. Mater.* **2002**, *12*, 665.

46 I-PCBM was synthesized by Dr. M.T. Rispens in the group of Prof. J.C. Hummelen at Groningen University.

47 L.R. Doolittle, Nucl. Instrum. Methods Phys. Res. B **1985**, 9, 344.

48 K.A. Welp, R.P. Wool, S.K. Satija, S. Pispas, J. Mays, *Macromolecules* **1998**, *31*, 4915.

49 H. Yokoyama, E.J. Kramer, M.H. Rafailovich, J. Sokolov, S.A. Schwarz, *Macromolecules* **1998**, *31*, 8826.

50 S.J. Valenty, J.J. Chera, D.R. Olson, K.K. Webb, G.A. Smith, W. Katz, *J. Am. Chem. Soc.* **1984**, *106*, 6155.

51 P.C. Zalm, *Mikrochim. Acta* **2000**, *132*, 243.

52 *d*5-PCBM was synthesized by Dr. A.B. Sieval in the group of Prof. J.C. Hummelen at Groningen University.

53 E. Niehuis, T. Grehl, *ToF-SIMS: Surface Analysis by Mass Spectrometry* (Ed: J.C. Vickerman, D. Briggs), Chapter 28, p. 753, IM Publications, Chichester, **2001**.

54 TOF-SIMS measurements were performed by Dr. C.W.T. Bulle-Lieuwma at Philips CFT.

55 It should be noted that with increasing polymer concentration the overlap in mass between the isotope clusters $^{13}C^{1}H$ with $^{12}C^{2}H$ (= CD), and $^{1}H_2$ with ^{2}H (=D) results in an increasing contribution of the non-deuterium related isotopes to the secondary ion intensities of CD, CHD, and C_2D from < 10% for 100 wt.-% *d*5-PCBM to ~30% at 40 wt.-% *d*5-PCBM as can be concluded from comparison with the undeuterated composites.

56 H. Hoppe, M. Niggeman, C. Winder, A. Hinsch, J. Kraut, R. Hiesgen, D. Meissner, N.S. Sariciftci, *Adv. Funct. Mater.* **2004**, *in press*.

57 TEM and SAED investigations were performed by Dr. X. Yang at the Dutch Polymer Institute.

58 X. Yang, J.K.J. van Duren, R.A.J. Janssen, M.A.J. Michels, J. Loos, *Macromolecules* **2004**, *in press*.

59 C.W.T. Bulle-Lieuwma, W.J.H. van Gennip, J.K.J. van Duren, P. Jonkheijm, R.A.J. Janssen, J.W. Niemantsverdriet, *Appl. Surf. Sci.* **2003**, *203-204*, 547.

60 X. Yang, J.K.J. van Duren, M.T. Rispens, J.C. Hummelen, R.A.J. Janssen, M.A.J. Michels, J. Loos, *Adv. Mater.* **2004**, *in press*.

61 T.J. Savenije, J.E. Kroeze, M.M. Wienk, J.M. Kroon, J.M. Warman, *submitted*.

62 (a) K. Yoshino, Y.X. Hong, K. Muro, S. Kiyomatsu, S. Morita, A.A. Zakhidov, T. Noguchi, T. Ohnishi, *Jpn. J. Appl. Phys., Part 2* **1993**, *32*, L357; (b) J.J.M. Halls, K. Pichler, R.H. Friend, S.C. Moratti, A.B. Holmes, *Appl. Phys. Lett.* **1996**, *68*, 3120; (c) A. Haugeneder, M Neges, C. Kallinger, W. Spirkl, U. Lemmer, J. Feldmann, *Phys. Rev. B* **1999**, *59*, 15346.

63 M.L. Pacholski, N. Winograd, *Chem. Rev.* **1999**, *99*, 2977 (and references therein).

64 J. Hyun, H. Ma, Z. Zhang, T.P. Beebe Jr., A. Chilkoti, *Adv. Mater.* **2003**, *15*, 576.

65 J. Raczkowska, J. Rysz, A. Budkowski, J. Lekki, M. Lekka, A. Bernasik, K. Kowalski, P. Czuba, *Macromolecules* **2003**, *36*, 2419.

66 See previous paragraphs on AFM and TEM.

67 S. Yin, W.Z. Liu, C. Liu, Z.Y. Zhong, C.A. Wang, *Yejing Yu Xianshi* **2003**, *18*, 175.

68 T. Gray, C. Buenviaje, R.M. Overney, S.A. Jenekhe, L. Zheng, A.K.Y. Jen, *Appl. Phys. Lett.* **2003**, *83*, 2563.

69 Dynamic mechanical thermal analysis (DMTA) on MDMO-PPV synthesized via the sulfinyl-route gave T_g = 90°C, whereas others previously found T_g = 70°C for MDMO-PPV synthesized via the Gilch-route.

70 MDMO-PPV was generously provided by Philips Research Laboratories Eindhoven. Synthesis as described in H. Becker, H. Spreitzer, W. Kreuder, E. Kluge, H. Schenk, I. Parker, Y. Cao, *Adv. Mater.* **2000**, *12*, 42 (and references therein).

71 J.C. Hummelen, B.W. Knight, F. LePeq, F. Wudl, J. Yao, C.L. Wilkins, *J. Org. Chem.* **1995**, *60*, 532.

72 (a) X. Crispin, S. Marciniak, W. Osikowicz, G. Zotti, A.W. Denier van der Gon, F. Louwet, M. Fahlman, L. Groenendaal, F. De Schryver, W.R. Salaneck, *J. Pol. Sci. B* **2003**, *41*, 2561; (b) L. Groenendaal, G. Zotti, P.H. Aubert, S.M. Waybright, J.R. Reynolds, *Adv. Mater.* **2003**, *15*, 855; (c) L. Groenendaal, F. Jonas, D. Freitag, H. Pielartzik, J. R. Reynolds, *Adv. Mat*. **2000**, *12*, 481.

73 ITO covered glass substrates were generously provided by Philips Research Laboratories Eindhoven.

74 Synonymous to resonant mode is dynamic, vibrational, and tapping mode.

75 M.P. de Jong, *Interface Stability in Polymer Light-Emitting Diodes*, Ph. D. Thesis, Eindhoven University of Technology, **2000**.

76 A.J. Heeger, A.N. Aleshin, S.R. Williams, *Synth. Met.* **1998**, *94*, 173.

Chapter 5

Relating morphology of poly(*p*-phenylene vinylene):methanofullerene composites to solar cell performance*

Abstract

The performance of bulk-heterojunction solar cells based on a phase-separated mixture of donor and acceptor materials is known to be critically dependent on the morphology of the active layer. As shown in the previous chapter for the two materials used in this study, viz. 1-(3-methoxy-carbonyl)propyl-1-phenyl-[6,6]-methanofullerene (PCBM) and poly[2-methoxy-5-(3′,7′-dimethyloctyloxy)-1,4-phenylene vinylene] (MDMO-PPV), phase separation is not observed up to 50 weight-percentages (wt.-%) PCBM. Nanoscale phase separation throughout the film sets in for concentrations of more than 67 wt.-% PCBM, to give domains of rather pure PCBM in a homogenous matrix of 50:50 wt.-% MDMO-PPV:PCBM. Here these results are related to the performance of the corresponding solar cells. Electrical characterization, under illumination and in the dark, of the photovoltaic devices revealed a strong increase of the power conversion efficiency when the phase-separated network develops, with a sharp increase of the photocurrent and fill factor between 50 and 67 wt.-% PCBM. As the phase separation sets in, enhanced electron transport and a reduction of bimolecular charge recombination provide the conditions for improved performance. The results are interpreted in terms of a model that proposes a hierarchical build up of two cooperative interpenetrating networks at different length scales.

*Part of this work has been published: (a) J.K.J. van Duren, X. Yang, J. Loos, C.W.T. Bulle-Lieuwma, A.B. Sieval, J.C. Hummelen, R.A.J. Janssen, *Adv. Funct. Mater.* **2004**, *in press*; (b) J.K.J. van Duren, X. Yang, J. Loos, C.W.T. Bulle-Lieuwma, A.B. Sieval, J.C. Hummelen, R.A.J. Janssen, *Proceedings of SPIE Vol. 5215 Organic Photovoltaics IV*, (Ed: Z.H. Kafafi), SPIE, Bellingham WA, **2004**, *in press.*

5.1 Introduction

Although some useful insights on the interplay between morphology and bulk-heterojunction solar cell performance have been obtained,[1-9] and examples can be found where devices have been investigated with varying composition,[9-14] a comprehensive understanding is lacking and so far no systematic study has been performed in which morphology and performance have been studied in detail for polymer:fullerene blends. On the other hand, detailed studies on the relation between morphology and performance have been described for photoactive layers based on donor and acceptor polymer blends.[15,16] In this chapter the performance of solar cells based on MDMO-PPV as a donor and PCBM as an acceptor (Figure 5.1) is considered and its relation with morphology. Since the breakthrough discovery by the Linz group that solar cells with a power conversion efficiency of 2.5% under AM1.5 conditions can be obtained by using chlorobenzene as a solvent for spin coating,[1] this combination of materials has become subject of detailed studies. In general the performance of donor-acceptor bulk-heterojunction solar cells relies on an intricate balance between light absorption, charge generation, transport and collection of charges. In these cells, the polymer absorbs most of the light, because C_{60} derivatives such as PCBM have an almost negligible absorption coefficient in the visible region. It is therefore somewhat surprising that the most efficient solar cells based on MDMO-PPV and PCBM require a high content (80 wt.-%) of the latter.[1] This point became even more startling when it turned out recently that the charge-carrier mobility for electrons in pure PCBM is more than three orders of magnitude larger than that for the holes in pure MDMO-PPV.[17,18] This poses an intriguing and fundamental question to the future design of more efficient plastic solar cells: Why do the cells require 80 wt.-% of a material that hardly contributes to light absorption and more efficiently transports charges? Intuitively one would reason that increasing the concentration of MDMO-PPV would be beneficial, for absorption and the number of hole-transporting percolation pathways, but apparently it is not. As outlined above, it has been recognized that morphology and molecular organization on the nanometer scale is a key issue in this respect.

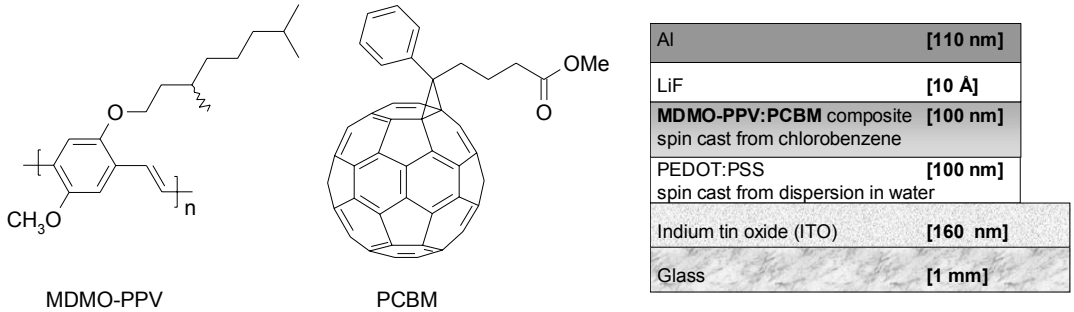

Figure 5.1 *Molecular structures of materials and device configuration used.*

To obtain a deeper insight in the relation between morphology and performance of polymer:fullerene bulk-heterojunction solar cells, both have to be characterized. The same, as for these composite photovoltaic diodes,[19] holds for composite light-emitting diodes.[20-24] In the

previous chapter the morphological characterization has been described in detail. In this chapter a comprehensive study is presented on solar cells made with varying weight percentages of PCBM in MDMO-PPV in the active layer. These films have been incorporated into devices with an improved device configuration (Figure 5.1) where both ITO/PEDOT:PSS[25,26] and LiF/Al[26-28] electrodes are employed. These devices have been fully characterized in the dark, under illumination, and for their monochromatic spectral response. By combining the morphological and electro-optical characterization, a model is proposed that rationalizes some of the intriguing issues described above.

5.2 Dark current density

5.2.1 Rectifying behavior

Percolation pathways from bottom to top electrode for both *p*- and *n*-type semiconductors in thin-film bulk-heterojunction diodes result in an increased conductivity compared to bilayer or stratified structures. In accordance, the current in reverse bias increases with increasing wt.-% PCBM from typically 10^{-3}-10^{-2} mA/cm^2 at –2 V (reverse bias) for 0-40 wt.-% to 0.1 mA/cm^2 for 60-90 wt.-% (Figure 5.2a) with a clear transition at the concentration where phase separation starts to set in (at 50-75 wt.-% PCBM). An additional step from 0.1 mA/cm^2 for 60-90 wt.-% to 1 mA/cm^2 for 95-100 wt.-% PCBM can be observed. This last increase is mainly attributed to shunting due to a decrease in film quality for these highly phase separated films.

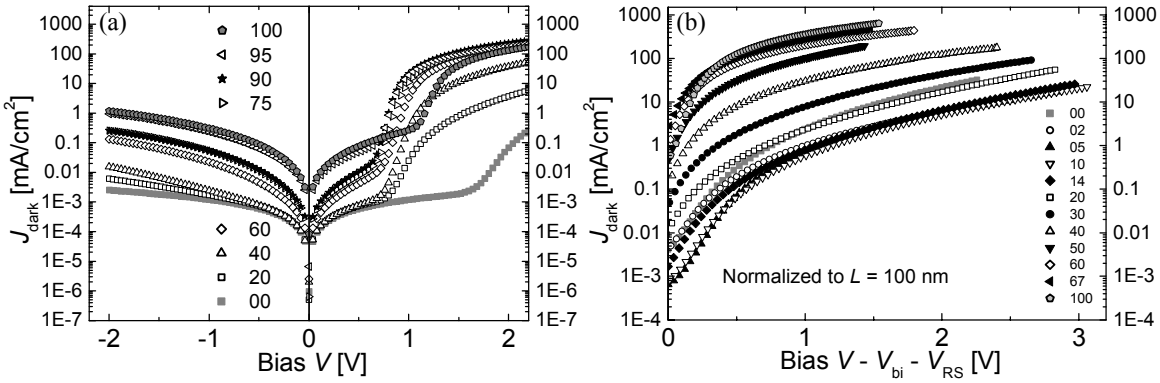

Figure 5.2 (a) *Uncorrected dark current densities (J_{dark}) for some composite devices with varying wt.-% PCBM from –2 V to +2 V.* **(b)** *Some corrected dark current densities (J_{dark}), normalized to L = 100 nm, using the compensation voltage V_0 as the built-in voltage V_{bi} and the voltage drop over the contacts $V_{RS} = I \times R_S$ with R_S = 25 Ω.*

The rectification ratio RR (at +/- 2V) of these devices starts at 10^2 for pure MDMO-PPV, goes through a maximum of 4×10^3 at 40 wt.-% PCBM, subsequently more or less levels at 10^3 until 90 wt.-% PCBM, after which it rapidly drops to 10^2 for pure PCBM. The rectifying behavior of these photodiodes with a composition above 10 wt.-% PCBM is determined mainly by the leakage current and the charge-carrier mobility of the photoactive film, strongly influencing the current in reverse and

forward bias, respectively. Both the leakage current and the mobility of the majority carrier (see below) increase when adding more fullerenes, resulting in a maximum of RR with varying composition. Below 10 wt.-% PCBM, RR is also affected by the large built-in voltage V_{bi} resulting in a low current at +2 V.

5.2.2 Space-charge-limited currents

Previously it has been shown that the dark current in pure MDMO-PPV and PCBM is space-charge limited under forward bias, when the materials are sandwiched between Ohmic PEDOT:PSS[25,26] and LiF/Al[26-28] contacts, as used in this study. For these device configurations, the dark current in pure MDMO-PPV is bipolar with the hole as the majority carrier,[29] whereas for pure PCBM the dark current is unipolar and consists of only electrons.[17,30] Because the mobility of the holes in pure MDMO-PPV[18,31] is 4000 times less than the electron mobility in pure PCBM,[17] it is of interest to study the *J-V* characteristics in the dark and see whether it is possible to relate the changes in the dark current with varying composition to the formation of a fullerene electron-transporting network and to possibly identify a percolation threshold. The morphology studies described in the previous chapter showed no stratification or related structures that could significantly influence the dark current for our composites. Therefore, it can be expected that the dark current in all these composite devices will be SCLC, where below the percolation threshold (for electrons) dark charge-recombination processes might differ considerably of those above the percolation threshold.

The measured dark currents are shown in Figure 5.2. On the horizontal axis of Figure 5.2b the applied voltage is shown, corrected for the built-in voltage V_{bi} (which was taken as the compensation voltage V_0[32-35]) and the voltage drop (V_{RS}) over the contacts.[36] Because space-charge-limited current (SCLC) strongly depends on film thickness ($J_{SCLC} \propto L^{-3}$), the values of J_{dark} in Figure 5.2b have been corrected for the small variations in film thickness (normalized at L = 100 nm).[37] At values of V-V_{bi}-$V_{RS} > 1$, J_{dark} scales approximately with $(V\text{-}V_{bi}\text{-}V_{RS})^2$ as expected for SCLC behavior. Figure 5.2b shows that from 2 wt.-% PCBM the dark current drops below that of the hole-governed device of MDMO-PPV and becomes minimal at 2-14 wt.-% PCBM. Subsequently, the dark current strongly increases, where it exceeds the hole-governed current from pure MDMO-PPV for 30 wt.-% PCBM, and saturates at approximately 67 wt.-% PCBM. With increasing fullerene concentration the electron transport starts to dominate the dark current in these devices. Exceeding the current from pure MDMO-PPV for 30 wt.-% PCBM could be related to the percolation threshold of 25 wt.-% PCBM. The saturation behavior at 67 wt.-% seems closely related to the transition from one to two phases as observed with AFM and TEM and coincides with the composition where several other electro-optical characteristics show a transition (see section 5.3.7 and 5.4.1).

Polymer/fullerene composites studied in literature[38-42] showed charge transport to change from hole-only, via double-carrier, to electron-only with increasing fullerene concentration, in agreement with

our findings.[43] Even when replacing LiF/Al for the electron-blocking-contact Au, it is found that in pure PCBM[44] the current is still governed by the electron. Comparison of the latter with the *J-V* characteristics of the 80 wt.-% composite with an Au top electrode suggests the same for this composite. Finally, it should be noted that where the forward-bias dark current injected from the electrodes will be governed by the majority charge-carrier, the relevant photocurrent (below the open-circuit voltage, reversed field direction) collected at the electrodes will be determined by the minority charge-carrier.

5.3 Device performance under illumination

5.3.1 Introduction on photoconduction

In contrast to the well-established theory of photoconduction for inorganic homojunctions and (bilayer) heterojunctions, the theory of photoconduction for (organic composite) bulk-heterojunctions is not yet established. In first-order approximation, these organic solar cells consist of an insulator sandwiched between two blocking contacts. Therefore, a simple physical model describing the double extraction of uniformly generated electron-hole pairs from insulators with blocking contacts will be discussed in this section and in the following sections related to the experimental results.

The model deals with an insulator sandwiched between two transparent, blocking contacts[45] in which uniformly absorbed light enters normal to one face.[46] The lateral dimensions of the insulating layer are large compared to its film thickness making the problem one dimensional. Diffusion current superimposed over drift current is neglected and the mobility μ is assumed to be independent of electric field E and charge density ρ. Additionally, all physical parameters are constant throughout the layer and space charge effects can be neglected. Furthermore, in the dark the bands are assumed to be "rigid". Good agreement between the theory based on this model with measurements on micrometer-thick lead oxide vidicons is obtained.[46] It should be noted that this model is an oversimplification of the polymer:fullerene bulk-heterojunction solar cell.[47]

The model will be exemplified by the specific case in which the mean carrier drift length of the electron $w_e = \mu_e E \tau_e$ with μ_e the electron drift mobility, E the electric field, and τ_e the lifetime before deep trapping (as a result of e.g. imperfections), is smaller than the layer thickness l. The mean carrier drift length of the hole w_h ($=\mu_h E \tau_h$ with μ_h the hole drift mobility, and τ_h the lifetime before deep trapping) is taken larger than w_e. This way trapped charge will accumulate in the layer and τ_e and τ_h are governed by recombination (instead of imperfections).

For this specific case with $w_e < w_h$, the net trapped charge is negative and the electron energy-band bending in the steady state is such, that close to the positive contact (e.g. LiF/Al) the electric field E ($= \partial V/\partial x$) is increased enhancing the extraction of electrons, whereas close to the negative contact (e.g. ITO/PEDOT:PSS) the electric field E is decreased, diminishing the extraction of holes

(Figure 5.3). Based on the dominant electronic processes, the photoactive layer can be divided in three regions. In the two regions close to the contacts (regions 1 and 3, see Figure 5.3), recombination of photogenerated carriers is neglected. All electrons (holes) generated in region 1 (region 3) are extracted to the positive (negative) contact whereas all holes (electrons) drift into region 2. In region 2 the recombination rate is taken equal to the generation rate. The electric field is assumed to be constant in each region. The resulting electron and hole current density J_e and J_h respectively, are shown in Figure 5.3.

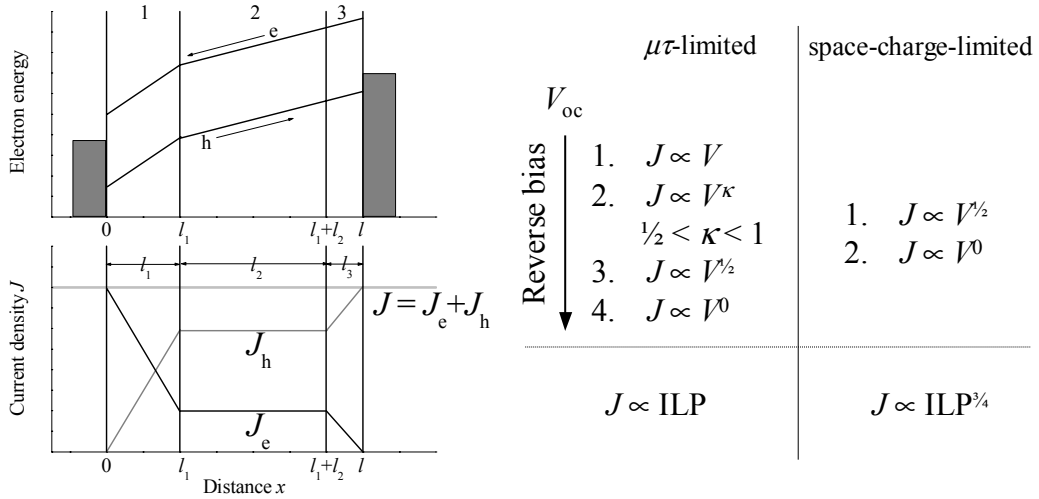

Figure 5.3 *Left: Energy-band diagram and current density distribution for the $\mu\tau$-limited case. The total current density (J) is the sum of the current density of the electron (J_e) and the hole (J_h). Right: The number of regimes and their dependencies on the applied voltage (V) as predicted for low incident light power (ILP), the $\mu\tau$-limited case, and high ILP, the space-charge-limited case, respectively.*

The current density J as a function of the applied bias V can be solved analytically for the considerations above.[46] Depending on the values of w_e, w_h, and l the thickness of region 1 (l_1), region 2 (l_2), and region 3 (l_3) varies, where for $w_h < w_e$ the band bending will be upward instead of downward and the net trapped charge will be positive.

The model predicts the existence of four distinct regimes. A low voltage or linear regime where $J \propto V^{\kappa}$ with $\kappa = 1$, an intermediate or transition regime with $\frac{1}{2} < \kappa < 1$, a high voltage or square-root regime with $\kappa = \frac{1}{2}$, and a very high voltage or saturation regime with $\kappa = 0$. As soon as the smallest mean carrier drift length (w_e) exceeds the thickness of the photoconducting layer the photocurrent becomes independent of the applied bias, and the saturation regime ($\kappa = 0$) sets in. For all regimes, the photocurrent J depends linearly on the incident light power (ILP), $J \propto$ ILP.

The band bending in region 1 (see Figure 5.3) is caused by space charge. This space charge sets an upper limit to the photocurrent that can be extracted, the space-charge-limited current. As long as the photocurrent is below this upper limit, the previously described model can be used (space

charge effects can be neglected). In this model the photocurrent is not limited by space charge, but the mean carrier drift length of the carrier w_c. This is called the $\mu\tau$-limited case or space-charge-free case.

For the space-charge-limited case, two distinct regimes can be recognized, instead of four regimes for the $\mu\tau$-limited case. A square-root regime where $J \propto V^{\kappa}$ with κ = ½, and a saturation regime with κ = 0. For both regimes, the exponent α in $J \propto \mathrm{ILP}^{\alpha}$ equals ¾, instead of α = 1 for the space-charge-free case. With increasing ILP, a transition from space-charge-free (α = 1) to space-charge-limited (α = ¾) behavior can be expected. Furthermore, one would expect that the space-charge-limited regime sets in at lower current densities for higher bandgap materials where trapping plays a larger role.

In the following, some of the experimental results of the polymer:fullerene bulk-heterojunction solar cells will be compared to this model.

5.3.2 Comparison of device performance under illumination

For each composition several devices from different preparation batches were made and subsequently measured, both in the dark (see section 5.2) and under illumination. Typical *J*-*V* curves recorded under illumination with filtered white light from a tungsten-halogen lamp[48] are shown in Figure 5.4 for different compositions. Figure 5.5 shows the dependence of the short-circuit current density J_{sc}, open-circuit voltage V_{oc}, fill factor FF, and power conversion efficiency η_{pc} as function of the wt.-% of PCBM in the blend.[49] Gathering the large amount of photovoltaic measurements on sandwich cell geometries in literature, both for pure PPV derivatives[33,34,50-52] and PPV/fullerene composites[1,9-14,28,32,52-56] should result in a similar picture. Unfortunately, comparison in detail is often hampered by a variety in contacting electrodes, processing conditions,[57] film thickness, material properties,[58] light source used for illumination, and electro-optical parameters reported. On the contrary, the set of data presented here does allow a detailed comparison.

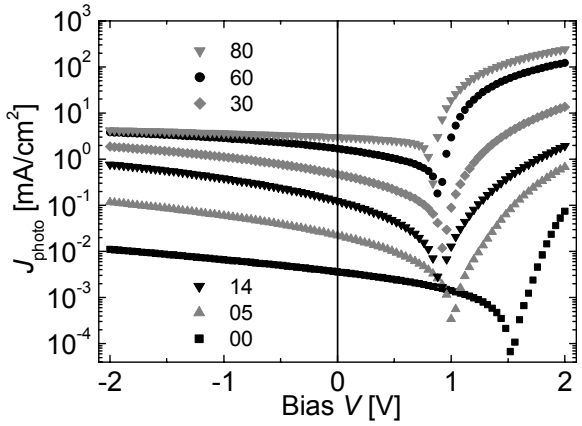

Figure 5.4 *Some photocurrents for several wt.-% PCBM with MDMO-PPV.*

5.3.3 Short-circuit current density

The plot of J_{sc} versus composition (Figure 5.5a) reveals that J_{sc} increases gradually with increasing fullerene concentration until it reaches a maximum at 75-80 wt.-%, followed by a rapid decrease.[59] If the PCBM phase would relate to a random 3D network, the completion of the PCBM electron-transporting phase would have been expected at the theoretical percolation threshold of ~17 volume percent (vol.-%),[60] corresponding to ~25 wt.-% PCBM.[61] However, Figure 5.5a does not reveal a well-defined percolation threshold for J_{sc}.[62] Instead, the steepest increase in J_{sc} is found in the range of 50-67 wt.-% PCBM,[63] nicely corresponding to the onset of phase separation in the blend as inferred from the AFM and TEM experiments. J_{sc} increases with the further development of the phase separation up to 80 wt.-% PCBM. Beyond 80 wt.-%, the decreasing optical density of the film due to the low absorption cross-section of PCBM compared to MDMO-PPV, eventually results in a drop of J_{sc}.[64]

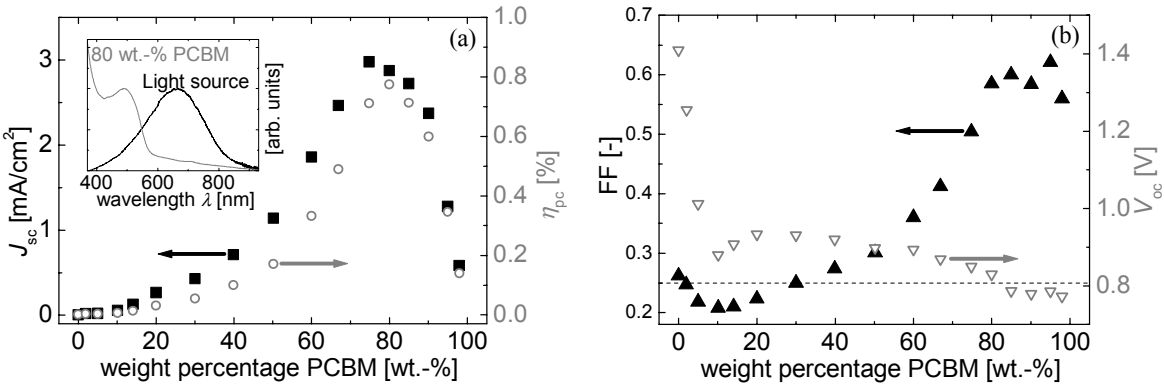

Figure 5.5 (a) *Short-circuit current density (J_{sc}), power conversion efficiency (η_{pc}),* **(b)** *fill factor (FF), and open-circuit voltage (V_{oc}) with varying composition. Inset in (a) shows spectral overlap between light source used and an 80 wt.-% PCBM film. The dotted line in (b) represents FF = 0.25.*

5.3.4 Open-circuit voltage

The origin of V_{oc} in these devices is still under some debate.[9,32,65] Recent studies by Michailetchi *et al.* show that in case of Ohmic contacts, such as used in this study, the negative and positive electrodes match the LUMO of the acceptor and the HOMO of the donor, respectively, which govern the V_{oc}.[66] Additionally, the band bending at these Ohmic contacts reduces V_{oc}.

The concentration dependence of V_{oc} is rather different from that of J_{sc} (Figure 5.5). The V_{oc} is found to be much less dependent on concentration. Furthermore, no significant effect of phase separation on V_{oc} can be observed. This smaller influence of the morphology on V_{oc} seems to be consistent with the proposition made by Michailetchi *et al*. where the origin of V_{oc} is not related to morphology, but merely to the electronic levels.[66] Already at low concentrations of PCBM in

MDMO-PPV, V_{oc} is reduced from the value of 1.4 V[49] for pure MDMO-PPV, to an almost constant value in the range of 0.78 to 0.95 V for more than 10 wt.-% PCBM, in agreement with previous work.[9,12,14]. Finally, a local maximum in V_{oc} can be observed at ~25 wt.-% PCBM, equal to the theoretical percolation threshold (17 vol.-%) for the PCBM electron-transporting network.

5.3.5 Fill factor and power conversion efficiency

The evolution of the fill factor (FF) as function of the PCBM concentration resembles that of J_{sc} (Figure 5.5). The overall rise of FF with increasing wt.-% PCBM indicates a smaller series resistance,[67] and is attributed to more efficient charge transport.[68] In accordance, charge transport has been found to strongly increase in this concentration range, as shown in section 5.2. The strongest increase in FF is observed between 60 and 75 wt.-%, again corresponding to the range where the phase separation develops. The fill factor reaches its maximum of FF = 0.6 at approximately 80 wt.-% PCBM where it saturates. Below 50 wt.-%, the FF is extremely low (0.2-0.3), showing that the series resistance[67] governs the *J-V* curves, as found for pure MDMO-PPV where both the electrons and holes have a rather low mobility. Between 2 and 30 wt.-% PCBM the FF is actually less than 0.25, which is the theoretical minimum in a simple single-semiconductor photovoltaic model with a large limiting series resistance.[69] It is tempting to relate this phenomenon to an incomplete fullerene electron-transporting network. Note that charge transport depends on both percolation and mobility of each charge carrier. In contrast to pure MDMO-PPV, photogenerated electrons in these blends are mainly localized on PCBM molecules. When the fullerene network is incomplete as a result of a low amount of fullerenes, electron transport is hindered and likely to be strongly field dependent. As a result, the recombination of photogenerated charges will be extremely large and J_{sc} low.[34] Going from V_{oc} to 0 V (J_{sc}), transport will be enhanced by the increasing electric field (which is zero at V_{oc}), resulting in a bending of the *J-V* curve in the wrong direction (FF < 0.25).[70] The fill factor reaches 0.25 at 30 wt.-% PCBM and starts to rise above its theoretical limit of 0.25 with increasing wt.-%, just above the theoretical percolation threshold of 25 wt.-%, where the network should be completed.

The change in power conversion efficiency η_{pc} (Figure 5.5a) with varying composition is of course a straightforward combination of the changes in J_{sc}, V_{oc} and FF, and confirms that the cells reach a maximum performance at 80 wt.-% PCBM.[1] It is important to note that the absolute values for η_{pc} in Figure 5.5a, are not related to standard solar light (AM1.5) conditions because a filtered tungsten-halogen lamp was used instead of a calibrated solar simulator.[71] Based on the maximum IPCE, V_{oc}, and FF, however it can be concluded that these devices have a similar performance as those published by Shaheen *et al.*[1]

5.3.6 Photocurrents with varying bias

Here, the photocurrent (J_{photo}) is the current under illumination and the *net* photocurrent ($J_{net\ photo}$) equals the current under illumination subtracted with the dark current. When looking in the region below V_{oc}, the *net* photocurrent is used instead of the regular photocurrent to avoid misinterpretation originating from variations in leakage current with composition. In this region it can be observed (Figure 5.6) that above 67 wt.-% PCBM the dependence of $J_{net\ photo}$ on the applied reverse bias (electric field) decreases with increasing wt.-% PCBM, resulting in more horizontal *J-V* curves. The reason for this might be that the (*net*) photocurrent suffers from charge recombination below 67 wt.-% PCBM, and therefore strongly depends on the electric field in the device,[14,34,51,72] whereas this recombination limitation is less pronounced above 67 wt.-% PCBM. This change in electric field dependence occurs at more or less the same composition where a steep increase in J_{sc} and FF could be observed and corresponds to the transition of one to two phases as inferred from TM-AFM and TEM. Phase separation and charge recombination therefore seem to be related.

For a meaningful comparison of experimental *J-V* curves with the model as described in section 5.3.1 the bias needs to be varied over several orders of magnitude, preferably in a broad range of incident light power. Additionally, a large number of data points are required between V_{oc} and V_{oc} - 0.1 V. Unfortunately, the experiments performed do not allow such a detailed comparison. What can be observed, however, is the start of the saturation regime ($\kappa = 0$, J = constant) for 90 and 95 wt.-% PCBM within the bias range measured.

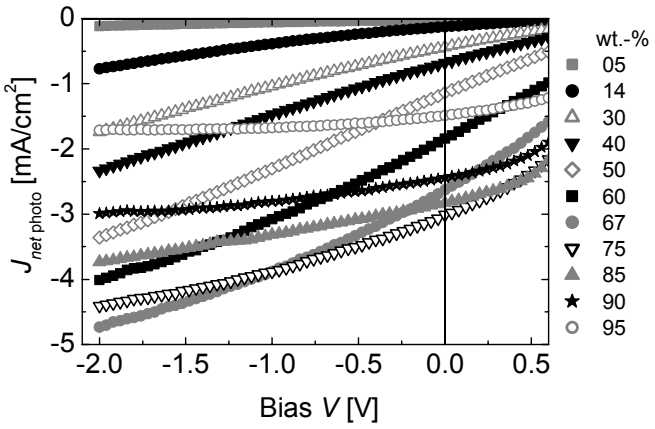

Figure 5.6 *Net photocurrent densities ($J_{net\ photo}$) for varying wt.-% PCBM in MDMO-PPV.*

5.3.7 Discussion

A steep increase in J_{sc} and FF, accompanied by a change in the electric field dependence of the *net* photocurrent below V_{oc} can be observed at ~67 wt.-% PCBM, the composition where phase separation starts to set in. These results suggest a decrease in charge recombination with the

development of phase separation. Recent results from Savenije *et al*. using electrodeless flash-photolysis time-resolved microwave conductivity (FP-TRMC),[73,74] and from Blom *et al.* using mobility measurements,[75] showed a clear transition in the product, $\phi\Sigma\mu$ and the electron mobility, respectively, at 50-75 wt.-% PCBM in agreement with our findings.

5.4 Incident light power (ILP) dependence

To gain a further insight in the operation of the devices, J_{sc}, V_{oc}, and FF have been studied as function of incident light power ILP (Figure 5.7 and 5.8). All compositions show similar behavior. J_{sc}, V_{oc}, and FF increase with increasing incident light power (ILP) over the whole measured ILP-range (5 orders of magnitude up to 150 mW/cm^2).[48] Where V_{oc} and FF clearly show a sharp onset at a certain ILP and subsequently start to saturate and slightly decrease, respectively, J_{sc} increases gradually over the whole measured ILP-range.

5.4.1 Short-circuit current density with varying incident light power

The short-circuit current density J_{sc} was found to increase with incident light power (ILP) according to a power-law behavior $J_{sc} \propto \text{ILP}^{\alpha}$ (Figure 5.7a). For compositions in the range of 67-90 wt.-% PCBM and pure polymer, the power-law exponent α equals 0.94 (Figure 5.7b),[76] consistent with previous results.[14,32,34,50,51,77,78] The model discussed in section 5.3.1 relates the exponent α to the amount of space charge present, and is either ¾ (space-charge-limited) or 1 (space-charge-free). Comparison of the experimental results with this model suggests that the photocurrent might be slightly influenced by space charge. This space charge finds its origin in unbalanced mean carrier drift lengths for electrons and holes with a part of the layer suffering from charge recombination.[46] Recent work by others[38,77] also suggests that the slightly sub-linear dependence ($\alpha < 1.0$) is related to some

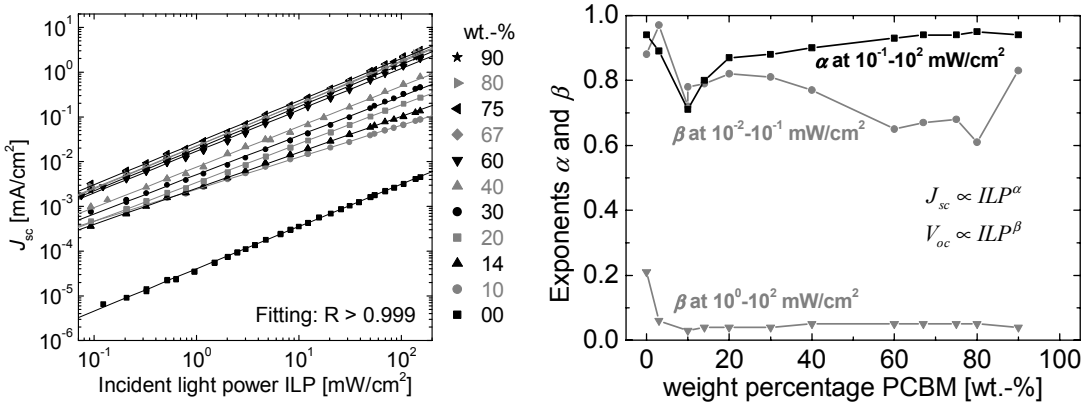

Figure 5.7 *Left: Experimental short-circuit current density J_{sc} (symbols) and linear fit (solid lines) versus incident light power (ILP) for composite solar cells with the wt.-% PCBM in MDMO-PPV given at the right of the graph. Right: The exponents α in $J_{sc} \propto ILP^{\alpha}$ and β in $V_{oc} \propto ILP^{\beta}$ versus the wt.-% PCBM.*

bimolecular recombination of positive and negative photogenerated charges. For blends with less than 67 wt.-% PCBM, α gradually decreases to 0.71 at 10 wt.-%. This reduction is attributed to an increased bimolecular recombination. Because phase separation is not observed below 67 wt.-%, charge recombination is stronger in the homogenous MDMO-PPV:PCBM phase.

5.4.2 Open-circuit voltage with varying incident light power

Most samples show an onset of V_{oc} at ILP ≈ 10^{-2} mW/cm^2, where the sharp increase in V_{oc} with ILP is followed by a less steep increase above ~1 mW/cm^2 (Figure 5.8a, for clarity only a few curves are shown). At high ILP (Figure 5.8a), the V_{oc} was found to increase with ILP according to a power-law behavior $V_{oc} \propto \text{ILP}^{\beta}$ with $\beta \approx 0.05$ (Figure 5.7b). The values for β at low ILP vary from 0.6 to almost 1.0 (Figure 5.7b). The onset of V_{oc} with ILP is strongly related to the film thickness. For films with 80 wt.-% PCBM the onset at 10^{-2} mW/cm^2 decreases to 10^{-4} mW/cm^2 when the thickness of the film is increased from 110 to 170 nm. Compared to the blends, the onset of V_{oc} for devices prepared using (almost) pure materials (0, 3, and 90 wt.-%) occurs at much higher light intensities (10^{-1}-1 mW/cm^2). The onset of V_{oc} is determined by the minimum amount of photogenerated charges, present in the bulk, necessary to oppose the applied electric field. Therefore, the dependence on film thickness (optical density) and composition (*i.e.* charge-generation efficiency) seem straightforward. For all devices, a voltage can be recognized at which the current density is independent of the incident light power (ILP) with a finite, nonzero value, equal to the compensation voltage V_0,[32-34] although less pronounced for concentrations of 30 wt.-% PCBM and higher. Frohne *et al*. ascribed this to a light-induced change in injection behavior.[32]

5.4.3 Fill factor with varying incident light power

Just as V_{oc}, the fill factor also shows an onset at ILP ≈ 10^{-2} mW/cm^2 but then goes through a

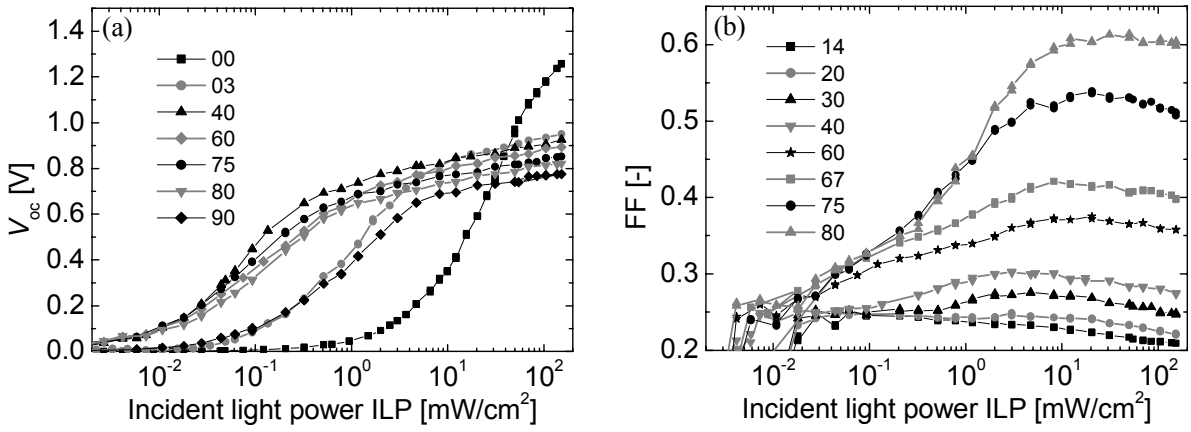

Figure 5.8 *V_{oc} (a) and FF (b) with varying incident light power (ILP) for several compositions with the numbers in the legends corresponding to the wt.-% PCBM in MDMO-PPV.*

maximum value, followed by a small decrease (Figure 5.8b). With increasing wt.-% PCBM the maximum of FF is observed for higher ILP. Although FF depends on J_{sc}, V_{oc}, leakage (parallel resistance) and series resistance,[68] the shift of the maximum to higher ILP with increasing wt.-% seems to be related to the simultaneously improving charge transport.

5.5 Wavelength dependence or incident photon to current conversion efficiency (IPCE)

The incident photon to current conversion efficiency (IPCE, Figure 5.9) for a range of compositions reveals that light absorbed by either MDMO-PPV or PCBM contributes to the photocurrent. This is in accordance with recent photophysical data, showing that both excitation of the polymer and the fullerene result in charge separation.[3,74] In the graphs, the contribution of PCBM to the photocurrent can be easily recognized above 580 nm, with a highly characteristic peak of the lowest singlet-excited state of PCBM at 705 nm,[79] while the MDMO-PPV absorption is evident from the peak at 500 nm. Hence, there is no doubt that for these composite devices the contribution of both photoinduced electron and hole transfer play a significant role.

The absolute value of IPCE at the absorption maximum of MDMO-PPV follows the same trend as J_{sc} (Figure 5.5a) with varying composition. Additionally, a blue shift in this maximum with increasing wt.-% PCBM can be observed, just as for the absorption (see previous chapter).

Remarkably, the characteristic signatures of PCBM in the IPCE spectra below 400 nm and at 705 nm, become more pronounced above 60 wt.-%. However, unraveling the quantitative contributions of MDMO-PPV and PCBM to the IPCE spectra needs further investigations where the influence of different charge-transfer efficiencies, wave-guiding effects, space-charge distribution, and a possible charge-generation depth profile have to be taken into consideration.

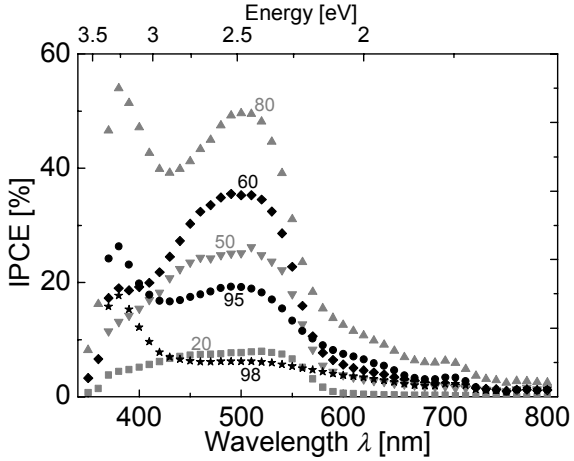

Figure 5.9 *Incident photon to current conversion efficiency (IPCE) spectra for some composite solar cells with varying wt.-% PCBM in MDMO-PPV.*

5.6 Conclusions

Electrical characterization of the composite photovoltaic devices, both in the dark and under illumination (J_{sc}, V_{oc}, and FF), reveals that in the range of 50-75 wt.-% PCBM, where phase separation sets in, a dramatic increase in J_{sc} and FF, accompanied by a change in the electric field dependence of the *net* photocurrent below V_{oc}, occurs. In accordance, the exponent α in $J_{sc} \propto \mathrm{ILP}^{\alpha}$ and the dark currents in forward bias start to saturate above 67 wt.-% PCBM, with a clear increase in the shunting as observed in reverse bias. As a consequence of the increased charge transport and collection efficiency, less recombination occurs with increasing fullerene concentration. The open-circuit voltage V_{oc} is much less dependent on the concentration as it seems to be related to the nature of the components and less to the morphology.

The results described above point to an intricate relation between the morphology and device performance. The virtually homogeneous blend that is present up to 50 wt.-% PCBM represents without much doubt, a perfect morphology for very efficient charge generation. The PL lifetime experiments (previous chapter) have shown that virtually every excitation created in this phase on either MDMO-PPV or PCBM is quenched and, hence, provides charges. The fact that, more (80 wt.-%) PCBM is necessary to have the optimum performance of the solar cell, must therefore be due to the fact that not all photogenerated charges can be collected at the electrodes and recombine, either geminately or non-geminately. At 67 wt.-% PCBM, nanoscale phase separation sets in, which apparently enhances transport and reduces recombination. One could envision that a negative charge injected into a pure PCBM phase delocalizes and does not easily recombine with the hole left in the polymer matrix. The fact that 80 wt.-% is the optimum, can be rationalized by considering that also the pure PCBM phase must build a percolating network with pathways large enough in lateral size to facilitate escape from the interface, which it can only do starting from 67 wt.-%. In that sense, one could think of a hierarchical build up of two cooperative interpenetrating networks on different length scales. The first one is a percolating network of molecularly dispersed fullerenes (or tiny clusters thereof) in the 50 wt.-% PCBM homogenous matrix, and the second one is a percolating network of a dimension that is one order of magnitude larger and consists of pure PCBM domains. Such a fractal-like combination of percolating PCBM networks, bears similarities to the vascular system consisting of a capillary system and arterioles.

The combination of MDMO-PPV, PCBM, chlorobenzene, substrate, and casting conditions results in an optimum of 80 wt.-% PCBM. Of course, for other materials and processing conditions the morphology and optimum might be completely different, but the necessity of both continuous percolating pathways and a minimum domain size to facilitate escape from the interface and overcome excessive recombination losses will certainly prove to be general for other systems as well. This systematic study provides the opportunity to speed up optimization work of bulk-heterojunction

solar cell performance for a combination of two new materials by extraction of morphological issues from the device characteristics.

5.7 Experimental section

Materials. The materials used were poly[2-methoxy-5-(3′,7′-dimethyloctyloxy)-1,4-phenylene vinylene] (MDMO-PPV) synthesized via the Gilch-route[80], 1-(3-methoxycarbonyl)propyl-1-phenyl-[6,6]-methanofullerene (PCBM)[81], polyethylenedioxythiophene:polystyrenesulfonate[82] (PEDOT:PSS) from Bayer AG (Baytron P VPAI 4083), LiF from Aldrich, and Al from Engelhard-Clal. For molecular structures, see Figure 5.1. Glass plates covered with 160 nm patterned ITO resulting in 4 different device areas (0.1, 0.15, 0.33, 1.0 cm^2) were used for device preparation.[83]

Device preparation. The ITO covered glass substrates were first cleaned by ultrasonic treatment in acetone, rubbing with soap, rinsing with de-mineralized water, refluxing with iso-propanol, and finally 20 minutes UV ozone treatment. Subsequently, a ~100 nm thick layer of PEDOT:PSS was spin coated from an aqueous dispersion under ambient conditions on the cleaned substrates and the layer was dried by annealing the substrate for 1 minute at 180 °C and subsequently cooled for 1 minute at 25 °C.[84,85] Then the 80-130 nm thick composite layer of MDMO-PPV and PCBM (thickness variation between compositions) was spin coated from a chlorobenzene solution on top of the PEDOT:PSS layer and the sample was transferred to an N_2 atmosphere glove box. The organic solutions are stirred vigorously overnight while keeping them in the dark. Film thickness for the different composite samples was controlled by reducing the concentration of the composite solution from 5.4 to 0.5 mg MDMO-PPV/ml chlorobenzene with increasing wt.-% PCBM. It should be noted that the variation in film thickness between substrates per composition is below 4 nm, whereas the film thickness varies randomly going from 0 wt.-% to 100 wt.-% PCBM. Film thickness measurements were performed with a Tencor P10 surface profiler. All polymer layers were spin cast via a two-step procedure employing a home-made chuck, which requires no vacuum, on a Chemat Technology spin coater model KW-4A placed in a laminar flowbox. First 7 seconds at 500 rpm followed by 35 seconds at 1500 rpm. Finally, ~10 Å LiF and subsequently ~110 nm aluminum layers were deposited by thermal evaporation in a vacuum chamber (5×10^{-6} mbar, 1 ppm O_2 and < 1 ppm H_2O). The samples were rotated at ~1 Hz during deposition to guarantee homogeneous films. All samples are stored in the dark in an N_2 atmosphere glove box.

Device measurements All measurements were performed in a N_2 atmosphere at room temperature. In forward bias the ITO electrode was positively biased. The devices were illuminated at the transparent ITO electrode. *J-V* characteristics were measured with a computer-controlled Keithley 2400 Source Meter, sweeping in steps of 0.04 V with a delay of 0.10 sec, in the dark or under ~180 mW/cm^2 illumination from a tungsten-halogen lamp filtered by a Schott KG1 and GG385 filter resulting in a spectral range of 400-900 nm with its maximum at ~650 nm[48] as determined with a calibrated Avantes AVS-PC2000 fiberoptic spectrometer. Light power is measured with an Ophir Laser Power Meter set at 610 nm. Incident light power dependence measurements were performed using a similar setup where the light power (ILP) is varied over 5 orders of magnitude with a series of metal-coated neutral-density filters (Melles Griot) with a constant optical density for the involved spectral range. Spectrally resolved photocurrents were measured using monochromatic light (~0.03 mW/cm^2), calibrated against a mc-Si solar cell with known spectral response. The stability of the devices was found to be more than sufficient to perform all the above measurements.

5.8 References and notes

1 S.E. Shaheen, C.J. Brabec, N.S. Sariciftci, F. Padinger, T. Fromherz, J.C. Hummelen, *Appl. Phys. Lett*. **2001**, *78*, 841.

2 T. Martens, J. D'Haen, T. Munters, Z. Beelen, L. Goris, J. Manca, M. D'Olieslaeger, D. Vanderzande, L. De Schepper, R. Andriessen, *Synth. Met.* **2003**, *138*, 243.

3 M.M. Wienk, J.M. Kroon, W.J.H. Verhees, J. Knol, J.C. Hummelen, P.A. van Hal, R.A.J. Janssen, *Angew. Chem. Int. Ed*. **2003**, *42*, 3371.

4 (a) W.U. Huynh, J.J. Dittmer, W.C. Libby, G.L. Whiting, A.P. Alivisatos, *Adv. Funct. Mater.* **2003**, *13*, 73; (b) W.U. Huynh, J.J. Dittmer, A.P. Alivisatos, *Science* **2001**, *295*, 2425.

5 W. Feng, Y.L. Xu, W.H. Yi, F. Zhou, X.G. Wang, K. Yoshino, *Chinese Physics* **2003**, *12*, 426.

6 (a) L. Schmidt-Mende, A. Fechtenkötter, K. Müllen, E. Moons, R.H. Friend, J.D. MacKenzie, *Science* **2001**, *293*, 1119; (b) L. Schmidt-Mende, M. Watson, K. Müllen, R.H. Friend, *Mol. Cryst. Liq. Cryst.* **2003**, *396*, 73.

7 (a) J.J. Dittmer, E.A. Marseglia, R.H. Friend, *Adv. Mater.* **2000**, *12*, 1270; (b) J.J. Dittmer, R. Lazzaroni, Ph. Leclère, P. Moretti, M. Granström, K. Petritsch, E.A. Marseglia, R.H. Friend, J.L. Brédas, H. Rost, A.B. Holmes, *Sol. Energy Mater. Sol. Cells* **2000**, *61*, 53.

8 L.S. Roman, M.R. Andersson, T. Yohannes, O. Inganäs, *Adv. Mater.* **1997**, *9*, 1165.

9 J. Liu, Y. Shi, Y. Yang, *Adv. Funct. Mater.* **2001**, *11*, 420.

10 G. Yu, J. Gao, J.C. Hummelen, F. Wudl, A.J. Heeger, *Science* **1995**, *270*, 1789.

11 H. Kim, K. Lee, Y. Park, H. Suh, *J. Korean Phys. Soc.* **2003**, *42*, 183.

12 M.C. Scharber, N.A. Schultz, N.S. Sariciftci, C.J. Brabec, *Phys. Rev. B*, **2003**, *67*, 085202.

13 C.J. Brabec, F. Padinger, V. Dyakonov, J.C. Hummelen, R.A.J. Janssen, N.S. Sariciftci, *Molecular Nanostructures* **1998**, *Meeting date 1997*, 128.

14 J. Gao, F. Hide, H. Wang, *Synth. Met.* **1997**, *84*, 979.

15 A.C. Arias, J.D. MacKenzie, R. Stevenson, J.J.M. Halls, M. Inbasekaran, E.P. Woo, D. Richards, R.H. Friend, *Macromolecules* **2001**, *34*, 6005.

16 H.J. Snaith, A.C. Arias, A.C. Morteani, C. Silva, R.H. Friend, *Nano Lett*. **2002**, *2*, 1353.

17 V.D. Mihailetchi, J.K.J. van Duren, P.W.M. Blom, J.C. Hummelen, R.A.J. Janssen, J.M. Kroon, M.T. Rispens, W.J.H. Verhees, M.M. Wienk, *Adv. Funct. Mater.* **2003**, *13*, 43.

18 It should be noted that mobility measurements on SCL hole-only devices of MDMO-PPV, spin cast from chlorobenzene, gave similar hole mobilities as reported in literature where mostly toluene was used as casting solvent.

19 J. Chappell, D.G. Lidzey, P.C. Jukes, A.M. Higgins, R.L. Thompson, S. O'Connor, I. Grizzi, R. Fletcher, J. O'Brien, M. Geoghegan, R.A.L. Jones, *Nature Mater.* **2003**, *2*, 616.

20 E. Moons, *J. Phys.*: *Condens. Matter* **2002**, *14*, 12235.

21 (a) M.M. Alam, C.J. Tonzola, S.A. Jenekhe, *Macromolecules* **2003**, *36*, 6577; (b) A.P. Kulkarni, S.A. Jenekhe, *Macromolecules* **2003**, *36*, 5258; (c) X. Zhang, D.M. Kale, S.A. Jenekhe, *Macromolecules* **2002**, *35*, 382; (d) X. Zhang, S.A. Jenekhe, *Macromolecules* **2000**, *33*, 2069.

22 N. Corcoran, A.C. Arias, J.S. Kim, J.D. MacKenzie, R.H. Friend, *Appl. Phys. Lett.* **2003**, *82*, 299.

23 H. Hänsel, D.C. Müller, M. Gross, K. Meerholz, G. Krausch, *Macromolecules* **2003**, *36*, 4932.

24 M. Berggren, O. Inganäs, G. Gustafsson, J. Rasmusson, M.R. Andersson, T. Hjertberg, O. Wennerström, *Nature* **1994**, *372*, 444.

25 T.M. Brown, J.S. Kim, R.H. Friend, F. Cacialli, R. Daik, W.J. Feast, *Appl. Phys. Lett.* **1999**, *75*, 1679.

26 (a) M. Fahlman, W.R. Salaneck, *Surf. Sci.* **2002**, *500*, 904; (b) T.M. Brown, F. Cacialli, *J. Pol. Sci. B* **2003**, *41*, 2649.

27 T.M. Brown, R.H. Friend, I.S. Millard, D.J. Lacey, T. Butler, J.H. Burroughes, F. Cacialli, *J. Appl. Phys.* **2003**, *93*, 6159.

28 C.J. Brabec, S.E. Shaheen, C. Winder, N.S. Sariciftci, P. Denk, *Appl. Phys. Lett.* **2002**, *80*, 1288.

29 P.W.M. Blom, M.C.J.M. Vissenberg, *Mater. Sci. Eng. R* **2000**, *27*, 53.

30 The injection barrier for holes from PEDOT:PSS (5.2 eV) into the HOMO of PCBM (6.1 eV) equals 0.9 eV, assuming vacuum level alignment and the absence of both dipole layer formation (as a result of e.g. interfacial chemistry) and strong band bending. Additionally, Brabec *et al.* (Siemens A.G.) showed at the DPI Winterschool on Organic and Polymer Photovoltaics that for PCBM $\mu_e \approx 2000 \times \mu_h$.

31 P.W.M. Blom, M.J.M. de Jong, M.G. van Munster, *Phys Rev B.* **1997**, *55*, R656.

32 H. Frohne, S.E. Shaheen, C.J. Brabec, D.C. Müller, N.S. Sariciftci, K. Meerholz, *ChemPhysChem* **2002**, *3*, 795.

33 G.G. Malliaras, J.R. Salem, P.J. Brock, J.C. Scott, *J. Appl. Phys.* **1998**, *84*, 1583 (and references therein).

34 X. Wei, M. Raikh, Z.V. Vardeny, Y. Yang, D. Moses, *Phys. Rev. B* **1994**, *49*, 17480.

35 $V_0 \approx V_{oc} + 0.2$ V for 0 and 2 wt.-%, whereas $V_0 \approx V_{oc} + 0.05$ V for all other concentrations.

36 For current densities larger than 100 mA/cm^2, the applied voltage should be corrected for the voltage drop (V_{RS}) across the indium tin oxide (ITO) series resistance (R_S), which typically amounts to $R_S = 25\ \Omega$ in our substrates.

37 The film thickness varies randomly with composition between 80-130 nm, with 90% within 85-110 nm.

38 S.A. Choulis, J. Nelson, Y. Kim, D. Poplavskyy, T. Kreouzis, J.R. Durrant, D.D.C. Bradley, *Appl. Phys. Lett.* **2003**, *83*, 3812.

39 R. Pacios, J. Nelson, D.D.C. Bradley, C.J. Brabec, *Appl. Phys. Lett.* **2003**, *83*, 4764.

40 E.J. Meijer, D.M. de Leeuw, S. Setayesh, E. van Veenendaal, B.-H. Huisman, P.W.M. Blom, J.C. Hummelen, U. Scherf, T.M. Klapwijk, *Nature Mater.* **2003**, *2*, 678.

41 W. Geens, Study of the Potential Energy Conversion Efficiency of Organic Solar Cells based on Donor/Acceptor Heterojunctions, Ph. D. thesis **2002**, University of Antwerp/IMEC.

42 I. Balberg, R. Naidis, M.-K. Lee, J. Shinar, L.F. Fonseca, *Appl. Phys. Lett.* **2001**, *79*, 197.

43 It should be noted that, except for Choulis *et al.* and Pacios *et al.*, charge transport in those reported configurations is parallel to the plane of the film, whereas in our system transport is perpendicular to the plane of the film.

44 J.K.J. van Duren, V.D. Mihailetchi, P.W.M. Blom, T. van Woudenbergh, J.C. Hummelen, M.T. Rispens, R.A.J. Janssen, M.M. Wienk, *J. Appl. Phys.* **2003**, *94*, 4477.

45 The contacts are assumed to be blocking in the sense that the injection currents are small compared to the currents as photogenerated in the bulk.

46 A.M. Goodman, A. Rose, *J. Appl. Phys.* **1971**, *42*, 2823.

47 The polymer:fullerene bulk-heterojunction solar cells have reasonable blocking contacts, as can be concluded from the analysis of the dark currents in the previous section. It can be expected that both the electron and hole mobility in the blend will be dependent on the electric field, just as for the pure components. However, this typically holds only for high electric fields and does not have to affect the *J-V* curves at low electric fields. Only one instead of two contacts is transparent. Combined with the strong absorption coefficient of MDMO-PPV the light does not have to be absorbed homogeneously in depth. Additionally, the homogeneity of light absorption depends on the morphology. Even for homogeneously absorbed light, charge generation mainly occurs at the donor-acceptor interface. The homogeneity of charge generation, therefore, will depend on morphology. The same holds for charge recombination.

48 The spectral overlap between the light source and the absorption spectrum of the 80 wt.-% PCBM film is shown in the inset of Figure 5.5a.

49 The standard deviation of the short-circuit current density (J_{sc}) and power conversion efficiency (η_{pc}) is below 10% of the average. The light source has a deviation of 3% in light power. The open-circuit voltage (V_{oc}) has a standard deviation of ~ 1% for every composition, except for the pure MDMO-PPV and 2 wt.-% PCBM devices whose standard deviation for V_{oc} is somewhat larger (~7%). The V_{oc} for these low fullerene concentrations is very sensitive to film thickness and shorts density as a result of the photocurrent and leakage current being of the same order of magnitude. The fill factor (FF) has a standard deviation of ~ 1% for every composition.

50 M.G. Harrison, J. Grüner, G.C.W. Spencer, *Phys. Rev. B* **1997**, *55*, 7831.

51 G. Yu, C. Zhang, A.J. Heeger, *Appl. Phys. Lett.* **1994**, *64*, 1540.

52 J. Li, N. Sun, Z.-X. Guo, C. Li, Y. Li, L. Dai, D. Zhu, D. Sun, Y. Cao, L. Fan, *J Phys. Chem. B* **2002**, *106*, 11509.

53 Q. Zhou, L. Zheng, D. Sun, X. Deng, G. Yu, Y. Cao, *Synth. Met.* **2003**, *135-136*, 825.

54 F.L. Zhang, M. Johansson, M.R. Andersson, J.C. Hummelen, O. Inganäs, *Synth. Met.* **2003**, *137*, 1401.

55 (a) J.V. Manca, T. Munters, T. Martens *et al.*, *Proc. SPIE* **2003**, *4801*, 15; (b) T. Munters, T. Martens, L. Goris *et al.*, *Thin Solid Films* **2002**, *403-404*, 247.

56 C.J. Brabec, N.S. Sariciftci, J.C. Hummelen, *Adv. Funct. Mater.* **2001**, *11*, 15.

57 e.g. inert/ambient atmosphere, casting conditions and solvent, and metal evaporation conditions.

58 e.g. molecular weight, polydispersity, defects, substituents, regio-regularity, end-groups, and purity of the polymer.

59 Due to poor film-forming properties of pure PCBM, the ~100 nm spin cast films contain tiny holes (as observed with AFM) making reproducibility of the solar cell results poor and the influence of leakage current extremely large. Therefore, no data of photocurrents coming from pure PCBM are included.

60 M. Sahimi, *Applications of Percolation Theory*, Taylor & Francis Ltd, London, **1994**.

61 This value is calculated assuming no change in composition going from solution to the spin cast film, and using the mass density for MDMO-PPV of 910 kg/m^3 and for PCBM of 1500 kg/m^3 as determined for their spin cast films. For mass densities, see C.W.T. Bulle-Lieuwma, W.J.H. van Gennip, J.K.J. van Duren, P. Jonkheijm, R.A.J. Janssen, J.W. Niemantsverdriet, *Appl. Surf. Sci.* **2003**, *203-204*, 547.

62 The absence of a clear percolation threshold in J_{sc} might have several causes. First of all, percolation theory assumes one component to be inactive and one to be active, whereas in our system both components absorb light, generate, and conduct charges. Additionally, with changing composition, the absorption spectrum of the film, and the number of exciton dissociation sites within the exciton diffusion length will vary. Furthermore, the efficiency of the charge transfer and recombination processes might differ with composition. Finally, apart from the hole and electron transport pathways (percolation), carrier mobility (and the mobility edge related to the filling of the localized states) might and collection at the contacts will vary with composition.

63 Plotting on a double logarithmic scale shows a straight line (with a slope of 1.86, R = 0.996) from 5 wt.-% up to 75 wt.-% PCBM indicating that one phenomenon seems to be responsible for the increase in photocurrent in this range.

64 Due to the combination of a low-mobility high-MW polymer with a high-mobility molecule no attempt is made by us to find the percolation threshold for the polymer. Conjugated polymers are known showing percolation at much smaller fractions than 17 vol.-%, see e.g. A.J. Heeger, *Trends Polym. Sci.* **1995**, *3*, 39.

65 C.J. Brabec, A. Cravino, D. Meissner, N.S. Sariciftci, T. Fromherz, M.T. Rispens, L. Sanchez, J.C. Hummelen, *Adv. Funct. Mater.* **2001**, *11*, 374.

66 V.D. Michailetchi, P.W.M. Blom, J.C. Hummelen, M.T. Rispens, *J. Appl. Phys.* **2003**, *94*, 6849.

67 The total series resistance $R_{St} = R_{cp} + R_b + R_{cn}$ where R_{cp} is the contact resistance at the positive contact, R_b is the bulk resistance (dependent on percolation and charge-carrier mobility), and R_{cn} is the contact resistance at the negative electrode.

68 FF is influenced by both parallel and series resistance. The parallel resistance is mainly governed by leakage (homogeneity film thickness). The series resistance depends on film thickness, percolation pathways, charge-carrier mobility, field-dependence of charge generation, and contact properties.

69 A.L. Fahrenbruch, R.H. Bube, *Fundamentals of Solar Cells*, Academic Press, New York, **1983**.

70 In this reasoning the electric field dependence of charge generation is taken constant throughout the samples.

71 J.M. Kroon, M.M. Wienk, W.J.H. Verhees, J.C. Hummelen, *Thin Solid Films* **2002**, *403-404*, 223.

72 G. Yu, K. Pakbaz, A.J. Heeger, *Appl. Phys. Lett.* **1994**, *64*, 3422.

73 Electrodeless flash-photolysis time-resolved microwave conductivity (FP-TRMC) measures the microscopic mobility via the product, $\phi\Sigma\mu$, of the quantum yield for charge separation, ϕ, and the sum of the charge-carrier mobilities, $\Sigma\mu$. Because of the short timescale of the measurements and the ultrahigh frequency of the electric field, the mobilities measured using TRMC may be considered to be trap-free values, free from effects of barriers to transport at grain and domain boundaries, therefore, mainly reflecting the mobility within well-organized domains within the material.

74 T.J. Savenije, J.E. Kroeze, M.M. Wienk, J.M. Kroon, J.M. Warman, *submitted*.

75 Blom *et al.*, to be published.

76 Fitting is performed over the upper part of the measured range (three orders of magnitude, R > 0.999) where both V_{oc} and FF are clearly beyond their threshold value. When fitted over the full range (five orders of magnitude) the trend in the slope with varying composition is unaffected, but statistics deteriorate.

77 P. Schilinsky, C. Waldauf, C. J. Brabec, *Appl. Phys. Lett.* **2002**, *81*, 3885.

78 V. Dyakonov, I. Riedel, C. Deibel, J. Parisi, C.J. Brabec, N.S. Sariciftci, J.C. Hummelen, *Mat. Res. Soc. Symp. Proc.* **2002**, *665*, 235.

79 R.A.J. Janssen, J.C. Hummelen, F. Wudl, *J. Am. Chem. Soc.* **1995**, *117*, 544.

80 MDMO-PPV was generously provided by Philips Research Laboratories Eindhoven. Synthesis as described in H. Becker, H. Spreitzer, W. Kreuder, E. Kluge, H. Schenk, I. Parker, Y. Cao, *Adv. Mater*. **2000**, *12*, 42 (and references therein).

81 J.C. Hummelen, B.W. Knight, F. LePeq, F. Wudl, J. Yao, C.L. Wilkins, *J. Org. Chem.* **1995**, *60*, 532.

82 (a) X. Crispin, S. Marciniak, W. Osikowicz, G. Zotti, A.W. Denier van der Gon, F. Louwet, M. Fahlman, L. Groenendaal, F. De Schryver, W.R. Salaneck, *J. Pol. Sci. B* **2003**, *41*, 2561; (b) L. Groenendaal, G. Zotti, P.H. Aubert, S.M. Waybright, J.R. Reynolds, *Adv. Mater.* **2003**, *15*, 855; (c) L. Groenendaal, F. Jonas, D. Freitag, H. Pielartzik, J. R. Reynolds, *Adv. Mat*. **2000**, *12*, 481.

83 ITO covered glass substrates were generously provided by Philips Research Laboratories Eindhoven.

84 J. Huang, P.F. Miller, J.C. de Mello, A.C. de Mello, D.D.C. Bradley, *Synth. Met.* **2003**, *139*, 569.

85 W.H. Kim, G.P. Kushto, H. Kim, Z.H. Kafafi, *J. Pol. Sci. B* **2003**, *41*, 2522.

Chapter 6

Interface integrity and electrode diffusion*

Abstract

Plastic solar cells typically consist of a photoactive layer sandwiched between an indium tin oxide (ITO) electrode covered with polyethylenedioxythiophene:polystyrenesulfonate (PEDOT:PSS), and an aluminum electrode with an additional thin intermediate layer, such as LiF. The interfaces between these various layers determine charge collection and, thereby overall device performance. Therefore, full-depth analysis is required to study interface integrity, layer-to-layer diffusion, and contamination levels. The field of depth-profiling and cross-sectioning multiple thin layers of hard and soft matter, however, is a relatively new field. Therefore, the applicability of some techniques has been investigated. Cryogenic Rutherford backscattering spectrometry (RBS), dynamic time-of-flight secondary ion mass spectrometry (TOF-SIMS), depth-profiling with X-ray photoelectron spectrometry (XPS depth-profiling), transmission electron microscopy (TEM), and electron energy loss spectrometry (EELS) have been used. The structural and elemental composition of device structures with the photoactive layer consisting of either a mixture of poly(p-phenylene vinylene) (MDMO-PPV) and a C_{60} derivative (PCBM), or the pure components have been assessed. Enrichment of oxygen at the interface between Al and the photoactive layer is observed. RBS, TOF-SIMS, and XPS depth-profiling show that during preparation diffusion of indium into the PEDOT:PSS occurs under the influence of water, while the diffusion of aluminum into the polymer layers is negligible. A polysiloxane contamination at the buried interface with the top contact can be observed with TOF-SIMS. Transmission electron microscopy of cross-sections, as prepared with a focused ion beam, of fully processed photovoltaic cells, provide a clear view of the individual layers and their interfaces. No dissociation of LiF upon evaporation of Al onto LiF-covered photoactive layers could be observed with quadrupole secondary ion mass spectrometry (Quad-SIMS).

*Part of this work has been published: (a) J.K.J. van Duren, P.C. Thüne, R.G. White, J.G.M. van Berkum, M. Kaiser, C.W.T. Bulle-Lieuwma, J.W. Niemantsverdriet, R.A.J. Janssen, *manuscript in preparation*; (b) C.W.T. Bulle-Lieuwma, W.J.H. van Gennip, J.K.J. van Duren, P. Jonkheijm, R.A.J. Janssen, J.W. Niemantsverdriet, *Appl. Surf. Sci.* **2003**, *203-204*, 547; (c) W.J.H. van Gennip, J.K.J. van Duren, P.C. Thüne, R.A.J. Janssen, J.W. Niemantsverdriet, *J. Chem. Phys.* **2002**, 117, 5031; (d) J. Loos, J.K.J. van Duren, F. Morrissey, and R.A.J. Janssen, *Polymer* **2002**, *43*, 7493; (e) J.K.J. van Duren, J. Loos, F. Morrisey, C.M. Leewis, K.P.H. Kivits, L.J. van IJzendoorn, M.T. Rispens, J.C. Hummelen, R.A.J. Janssen, *Adv. Funct. Mater.* **2002**, *12*, 665.

6.1 Introduction

Sandwich devices as plastic solar cells[1,2] and light-emitting diodes[3-5] (LEDs) consist of multiple thin layers of both organic and inorganic materials (Figure 6.1). The exact nature of the contacts between the active organic layer and the electrodes have proven to be of paramount importance for device performance.[6-13] Furthermore, it has been found that, apart from the nature of the interface, a large interface stability and smoothness are necessary to guarantee a uniform current density distribution, thereby minimizing the probability of device failure.[14] Recently, device degradation during operation has been related to migration of ionic impurities,[15] possibly originating from the electrodes.[16,17]

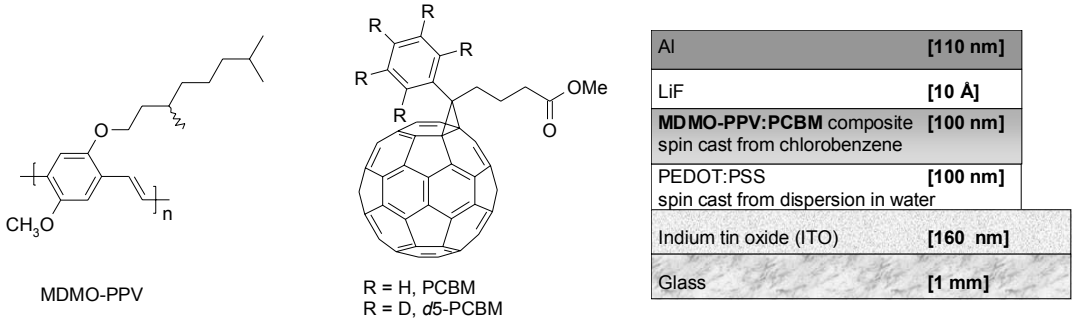

Figure 6.1 *Molecular structures of materials and device configuration used.*

It is clear that intrinsic material and device properties have to be distinguished from external influences in order to understand and, concomitantly, increase the stability, lifetime, and performance of these devices.[18-20] Therefore, full-depth analysis of these multi-layered devices has to be performed to determine both intrinsic properties and external influences.

Depth-profiling and cross-sectioning multiple thin layers of soft and hard matter is a relatively new field. Hence, the applicability of some of the techniques used needs to be investigated in order to interpret the results obtained accurately. The depth-profiling techniques used in this work are cryogenic Rutherford backscattering spectrometry (RBS), dynamic time-of-flight secondary ion mass spectrometry (TOF-SIMS), and X-ray photoelectron spectroscopy (XPS) depth-profiling. Furthermore, cross-sectional analysis is performed on a thin cross-section as prepared with a focused ion beam (FIB). This cross-section is then analyzed with both transmission electron microscopy (TEM) and electron energy loss spectrometry (EELS). The topography at different stages during device preparation is monitored with atomic force microscopy (AFM), and surface profilometry.

Additional to investigating the applicability of the depth-profiling and cross-sectioning techniques for plastic solar cell (and LED) analysis, this chapter addresses elementary questions regarding the integrity of interfaces in subsequent processing steps, the possible diffusion or concentration profiles of electrode metal species into the organic layers, and the presence of contaminations for plastic solar cells consisting of glass/ITO/PEDOT:PSS/photoactive layer/LiF/Al (for structures with and without LiF). The photoactive layer consists of either pure poly[2-methoxy-5-

(3′,7′-dimethyloctyloxy)-1,4-phenylene vinylene] (MDMO-PPV), pure 1-(3-methoxycarbonyl)propyl-1-phenyl-[6,6]-methanofullerene (PCBM) or a mixture of both (Figure 6.1).

6.2 Topology study of interfaces

As outlined in the previous paragraph, interface roughness strongly influences device performance and lifetime. As a first step in studying the interfaces between the consecutive layers, AFM was used to determine the surface topology. These AFM measurements were performed on the surfaces as present during preparation of the stacks and showed a rather smooth ITO surface with

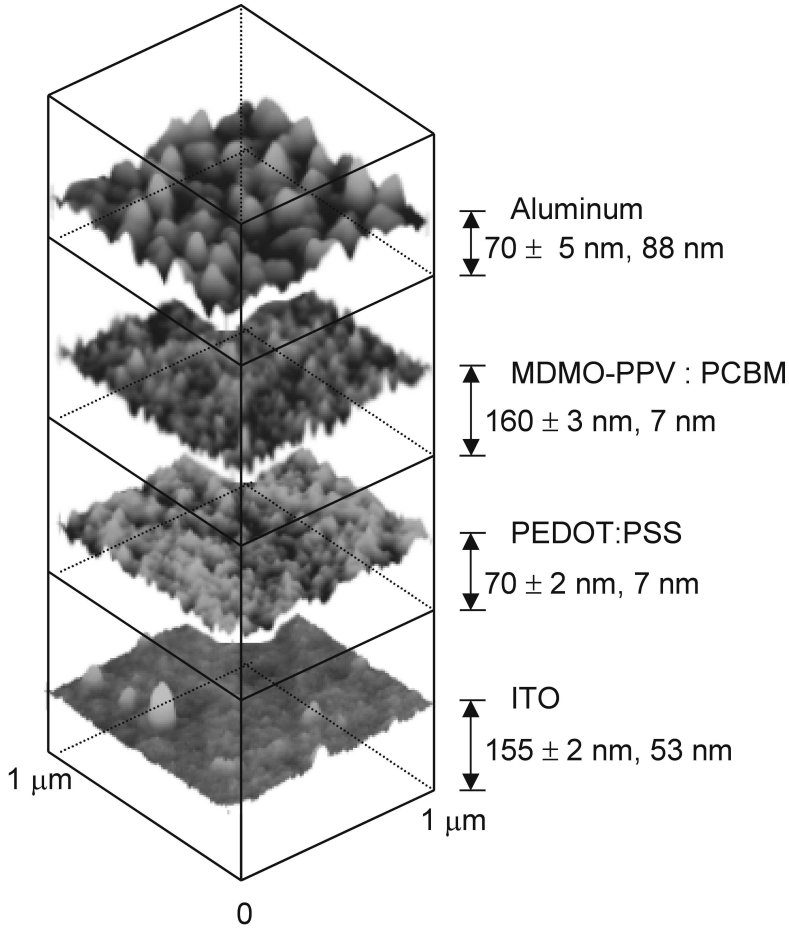

Figure 6.2 *1 × 1 μm² AFM height images of the surfaces of the different layers of a glass/ITO/PEDOT:PSS/MDMO-PPV:PCBM(1:4 by wt.)/Al solar cell. For each layer the thickness as determined by a surface profiler, the RMS roughness, and the peak-to-valley roughness as determined by AFM, respectively, are indicated in the graph. Both polymer layers are rather smooth and flat, the ITO is smooth, but contains spikes (see feature at the lower left corner), and the Al surface is extremely rough.*

local spikes reaching 50 nm,[21] smooth polymer films (RMS values of 1-2 nm for a 10×10 μm^2 area) and a rough surface for Al with spikes resulting in maximum height differences of 90 nm (Figure 6.2). A more detailed study (see Chapter 4) showed that some unevenness is typically observed for phase-separating mixtures of MDMO-PPV and PCBM, opposite to the extremely smooth films of the pure components. The films of pure PCBM contain some tiny pinholes. Line-scan investigations with a surface profiler (lateral resolution 200 nm) showed the organic films to be flat on a mm-lengthscale as well.

6.3 Cryogenic Rutherford backscattering spectrometry (RBS)

Cryogenic ($T \approx 30$ K) Rutherford backscattering spectrometry (RBS)[22] enables depth-profiling of the elemental composition in the sample without the use of ion sputtering or mechanically removing subsequent layers. For polymers, a cryogenic temperature ($T \approx 30$ K) during analysis is required in order to trap the radicals and small molecules formed by bond cleavage resulting from the large amount of energy introduced by the monoenergetic beam of He ions (2 MeV, few nA). Without cooling, small volatile molecules that escape from the material disrupt the sample structure and may even lead to gas bubbles trapped under the Al electrode.[23] Note that after the analysis, upon warm-up, the trapped radicals react and the small molecules still escape, disrupting the solar cell which does no longer function. The RBS spectra show the energy distribution of the He ions after scattering. This energy depends on the masses of the projectile and scattering atom, the scattering geometry (depicted in Figure 6.3a), and moreover on the depth at which the scattering atom is located. By carefully choosing the scattering angle θ and the angle between the incoming beam and the sample surface α, overlap of signals of different atoms can be circumvented. Both concentration depth profiles (resolution typically 10 nm) in separate layers as well as layer-to-layer diffusion can be determined. The RBS measurements are analyzed by simulation using the RUMP code.[24] This code provides the atomic composition (quantitatively) and the thickness of the layer.

6.3.1 Indium tin oxide bottom electrode studied with RBS

The indium diffusion into the PEDOT:PSS and MDMO-PPV:PCBM layers was investigated[25] for a glass/ITO/PEDOT:PSS/MDMO-PPV:PCBM sample for two different drying processes of the PEDOT:PSS layer, i.e. heating the substrate after spin coating on a hot plate for 1 min at 100°C or 2 min at 150 °C. The annealing removes residual water from the PEDOT:PSS layer, which otherwise may cause etching of ITO via protonation in the acidic environment of the sulfonic acid functional groups of PEDOT:PSS.[26] The results are shown in Figure 6.3b and 6.3c. The composition of the MDMO-PPV:PCBM layer, calculated based on the used weight ratio (1:4 by weight, 63.0 at.-% C, 34.1 at.-% H and 2.9 at.-% O), was used in the RUMP simulations. The large peak between 0.7 and 1.4 MeV corresponds to the indium in the ITO layer (Figure 6.3b). Scattered He

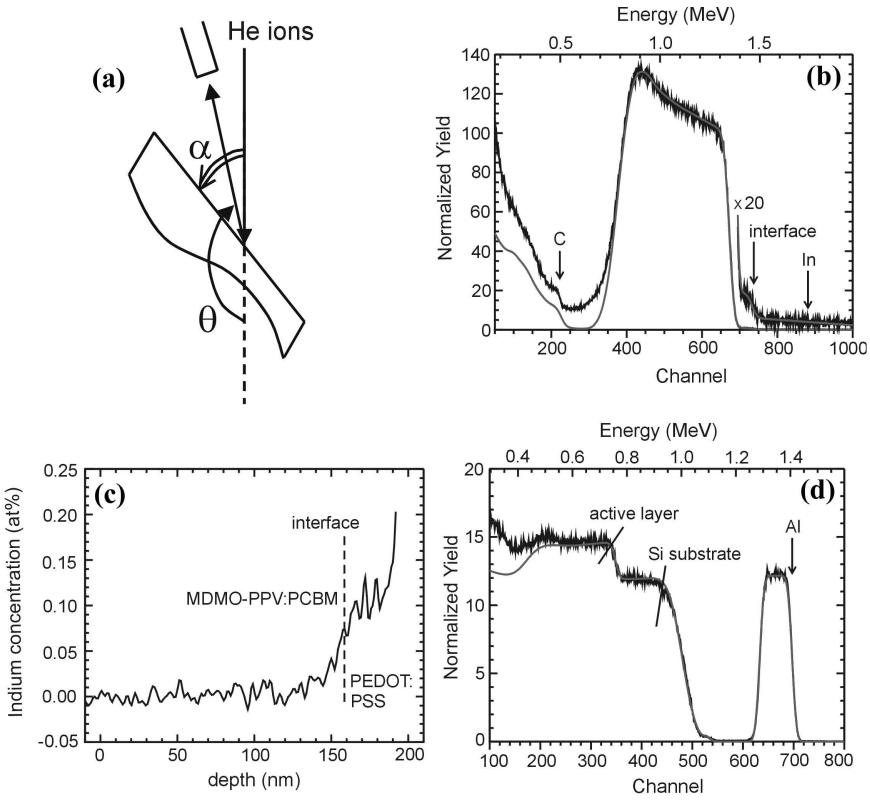

Figure 6.3 *RBS spectra (black) and their RUMP simulations (gray). The arrows indicate the energies that correspond to elements located at the surface.* **(a)** *RBS scattering geometry.* **(b)** *A glass/ITO/PEDOT:PSS/MDMO-PPV:PCBM stack, when PEDOT:PSS was dried at 150 ºC for 2 min. RBS geometry: $\alpha = 165°$ and $\theta = 170°$. The simulation shows that indium diffusion is detected up to the interface between PEDOT:PSS and MDMO-PPV:PCBM.* **(c)** *The indium depth profile calculated from the RBS spectrum in B assuming an atomic density of 1.3 10^{23} at/cm^3. The indium concentration in the PEDOT:PSS film is 0.1 ± 0.02 at% (corresponding to 1.3 ± 0.3 10^{20} at/cm^3).* **(d)** *A Si/MDMO-PPV:PCBM/Al sample, when Al was deposited at a rate of 1 nm/s, analyzed at a geometry of $\alpha = 90°$ and $\theta = 100°$.*

projectiles with an energy between approximately 1.4 MeV and the indium surface energy show indium diffusion into the PEDOT:PSS layer. Drying for only 1 min. at 100 ºC results in indium in the PEDOT:PSS layer with a concentration of 1 ±0.1 at.-% (1.3 ± 0.1 10^{21} at/cm^3). After drying for 2 min. at 150 ºC, the indium concentration in the PEDOT:PSS is significantly reduced. The indium depth profile given in Figure 6.3c reveals an indium concentration of 0.1 ±0.02 at.-% (1.3 ±0.3 10^{20} atoms/cm^3) in the PEDOT:PSS layer up to the interface with MDMO-PPV:PCBM. The background visible in the spectra of Figure 6.3b between the In peak and the C peak of the active layer is due to multiple scattering in the ITO layer (which is not incorporated in the simulation). The results are consistent with the fact that residual water promotes the diffusion of In. It should be noted that with RBS no distinction can be made between In and Sn.

6.3.2 Aluminum top electrode studied with RBS

Al diffusion into the active layer was investigated for Si/MDMO-PPV:PCBM/Al stacks for Al deposition rates of 1 and 10 nm/s. In these experiments a silicon substrate was chosen instead of glass/ITO to avoid overlap of the Al peak by Ca and In from the glass and ITO, respectively. The peak between 1.25 and 1.40 MeV for a deposition rate of 1 nm/s in Figure 6.3d corresponds to the Al layer. Aluminum diffusion into the MDMO-PPV:PCBM film might be observed at energies just below 1.25 MeV. For both deposition rates, however, no aluminum was detected in the active layer above the detection limit of 0.1 at.-% and since the RBS spectra of both samples are identical, only the spectrum of 1 nm/s is presented (Figure 6.3d). For both deposition rates, the sample can be simulated by RUMP with oxygen only in the first few nanometers. The roughness of the interface between the polymer layer and Al used in the RUMP simulations is less than 15% of the total polymer film thickness. Based on the simulations, no distinction can be made, however, between a mixed interface as a result of minor aluminum diffusion and roughness of the interface.

6.3.3 Conclusions on RBS studies

Polymer photovoltaic cells and their multiple layer substructures have been analyzed using cryogenic RBS in terms of interlayer diffusion of electrode materials. RBS revealed that diffusion of Al and In into the polymer layers is minor directly after preparation, provided that appropriate annealing is performed. It should be noted that the detection limit of RBS is typically 0.1 at.-%.

6.4 Sputter depth-profiling

The two sputter depth-profiling techniques as used in this chapter are XPS depth-profiling,[27] and dynamic TOF-SIMS in dual-beam mode.[28-30] In these experiments, sputtering with an ion beam for material removal was continuously alternated with analysis of the crater bottom. For XPS depth-profiling, analysis is performed by evaluation of peak intensity, peak shift, and peak shape changes of the binding state energy of the electrons liberated by excitation with an X-ray source. Mass detection of the charged particles ejected from the surface by an analysis ion beam (additional to the sputter ion beam) forms the basis for dynamic TOF-SIMS.

Ion sputtering can generate a large number of artifacts in the subsurface region and caution should be taken when interpreting XPS and TOF-SIMS depth profiles. The length of the redistribution region of the atoms in the surface region (atomic mixing length), the width of the analytically active region (information depth), a progressive change in the crater bottom roughness (roughness depth), compositional changes as a result of preferential sputtering of one of the components, bond breaking connected with decomposition, and changes in morphology, all can influence the depth profile.[30-33]

The extent of these changes depends both on sputtering conditions and material properties. Most existing knowledge in this field is based on inorganic (hard) matter.

6.4.1 Dynamic time-of-flight secondary ion mass spectrometry (TOF-SIMS)

6.4.1.1 Applicability of dynamic TOF-SIMS to plastic solar cells

One of the major advantages of TOF-SIMS[34] is its parallel acquisition that enables storage of the entire mass spectrum (mass range m/z = 0-900 amu) at each cycle of the depth profile, and consequently the choice of well-resolved peaks (mass resolution $m/\Delta m = 10^4$) in hindsight. Furthermore, detailed fragmentation information can be extracted by combining positive and negative mode mass spectra. Additionally, TOF-SIMS enables the detection of unknown contaminants at buried interfaces with a very high sensitivity (ppm to ppb level).

Depth-profiling of polymers and metal-polymer stacks by TOF-SIMS is a relatively new field and many questions remain regarding matrix and wall effects, depth resolution, sputter behavior, and the other artifacts previously mentioned. Consequently, the steady state part of the intensity-time profile does not necessarily have to be an exact representation of the concentration-depth profile.[30] One of the factors influencing the latter is the development of the crater bottom roughness during sputtering, possibly accompanied by ripple formation for instruments with a fixed sample holder.[35] This roughness development is strongly dependent on the morphology of each layer. Furthermore, a changing sputter rate, while going through the multiple layers, can further complicate the interpretation of intensity-time profiles. Especially, extraction of layer-to-layer diffusion can become complicated for multiple thin layers when the depth resolution is low and changes continuously. A typical plastic solar cell, and related structures were used to study some of these problems.[36]

Wall effects. To study possible wall effects, the sputter area was enlarged from 150 × 150 μm^2 to 300 × 300 μm^2 for several multi-layered device structures with a 3 keV Ar^+ sputter beam, while keeping the analysis area at 50 × 50 μm^2. No significant improvement of depth resolution was observed. In fact, the SIMS depth profiles overlapped exactly after dividing the total sputter time for the 300 × 300 μm^2 crater by four ($300^2/150^2$). Additionally, the crater shapes were measured by environmental scanning electron microscopy (ESEM), interferometry, and surface profilometry. All layers are clearly visible in the smooth wall of the crater in the ESEM-image (Figure 6.4). Both interferometry and surface profilometry showed rectangular craters with horizontal crater bottoms. Because the crater bottom was always the size of the chosen raster size, the 150×150 μm^2 crater was sufficiently large to exclude wall effects.

Crater bottom roughness. The development of the crater bottom roughness has been measured with AFM for three different multi-layered structures. For a glass/MDMO-PPV(200

nm)/Al(100 nm) structure[37] a gradual increase in roughness could be observed from the top surface to just underneath the glass/MDMO-PPV interface (peak-to-valley (MAX) roughness increasing from 42 to 127 nm and root-mean-square (RMS) values from 4 to 15 nm for 10.0 × 10.0 μm^2). The polycrystalline nature of the aluminum layer typically results in two instead of one sputter front, thereby increasing the crater bottom roughness tremendously.[38] Combined with the huge top surface roughness, extensive peak broadening is therefore commonly observed for structures with an aluminum top electrode (see below). Due to the lower sputter rate (for end front) of aluminum compared to MDMO-PPV, the forward sputter front is never caught up by the end sputter front. Furthermore, no stabilization of the crater bottom roughness has been observed.

This behavior is in contrast to the roughness development for a glass/ITO(40 nm)/PEDOT:PSS(75 nm)/MDMO-PPV(180 nm) structure.[39] A maximum in roughness (MAX = 168 nm and RMS = 17 nm for 10.0 × 10.0 μm^2 at ~185 nm depth)[40] with crater depth could be observed starting at the smooth MDMO-PPV top surface (MAX = 6.5 nm and RMS = 0.5 nm for 10.0 × 10.0 μm^2) and ending in the top end of the glass substrate (MAX = 50 nm and RMS = 5.5 nm for 10.0 × 10.0 μm^2). This increase and subsequent decrease in roughness results from the specific sequence in sputter rates for the individual layers.[41]

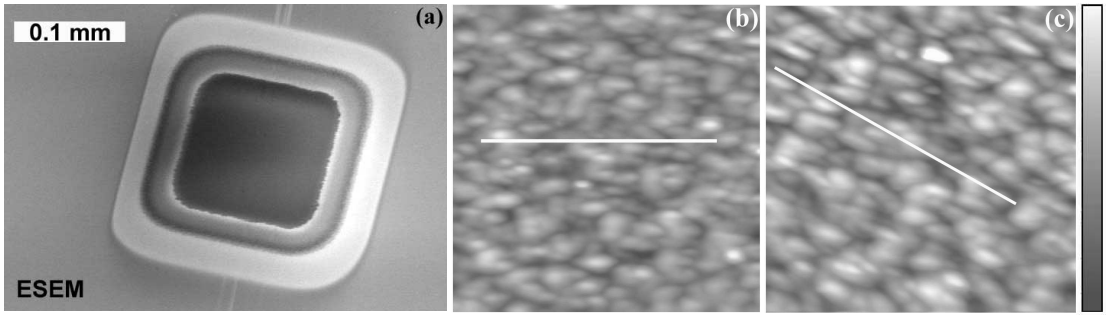

Figure 6.4 **(a)** *ESEM image of a more or less square crater sputtered in glass/ITO/ PEDOT:PSS/MDMO-PPV/Al with all layers clearly visible in the smooth walls. From top to bottom: Al ('white'), MDMO-PPV (dark gray), PEDOT:PSS (light gray), ITO ('white'), and glass ('black'). Note the slope of the walls as a result of the 45° sputtering angle.* **(b, c)** *2 × 2 μm^2 AFM height image of a crater inside ITO after sputtering through the complete device structure. A preferential ripple-like structure as indicated with the white line can be observed.* **(b)** *The ripple-like structure observed is in line with the ion sputtering direction. The AFM scan direction is parallel to the ion sputtering direction. Therefore, the sample is rotated (c) to ensure that this is not an artifact of the AFM conditions. Height bar (maximum peak-to-valley) represents 25 nm. Root-mean-square values (RMS) are 3.3 nm.*

Finally, a glass/ITO(40 nm)/PEDOT:PSS(75 nm)/MDMO-PPV:*d*5-PCBM(110 nm, 1:4 by wt.) structure has been investigated.[39] Apart from a local maximum at ~75 nm depth (MAX = 25 nm and RMS = 2.8 nm for $2.0 \times 2.0\ \mu m^2$), a subsequent local minimum in crater bottom roughness could be observed (the latter somewhere in between 90-190 nm depth), when sputtering from the slightly uneven top surface (MAX = 10 nm and RMS = 1.4 nm for $2.0 \times 2.0\ \mu m^2$). Furthermore, ripple formation was observed when ITO was reached (Figure 6.4).[42]

Summarizing, depth-profiling typical plastic solar cells can result in a complex crater bottom roughness development with significant roughness values. The latter not only results from the polycrystallinity of the aluminum top layer and the fixed sample holder, but also from the inhomogeneous sputtering of PEDOT:PSS (and ITO), MDMO-PPV:(*d*5-)PCBM, and pure MDMO-PPV. The inhomogeneous sputtering of these conjugated organic films is attributed to the inhomogeneity in their morphology. This roughness development leads to extensive peak broadening (see below).

Positioning the interface. To be able to distinguish between intrinsic properties of the multi-layered stack, e.g. diffusion and interface roughness, and analysis-induced changes, such as atomic mixing and crater bottom roughness, accurate determination of the interfaces plays a key role. Several fragments characteristic for both layers separately are necessary to position the interface. Positioning the interface accurately is a difficult task. However, typical regions can be recognized where most mass fragments show an identical steepness in peak intensity variation with depth. The interface involved is located somewhere within this region. As long as these regions for the successive interfaces are well separated, most device properties can be distinguished from analysis-induced changes. Therefore, the interface is set at 36% (e^{-1}) of the total decrease in signal for decreasing signals and at 64% of the total increase in signal for increasing signals. More signals than shown in the figures are employed to this end.

Sputter rate. When sputtering 100 nm thick films of pure MDMO-PPV, pure PCBM, or a 1:4 mixture by weight, the sputter time required changes drastically. Figure 6.5 (left) shows the SIMS depth profile in negative mode (sputter condition: 1 keV Ar^+, $150 \times 150\ \mu m^2$) for MDMO-PPV and PCBM in the upper and lower panel, respectively. The sputter speed of MDMO-PPV is at least twice that of PCBM (and that of the mixture of MDMO-PPV:PCBM=1:4). One factor contributing to the difference in sputter speed is the difference in density of the MDMO-PPV film (ρ = 910 kg/m^3) and PCBM film (ρ = 1500 kg/m^3).[43] Another contributing factor could be the much larger ratio of double to single bonds in PCBM compared to MDMO-PPV. Double carbon-carbon bonds are more difficult to break than single carbon-carbon bonds. Consequently, a larger ratio double to single bonds can

cause a decrease in sputter yield. Sputtering phase-separated mixtures of MDMO-PPV and PCBM, therefore, might give an extensive crater bottom roughness development.

Interpretation of intensity-time profiles. Although, the use of models, such as the mixing-roughness-information depth model (MRI model),[32,38] and multivariate statistical analysis of the ion intensities,[44] definitely improves the conversion of intensity-time profiles to concentration-depth profiles, in this thesis only immediately evident results from the intensity-time profiles are used.

6.4.1.2 Indium tin oxide bottom electrode studied with dynamic TOF-SIMS

Device structures with and without aluminum top electrode have been investigated. The depth profile (positive mode, sputtered with 3 keV Ar^+ and 150×150 μm^2, see Figure 6.5, right, lower panel) of glass/ITO(40 nm)/PEDOT:PSS(350 nm)/PCBM(100 nm) shows that a huge ^{113}In signal extends from ITO all the way to the interface between PEDOT:PSS and PCBM, where the signal drops dramatically. This holds for several other indium-related signals as well. The depth profile of a similar stack with aluminum on top (Figure 6.5, right, upper panel) shows the same behavior, however, the ^{113}In signal in PEDOT:PSS is much smaller (note the logarithmic scale). It is clear from Figure 6.5 that the diffusion of indium depends on the nature of the layers present. Close to the ITO/PEDOT:PSS

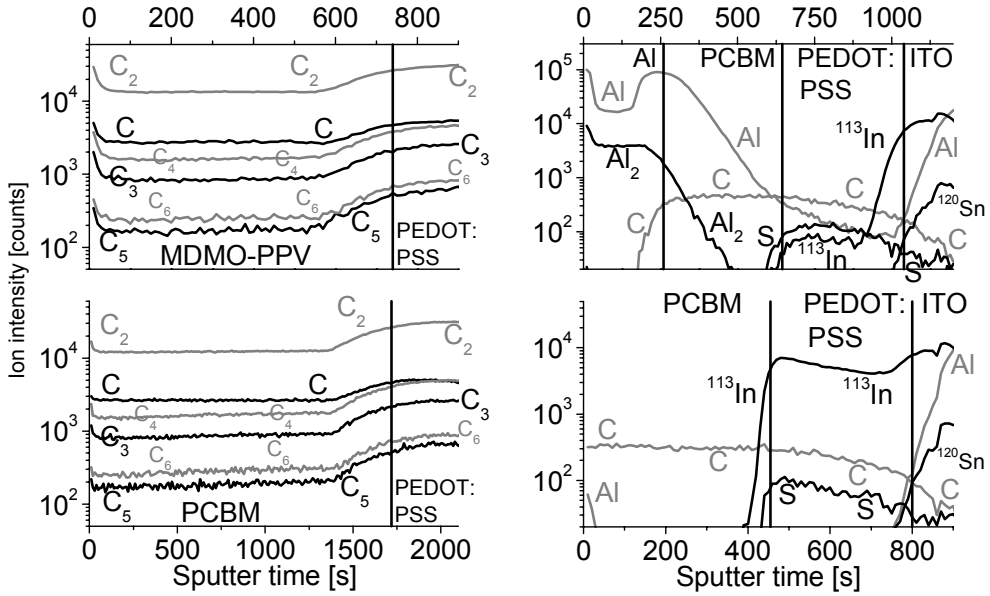

Figure 6.5 *Left: Negative mode depth profile of a glass/ITO/PEDOT:PSS/MDMO-PPV stack (upper panel) shows a twice as large sputter speed for 100 nm MDMO-PPV than for 100 nm PCBM in the same stack (lower panel). Right: The positive mode depth profile of a glass/ITO/PEDOT:PSS/PCBM stack shows that the diffusion of indium into PEDOT:PSS is much higher for the same stack without an aluminum top contact (lower panel) than for the stack with an Al top contact (upper panel).*

interface the indium signal can be explained by the ITO spikes. Because these samples were exposed to air for a few days, the indium diffusion into PEDOT:PSS is in accordance with the explanation of water-induced acidic etching of ITO.[26] The absence of indium in the PCBM layer is attributed to the more apolar nature of PCBM compared to the highly polar nature of PEDOT:PSS. Comparison of the stack with and without Al shows a dramatic decrease in indium signal in the bulk of PEDOT:PSS for the stack covered with Al. This is attributed to a decrease in water uptake by the stack resulting from the Al layer acting as a water barrier. When MDMO-PPV or a mixture of MDMO-PPV:PCBM was used instead of PCBM, the same behavior was observed, although less pronounced for MDMO-PPV.

It should be noted that multiple In-related mass fragments could be assigned without doubt. However, some Sn-related mass fragments cannot unambiguously be assigned, due to overlap with other fragments. This affects conclusive statements on the occurrence of Sn diffusion. Furthermore, for glass/ITO(40 nm)/PEDOT:PSS(75 nm)/MDMO-PPV:PCBM(1:4 by weight, 115 nm)/LiF(1.0 nm)/Al(100 nm) and related structures[39] where PEDOT:PSS is annealed at 180 °C and subsequently cooled for 1 minute at 25 °C, no clearly detectable In diffusion could be found.

6.4.1.3 Aluminum top electrode studied with dynamic TOF-SIMS

To investigate whether hot metal (aluminum) evaporation might cause metal diffusion into the underlying polymer layer (MDMO-PPV) depth profiles were taken in two different directions. By reversing the sputter direction, the impact of the crater bottom roughness development originating from the polycrystallinity of aluminum on the depth profiles can be studied. Comparison of both depth profiles should improve the distinction between possible aluminum diffusion (or a mixed interface) and analysis-induced changes.

The upper panel of Figure 6.6 (sputter condition: 3 keV Ar^+, 150×150 μm^2) shows the positive mode depth profile of the stack glass/ITO(40 nm)/PEDOT:PSS(350 nm)/MDMO-PPV(100 nm/Al(100 nm). The interface between Al and MDMO-PPV is found to be oxygen-rich, as visible from the O peak (positive ion!), and the oxygen-induced matrix effect on the Al ion. These results are supported by the clear increase in intensity of the O, AlO and AlO_2 species at the interface in the negative mode depth profile (not shown). The presence of oxygen is attributed to the formation of aluminum oxide (or hydroxide) during Al evaporation on MDMO-PPV as a result of a chemical reaction with the present residual gas (water) in the vacuum chamber,[45-47] and water present at the sample surface. Chemisorbed oxygen might play a role as well.[46] From the interface a long tail of Al extends all the way into PEDOT:PSS. Some accumulation of silicon attributed to polysiloxane contamination is also evident at the buried interface. Surface analysis by XPS, static Quad-SIMS, and low energy ion scattering (LEIS) on the spin cast films of MDMO-PPV and PCBM confirmed the presence of polysiloxanes on the top surface of the polymer films. XPS performed on the solids suggested that this contamination originates from the synthesis.

For the reverse direction, the MDMO-PPV/Al layers were removed from a glass substrate with adhesive tape. AFM images showed the new top surface to be remarkably smooth (RMS 1.3 nm for a 10×10 μm^2 area). Comparison of the forward and reversed direction (Figure 6.6) shows that the extensive tailing of Al in the forward direction mainly results from a huge increase in crater bottom roughness while going in depth. The depth profile of the reversed direction[37] shows that the Al signal within the polymer film drops dramatically, then changing to a smaller slope. The initially high Al signal in MDMO-PPV is attributed to both the roughness of this interface and the roughness development during sputtering. The very small signal of Al that decreases slowly is either due to actual aluminum diffusion into the polymer film or due to pinholes in the peeled-off film that escaped detection by AFM owing to their low density (only 0.1% of the analyzed area is needed for this explanation). Another explanation might be the long-range hilly landscape of the sample originating from the soft substrate (adhesive tape).

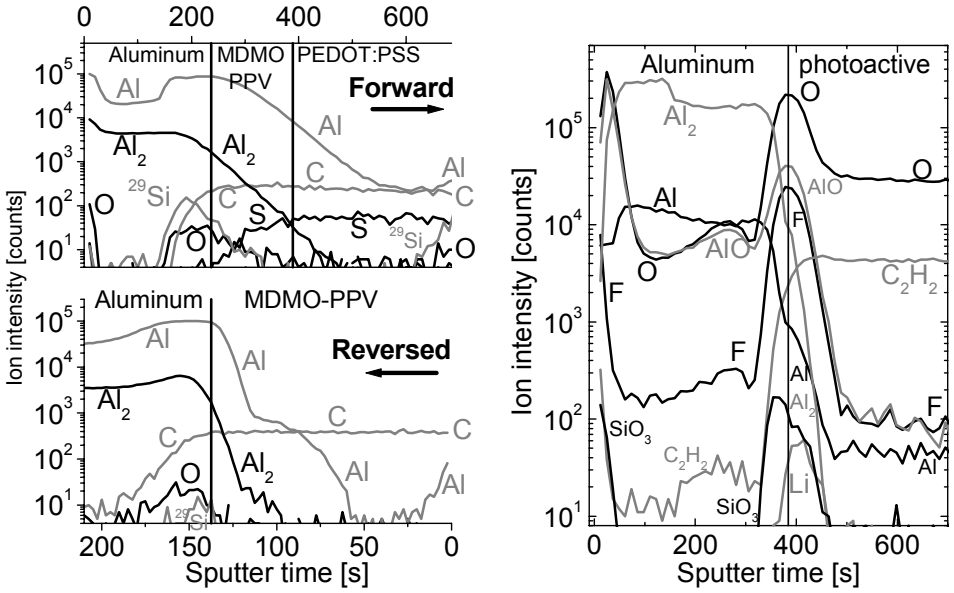

Figure 6.6 *Left: Positive mode depth profile of a glass/ITO/PEDOT:PSS/MDMO-PPV/Al stack in forward and reversed direction. The interface is enriched in O and Si. Right: Negative mode depth profile of a glass/ITO/PEDOT:PSS/MDMO-PPV:PCBM(1:4 by wt.)/LiF/Al stack. Again, the photoactive layer/LiF/Al interface is enriched in O and Si. Furthermore, Li and F are clearly visible.*

A glass/ITO(40 nm)/PEDOT:PSS(75 nm)/MDMO-PPV:PCBM(1:4 by weight, 115 nm)/LiF(1.0 nm)/Al(100 nm) structure incorporated with a thin LiF layer (1.0 nm) has been investigated in the negative mode (Figure 6.6).[39] Again, enrichment of oxygen at the interface can be observed. Furthermore, the presence of Li (negative ion!) and F at the interface are visible.

Unfortunately, the Li signal is rather low. The peaks of both signals are not positioned at the same depth. Whether this absence in coinciding peaks is related to doping,[45] or to an analysis-related artifact needs further investigation (with positive mode depth profiles). Recent results by Feng *et al.* suggest that apart from intact LiF, aluminum oxide and metallic Al, also Li^+ doped PPV is present at the interface.[48]

Concluding, an oxygen-rich interface between the organic layer and aluminum is found for all aluminum-covered samples. Furthermore, silicon can be found at this buried interface. The presence of oxygen is mainly attributed to a chemical reaction of residual gas (water) in the vacuum chamber with aluminum during evaporation, whereas the presence of silicon has been found to originate from a polysiloxane contamination.

6.4.1.4 Conclusions on dynamic TOF-SIMS studies

Sputter depth-profiling multiple thin layers as used in plastic electronics can result in a complex crater bottom roughness development with significant roughness values. This is mainly due to inhomogeneous sputtering of the individual layers. This roughness development leads to extensive peak broadening.

Degradation of ITO resulting in diffusion of indium into PEDOT:PSS as a result of water uptake has been observed. No detectable indium diffusion could be observed when PEDOT:PSS was annealed at 180 °C and subsequent exposure to water of the complete device structure was avoided. An oxygen-rich interface between the organic layer and aluminum is found for all aluminum-covered samples. Furthermore, silicon can be found at this buried interface. The presence of oxygen is mainly attributed to a chemical reaction of residual gas (water) in the vacuum chamber with aluminum during evaporation, whereas the presence of silicon has been found to originate from a polysiloxane contamination.

6.4.2 Depth-profiling using X-ray photoelectron spectrometry

Just as for RBS, depth-profiling using X-ray photoelectron spectrometry (XPS depth-profiling) is a quantitative technique. Furthermore, the same sputtering-related issues (in contrast to the analysis-related issues) influencing the conversion of the intensity-time profile into a concentration-depth profile, as discussed in detail for dynamic TOF-SIMS, hold for XPS depth-profiling. However, the impact of surface roughening is suppressed dramatically by sample rotation during sputtering.[31,32,38]

XPS depth-profiling has been performed[49] on a glass/ITO(160 nm)/PEDOT:PSS(100 nm)/MDMO-PPV:PCBM(110 nm)/LiF(1.0 nm)/Al(110 nm) structure. During transportation the samples have been exposed to an ambient atmosphere. As visible from the In 3*d*5 binding energy (437.3 eV) in depth, indium diffusion into PEDOT:PSS can be observed (Figure 6.7). No diffusion of

Sn (Sn 3*d*5, 479.2 eV) could be observed. Up to 20 at.-% oxygen (O 1*s*) can be found at the MDMO-PPV/LiF/Al interface. It should be noted that conversion into atomic concentrations is based only on the signals shown. Furthermore, both metallic and oxidized aluminum are present at this interface. Additionally, the ratio between metallic and oxidized aluminum is clearly larger in the bulk than at both interfaces, as can be concluded by comparison of the peak intensities of the Al 2*p* binding energy for metallic (65.4 eV) and oxidized (67.9 eV) Al. Finally, F (F 1*s*, 679.4 eV) can clearly be detected at this interface. Unfortunately, the Li signal (Li 1*s*) is too low (increasing this signal would require extremely long acquisition times).

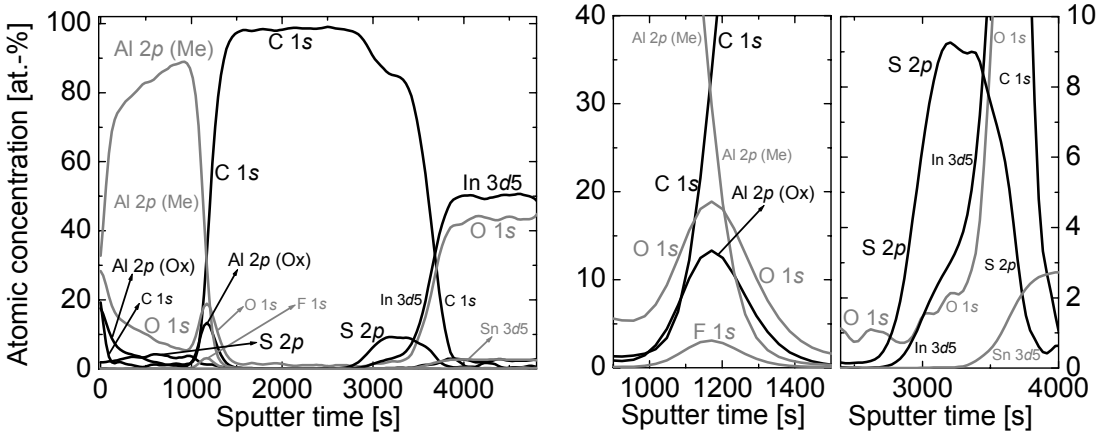

Figure 6.7 *Left: XPS depth profile of a glass/ITO/PEDOT:PSS/MDMO-PPV:PCBM(1:4 by wt.)/LiF/Al stack. The atomic concentrations are based only on the signals shown. Middle: Enlargement of the interface region of MDMO-PPV:PCBM/LiF/Al. Oxygen-enrichment at the interface is clearly visible. Right: Enlargement of the PEDOT:PSS region. Indium diffusion into PEDOT:PSS stops at the PEDOT:PSS/MDMO-PPV:PCBM interface.*

6.5 Electron microscopy on thin cross-sections

In order to characterize a cross-section of a multi-layered device with transmission electron microscopy (TEM) or electron energy loss spectrometry (EELS) in a scanning TEM (STEM), a thin slice has to be prepared. Commonly, microtomy[50] is used for the preparation of thin cross-sections. The devices described in this thesis typically consist of multiple layers of soft and hard matter. Cutting a slice with a conventional microtome would result in deformation of the soft layers while cutting the hard layers. Therefore, a focused ion beam (FIB)[51] is more suitable to 'cut' a slice from these devices. This thin slice is cut out of the sample, and subsequently lifted out with a sharp tip glass rod mounted on a micromanipulator, to be placed on a TEM-grid, known as the lift-out technique.

To investigate cross-sectional details of a working solar cell device a thin $12 \times 3.5 \times 0.3$ μm^3 slab from a fully processed polymer photovoltaic cell (i.e. glass/ITO/PEDOT:PSS/MDMO-PPV:PCBM/Al) was prepared using a FIB with a high Ga^+ beam current, and subsequently milled and polished with a low Ga^+ beam current to approximately 100 nm thickness.[52,53] The lift-out technique was used to place the slab on a TEM-grid. A similar procedure was used to cut a slab from a glass/ITO/PEDOT:PSS/MDMO-PPV:PCBM/LiF/Al device for STEM and EELS investigations.

6.5.1 Cross-sectional analysis by transmission electron microscopy

The TEM picture as obtained from a cross-section of a photovoltaic cell (Figure 6.8) shows no visible damage to the layers and reveals various features. First, the thickness of the individual layers is readily obtained from the cross-section: 155 nm ITO; 70 nm PEDOT:PSS; 160 nm MDMO-PPV:PCBM; and 70 nm aluminum. These values are consistent with the thickness of the layers determined using a surface profiler within an accuracy of 5 nm, except for ITO where the accuracy is 10-15 nm. At the interface of the photoactive MDMO-PPV:PCBM layer and the Al electrode a thin layer can be recognized, which has been identified using dual-beam dynamic time-of-flight secondary ion mass spectrometry (TOF-SIMS) to be an aluminum oxide or hydroxide, formed during thermal evaporation by reaction of aluminum with residual water at the polymer surface and in the gas phase. Likewise, a ~20 nm SiO_2 layer deposited on the glass surface can be seen in this picture. For simplicity reasons, this layer is never mentioned in the rest of this thesis, although, present in all the glass/ITO substrates.

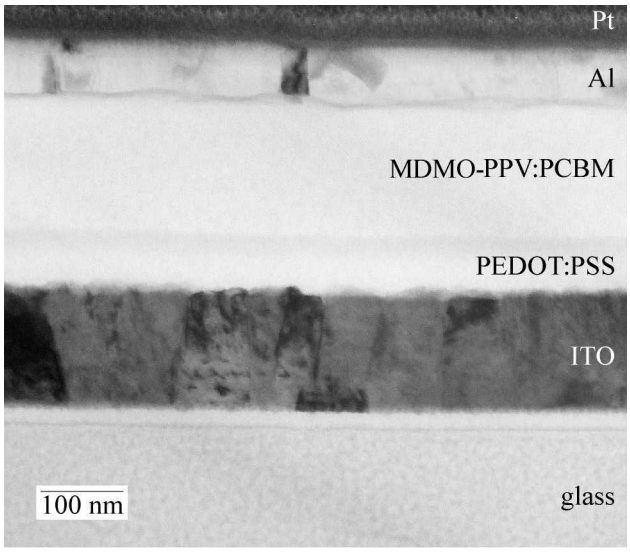

Figure 6.8 *TEM image of a ~100 nm thick slab of a glass/ITO/PEDOT:PSS/MDMO-PPV:PCBM(1:4 by wt.)/Al stack. The individual layers are clearly visible.*

TEM also gives an impression of the roughness of the different interfaces. Both the PEDOT:PSS and the MDMO-PPV:PCBM layers are rather smooth while the ITO and the thermally evaporated Al have a larger roughness. This conclusion is corroborated by the AFM measurements (Figure 6.2). The correspondence of the appearance of interfaces inferred from TEM and AFM, shows that subsequent processing steps do not significantly deteriorate layers or interfaces that were applied in previous steps.

No nanoscale morphology could be observed in the MDMO-PPV:PCBM layer. In contrast, TEM images of a cross-section made with cryo-ultramicrotomy of a spin cast film of an MDMO-PPV:PCBM composite on top of a PET substrate[54] and SEM images of a cross-section of the same composite film spin cast on glass/ITO[55] showed PCBM-rich domains all over depth. The absence of contrast within the active layer is attributed to FIB-induced damage.

The cutting process with a FIB results from the removal of material through ion sputtering. Similar sputtering artifacts as discussed for dynamic TOF-SIMS and XPS depth-profiling hold for FIB cutting and thinning.[31,32,51,56] Recent results indicate that amorphous damage might occur for organic specimen during FIB sputtering over the whole thickness of the slab,[51] or at least partially, even for extremely low bombardment energy.[57] Additionally, TEM-imaging of FIB-lift-out specimen can cause damage as well.[51] Therefore, it seems that FIB milling not necessarily shows the true nanoscale morphology of organic mixtures in subsequent TEM analysis.

6.5.2 Cross-sectional analysis by electron energy loss spectrometry

In transmission electron energy loss spectrometry (EELS), as performed in a scanning transmission electron microscope (STEM), inner-shell excitation of the atoms resulting in core-shell ionization by the monochromatic, highly energetic electron beam (> 100 keV) leads to characteristic edges in the electron energy loss spectrum of the transmitted electrons. The onset energies of each 'ionization' edge can be used to identify the presence of individual elements.[58] Additionally, the fine structure of the EELS spectrum can reveal binding state information (as in XPS).

Similar as for the TEM image in the previous paragraph, the dark layer in between Al and MDMO-PPV:PCBM in the STEM image is attributed to aluminum oxide, although LiF might also contribute to the contrast (Figure 6.9). Monitoring the intensity just after the Al L-edge, C K-edge, and S L-edge as recorded during an EELS line scan from Al down to ITO, clearly shows the individual organic layers (Figure 6.9a). Furthermore, sulfur can be found in MDMO-PPV:PCBM. Whether this is due to a contamination or migration of S during FIB preparation needs further investigation. Additionally, a higher resolution line scan is made at the MDMO-PPV:PCBM/LiF/Al interface. Enrichment of oxygen and the presence of F can be observed.[59]

At the MDMO-PPV:PCBM/LiF/Al interface an Al L-edge with more structural details and a stronger O K-edge can be observed than in the bulk of the Al layer. Furthermore, the Al L-edge signal

is stronger in the bulk. Therefore, it can be concluded that in the bulk of the aluminum layer more metallic Al is present in comparison with the MDMO-PPV:PCBM/LiF/Al interface where more oxidized Al is present.[60,61]

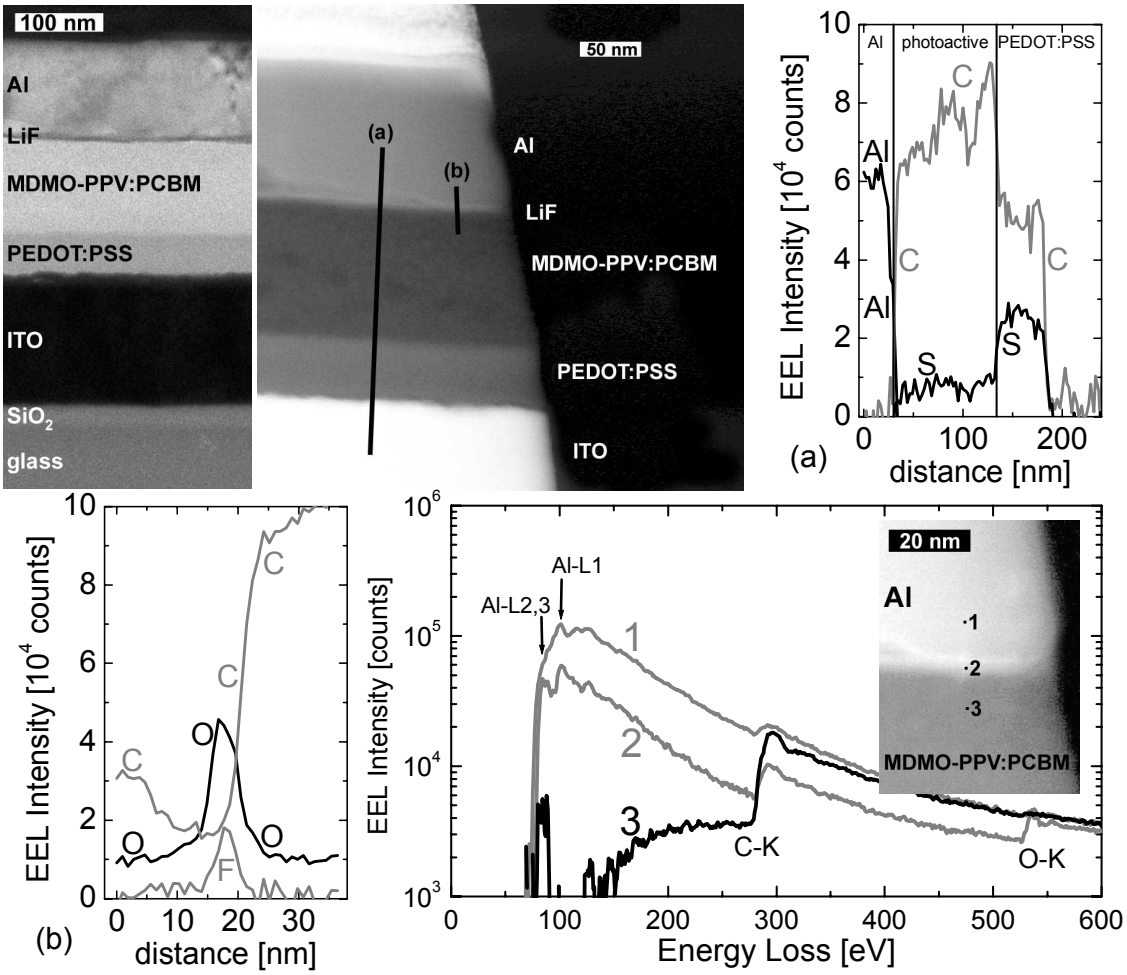

Figure 6.9 *Upper left: STEM image of a thin slab of a full glass/ITO/PEDOT:PSS/MDMO-PPV:PCBM(1:4 by wt.)/LiF/Al stack as used for EELS analysis. Middle: STEM image with the indications of the positions of the line scans (a) and (b) as taken during EELS analysis.* **(a, b)** *EELS line scans. Lower right: EELS spectra taken at the positions indicated in the STEM image.*

6.6 Interface study on ultrathin LiF/Al electrodes using static Quad-SIMS

Several mechanisms to explain the beneficial effect of a thin layer of LiF on the electron injection at the cathode have been suggested (for recent reviews, see ref. 6 and 9): the formation of a Li^+polymer$^-$ or Li^+molecule$^-$ charge-transfer complex after the reaction of LiF with Al to AlF_3 and liberated Li,[45,62-66] tunneling injection,[67,68] formation of a dipolar layer (or band bending caused by charge redistribution driven by the workfunction difference between LiF and the organic

underneath),[69-71] and the protection of the organic layer from reaction with aluminum.[62,64,69,72] For the latter, all authors involved agree that this can only be a secondary reason. Others showed that the tunneling mechanism alone cannot be the full explanation.[73-75] It should be noted that for all the above mentioned mechanisms, it is assumed that LiF forms a uniform layer completely covering the surface. Recent results showed that for the thickness typically used, LiF is more likely present as separate islands.[76]

Obviously, the two most likely mechanisms for electron injection enhancement, dubbed the doping and dipole mechanism, are mutually exclusive, but conclusive evidence for any of these two models is hard to find. Typically, photoemission spectroscopic techniques, such as XPS and UPS, are used to study these interfaces. Due to the complexity of the electronic and structural processes that take place in organic materials during photoemission spectroscopic measurements, the utmost care to establish the reliability of conclusions is required.[77] Unfortunately, XPS[78] and UPS[9] cannot always give unequivocal information on the discrimination between the different mechanisms. Therefore, another surface analysis technique is used here, static Quad-SIMS.[79]

Knowledge about the presence or absence of the elements and compounds around the interface enables us to discriminate between the dipole and the doping model. Just as for the mixture of MDMO-PPV and PCBM, the same beneficial effect of LiF/Al has been observed for the pure compounds. Therefore, SIMS spectra were measured at the interface of the organic and the LiF layers to determine the chemical state of the LiF layer on the surfaces of MDMO-PPV and PCBM substrates, taking into account the possible influence of aluminum. The samples investigated were prepared as regular devices where it is assumed that the interface does not differ significantly between devices with a metal top layer of a few angstroms thick compared to a 100 nm thick metal top electrode.

A popular explanation of the improved electron injection by LiF is the doping of the active polymer by Li liberated by a reaction between LiF and Al deposited on top of this. Although the Gibbs free energy required to liberate Li was estimated at 112.8 kJ/mol, making it an endothermic and hence unfavorable reaction, Mason *et al.* suggested that this is only the case for bulk LiF and that the reaction might be exothermic in the case of small isolated clusters of LiF.[64]

Because the reaction would give rise to AlF_3 on the surface of the organic layer, the presence of AlF_3 has been investigated. Figure 6.10 shows the comparison between the SIMS spectra of a pure AlF_3 reference sample and of the MDMO-PPV/LiF/Al and PCBM/LiF/Al interfaces. The peaks of interest of the AlF_3 reference samples are Al^+, AlF^+, and AlF_2^+ at the *m*/*z* values of 27, 46, and 65 D. The AlF^+ and AlF_2^+ peaks should be present for the MDMO-PPV/LiF/Al and PCBM/LiF/Al samples, but they either have very low intensity or are completely missing. The low intensity of the AlF^+ and AlF_2^+ signals that are present are background signals caused by the underlying layers of MDMO-PPV and PCBM. Note that the drop in intensity for these peaks cannot be explained with the matrix effect,

because then all signal intensities should drop by more or less the same amount, but the decrease in the Al ion signal is much less dramatic than that of the AlF^+ and AlF_2^+ signals.

Hence, the absence of AlF_3 related signals in the SIMS spectra of the MDMO-PPV/LiF/Al and PCBM/LiF/Al samples is strong evidence that the proposed reaction between LiF and Al does not occur on MDMO-PPV or PCBM. Greczynski *et al.*[72] claimed that CsF decomposes on PFO, based on the ratio of CsF to the amount of Al needed to completely decompose CsF, and others have made the suggestion for LiF on Alq_3 based on rather indirect methods. However, Greczynski *et al.* showed with XPS that for the case of LiF on PFO no evidence can be found that LiF decomposes in the presence of Al.

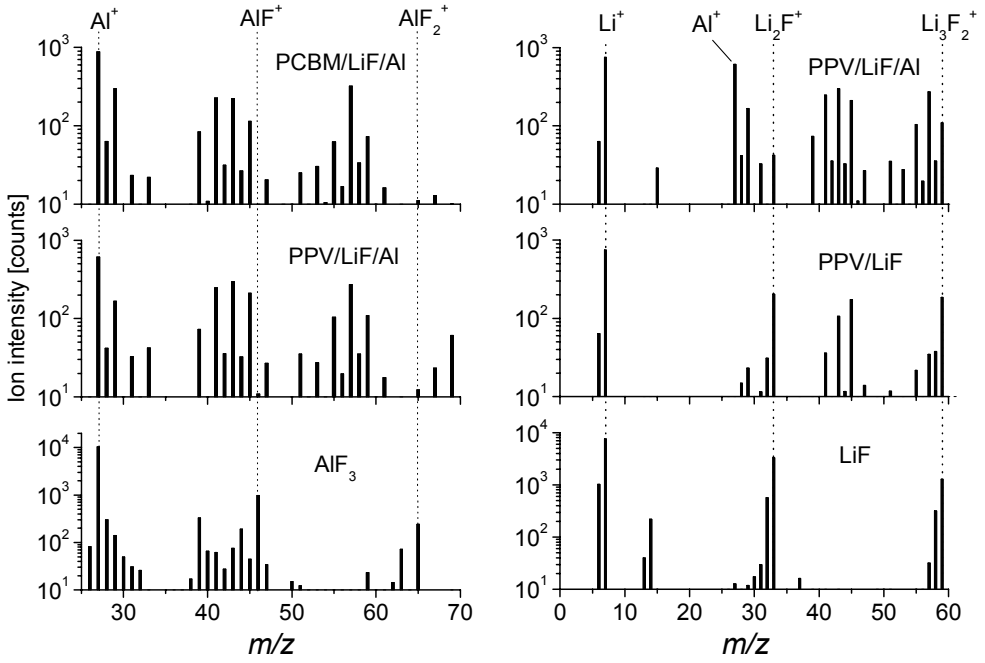

Figure 6.10 *Left: Comparison of the AlF_3 reference with MDMO-PPV/LiF/Al and PCBM/LiF/Al. Note the logarithmic scale of the ion intensity axis. Right: The comparison between a LiF reference sample, an MDMO-PPV/LiF and an MDMO-PPV/LiF/Al sample shows that LiF stays intact on the surface of MDMO-PPV, regardless of the presence of Al.*

Because all studied alkali and alkaline earth metal fluorides seem to improve the electron injection of the cathode,[73] a general mechanism is likely to exist. These results indicate, together with those of Greczynski *et al.* that the proposed LiF/Al reaction to AlF_3 is *not* that general mechanism.

However, the reaction to AlF_3 was only proposed as a possible mechanism to obtain free Li atoms, which could subsequently dope the organic material. Kido *et al.* showed[80] that a Li-doped Alq_3 layer exhibited a luminance an order of magnitude higher than an Alq_3 layer without Li, suggesting that Li-doping of the organic layer may also occur for alkali and alkaline earth metal fluoride containing devices.

If Li is liberated on the surface of the organic material, by reaction with Al or in any other conceivable way, then LiF should no longer be visible on the surface of the organic material. Figure 6.10 shows a comparison between static Quad-SIMS spectra from a LiF reference sample, and of LiF on MDMO-PPV, with and without Al on top. The LiF panel at the top of Figure 6.10 shows a clear ion cluster series of $Li_nF^+_{n-1}$, although only a small part is shown here. The MDMO-PPV/LiF panel in the middle clearly shows the same ion pattern for LiF. Unfortunately, an Al layer on top of the LiF layer attenuates the LiF cluster ion signals, as shown in the MDMO-PPV/LiF/Al panel. Identical results have been obtained for the PCBM samples.

Because of the small amount of LiF deposited, the presence of LiF on top of the organic layers indicates that no liberation of Li takes place in any way, as the ion cluster series of $Li_nF^+_{n-1}$ can only be formed if there are large clusters of LiF on the surface, which is a rather unlikely occurrence if most of the LiF has reacted. Hence, a mechanism in which Li dopes the underlying organic layer is unlikely.

Concluding, static Quad-SIMS investigations show that LiF does not completely dissociate or react with aluminum to AlF_3 on both pure MDMO-PPV and pure PCBM, excluding the doping model as the dominant mechanism for the explanation of enhanced electron injection. Note that the validity of the dipole mechanism has not been proved, but that the validity of the doping model has been disproved. Recent results by Feng *et al.* suggest that apart from intact LiF, aluminum oxide and metallic Al, also Li^+ doped PPV is present at the interface.[48]

Additionally, to study possible interactions between deposited aluminum and the underlying organic layer, XPS measurements were performed using only relative shifts. These shifts indicated a reaction between aluminum and the carboxylic oxygen of PCBM. MDMO-PPV is resistant to reaction with aluminum.[41]

6.7 Conclusions

The applicability of several depth-profiling and cross-sectioning techniques for the analysis of plastic solar cells has been investigated. Cryogenic RBS has found to be very useful for quantifying layer-to-layer diffusion, while dynamic TOF-SIMS is very useful for identifying contaminations, layer-to-layer diffusion, and studying buried interfaces. The latter also holds for XPS depth-profiling and EELS in a STEM. Cross-sectioning plastic solar cells with a FIB does not damage the layered structure, but causes damage to the nanoscale morphology within the individual layers. For the sputter depth-profiling techniques, conversion of the intensity-time profile to a concentration-depth profile is hampered mainly by the inhomogeneous sputtering behavior of the individual layers.

Interface integrity has been investigated with AFM on consecutive layers, and TEM on a thin cross-section. AFM shows that the spikes of ITO do not result in a rough PEDOT:PSS surface. The spin cast PEDOT:PSS film on top of ITO is extremely smooth. The same holds for the subsequent

organic layer, although some unevenness can be observed for phase-separating mixtures. Thermal evaporation of Al onto conjugated organics results in extremely rough top Al contacts. The interface investigations as performed with TEM on cross-sections of the fully processed solar cells corroborate with these AFM measurements.

The buried interface between the photoactive layer and the top aluminum contact has been investigated with several techniques. The combined results of dynamic TOF-SIMS, XPS depth-profiling, and EELS show without doubt that the interface between the organic layer and the top aluminum contact is enriched in oxygen. This enrichment is attributed to the formation of aluminum oxide during the evaporation of aluminum. Formation of aluminum oxide is thought to take place with the water present as residual gas in the vacuum chamber and on the sample surface. A thin layer of aluminum oxide at the buried interface might act as an insulating layer. Additionally, XPS depth-profiling suggests that both metallic and oxidized Al are present at the MDMO-PPV/LiF/Al interface.[81] No Al diffusion into the organic layers could be detected.[82] Quad-SIMS investigations showed that evaporation of Al on the LiF-covered organic surfaces studied does not result in complete dissociation of LiF. Therefore, doping as the main mechanism for the electron injection enhancement into MDMO-PPV or PCBM seems unlikely.

Furthermore, the stability of the ITO electrode has been investigated. Indium diffusion into PEDOT:PSS is promoted by water uptake. Water is thought to liberate the proton of PSS. Acidic etching, subsequently, leads to degradation of ITO. Indium diffusion has been found to stop at the interface with the active layer, and can be suppressed by appropriate annealing of PEDOT:PSS during the device preparation. No Sn diffusion has been observed. Polysiloxane contamination at the buried interface with the top Al contact has been observed with dynamic TOF-SIMS. It seems to originate from the synthesis. Because of the surfactant nature of polysiloxanes it floats to the surface of the active layer (during spin casting).

Concluding, it has been shown that compositional and structural analysis of plastic solar cells can reveal many aspects of the interior of the layered structure. Others have shown that lifetime and stability issues of plastic LEDs often are related to diffusion of contaminations or electrode species. The detailed information that can be obtained by the depth-profiling and cross-sectioning techniques used here make them therefore very suitable for investigating lifetime and stability issues of plastic solar cells.

6.8 Experimental section

Materials. The materials used were poly[2-methoxy-5-(3′,7′-dimethyloctyloxy)-1,4-phenylene vinylene] (MDMO-PPV) synthesized via the Gilch-route[83], 1-(3-methoxycarbonyl)propyl-1-phenyl-[6,6]-methanofullerene (PCBM)[84], 1-[3-(methoxycarbonyl)propyl]-1-(*d*5-phenyl)[6,6]C_{61} (*d*5-PCBM),[85] polyethylenedioxythiophene:polystyrenesulfonate[86] (PEDOT:PSS) either from Bayer AG (Baytron P VPAI 4083) resulting in 75-100 nm thick films, or generously provided by Philips

Research Laboraties Eindhoven resulting in 350 nm thick films, LiF and anhydrous AlF_3 from Aldrich, and Al from Engelhard-Clal. A glass plate fully covered with a 40 nm thick layer of indium tin oxide (ITO) was used as the substrate for TOF-SIMS and Quad-SIMS. For RBS and TEM, the glass plate was fully covered with 155 nm thick ITO. Glass plates covered with 160 nm patterned ITO were used for XPS depth-profiling and EELS.[87] Schott D263 glass plates were occasionally used as substrate for dynamic TOF-SIMS.

Sample preparation. The ITO covered glass substrates were first cleaned by ultrasonic treatment in acetone, rubbing with soap, rinsing with de-mineralized water, refluxing with iso-propanol, and finally 20 minutes UV ozone treatment. Subsequently, a 70-350 nm thick layer of PEDOT:PSS (thickness variation between samples as a result of differences in batches PEDOT:PSS and substrates) was spin coated from an aqueous dispersion under ambient conditions on the cleaned substrates and the layer was dried by annealing the substrate for 1 minute, either at 100 °C without cooling (for Ar^+ dual-beam TOF-SIMS, Quad-SIMS, TEM, and RBS, unless stated otherwise), or at 180 °C and subsequently cooled for 1 minute at 25 °C (for Cs^+/Ga^+ dual-beam TOF-SIMS, XPS depth-profiling, and EELS). Then the ~100 nm thick active layer of either pure MDMO-PPV, pure PCBM or a mixture of both was spin coated from a chlorobenzene solution (or from *o*-xylene solution at ~60 °C for RBS) on top of the PEDOT:PSS layer and the sample was transferred to an N_2 atmosphere glove box. The organic solutions are stirred vigorously overnight while keeping them in the dark. All polymer layers were spin cast via a two-step procedure employing a home-made chuck, which requires no vacuum, on a Chemat Technology spin coater model KW-4A placed in a laminar flowbox. First 7 seconds at 500 rpm followed by 35 seconds at 1500 rpm. Finally, for the full device structures ~10 Å LiF and subsequently 100-110 nm aluminum layers were deposited by thermal evaporation in a vacuum chamber (5×10^{-6} mbar, 1 ppm O_2 and < 1 ppm H_2O). The samples were rotated at ~1 Hz during deposition to guarantee homogeneous films. For Quad-SIMS, samples without top contact, with LiF (5 Å), with Al (5 Å), and with LiF(5 Å)/Al(5 Å) were prepared. The reference samples prepared for Quad-SIMS were 60 nm Al or LiF evaporated on a previously cleaned silicon (100) wafer, and AlF_3 powder pressed into indium foil. All samples are stored in the dark in an N_2 atmosphere glove box.

Atomic force microscopy and surface profilometry. Either a solver P47H scanning probe microscope (NT-MDT Co., Moscow, Russia), a Digital Instruments Dimension 3100, or a Digital Instruments Multimode with a Nanoscope IV controller, all in resonant mode,[88] were used to measure topography. All AFM measurements were performed under ambient conditions using both NT-MDT NSG01 (force constant is typically 5.5 N/m) and NSG10 (force constant is typically 11.5 N/m) cantilevers. Film thickness, surface profiles, and crater depths were measured with a Tencor P10 surface profiler.

Rutherford backscattering spectrometry*:* Samples for RBS of approximately 1.1×2.5 cm^2 were mounted on the sample holder in the glove box. A cryo paste was used to improve heat conduction between the sample and sample holder during the cryogenic measurements. The samples were transported to the cryogenic RBS setup in a sealed holder in N_2 atmosphere and transferred to the analysis chamber by a load lock, without exposure to air. The RBS measurements were performed using a 2 MeV He^+ beam from the 2-30 MeV AVF cyclotron at Eindhoven University of Technology using a current of typically 10 nA. Using a solid-state detector with a solid angle of 2.5 mrad, the count rate was limited to approximately 1000 counts/s minimizing pile up. The size of the beam spot is 1×1 mm^2. The angle of incidence of the beam relative to the sample surface could be adjusted between 0° and 90°, while the RBS detector could be moved to select any scattering angle between 0° and 180°. The simulations of the RBS measurements were performed with the RUMP code.[24] For accurate RUMP simulations it was necessary to determine the composition of the glass and ITO in separate experiments. The composition of the glass was determined with the beam directed along the surface normal ($\alpha = 90°$ and $\theta = 165°$) and gave 62.0 at.-% O, 25.6 at.-% Si, 9.6 at.-% Na and 2.8 at.-% Ca. The composition of ITO, determined at the same geometry equals 61 at.-% O and 39 at.-% In.

The Sn fraction was disregarded because In and Sn were indistinguishable in the RBS measurements and the Sn fraction in ITO is small (1-10%).[22] In the simulations the composition of the PEDOT:PSS was assumed to be 43 at.-% C, 34 at.-% H, 17 at.-% O and 5 at.-% S.[89]

Dynamic TOF-SIMS. The samples have been exposed to an ambient atmosphere while mounting the samples on the sample holder (~30 min.), unless stated otherwise. The dynamic SIMS depth-profiling measurements were performed on an ION-TOF TOF-SIMS IV apparatus (which saturates at 1-3 $\times 10^5$ counts) in dual-beam[28] mode: either 10 to 35 nA Ar^+ (1 and 3 keV) at 45° rastered over at least 150×150 μm^2 for sputtering and a 1.5 pA 11 keV Ar^+ beam at 45° rastered over 50×50 μm^2 for analysis, or 73 nA 1 keV Cs^+ at 45° rastered over 300×300 μm^2 for sputtering and a 15 keV Ga^+ beam (1.9, 2.5, and 3.0 pA ac) at 45° rastered over 50×50 μm^2 for analysis. The depth profiles were measured in the non-interlaced mode (longer sputter and data acquisition cycles) to avoid charging. Effective charge compensation was obtained by using an electron flood gun (20 eV). All depth profiles were mass calibrated on C_xH_y fragments.

XPS depth-profiling. During transportation the samples have been exposed to an ambient atmosphere. XPS depth-profiling measurements were performed with a VG-Theta-Probe using a monochromatic Al Kα anode X-ray source. Sputtering was performed with a 2.5 μA Ar^+ (2 keV) beam scanned over a 3 × 3 mm^2 area whilst rotating the sample. Effective charge compensation was obtained by using an electron flood gun (20 eV). A 400 μm X-ray spot size was used for analysis. XPS spectra were recorded with a resolution of 0.2 eV.

Cross-sectioning with a focused ion beam. During transportation the samples have been exposed to an ambient atmosphere. To investigate cross-sectional details of a working solar cell device a thin 12 × 3.5 × 0.3 μm^3 slab from a fully processed polymer photovoltaic cell was prepared via coarse milling with a FIB (beam diameter is ~ 10 nm, FEI Strata FIB200) with a high Ga^+ beam current, and subsequently milled and polished with a low Ga^+ beam current to approximately 100 nm thickness.[52] This thin slice is cut out of the sample, and subsequently lifted out with a sharp tip glass rod mounted on a micromanipulator, to be placed on a TEM-grid. A similar procedure was used to cut (7000 pA, 30 keV Ga^+ under an angle of 52°) a slab for combined STEM and EELS investigations. Here, the slab is 'glued' on a Si rod and, subsequently milled further (100 pA Ga^+) until electron transparency was obtained. The thickness of the obtained electron transparent window was between 75 - 200 nm.

Transmission electron microscopy and electron energy loss spectrometry. For transmission electron microscope (TEM) investigations the cross-sections were transferred on copper grids coated with a carbon film consisting of woven-mesh-like holes of different sizes and shapes. TEM was performed using a Jeol 2000FX operated at 80 kV, except for the combined STEM and EELS investigations. For the latter the slab glued on a Si rod was analyzed with a FEI Tecnai F30ST STEM operated at 300 kV with a Gatan image filter (GIF). All EELS spectra were recorded with a collection angle of ~10 mrad.

Static quadrupole secondary ion mass spectrometry. All samples were transported in a dry nitrogen atmosphere to a VG Ionex system equipped with a VG Clam II analyzer, Mg/Al Kα dual anode X-ray source, VG MIG-102 Ga^+ and VG FAB61 ion source, LEG 31F electron flood gun and M12-2 s (<800 amu) quadrupole. The static SIMS measurements were performed with the electron impact gun (FAB 61) using Xe at 5 keV, while taking care to keep the total ion dose for each measurement within the static limit.

6.9 References and notes

1 C.J. Brabec, V. Dyakonov, J. Parisi, N.S. Sariciftci (Eds.), *Organic Photovoltaics*: *Concepts and Realization, Springer Series in Materials Science Vol. 60* Springer-Verlag, London, **2003**.

2 J.-M. Nunzi, *C. R. Physique* **2002**, *3*, 523.

3 T.P. Nguyen, P. Destruel, in *Handbook of Luminescence, Display Materials, and Devices* (Ed: H.S. Nalwa, L.S. Rohwer), vol. 1, p. 1, Am. Sci. Publishers, Stevenson Ranch, **2003**.

4 D. Braun, *Materials Today* **2002**, *5*, 32.

5 R.H. Friend, R.W. Gymer, A.B. Holmes, J.H. Burroughes, R.N. Marks, C. Taliani, D.D.C. Bradley, D.A. Dos Santos, J.L. Brédas, M. Löglund, W.R. Salaneck, *Nature* **1999**, *397*, 121.

6 (a) T.M. Brown, F. Cacialli, *J. Pol. Sci. B* **2003**, *41*, 2649; (b) T.M. Brown, J.S. Kim, R.H. Friend, F. Cacialli, R. Daik, W.J. Feast, *Appl. Phys. Lett.* **1999**, *75*, 1679.

7 (a) D. Cahen, A. Kahn, *Adv. Mater.* **2003**, *15*, 271; (b) A. Kahn, N. Koch, W. Gao, *J. Pol. Sci. B* **2003**, *41*, 2529.

8 S.C. Veenstra, H.T. Jonkman, *J. Pol. Sci. B* **2003**, *41*, 2549.

9 (a) M. Fahlman, W.R. Salaneck, *Surf. Sci.* **2002**, *500*, 904; (b) W.R. Salaneck, M. Lögdlund, M. Fahlman, G. Greczynski, Th. Kugler, *Mater. Sci. Eng. R* **2001**, *34*, 121.

10 L. Yan, Y. Gao, *Thin Solid Films* **2002**, *417*, 101.

11 H. Ishii, K. Sugiyama, E. ITO, K. Seki, *Adv. Mater.***1999**, *11*, 605.

12 A. van Dijken, A. Perro, E.A. Meulenkamp, K. Brunner, *Org. Electr.* **2003**, *4*, 131.

13 C.J. Brabec, S.E. Shaheen, C. Winder, N.S. Sariciftci, P. Denk, *Appl. Phys. Lett.* **2002**, *80*, 1288.

14 (a) L. Ke, K. Zhang, N. Yakovlev, S.J. Chua, P. Chen, *Mater. Sci. Eng. B* **2003**, *97*, 1; (b) L. Ke, S.J. Chua, K. Zhang, N. Yakovlev, *Appl. Phys. Lett.* **2002**, *80*, 2195; (c) S.J. Chua, L. Ke, R.S. Kumar, K. Zhang, *Appl. Phys. Lett.* **2002**, *81*, 1119; (d) K.K. Lin, S.J. Chua, W. Wang, *Thin Solid Films* **2002**, *417*, 36; (e) K.K. Lin, S.J. Chua, S.F. Lim, *J. Appl. Phys.* **2001**, *90*, 976; (f) S.F. Lim, L. Ke, W. Wang, S.J. Chua, *Appl. Phys. Lett.* **2001**, *78*, 2116.

15 P. Cusumano, F. Buttitta, A. Di Cristofalo, C. Cali, *Synth. Met.* **2003**, *139*, 657.

16 D.Y. Kondakov, J.R. Sandifer, C.W. Tang, R.H. Young, *J. Appl. Phys.* **2003**, *93*, 1108.

17 M. Ishii, *R&D Rev. Toyota CRDL* **2003**, *38*, 55.

18 G. Xu, *Chin. J. Pol. Sci.* **2003**, *21*, 527.

19 M. Koeberg, D.S. Elson, P.M.W. French, D.D.C. Bradley, *Synth. Met.* **2003**, *139*, 925.

20 J.S. Kim, P.K.H. Ho, C.E. Murphy, N. Baynes, R.H. Friend, *Adv. Mater.* **2002**, *14*, 206.

21 It should be noted that the topology of ITO strongly depends on the batch of substrates used. The AFM measurement shown represents the smoothest ITO surfaces encountered.

22 M.P. de Jong, *Interface Stability in Polymer Light-Emitting Diodes*, Ph. D. Thesis, Eindhoven University of Technology, **2000**.

23 M.P. de Jong, L.J. van IJzendoorn, M.J.A. de Voigt, *Nucl. Instrum. Methods Phys. Res. B.* **2000**, *161-163*, 207.

24 L.R. Doolittle, *Nucl. Instrum. Methods Phys. Res. B* **1985**, *9*, 344.

25 RBS measurements have been performed by K.P.H. Kivits and Dr. C.M. Leewis in the group of Dr. L.J. van IJzendoorn and Prof. M.J.A. de Voigt at the Eindhoven University of Technology.

26 M.P. de Jong, L.J. van IJzendoorn, M.J.A. de Voigt, *Appl. Phys. Lett.* **2000**, *77*, 2255.

27 S. Oswald, R. Reiche, *Appl. Surf. Sci.* **2001**, *179*, 307.

28 E. Niehuis, T. Grehl, *ToF-SIMS: Surface Analysis by Mass Spectrometry* (Ed: J.C. Vickerman, D. Briggs), Chapter 28, p. 753, IM Publications, Chichester, **2001**.

29 E. Darque-Ceretti, R. Combarieu, M. Aucouturier, *Sci. Techn. Appl.* **1999**, *292*, 141.

30 P.C. Zalm, *Mikrochim. Acta* **2000**, *132*, 243.

31 S. Oswald, S. Baunack, *Thin Solid Films* **2003**, *425*, 9.

32 S. Hofmann, *Surf. Interface Anal.* **2000**, *30*, 228.

33 It should be noted that loss of conjugation in (semi)conductive organic layers as a result of ion sputtering can result in loss of heat and charge conductivity, thereby influencing heat dissipation and charge neutralization. Care should be taken to ensure charge neutralization and a constant temperature during analysis.

34 This only holds for the type of instrument used.

35 In the TOF-SIMS instrument used, the samples are not rotated. During sputtering the ion beam typically scans the surface in a regular fashion. Consequently, this may lead to a regular array of well-aligned low and high regions, called ripples.

36 TOF-SIMS measurements were performed by Dr. C.W.T. Bulle-Lieuwma at Philips CFT.

37 Both the sputter and analysis beam bombard the sample with Ar^+ ions.

38 (a) S. Hofmann, *Surf. Interface Anal.* **2003**, *35*, 556; (b) T. Wöhner, G. Ecke, H. Rössler, S. Hofmann, *Surf. Interface Anal.* **1998**, *26*, 1.

39 A Cs^+ beam is used for sputtering, whereas a Ga^+ beam is used for analysis.

40 It should be noted that the crater depths are measured with line scans using a surface profiler. Due to the dimensions of the probe tip used, the lateral resolution is only 200 nm.

41 W.J.H. van Gennip, *The Analysis of Polymer Interfaces, a Combined Approach*, Ph. D. Thesis, Eindhoven University of Technology, **2003**.

42 It should be noted that the sputtering conditions for the three different multi-layered device structures, as investigated with AFM, were not identical.

43 Film densities were calculated by combining the carbon content of the material with the total mass of carbon present in the films. The latter was measured by combustion and subsequent IR detection in He carrier gas with a carbon and sulfur analyzer.

44 W.J.H. van Gennip, J.K.J. van Duren, A.B. Sieval, J.C. Hummelen, R.A.J. Janssen, J.W. Niemantsverdriet, *manuscript in preparation*.

45 H. Heil, J. Steiger, S. Karg, M. Gastel, H. Ortner, H. von Seggern, M. Stössel, *J. Appl. Phys.* **2001**, *89*, 420.

46 (a) R.I.R. Blyth, S.A. Sardar, F.P. Netzer, M.G. Ramsey, *Appl. Phys. Lett.* **2000**, *77*, 1212; (b) N. Koch, A. Pogantsch, E.J.W. List, G. Leising, R.I.R. Blyth, M.G. Ramsey, F.P. Netzer, *Appl. Phys. Lett.* **1999**, *74*, 2909.

47 T.P. Nguyen, S. de Vos, V.H. Tran, *J. Appl. Phys.* **1997**, *81*, 6809.

48 X.D. Feng, D. Grozea, Z.H. Lu, *Mat. Res. Soc. Symp. Proc.* **2003**, *734*, 175.

49 XPS depth-profiling measurements have been performed by Dr. R.G. White at Thermo Electron Corporation (United Kingdom) in collaboration with Dr. P.C. Thüne (Dutch Polymer Institute).

50 H.K. Plummer, *Microsc. Microanal.* **1997**, *3*, 239.

51 L.A. Giannuzzi, F.A. Stevie, *Micron* **1999**, *30*, 197.

52 J. Loos, J.K.J. van Duren, F. Morrissey, and R.A.J. Janssen, *Polymer* **2002**, *43*, 7493.

53 The combined FIB and TEM investigations were performed by Dr. J. Loos (Dutch Polymer Institute) and Dr. F. Morrisey (FEI company, Eindhoven). The combined FIB, EELS, and STEM studies were performed by Dr. M. Kaiser and Dr. J.G.M. van Berkum at Philips CFT.

54 T. Martens, J. D'Haen, T. Munters, Z. Beelen, L. Goris, J. Manca, M. D'Olieslaeger, D. Vanderzande, L. De Schepper, R. Andriessen, *Synth. Met.* **2003**, *138*, 243.

55 H. Hoppe, M. Niggeman, C. Winder, A. Hinsch, J. Kraut, R. Hiesgen, D. Meissner, N.S. Sariciftci, *Adv. Funct. Mater.* **2004**, *in press*.

56 The damage induced by the FIB is, however, less than for the ion sputtering depth-profiling techniques because of the smaller angle between the sample surface and ion beam while cutting with a FIB. Typical penetration depth of Ga^+ during FIB-cutting is 10 nm.

57 Zs. Czigany, J. Neidhardt, I.F. Brunell, L. Hultman, *Ultramicroscopy* **2003**, *94*, 163.

58 (a) J. Mayer, *Adv. Imaging. Elect. Phys.* **2002**, *123*, 399; (b) J. Mayer, J.M. Plitzko, *Mat. Res. Soc. Symp. Proc.* **2001**, *589*, 279.

59 The slab investigated is too thick to measure Li (low ionisation energy of 54.7 eV).

60 C.C. Ahn, O.L. Krivanek, *EELS Atlas*, ASU HREM Facility & Gatan, Tempe, **1983**.

61 AlO gives more details as a result of the more discrete electronic energy levels, whereas Al contains a continuum of energy levels (band structure). The thickness of the slab influences to what extent AlO can be separated from Al by EELS.

62 S.D. Wang, S.K. Fung, S.L. Lai, S.W. Tong, C.S. Lee, S.T. Lee, H.J. Zhang, S.N. Bao, *J. Appl. Phys.* **2003**, *94*, 169.

63 Q.T. Le, L. Yan, Y. Gao, M.G. Mason, D.J. Giesen, C.W. Tang, *J. Appl. Phys.* **2000**, *87*, 375.

64 M.G. Mason, C.W. Tang, L.S. Hung, P. Raychaudhuri, J. Madathil, D.J. Giesen, L. Yan, Q.T. Le, Y. Gao, S.T. Lee, L.S. Liao, L.F. Cheng, W.R. Salaneck, D.A. dos Santos, J.L. Brédas, *J. Appl. Phys.* **2001**, *89*, 2756.

65 G. Parthasarathy, C. Shen, A. Kahn, S.R. Forrest, *J. Appl. Phys.* **2001**, *89*, 4986.

66 L.S. Hung, S.T. Lee, *Mater. Sci. Eng. B* **2001**, *85*, 104.

67 L.S. Hung, C.W. Tang, M.G. Mason, *Appl. Phys. Lett.* **1997**, *70*, 152.

68 J. Yoon, J.J. Kim, T.W. Lee, O.O. Park, *Appl. Phys. Lett.* **2000**, *76*, 2152.

69 K. Ihm, T.H. Kang, K.J. Kim, C.C. Hwang, Y.J. Park, K.B. Lee, B. Kim, C.H. Jeon, C.Y. Park, K. Kim, Y.H. Tak, *Appl. Phys. Lett.* **2003**, *83*, 2949.

70 S.E. Shaheen, G.E. Jabbour, M.M. Morrell, Y. Kawabe, B. Kippelen, N. Peyghambarian, M.F. Nabor, R. Schlaf, E.A. Mash, N.R. Armstrong, *J. Appl. Phys.* **1998**, *84*, 2324.

71 M.A. Baldo, S.R. Forrest, *Phys. Rev. B* **2001**, *64*, 085201.

72 G. Greczynski, W.R. Salaneck, M. Fahlman, *Appl. Surf. Sci.* **2001**, *175-176*, 319.

73 X. Yang, Y. Mo, W. Yang, G. Yu, Y. Cao, *Appl. Phys. Lett.* **2001**, *79*, 563.

74 B. Masenelli, E. Tutis, M.N. Bussac, L. Zuppiroli, *Synth. Met.* **2001**, *122*, 141.

75 M. Stössel, J. Staudigel, F. Steuber, J. Blässing, J. Simmerer, A. Winnacker, *Appl. Phys. Lett.* **2000**, *76*, 115.

76 T. Yokoyama, D. Yoshimura, E. Ito, H. Ishii, Y. Ouchi, K. Seki, *Jpn. J. Appl. Phys.* **2003**, *42*, 3666.

77 N. Koch, C. Chan, A. Kahn, J. Schwartz, *Phys. Rev. B* **2003**, *67*, 195330.

78 G. Greczynski, M. Fahlman, W.R. Salaneck, *J. Chem. Phys.* **2001**, *114*, 8628.

79 Static Quad-SIMS and XPS measurements have been performed by Dr. W.J.H. van Gennip in the group of Prof. J.W. Niemantsverdriet at the Eindhoven University of Technology.

80 J. Kido, T. Matsumoto, *Appl. Phys. Lett.* **1998**, *73*, 2866.

81 It should be noted that further investigations are necessary to ensure that this is not due to a limited depth resolution as a result of sputtering-induced roughness of the crater bottom.

82 It should be noted that the diffusion length (3 nm) typically found for Al into underlying conjugated organics cannot be resolved with the techniques used.

83 MDMO-PPV was generously provided by Philips Research Laboratories Eindhoven. Synthesis as described in H. Becker, H. Spreitzer, W. Kreuder, E. Kluge, H. Schenk, I. Parker, Y. Cao, *Adv. Mater*. **2000**, *12*, 42 and references therein.

84 J.C. Hummelen, B.W. Knight, F. LePeq, F. Wudl, J. Yao, C.L. Wilkins, *J. Org. Chem.* **1995**, *60*, 532.

85 *d*5-PCBM was synthesized by Dr. A.B. Sieval in the group of Prof. J.C. Hummelen at Groningen University.

86 (a) L. Groenendaal, G. Zotti, P.H. Aubert, S.M. Waybright, J.R. Reynolds, *Adv. Mater.* **2003**, *15*, 855; (b) L. Groenendaal, F. Jonas, D. Freitag, H. Pielartzik, J. R. Reynolds, *Adv. Mat*. **2000**, *12*, 481.

87 ITO covered glass substrates were generously provided by Philips Research Laboratories Eindhoven.

88 Synonymous to resonant mode is dynamic, vibrational, and tapping mode.

89 A.J. Heeger, A.N. Aleshin, S.R. Williams, *Synth. Met.* **1998**, *94*, 173.

Summary

Plastic solar cells have attracted considerable attention in the past few years owing to their potential of providing environmentally safe, flexible, lightweight, inexpensive, efficient solar cells. Especially, bulk-heterojunction solar cells consisting of a mixture of a conjugated donor polymer with a methanofullerene acceptor sandwiched between two electrodes (Figure 1) are considered as a promising approach. In 2000 fullerene-based bulk-heterojunction solar cells reached power conversion efficiencies of < 1%. Improving the performance, stability, and lifetime of bulk-heterojunction solar cells requires more insight in the preparation, and operation of these devices.

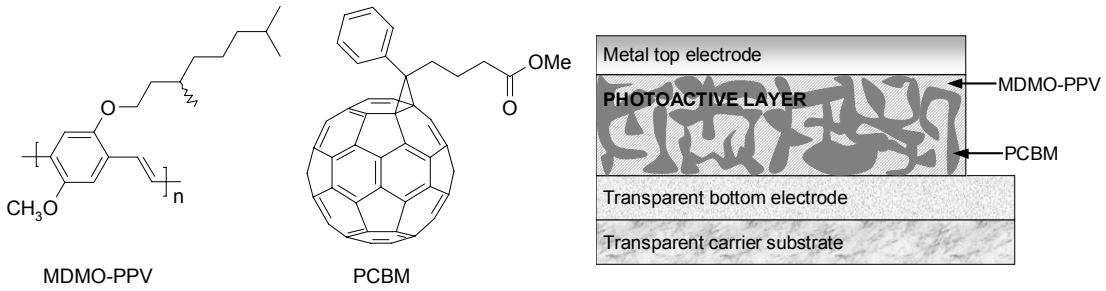

Figure 1 *Left: Molecular structures of MDMO-PPV and PCBM. MDMO-PPV and PCBM are present as a mixture in the photoactive layer of the bulk-heterojunction solar cell with a device configuration as depicted on the right.*

This thesis discusses the preparation, and morphological and electrical characterization of devices made from poly[2-methoxy-5-(3′,7′-dimethyloctyloxy)-1,4-phenylene vinylene] (MDMO-PPV), 1-(3-methoxycarbonyl)propyl-1-phenyl-[6,6]-methanofullerene (PCBM), and their mixtures (Figure 1). Bulk-heterojunction solar cells made from MDMO-PPV and PCBM reach power conversion efficiencies of 2.5% under simulated solar light. It is shown for the first time that replacing the orange MDMO-PPV with a low-bandgap conjugated material results in a more red-shifted spectral response of these solar cells, necessary for a larger overlap with the solar emission spectrum. Additionally, in an attempt to control the nanoscale morphology of the photoactive layer the first example of a covalently linked donor polymer with pendant fullerenes incorporated in working solar cells is reported. Unfortunately, both experiments resulted in a decrease of the power conversion efficiency compared to the mixture of MDMO-PPV and PCBM. These results indicated that more fundamental questions concerning the operation of the device and the influence of morphology must be addressed, before a rational improvement can be expected.

Morphology strongly influences transport of charge carriers in organic semiconductor films. First, films of the pure components have been investigated. It has been found that the zero-field electron mobility in pure PCBM (2×10^{-3} cm^2/Vs) is 4000 times larger than the zero-field hole mobility in pure MDMO-PPV (5×10^{-7} cm^2/Vs). Furthermore, electron transport through spin cast PCBM films can consistently be described by the correlated Gaussian disorder model (CDM). This model is based on energetic and spatial disorder. Transmission electron microscopy (TEM) shows that the spin cast films of pure PCBM are homogeneous in appearance, whereas selected-area electron diffraction (SAED) indicates that the films consist of a large number of randomly oriented nanocrystals. The latter, therefore, confirms the disorder as inferred from the CDM-behavior.

A preference for straight and worm-like conformations is observed with scanning force microscopy (SFM) for cast films of symmetrically substituted poly(*p*-phenylene vinylene)s (PPVs), compared to more spiraling conformations for asymmetrically substituted PPV. For thin cast films of symmetrically substituted PPVs, the larger tendency to aggregate into ordered domains and, consequently, the larger zero-field hole mobility observed for symmetrically substituted PPVs seem to result from more linear conformations, as compared to asymmetrically substituted PPVs.

Subsequently, the morphology and performance of solar cells based on mixtures of MDMO-PPV and PCBM have been investigated. A combination of techniques is used to resolve the morphology of these spin cast films on a nanometer scale. These investigations clearly show that a rather homogeneous polymer matrix containing tiny PCBM crystals is present up to 50 weight-percentages (wt.-%) PCBM. Phase separation resulting in large, separate domains of rather pure PCBM in a homogenous matrix of 50:50 wt.-% MDMO-PPV:PCBM sets in for concentrations of more than 67 wt.-% PCBM. Also the large, almost pure PCBM domains consist of tiny PCBM crystals, similar to the nanocrystals of pure PCBM films.

These results are related to the performance of the corresponding solar cells. Electrical characterization, under illumination and in the dark, of the photovoltaic devices revealed a strong increase of the power conversion efficiency when the phase-separated network develops, with a sharp increase of the photocurrent and fill factor between 50 and 67 wt.-% PCBM. As the phase separation sets in, enhanced electron transport and a reduction of bimolecular charge recombination provide the conditions for improved performance.

Finally, the applicability of the full-depth analysis of bulk-heterojunction solar cells has been investigated. A variety of analysis techniques is used to study interface integrity, layer-to-layer diffusion, and contamination levels. Enrichment of oxygen at the interface between Al and the photoactive layer is observed. Furthermore, depth-profiling showed that during preparation diffusion of indium into the PEDOT:PSS occurs under the influence of water, while the diffusion of aluminum into the polymer layers is negligible. TEM of cross-sections, as prepared with a focused ion beam, of fully processed photovoltaic cells, provide a clear view of the individual layers and their interfaces.

No dissociation of LiF upon evaporation of Al onto LiF-covered photoactive layers could be observed with static secondary ion mass spectrometry (SIMS), excluding the doping model as the dominant mechanism for the explanation of the enhanced electron injection by LiF.

The work as described in this thesis clearly shows the necessity for control over nanoscale morphology to guarantee percolation and suppress recombination losses in order to improve the power conversion efficiency. Synergy of material design and film deposition will prove to be of paramount importance to create excellent opto-electronic properties on the one hand, and an optimum balance between a large charge-generation interface and minimal recombination losses in the photoactive layer on the other.

Samenvatting

Plastic zonnecellen staan de afgelopen jaren enorm in de belangstelling als gevolg van de vooruitzichten die zij bieden voor het maken van milieuvriendelijke, flexibele, lichte, goedkope en efficiënte zonnecellen. Met name plastic zonnecellen opgebouwd uit twee elektrodes met daartussen een mengsel van een geconjugeerd donor polymeer en een acceptor fullereen (Figuur 1) worden gezien als veelbelovend. Zonnecellen gebaseerd op zo'n mengsel van een geconjugeerd polymeer met een fullereen bereikten in 2000 een efficiëntie van minder dan 1%. Het verbeteren van de efficiëntie, stabiliteit en levensduur van deze zonnecellen vraagt om meer inzicht in zowel het maken als de werking van dit type zonnecellen.

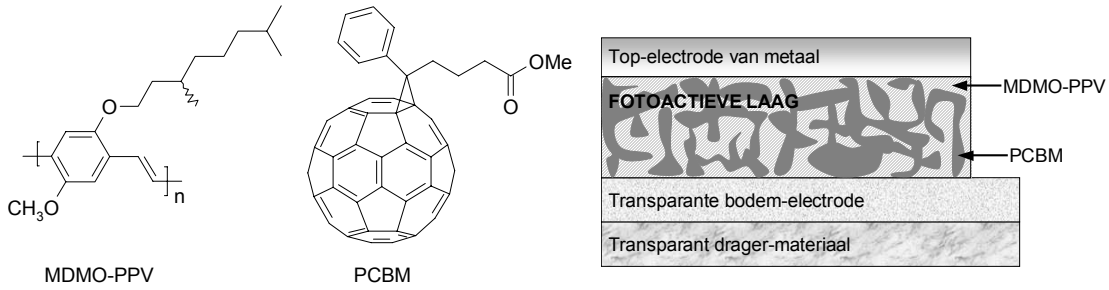

Figuur 1 *Links: Moleculaire structuren van MDMO-PPV en PCBM. De fotoactieve laag bestaat uit een mengsel van MDMO-PPV en PCBM. De structuur van de gehele zonnecel staat rechts weergegeven.*

In dit proefschrift wordt de bereiding en daarnaast de morfologische en elektrische karakterisering behandeld van zonnecellen gemaakt met poly[2-methoxy-5-(3′,7′-dimethyloctyloxy)-1,4-fenyleen vinyleen] (MDMO-PPV), 1-(3-methoxycarbonyl)propyl-1-fenyl-[6,6]-methanofullereen (PCBM) en hun mengsels (Figuur 1). Zonnecellen bestaande uit een mengsel van MDMO-PPV en PCBM halen een efficiëntie van 2.5% onder gesimuleerd zonlicht. Een eerste voorbeeld wordt gegeven waarin MDMO-PPV vervangen is door een materiaal met een nauwe bandafstand, resulterend in een roodverschuiving in de spectrale respons van deze zonnecellen. Deze roodverschuiving is noodzakelijk voor een grotere overlap met het zonnespectrum. In een poging de morfologie op nanometerschaal te controleren wordt ook het eerste voorbeeld beschreven van een werkende zonnecel gebaseerd op een oplosbaar donor polymeer met daaraan covalent gebonden fullerenen. Helaas resulteerden beide experimenten in een afname van de efficiëntie van de zonnecellen in vergelijking met het mengsel van MDMO-PPV en PCBM. Deze resultaten tonen aan dat meer fundamentele vraagstukken aangaande de werking van dit type zonnecellen en de invloed

van de morfologie eerst onderzocht moeten worden, alvorens een rationele verbetering verwacht kan worden.

De morfologie heeft een grote invloed op het transport van ladingsdragers in organische halfgeleidende films. Allereerst zijn films van de afzonderlijke componenten onderzocht. De nul-veld elektronenmobiliteit van puur PCBM (2×10^{-3} cm^2/Vs) bleek 4000 maal groter dan de nul-veld gatenmobiliteit in puur MDMO-PPV (5×10^{-7} cm^2/Vs). Verder kan het elektrontransport door gespincoate PCBM films consistent beschreven worden met het gecorreleerde Gaussische wanordemodel (CDM). Dit model is gebaseerd op energetische en positionele wanorde. In opnames gemaakt met transmissie elektronenmicroscopie (TEM) zijn de gespincoate films van puur PCBM homogeen in voorkomen. Opnames gemaakt met elektronendiffractie, daarentegen, laten zien dat deze films bestaan uit een groot aantal willekeurig georiënteerde nanokristallen. De opnames gemaakt met elektronendiffractie bevestigen dan ook de wanorde afgeleid uit het CDM-gedrag.

Een voorkeur voor (min of meer) rechte ketenconformaties wordt waargenomen met scanning force microscopie (SFM) voor gespincoate films van symmetrisch gesubstitueerde poly(*p*-fenyleen vinylenen) (PPVs). Voor asymmetrisch gesubstitueerde PPVs worden, daarentegen, meer spiraliserende ketenconformaties waargenomen. De grotere neiging om te aggregeren in geordende domeinen en daarmee samenhangend, de grotere nul-veld gatenmobiliteit voor symmetrisch gesubstitueerde PPVs in vergelijking met asymmetrisch gesubstitueerde PPVs, lijkt voort te komen uit de voorkeur voor meer rechte ketenconformaties.

Vervolgens is de morfologie en prestatie van zonnecellen gebaseerd op mengsels van MDMO-PPV en PCBM onderzocht. Een combinatie van technieken is gebruikt om de morfologie van deze gespincoate films op nanometerschaal bloot te leggen. Dit onderzoek laat duidelijk zien dat een vrij homogene polymere matrix met uiterst kleine PCBM kristallen aanwezig is voor samenstellingen tot 50 gewichtsprocenten (gew.-%) PCBM. Fasescheiding resulterend in grote, afzonderlijke domeinen van nagenoeg puur PCBM in een homogene matrix van 50:50 gew.-% MDMO-PPV:PCBM treedt op voor concentraties boven 67 gew.-% PCBM. Verder bestaan ook deze grote, nagenoeg pure PCBM domeinen uit uiterst kleine PCBM kristallen, gelijk aan de nanokristallen in pure PCBM films.

Dit morfologieonderzoek is vervolgens gekoppeld aan de elektrische karakterisering van de corresponderende zonnecellen. Elektrische karakterisering onder belichting en in het donker van deze zonnecellen, laat een sterke toename in de efficiëntie zien wanneer fasescheiding begint. Dit gaat gepaard met een scherpe toename in de fotostroom en vulfactor tussen 50 en 67 gew.-% PCBM. Bij het intreden van de fasescheiding verschaffen een toegenomen elektronenmobiliteit en een afname in de bimoleculaire ladingsrecombinatie de voorwaarden voor een hogere efficiëntie.

Als laatste is de toepasbaarheid onderzocht van analysetechnieken voor het bepalen van de samenstelling in de diepte van de hier beschreven type zonnecellen. Een verscheidenheid aan analysetechnieken is gebruikt om de integriteit van grensvlakken, diffusie tussen lagen en het gehalte

aan vervuilingen te onderzoeken. Een verrijking met zuurstof aan het grensvlak tussen aluminium en de fotoactieve laag is waargenomen. Verder lieten diepte-profileertechnieken zien dat, gedurende de bereiding, diffusie van indium optreedt onder invloed van water, terwijl diffusie van aluminium in de polymeerlagen verwaarloosbaar is. TEM aan dwarsdoorsneden, gemaakt met een gefocusseerde ionenbundel, van complete zonnecellen, geven een duidelijk beeld van de individuele lagen en hun grensvlakken. Dissociatie van LiF na opdampen van aluminium op fotoactieve lagen bedekt met LiF, kon niet worden waargenomen met statische secundaire ionen massaspectrometrie (SIMS). Deze SIMS-metingen sluiten daarom uit dat de verhoogde elektroneninjectie als gevolg van LiF verklaard kan worden met het doteringsmodel als overheersend mechanisme.

Het werk, zoals beschreven in dit proefschrift, laat duidelijk de noodzaak zien voor controle over de morfologie op nanometerschaal om de percolatie van beide componenten te garanderen en verliezen als gevolg van recombinatie te onderdrukken. Dit alles is nodig voor het verhogen van de efficiëntie van de zonnecellen. Synergie van materiaalontwerp en het aanbrengen van de film zal van enorm belang blijken voor het vervaardigen van uitstekende optisch-elektronische eigenschappen aan de ene kant, en een optimale balans tussen een groot grensvlak voor ladingsscheiding en een minimaal verlies als gevolg van ladingsrecombinatie in de fotoactieve laag, aan de andere kant.

Curriculum Vitae

Jeroen van Duren werd geboren op 8 november 1971 te Someren. Na de VWO-opleiding aan het College Asten Someren te Asten, werd in september 1990 begonnen aan de studie Scheikundige Technologie aan de Technische Universiteit Eindhoven. Na een onderbreking van meer dan een jaar, werkzaam als dakdekker en stratenmaker in voornamelijk Duitsland, werd in september 1994 begonnen met 1 jaar psychologie aan de Universiteit van Tilburg. Vanaf september 1995 pakte de auteur van dit proefschrift de draad weer op aan de Technische Universiteit Eindhoven, waar hij in november 1999 het afstudeerproject binnen de capaciteitsgroep Macromoleculaire en Organische Chemie (prof.dr. E.W. Meijer) afrondde. Vervolgens was hij werkzaam voor EET-project EETK97115 als promovendus in dezelfde capaciteitsgroep, onder leiding van prof.dr.ir. R.A.J. Janssen. De belangrijkste resultaten van dit onderzoek staan beschreven in dit proefschrift. Vanaf maart 2004 is hij werkzaam bij Nanosolar te Palo Alto (Californië, Verenigde Staten).

Jeroen van Duren was born in Someren, the Netherlands on November 8th, 1971. He attended the College Asten Someren where he obtained his VWO (pre-university education) degree in 1990. In September 1990 he started the study of Chemical Engineering and Chemistry at the Eindhoven University of Technology. After an interruption of more than a year, working in the road and building industry, mainly in Germany, he studied psychology for a year at the Tilburg University. Subsequently, the author of this thesis went back to the Eindhoven University of Technology in September 1995. He graduated for his Master of Science program in November 1999 with the graduation project at the Laboratory of Macromolecular and Organic Chemistry (Prof. Dr. E.W. Meijer). In December 1999 he started as a Ph. D. student within the EET-project EETK97115, in the Laboratory of Macromolecular and Organic Chemistry under the supervision of Professor Dr. R.A.J. Janssen. The most important results of these investigations are described in this thesis. As of March 2004 he works at Nanosolar in Palo Alto (California, United States of America).

List of Publications

"Synthesis, characterization, and electro-optical properties of a new alternating N-dodecyl pyrrole-benzothiadiazole copolymer", A. Dhanabalan, J.L.J. van Dongen, J.K.J. van Duren, H.M. Janssen, P.A. van Hal, R.A.J. Janssen, *Macromolecules* **2001**, *34*, 2495.

"Design and synthesis of processable functional copolymers", A. Dhanabalan, P.A. van Hal, J.K.J. van Duren, J.L.J. van Dongen, R.A.J. Janssen, *Synthetic Metals* **2001**, *119*, 169.

"Low-bandgap polymer photovoltaic cells", J.K.J. van Duren, A. Dhanabalan, P.A. van Hal, R.A.J. Janssen, *Synthetic Metals* **2001**, *121*, 1587.

"Photoinduced electron transfer and photovoltaic devices of a conjugated polymer with pendant fullerenes", A. Marcos Ramos, M.T. Rispens, J.K.J. van Duren, J.C. Hummelen, R.A.J. Janssen, *Journal of the American Chemical Society* **2001**, *123*, 6714.

"Synthesis and characterization of a low-bandgap conjugated polymer for bulk-heterojunction photovoltaic cells", A. Dhanabalan, J.K.J. van Duren, P.A. van Hal, J.L.J. van Dongen, R.A.J. Janssen, *Advanced Functional Materials* **2001**, *11*, 255.

"Supramolecular hydrogen-bonded oligo(*p*-phenylene vinylene) polymers", A. El-Ghayoury, A.P.H.J. Schenning, P.A. van Hal, J.K.J. van Duren, R.A.J. Janssen, E.W. Meijer, *Angewandte Chemie, International Edition* **2001**, *40*, 3660.

"Real-space measurement of the potential distribution inside organic semiconductors", M. Kemerink, P. Offermans, J.K.J. van Duren, P.M. Koenraad, R.A.J. Janssen, H.W.M. Salemink, J.H. Wolter, *Physical Review Letters* **2002**, *88*, 096803.

"Side-chain-functionalized polyacetylenes, 2a photovoltaic properties", A.P.H.J. Schenning, M. Fransen, J.K.J. van Duren, P.A. van Hal, R.A.J. Janssen, E.W. Meijer, *Macromolecular Rapid Communications* **2002**, *23*, 271.

"Measuring the potential distribution inside soft organic semiconductors with a scanning-tunneling microscope", M. Kemerink, P. Offermans, P.M. Koenraad, J.K.J. van Duren, R.A.J. Janssen, H.W.M. Salemink, J.H. Wolter, *Physica E: Low-Dimensional Systems & Nanostructures* **2002**, *13*, 1247.

"The interfaces of poly(*p*-phenylene vinylene) and fullerene derivatives with Al, LiF, and Al/LiF studied by secondary ion mass spectroscopy and x-ray photoelectron spectroscopy: Formation of AlF_3 disproved", W.J.H. van Gennip, J.K.J. van Duren, P.C. Thüne, R.A.J. Janssen, J.W. Niemantsverdriet, *Journal of Chemical Physics* **2002**, *117*, 5031.

"In-situ compositional and structural analysis of plastic solar cells", J.K.J. van Duren, J. Loos, F. Morrissey, C.M. Leewis, K.P.H. Kivits, L.J. van IJzendoorn, M.T. Rispens, J.C. Hummelen, R.A.J. Janssen, *Advanced Functional Materials* **2002**, *12*, 665.

"The use of the focused ion beam technique to prepare cross-sectional transmission electron microscopy specimen of polymer solar cells deposited on glass", J. Loos, J.K.J. van Duren, F. Morrissey, R.A.J. Janssen, *Polymer* **2002**, *43*, 7493.

"Stimulation of electrical conductivity in a pie-conjugated polymeric conductor with infrared light", S.C.J. Meskers, J.K.J. van Duren, R.A.J. Janssen, *Journal of Applied Physics* **2002**, *92*, 7041.

"Comparison of electrochemical and spectroscopic data of the low-bandgap polymer PTPTB", D. Muehlbacher, H. Neugebauer, A. Cravino, N.S. Sariciftci, J.K.J. van Duren, A. Dhanabalan, P.A. van Hal, R.A.J. Janssen, J.C. Hummelen, *Molecular Crystals and Liquid Crystals Science and Technology, Section A: Molecular Crystals and Liquid Crystals* **2002**, *385*, 85.

"Characterization of polymer solar cells by TOF-SIMS depth-profiling", C.W.T. Bulle-Lieuwma, W.J.H. van Gennip, J.K.J. van Duren, P. Jonkheijm, R.A.J. Janssen, J.W. Niemantsverdriet, *Applied Surface Science* **2003**, *203-204*, 547.

"Electron transport in a methanofullerene", V.D. Mihailetchi, J.K.J. van Duren, P.W.M. Blom, J.C. Hummelen, R.A.J. Janssen, J.M. Kroon, M.T. Rispens, W.J.H. Verhees, M.M. Wienk, *Advanced Functional Materials* **2003**, *13*, 43.

"Infrared detectors with poly(3,4-ethylenedioxythiophene):poly(styrene sulfonic acid) (PEDOT:PSS) as the active material", S.C.J. Meskers, J.K.J. van Duren, R.A.J. Janssen, F. Louwet, L. "Bert" Groenendaal, *Advanced Materials* **2003**, *15*, 613.

"Alternating oligo(*p*-phenylene vinylene)-perylene bisimide copolymers: synthesis, photophysics, and photovoltaic properties of a new class of donor-acceptor materials", E.E. Neuteboom, S.C.J. Meskers, P.A. van Hal, J.K.J. van Duren, E.W. Meijer, R.A.J. Janssen, H. Dupin, G. Pourtois, J. Cornil, R. Lazzaroni, J.L. Brédas, D. Beljonne, *Journal of the American Chemical Society* **2003**, *125*, 8625.

"Relating substitution to single-chain conformation and aggregation in poly(*p*-phenylene vinylene) films", M. Kemerink, J.K.J. van Duren, P. Jonkheijm, W.F. Pasveer, P.M. Koenraad, R.A.J. Janssen, H.W.M. Salemink, J.H. Wolter, *Nano letters* **2003**, *3*, 1191.

"Injection-limited electron current in a methanofullerene", J.K.J. van Duren, V.D. Mihailetchi, P.W.M. Blom, T. van Woudenbergh, J.C. Hummelen, M.T. Rispens, R.A.J. Janssen, M.M. Wienk, *Journal of Applied Physics* **2003**, *94*, 4477.

"Imaging individual chains and aggregates on conjugated polymer films", M. Kemerink, J.K.J. van Duren, P. Jonkheijm, P.M. Koenraad, R.A.J. Janssen, H.W.M. Salemink, J.H. Wolter, *Materials Research Society Symposium Proceedings* **2003**, *771*, 23.

"Thermally induced transient absorption of light by poly(3,4-ethylenedioxythiophene):poly(styrene sulfonic acid) (PEDOT:PSS) films: a way to probe charge-carrier thermalization processes", S.C.J. Meskers, J.K.J. van Duren, R.A.J. Janssen, *Advanced Functional Materials* **2003**, *13*, 805.

"Relating the morphology of poly(*p*-phenylene vinylene):methanofullerene blends to solar cell performance", J.K.J. van Duren, X. Yang, J. Loos, C.W.T. Bulle-Lieuwma, A.B. Sieval, J.C. Hummelen, R.A.J. Janssen, *Advanced Functional Materials* **2004**, *in press*.

"Non-linearity in the *I-V* characteristics of poly(3,4-ethylenedioxythiophene):poly(styrenesulfonate) (PEDOT:PSS) due to Joule heating", S.C.J. Meskers, J.K.J. van Duren, R.A.J. Janssen, *Organic Electronics* **2004**, *in press*.

"Relating the morphology of a poly(*p*-phenylene vinylene):methanofullerene blend to bulk-heterojunction solar cell performance", J.K.J. van Duren, X. Yang, J. Loos, C.W.T. Bulle-Lieuwma, A.B. Sieval, J.C. Hummelen, R.A.J. Janssen, *Proceedings of SPIE Vol. 5215 Organic Photovoltaics IV* **2004**, *in press*.

"Characterization of poly(*p*-phenylene vinylene):methanofullerene blends of polymer solar cells by time-of-flight secondary ion mass spectrometry", C.W.T. Bulle-Lieuwma, J.K.J. van Duren, X. Yang, J. Loos, A.B. Sieval, J.C. Hummelen, R.A.J. Janssen, *Applied Surface Science* **2004***, in press*.

"Crystalline organization of methanofullerene thin films", X. Yang, J.K.J. van Duren, M.T. Rispens, J.C. Hummelen, R.A.J. Janssen, M.A.J. Michels, J. Loos, *Advanced Materials* **2004**, *in press*.

"Morphology and thermal stability of the active layer in poly(*p*-phenylene vinylene):methanofullerene photovoltaic devices", X. Yang, J.K.J. van Duren, R.A.J. Janssen, M.A.J. Michels, J. Loos, *Macromolecules* **2004**, *in press*.

"Plastic infrared detectors based on poly(3,4-ethylenedioxythiophene):poly(styrenesulfonate) (PEDOT:PSS)", S.C.J. Meskers, J.K.J. van Duren, R.A.J. Janssen, *Modern Physics Letters B* **2004**, *in press.*

"Substitution and preparation effects on the morphology of PPV", M. Kemerink, J.K.J. van Duren, A.J.J.M. van Breemen, H.F.M. Schoo, R.A.J. Janssen, *manuscript in preparation.*

"Supramolecular plastic electronics: morphology and performance properties", P. Jonkheijm, J.K.J. van Duren, M. Kemerink, R.A.J. Janssen, A.P.H.J. Schenning, E.W. Meijer, *manuscript in preparation*.

"Depth-profiling and cross-sectioning of plastic solar cells", J.K.J. van Duren, P.C. Thüne, R.G. White, J.G.M. van Berkum, M. Kaiser, C.W.T. Bulle-Lieuwma, J.W. Niemantsverdriet, R.A.J. Janssen, *manuscript in preparation*.

"Quantification by multivariate statistical analysis of binary polymer blend depth profiles measured with dynamic secondary ion mass spectrometry", W.J.H. van Gennip, J.K.J. van Duren, A.B. Sieval, J.C. Hummelen, R.A.J. Janssen, J.W. Niemantsverdriet, *manuscript in preparation*.

"Substitution and preparation effects on the morphology of poly(*p*-phenylene vinylene)", M. Kemerink, J.K.J. van Duren, J. Wildeman, A.J.J.M. van Breemen, H.F.M. Schoo, R.A.J. Janssen, *manuscript in preparation.*

Dankwoord

De afgelopen vier jaar heb ik ontzettend veel geleerd en ben daarbij gesteund en geholpen door een groot aantal mensen waarvan ik een aantal mensen met name wil bedanken. Op de eerste plaats wil ik prof.dr.ir. René Janssen bedanken. De vrijheid die jij mij hebt gegeven gedurende mijn promotie is werkelijk fantastisch. Daarnaast wil ik je bedanken voor alles wat ik van je heb geleerd, met name als het gaat om het opschrijven van onderzoeksresultaten. Als laatste ben ik zeer dankbaar voor het feit dat jij altijd bereid bent om op verzoek tijd vrij te maken. Verder wil ik prof.dr. Bert Meijer bedanken voor de gelegenheid die hij mij heeft geboden om in een groep aan de slag te gaan waar het werkelijk aan niets ontbreekt en me daarnaast vaak met weinig enorm wist te stimuleren.

Graag zou ik prof.dr. Kees Hummelen en de zijnen, met name dr. Minze Rispens en dr. Alex Sieval, willen bedanken voor de gulle giften van fullerenen. Kees, ik wil je in het bijzonder bedanken voor de bereidheid om de gedeutereerde methanofullerenen te synthetiseren. Daarnaast wil ik Philips Research Laboratories, met name dr. Margreet de Kok en dr. Sepas Setayesh bedanken voor de gulle giften van zowel polymeer als substraten. Furthermore, I would like to thank prof.dr.ir. Paul Blom, drs. Valentin Michailetchi, and colleagues for the fruitful collaboration within the EET-project, and the willingness to clarify the organic semiconductor physics when requested. Ook alle andere leden van het EET-project wil ik bedanken voor hun kritische op- en aanmerkingen.

De samenwerking met dr. Corrie Bulle-Lieuwma en dr.ir. Wouter van Gennip resulteerde in een enorme interesse mijnerzijds voor het graven en detecteren met ionenbundels. Allereerst wil ik Corrie bedanken voor haar bereidheid en enthousiasme om deel te nemen aan het zonnecelwerk. Jouw ervaring op het gebied van diepteprofileren aan polymere ‘monsters’ was onontbeerlijk. Daarnaast wil ik Wouter bedanken voor zijn bijdrage aan zowel het diepteprofileren als de oppervlakte analyses. Mijn inziens verschijnt het mooiste SIMS-werk van al onze inspanningen binnenkort van jouw hand.

Verder wil ik dr. Leo van IJzendoorn, dr.ir. Cristian Leewis en ir. Koen Kivits bedanken voor hun interesse en bereidheid de kostbare cyclotron-meettijd met ons te delen. Tevens bedankt dat jullie mij de mogelijkheid hebben geboden om de metingen bij het cyclotron ‘life’ bij te wonen.

I would like to thank dr. Joachim Loos and dr. Xiaoniu Yang for their beautiful electron microscopy contributions. Joachim, thank you for your willingness to collaborate, far before the joint forces within the DPI-project. Xiaoniu, thanks a lot for your time and effort. Especially, your selected-area electron-diffraction contribution was marvellous.

Met veel plezier bedank ik dr.ir. Martijn Kemerink, dr. Stefan Meskers en dr. Albert Schenning. Alleerst Martijn. Jouw harde III-V aanpak in combinatie met mijn zachte, polymere aanpak heeft toch mooi geleid tot een prachtig stukje werk. Ik wil je dan ook bedanken voor de prachtige bijdrage en daarnaast voor je bereidheid de (organische) half-geleider physica op verzoek

toe te lichten. Verder wil ik Stefan bedanken voor de kritische opmerkingen tijdens de werkbesprekingen en de heldere uitleg van fotospectroscopische processen. Ik wil je in het bijzonder bedanken dat je mijn kleine bijdrage aan jouw werk zo hebt gewaardeerd. Als laatste, Appie. Naast het vervaardigen van de gesubstitueerde polyacetylenen ben ik er van overtuigd dat je het minstens zo goed had gedaan als Ghandhi in de animatie-serie "Ghandhi embracing the brandhout troffee for life".

Van de TNO-collega's op het lab wil ik met name ing. Kornel Hoekerd bedanken. Je bereidheid om je opgedane ervaring met het maken en meten van polyLEDs met mij te delen, heeft ervoor gezorgd dat ik bij aanvang van mijn promotie niet vooraan hoefde te beginnen. Dr. Marc Koetse wil ik bedanken voor het meten van een groot aantal spectrale responsen.

Gedurende de eerste twee jaar van mijn promotie heb ik mogen werken met mooie, nieuwe SMO-materialen waarvan er slechts twee staan beschreven (hoofdstuk 2) in dit proefschrift. Zeker daar synthese van nieuwe materialen soms een tijdrovend karwei kan zijn, wil ik jullie allemaal bijzonder bedanken dat jullie bereid waren de wereldvoorraad van deze nieuwe aanwinsten aan mij te overhandigen, opdat ik deze er vervolgens in een mum van tijd doorheen kon jassen. First of all, King Dhan (dr. Anantharaman Dhanabalan). Thanks man! All the best for you, your wife, and your children. Second, dr. Alicia Marcos Ramos for the beautiful double cable. Third, ir. Pascal Jonkheijm and dr. Abdelkrim El-Ghayoury. Pascal, ook al ben je een Zeeuw, je bent niet 'zunig' met je tijd voor anderen. Abdel, it is a shame you leave to France. Now you will never learn how to play soccer.

Ir. Owen Plaisier, Frans Snik, Frank Verbakel en Marijn Kappers wil ik bedanken voor hun inzet en interesse. Succes met het vervolg van jullie opleiding. Verder wil ik mijn kamergenoten dr. Bea Langeveld-Voss, dr. John van Haare en ir. Waldo Beek bedanken voor de vele discussies. Furthermore, I would like to thank dr. Francis Morrisey, dr. Monja Kaiser, dr. Jurgen van Berkum, dr. Peter Thüne, and dr. Richard White for their contributions.

Daarnaast wil ik Hans Damen, Hanneke Veldhoen, Ingrid Dirkx, Joke Rediker, Carine van der Vaart, Henk Eding, Hannie van der Lee (olé olé), Ingrid Schepens en Dianne Vogels bedanken dat zij binnen SMO alles gesmeerd laten verlopen. Verder wil ik Theo Maas, Jos de Laat, Frans Kuijpers en medewerkers van de gemeenschappelijke technische dienst bedanken voor hun goude handjes.

Naast alle wetenschappelijke activiteiten, heb ik de afgelopen jaren ook enorm kunnen lachen. Hard gelach, de schaterlach, de glimlach, de boer met kiespien en buikpijn van het lachen. Zowel tijdens als buiten werktijd heb ik enorm gelachen met ing. Joost van Dongen, dr.ir. Henk Janssen en dr. Tonny Bosman. Joost, probeer je outfits van de 70ties en 80ties parties eens niet te dragen tijdens werktijd. Henk, waarom onderbreek je ieder gesprek om onze aandacht te vestigen op de vrouwen die voorbij lopen? Tonny, een Elvis fan zonder bakkebaarden is als een hitsige dame alleen.

Als laatste, wil ik mijn familie en vrienden enorm bedanken voor hun steun en de broodnodige ontspanning en relativering die ik de afgelopen paar jaar bij hen heb gevonden.

Jeroen